HHS Public Access

Author manuscript

Chem Rev. Author manuscript; available in PMC 2023 May 20.

Published in final edited form as:

Chem Rev. 2022 July 27; 122(14): 11974–12045. doi:10.1021/acs.chemrev.2c00106.

Designing Artificial Metalloenzymes by Tuning of the Environment beyond the Primary Coordination Sphere

Casey Van Stappen[†],
Department of Chemistry, University of Texas at Austin, Austin, Texas 78712, United States

Yunling Deng[†],
Department of Chemistry, University of Texas at Austin, Austin, Texas 78712, United States

Yiwei Liu,
Department of Chemistry, University of Illinois, Urbana-Champaign, Urbana, Illinois 61801, United States

Hirbod Heidari,
Department of Chemistry, University of Texas at Austin, Austin, Texas 78712, United States

Jing-Xiang Wang,
Department of Chemistry, University of Texas at Austin, Austin, Texas 78712, United States

Yu Zhou,
Department of Chemistry, University of Texas at Austin, Austin, Texas 78712, United States

Aaron P. Ledray,
Department of Chemistry, University of Texas at Austin, Austin, Texas 78712, United States

Yi Lu
Department of Chemistry, University of Texas at Austin, Austin, Texas 78712, United States;
Department of Chemistry, University of Illinois, Urbana-Champaign, Urbana, Illinois 61801, United States

Abstract

Metalloenzymes catalyze a variety of reactions using a limited number of natural amino acids and metallocofactors. Therefore, the environment beyond the primary coordination sphere must play an important role in both conferring and tuning their phenomenal catalytic properties, enabling active sites with otherwise similar primary coordination environments to perform a diverse array of biological functions. However, since the interactions beyond the primary coordination sphere are numerous and weak, it has been difficult to pinpoint structural features responsible for the tuning of activities of native enzymes. Designing artificial metalloenzymes (ArMs) offers an excellent basis to elucidate the roles of these interactions and to further develop practical biological catalysts. In this review, we highlight how the secondary coordination spheres of ArMs influence metal binding and catalysis, with particular focus on the use of native protein scaffolds

Corresponding Author Yi Lu – Department of Chemistry, University of Texas at Austin, Austin, Texas 78712, United States; Department of Chemistry, University of Illinois, Urbana-Champaign, Urbana, Illinois 61801, United States; yi.lu@utexas.edu.
[†]C.V.S. and Y.D. contributed equally.

as templates for the design of ArMs by either rational design aided by computational modeling, directed evolution, or a combination of both approaches. In describing successes in designing heme, nonheme Fe, and Cu metalloenzymes, heteronuclear metalloenzymes containing heme, and those ArMs containing other metal centers (including those with non-native metal ions and metallocofactors), we have summarized insights gained on how careful controls of the interactions in the secondary coordination sphere, including hydrophobic and hydrogen bonding interactions, allow the generation and tuning of these respective systems to approach, rival, and, in a few cases, exceed those of native enzymes. We have also provided an outlook on the remaining challenges and future directions gain a deeper understanding of the secondary coordination sphere, and in turn guide the design of a broader and more efficient variety of ArMs.

Graphical Abstract

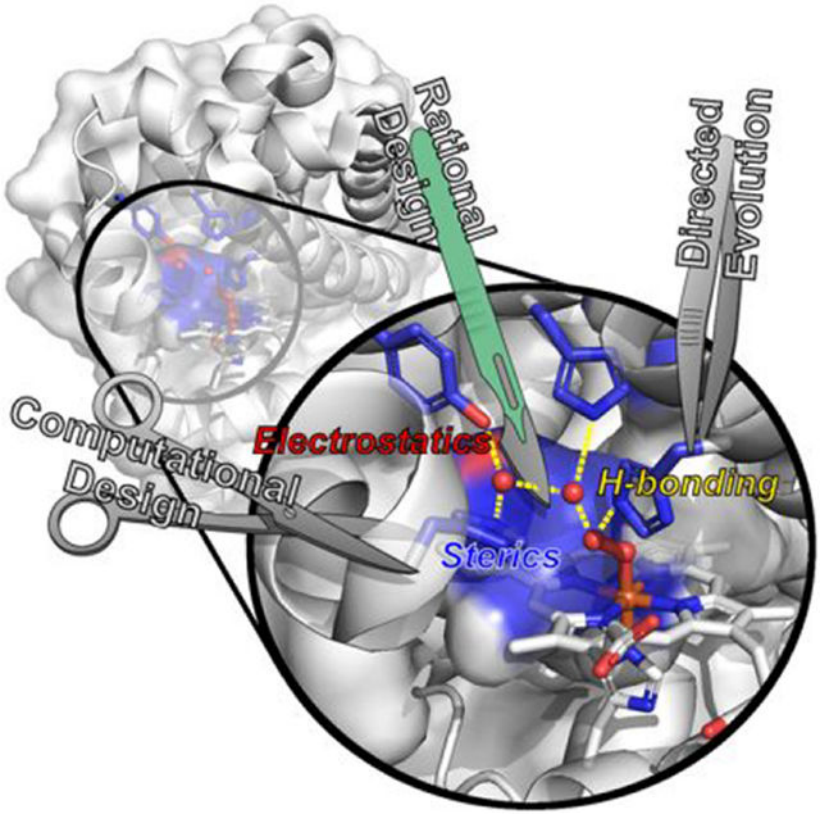

1. INTRODUCTION

Metalloproteins are ubiquitous in nature; a bioinformatic search of three-dimensional protein structures deposited in the Protein Data Bank in 2008 found ~40% to bind metal ions, with estimates ranging between 36 and 59% in different classes.[1] A metallomics study in 2010 indicated that microbial metalloproteomes are largely uncharacterized,[2] putting the estimate of metalloproteins among all proteins over 50%. Many of these metalloproteins function as metalloenzymes, performing the essential processes to support life as it is known, ranging from metabolism[3-14] and DNA synthesis[15-18] to the generation of atmospheric O_2[19,20] and

nitrogen fixation.[21-24] Even more so, the stunning range of chemistry performed in these native systems is done so not only within the limited conditions conducive to life but also using a comparatively narrow range of biologically available ligands and metallocofactors. It is little wonder then that metalloenzymes have captivated chemists and biochemists alike for decades, and tremendous efforts have been undertaken across these fields to understand the intimate details of metalloenzyme functions.

The biologically available ligands for the formation of the primary coordination sphere (PCS) in metalloenzymes include the side chains of nucleophilic amino acid residues such as His, Asp, Glu, Arg, Met, Ser, Tyr, and Cys, the amine and carboxylate protein termini, the carbonyl and amide moieties of the protein backbone, small molecules such as CO, CN^-, H_2O, O_2, S^{2-}, and ^-OH, and biosynthesized organic cofactors such as protoporphyrins, corrins, pterins, azadithiolate, and homocitrate.[25] These PCSs play critical roles in defining the available chemistry of an active site. A primary example is the heme *b* center, which consists of an iron center equatorially coordinated by the four nitrogen atoms of the protoporphyrin IX macrocycle and axially by one or two amino acids above and/or below the protoporphyrin ring. While undeniably important, abundant evidence from the study of metalloenzymes has shown that the same PCS environment, such as heme *b*, can display a variety of different properties from electron transfer to reversible O_2 binding, dioxygen reduction, and small molecule functionalization.[26] As a result, these heme proteins perform a wide range of biological processes, including O_2 transport (globins),[27-29] cell signaling,[30-32] electron transfer,[33-35] and enzymatic activities such as catalases,[36-40] oxidases,[41,42] oxygenases,[43-45] peroxidases,[46-48] nitric oxide reductases,[49-51] and sulfite reductases.[52-54] Therefore, features of the protein environment beyond the PCS are essential in not only fine-tuning the activities of metalloenzymes but also conferring new activities in otherwise similar systems.

Unlike the PCS itself, the environment surrounding the PCS consists of many weak and noncoordinating interactions such as hydrogen bonding (H-bonding), electrostatic, and hydrophobic interactions. Some may contribute little, if any, to protein function, while others play major roles that enable many metalloenzymes to catalyze reactions that are currently unparalleled by synthetic catalysts in terms of activity and/or reaction efficiency. Therefore, elucidating the structural features in these secondary coordinate spheres (SCSs) that are responsible for activity not only advances our knowledge about biology but can also result in novel synthetic catalysts or artificial metalloenzymes (ArMs) with new activity or reactivity for many industrial applications, such as producing energy from sustainable sources and synthesizing pharmaceutical drugs.

The study of native metalloenzymes is undeniably essential in providing a detailed understanding of their function. Despite major progress in many facets, however, it has been difficult to comprehensively elucidate how these enzymes catalyze so many reactions highly efficiently using structural features beyond the PCS. Such difficulties arise in large part because the PCSs of many native enzymes reside in large and complicated proteins, some of which are membrane proteins, that are not (yet) compatible with heterologous expression. As a result, it is very difficult to carry out site-directed mutagenesis (SDM) to probe the roles of SCS residues and to purify them to homogeneity in high

enough yields for traditional studies. In addition, many native metalloenzymes contain multiple metallocofactors that can produce overlapping spectroscopic signals which make it challenging to focus on the PCS of interest.[12,55,56] Furthermore, many similar PCSs reside in very different protein scaffolds containing numerous different residues, making it difficult to identify the key SCS residues responsible for the different reactivity. Designing artificial metalloenzymes (ArMs) using small robust protein scaffolds that can be readily constructed, expressed, and purified in simple hosts such as *E. coli* can overcome the above limitations, because these ArMs contain only the PCS of interest and free of interferences from other cofactors. By placing the same PCS in the same protein scaffold and systematically introducing SCS residues from different enzymes with varying reactivity, we can provide a holistic view of the key structural features responsible for the differences in activity. Therefore, designing ArMs that reproduce the catalytic capacities of native enzymes not only provides the ultimate basis to test what we know about native catalytic mechanisms but also reveals new insights that are not readily obtainable from studying native enzymes, much in spirit with a quote from the late Prof. Richard Feynman, “What I cannot create, I do not understand.”[57] Given their small, robust scaffolds, ArMs provide a new, *divergent* opportunity to combine the benefits of both chemical catalysis and biocatalysis, allowing the power of SCS interactions to be harnessed to enhance catalytic selectivity in new-to-nature reactions.

ArMs can be generally designed using one of the following systems: (1) modifying an existing meta-binding site in a native enzymatic scaffold to promote non-native reactivity, (2) introducing a new metal-binding site to a native protein scaffold without such a site, and (3) designing a metal-binding site in a *de novo* designed protein scaffold. To achieve this goal, the most common strategies employed include rational design and directed evolution. Rational design involves the purposeful mutation of select residues or regions of a protein scaffold using SDM to incorporate a metal-binding site and/or modulate activity based on careful deliberation over available structural information and often from comparisons with related systems. Such design is often aided by comparing key residues between the native enzymes and ArMs and using the experience and knowledge gained from studying native enzymes, or by computations, to predict and then experimentally verify the roles of these residues. Although immensely successful, this approach is still limited by human intuition and/or the ability of computational programs to capture the structural and functional properties of metalloenzymes, and remains challenging because of highly variable PCSs and weak SCS interactions. Alternatively, directed evolution based on a random library to screen or select for desired activity followed by detailed structural and mechanistic studies of the “winners” can provide an understanding of the roles of residues in not only the SCS but also those much further away in conferring and fine-tuning the activities.[58-60] More recently, computational methods using programs that employ large structural databases and machine learning, such as Rosetta[61,62] and AlphaFold,[63,64] have emerged as powerful tools for the exploratory design of novel ArMs *in silico,* allowing a much broader scope of protein scaffolds and variants to be surveyed for desired properties, which can then be tested *in vitro.*

In the present review, we focus on how rational design and directed evolution have provided insight into the roles of the SCS in tuning the functionality of ArMs, with particular

emphasis toward systems employing natural protein scaffolds and exhibiting catalytic activity. A more comprehensive perspective on catalysis and electron transfer by *de novo* metalloenzymes can be found in the review of Pecoraro and co-workers in this issue, and several recent reviews provide detailed coverage of the design and breadth of applications of these scaffolds.[65-68] For extensive reviews of the design and catalytic capabilities of ArMs, we refer the reader to many outstanding reviews in this area.[69-77] Fe- and Cu-based ArMs constitute a major portion of designed metalloenzymes, and therefore, this review has been broadly organized into sections addressing the fields of heme Fe, nonheme Fe, and Cu followed by multinuclear ArMs, and finally systems containing alternative metal cofactors including V, Cr, Mn, Co, Ni, Zn, Ru, Rh, Pd, and Ir.

2. CATALYSIS BEYOND THE PRIMARY COORDINATION SPHERE BY HEME PROTEINS WITH NON-NATIVE FUNCTIONS

Heme proteins are among the most, if not the most, studied metalloproteins, and their functions range from electron transfer to O_2 carrier, catalases, peroxidases, oxidase, and oxygenase. They perform these functions using different types of heme, such as heme *a, b, c, d,* and *f.* The different types of the heme have a similar core consisting of Fe and a porphyrin ring. Even the same type of heme (e.g., heme *b*) can catalyze very different and diverse reactions. Therefore, structural features beyond such PCSs must play important roles in defining and tuning the functions. Designing ArMs to mimic these native heme proteins using much smaller and robust heme proteins, such as myoglobin (Mb), cytochrome *c* (C*c*), and cytochrome *c* peroxidase (C*c*P), allows not only testing of what we know about similarities and differences among these proteins but also revelation of new insights.

2.1. Rational Design Using Myoglobin as a Scaffold

Myoglobin (Mb) is a molecular oxygen carrier that natively serves to reversibly bind O_2 using a heme *b* center.[78,79] The ready heterologous expression of Mb variants in *E. coli.* has made this enzyme a popular scaffold for rational designs of heme enzymes with a range of activity far beyond its native function.[80-82] Furthermore, the small size, high solubility in water, and ready crystallizability of Mb have also made it accessible to an array of biochemical and biophysical methods to investigate the role of SCSs in catalysis.[83-88]

Myoglobin belongs to the globin superfamily of proteins, consisting of eight α-helices connected by a short loop region (Figure 1a).[89] The endogenous active site of Mb consists of a heme *b* center (Figure 1b) in which Fe is proximally coordinated by histidine through the N_ε position. This PCS is ubiquitous among globins and is presented in some heme peroxidases as well.[90-92] Therefore, the differences in activity observed between Mb, other globins, and peroxidases must arise from differences in structure beyond the PCS.

2.1.1. From Myoglobin to Peroxidase.—In addition to its well-known function as an O_2 carrier, Mb is also capable of performing oxidation reactions in the presence of hydrogen peroxide (H_2O_2).[93-95] However, the peroxidase activity of wild-type (WT) Mb is much lower than that of native peroxidases (2.7 $M^{-1}s^{-1}$ vs 130 $M^{-1}s^{-1}$).[96] Native peroxidases are a large group of enzymes that catalyze several critical redox reactions,

including alkene oxidation, sulfoxidation, and dehalogenation. All peroxidases share similar PCS environments to that of ferric Mb, with the fifth coordination site of Fe occupied by a proximal histidine side chain and the sixth coordination position occupied by a water in the resting state. However, peroxidases possess a highly conserved Arg residue in the distal pocket, which is absent in Mb (Figure 1c).[97,98] Interestingly, both Mb and peroxidases contain a His residue in the distal pockets (His64 in Mb and His52 in C*c*P). Comparing the X-ray structures of C*c*P and Mb reveals that the distal His of Mb is closer to the heme iron than in C*c*P, which may be responsible for the differences in the interaction of these enzymes with the H_2O_2 substrate.[89,97] By relocating the distal His residue in Mb through a F43H/H64L double mutant, the Watanabe group was able to produce a Mb with catalytic rates for sulfoxidation and epoxidation similar to those of native C*c*P, without introducing Arg.[99] The distal His64 in WT-Mb, which is 4.3 Å from the heme iron, was determined to be a critical residue for the lifetime of the active intermediate (**compound I**) and, therefore, activity with H_2O_2. The presence of His64 in WT-Mb presumably results in rapid electron transfer from **compound I** to His64. Replacement of His64 with a non-oxidizable Leu residue may prevent generation of the protein radical. As the His64 in native Mb is too close to the heme Fe to support the heterolytic cleavage of H_2O_2, the relocation of the distal His by F43H mutation led to a proper distancing between the N_ε atom of His and the heme Fe, which perfectly resembled the corresponding distances in native peroxidases. The appropriate positioning of the distal His in F43H/H64L allows the distal His to function as both a general base to facilitate the H_2O_2 binding through the deprotonation step and a general acid to aid the heterolytic cleavage of the O—O bond in H_2O_2 via H-bonding. As another corroboration of the importance of the proper positioning of the distal His in Mb for peroxidase functions, the L29H/H64V mutant exhibited a ~3–6 slower reaction rate with H_2O_2 relative to the native Mb as the imidazole of His29 is too far away to interact with the H_2O_2 substrate.[100] As another example of mimicking the structural features of the native peroxidase, Wu, et al. found that introduction of two His residues near the active site through the L29H/F43H double mutant produces a SCS resembling the His-Arg pair that is frequently observed in native peroxidases.[101] An additional H64A mutation further opened a channel to the heme active center, positively influencing the peroxidase activity.

In addition to enhancing the sulfoxidation and epoxidation reactions in Mb, arene oxidation activity has also been introduced into Mb by mimicking the active site of cytochrome P450 (P450). The differences in reactivity between WT-Mb and P450 may arise from variations in the SCS; for example, *d*-camphor is capable of tightly binding to the hydrophobic heme pocket of P450 through a hydrogen bonding interaction with the hydroxyl group of Tyr96,[103] while the active site of WT-Mb does not afford specific interactions for accommodating organic substrates. Using crystallography, it was found that the distance between carbon atoms C6 and C7 of the electron-rich Trp43 residue and the heme iron in the F43W/H64L Mb mutant was similar to the distance between C5 of *d*-camphor and the iron in $P450_{cam}$ (Figure 2). The development of the double mutant F43W/H65L Mb resulted in a six-electron oxidative modification of Trp43 in the presence of strong sacrificial oxidant, *m*-chloroperbenzoic acid (*m*CPBA), representing the first example of oxidation of an aromatic ring by Mb.[104]

As conserved residues near the active site of Mb, both His64 and Val68 have been shown to influence the affinity of ligand binding (e.g., O_2 and CO).[105,107] To investigate the role of Val68 in influencing the rate and enantioselectivity of oxidative reactions, Yang et al. engineered a series of H64D/V68X Mb mutants (X = Ala, Ser, Val, Ile, Leu, and Phe) (Figure 3).[106] Along this series, the V68L mutation was observed to activate H_2O_2 most efficiently, while decreased peroxidase activity was found for both V68I and V68A variants, highlighting that subtle changes in the interactions between residue 68 and the substrate can have profound effects on catalysis. In this case, the restricted rotation of the Ile side chain was found to hinder the association of H_2O_2 at the heme iron center. While removing this steric constraint via a V68A mutation should hypothetically allow association, structural data indicate that this variant allows for the introduction of a distal water molecule which then blocks substrate entrance, demonstrating the balance required for optimization of catalytic activity.

As another route to engineering peroxidase activity, the introduction of stabilizing forces through disulfide bond formation offers a great opportunity to increase protein stability while tuning enzymatic function. For instance, disulfide bonds have been observed in neuroglobin (Ngb)[108] and cytoglobin (Cgb)[109] and have been shown to regulate ligand binding and migration. Similar disulfide bonds have been incorporated into Mb at different positions through variants containing F46C/M55C and V21C/V66C/F46S mutations (Figure 4).[110,111] The presence of the disulfide bond in F46C/M55C Mb was found to increase both protein stability and peroxidase function.[110] Meanwhile, the V21C/V66C/F46S Mb variant demonstrated comparable activity to F46S Mb, but with a ~30% reduction in K_m, indicating that the presence of the disulfide bond stabilizes a favorable conformation for substrate binding.[111]

2.1.2. From Myoglobin to Dehaloperoxidase.—Dehaloperoxidase (DHP) is a heme protein that catalyzes the dehalogenation of halophenols to nontoxic quinone products.[112,113] Halophenols are involved in the synthesis of pesticides and even used as pesticides themselves, which may lead to severe damage to the mammalian liver and immune system.[82] They can also be readily oxidized to produce carcinogenic radicals capable of modifying DNA bases. Therefore, native peroxidases such as DHP may have important environmental and economic implications for degradation of industrial dyes and halophenols. Despite their potential applications, the use of bioremediation is often hindered by the limited catalytic efficiency of native enzymes.[82] Rationally designed artificial enzymes offer an alternative route to generating functional biocatalysts. Mb-based ArM models for DHP have emerged as efficient catalysts for biodegradation. Despite the low sequence homology between DHP and Mb, the two proteins share a remarkably similar protein fold, with the RMSD between the positions of C atoms being 1.8 Å (Figure 5).[92]

The mechanism of dehalogenation by dehaloperoxidases has also been analyzed using both “peroxidase-like” Mb mutants and “Mb-like” DHP.[114] To mimic the distal His-to-Fe distance in DHP, the authors successfully generated G65T and G65I Mb variants in an effort to position the distal His64 farther from the heme iron (Figure 5). As a result, a more than 5-fold increase in k_{cat} for the oxidative dichlorination reaction was observed relative to WT-Mb, highlighting the subtle changes of nonactive site residues can induce changes in the

PCS through both the restrictions imposed by the position of the peptide backbone as well as through the hydrogen bond network.

Studies have shown that a novel tyrosine-heme covalent C—O bond cross-link can be formed in the F43Y Mb mutant (Figure 6a),[115] which has provided a platform for engineering Mb variants as biosynthetic models of dehaloperoxidases. The F43Y Mb variant itself displays enhanced dehaloperoxidase activity 115-fold higher than WT-Mb and 9-fold higher than native DHP in the presence of 2,4,6-trichlorophenol (TCP) substrate.[116] The presence of multiple Tyr and Trp residues in native dye-decolorizing peroxidases (DyPs) has also inspired the engineering of Mb variants with additional Tyr or Trp mutations, building on the F43Y Mb platform. Interestingly, the double mutant F43Y/F138W exhibits ~4.3-fold greater peroxidase activity than native DyP from *Vibrio cholerae*.[117] This enhanced activity presumably arises from the more rapid generation of the oxidizing species and protein radicals.

In 2018 Yin et al. combined structural features from both chloroperoxidase (distal Glu) and DHP (distal Tyr) by generating a F43Y/H64D Mb mutant (Figure 6b), which resulted in a 1000-fold increase in catalytic efficiency relative to native DHP from *A. ornata*.[118] The crystal structure (Figure 6c) of this mutant in complex with TCP revealed that Asp64 adapts an open conformation when substrate is bound, highlighting the crucial role of this residue in modulating the substrate binding.

Beyond dehalogenation, the F43Y Mb platform has been employed in the biosynthesis of indigo from indole. While it has been shown that replacement of the distal His64 in Mb with Asp would favor the H_2O_2-dependent oxidation reaction,[120] the double mutant F43Y/H64D exhibits the highest efficiency toward the oxidation of indole to indigo reported to-date.[121] More recent work employing a triple mutant based on the F43Y platform has achieved comparable catalytic efficiency to the most efficient native horseradish peroxidase (HRP), where the combination of T67R and F138W mutations is used to mimic the His-Arg pair and conserved Trp residues of native peroxidases.[122] The scope of engineered Mb-based catalysts has also been expanded to biodegradation applications; for example, the F43H/H64A Mb mutant successfully catalyzed the biodegradation of malachite green (MG) with even higher efficiency than natural enzymes such as dye-decolorizing peroxidase and laccase.[123] Molecular modeling indicates that these active site mutations favor the binding of MG in the heme distal pocket.

2.1.3. From Myoglobin to Carbene Transferase.—Beyond peroxidase and dehaloperoxidase activity, Mb has also been redesigned to promote carbene transfer reactions.[124-128] Carbenes are formally neutral divalent carbon species whose activity can be attributed to an incomplete octet electronic configuration.[129] Recent protein engineering efforts have revealed that carbene transfer can be catalyzed in heme proteins, including Mb, via an iron porphyrin carbene intermediate, providing a whole new pathway for the biosynthesis of important molecules (Scheme 1).[130] In 2015, Bordeaux et al. discovered that WT-swMb exhibits cyclopropanation activity without asymmetric induction.[124] Inspired by these results, further Mb-based catalysts have since been developed with both higher activity

and selectivity toward cyclopropanation, as well as expanded the substrate scope, including olefin cyclopropanation,[124] carbene NH insertion,[131] and carbene SH insertion reactions.[125]

One of the first efforts to improve the cyclopropanation activity of Mb involved varying the steric bulk properties at the active site residues Phe43, His64, and Val68 of Mb, resulting in the development of the H64V/V68AMb variant, which exhibits high activity and selectivity toward the cyclopropanation of styrene with ethyl diazoacetate (EDA) (Figure 7).[124] Based on the available crystal structures of related Mb- and Fe-(porphyrin)/carbene complexes, it has been proposed that the H64V mutation aids in promoting substrate access to heme, while the V68A mutation expands the size of the distal cavity and, thus, has a dramatic effect on enantioselectivity.

The reaction scope of the H64V/V68A Mb mutant has also been explored beyond cyclopropanation, demonstrating activity toward carbene N-H insertion with arylamine substrates.[131] For the H64V/V68A Mb mutant, the yield for *N*-methylaniline was relatively low. An improved activity could be achieved through the L29A, H64V, and L29A/H64V variants. The beneficial effects of the L29A mutation may arise from a decrease in steric bulk directly above the heme iron site, allowing the amine substrate to be accommodated. In addition, H64V/V68A Mb has also exhibited promising reactivity toward C-H functionalization of indole at the C3 position.[132] This enhanced activity (relative to WT-Mb and H64V Mb) is mainly attributed to the V68A mutation, which enlarges the active site near the heme group to facilitate attack of the heme-bound carbene by indole. The presence of an N1 or C2 substituent on indole resulted in significantly diminished substrate conversions, a limitation that was partially overcome in L29F/H64V Mb. This increase in activity was hypothesized to arise from Phe29 helping to orient the indole substrate into a favorable position via π-stacking interactions.

Along a similar vein, Tyagi et al. identified the L29A/H64V mutant as a promising catalyst for carbene S-H insertion by examining a panel of Mb variants with mutations at residues lining the active site, specifically 29, 43, 64, 68, and 107.[125] The greatest enhancement for a single mutation was observed in the L29A Mb variant, which may arise from its role in facilitating the nucleophilic attack of thiol or amine to the heme-bound carbene intermediate by expanding the distal cavity above the heme. Further examination of mutations at these positions has also revealed the F43V/V68F Mb variant, which catalyzes the olefination of aldehydes with excellent efficiency and E diastereoselectivity.[128]

In 2019, Vargas et al. expanded the substrate scope of Mb to accommodate the larger benzofuran substrate and, in doing so, established the important role of residue 64 in H64X/V68A variants in controlling access of the olefin substrate.[133] By decreasing side chain steric bulk, progressively improved catalytic activity could be achieved along the series His$\ll$Val < Ala < Gly. This “gating” effect has also been manifested in more recent work, where a decreasing size of the residue 64 side chain enhanced the cyclopropanation activity in the presence of a diazoketone carbene donor by removing the steric hindrance.[134]

Taken together, these experimental results illustrate how the catalytic activity and selectivity toward different amine substrates can be modulated by modification of the Mb active

site. Although the engineered Mb variants represent a superb platform for carbene transfer catalysis, the precise structural features that govern protein-mediated stereocontrols are yet to be fully elucidated. This problem was not resolved until a crystallographic and computational (DFT) analysis of the H64V/V68A mutant (Figure 7) revealed that stereocontrol of the cyclopropanation reaction by active site mutagenesis is achieved by favoring a specific conformation of the heme-bound carbene and control geometry of the attack of the olefin through steric obstruction, van der Waals forces, and $\pi-\pi$ interactions.[135]

2.1.4. From Mb to Nitrite Reductase (NiR).—To study the Tyr-Cys cross-linking phenomenon, which is ubiquitous in a variety of metalloenzymes, an unnatural amino acid 2-amino-3-(4-hydroxy-3-(methylthio)phenyl)propanoic acid (MtTyr) was incorporated into a functional model of *T. nitratireducens* cytochrome *c* nitrite reductase (TvNiR) engineered into swMb by Zhou, et al. The enzymatic activity was determined based on the reduction of hydroxylamine to ammonium by models both containing and lacking MtTyr (MtTyrMb and TyrMb, respectively) as mimics for the presence/absence of the Tyr-Cys cross-link. A 4-fold increase in k_{cat} was found for the MtTyrMb variant, supporting the hypothesis that thioester modification on Tyr helps to enhance NiR activity.[136]

2.2. Rational Design Using Cytochrome *c* Peroxidase as a Scaffold

Peroxidases are a large family of enzymes that function to catalyze the reduction of H_2O_2 in the presence of various substrates. Notably, cytochrome *c* peroxidase (C*c*P) and ascorbate peroxidase (APX), two iconic members of this family, do not share any common reducing substrates despite having numerous structural similarities. Since the structures of C*c*P and APX mainly differ in the ascorbate binding site, Meharenna et al. engineered an ascorbate-binding site into C*c*P to repurpose the function of C*c*P toward the non-native substrate (Figure 8a).[137] This hybrid protein was generated by replacing native residues 30–42 in C*c*P with the ascorbate binding site residues 27–32 in APX. In addition, a conserved Arg residue in APX, which is thought to facilitate ascorbate binding via H-bonding, was anchored at position 184 in C*c*P. The resulting hybridized mutant was found to catalyze the peroxidation of ascorbate at a rate of about 12 min^{-1}.

Peroxidases are natural platforms for engineering peroxygenation reactions since they react efficiently with hydrogen peroxide. The low peroxygenase activity of C*c*P may be attributed to the low affinity of the heme pocket for apolar substrates. In 2013, Erman et al. employed the C*c*P platform to build specific peroxygenation activity into C*c*P to mimic P450 monooxygenases.[138] In particular, a triple C*c*P variant, R48A/W51A/H52A (Figure 8b), was designed to replace the H-bonding residues in the distal heme pocket with residues containing apolar side chains in order to promote binding of the organic substrate 1-methoxynaphthalene. The naphthalene hydroxylation activity of this engineered C*c*P mutant was 34-fold greater than that ofWT-C*c*P and even comparable to that of WT-P450.

In many cases, the catalytic potentials of native enzymes originate from key transition metal centers in the active site. However, redox active amino acids, such as Trp and Tyr, can also play a pivotal role in catalysis, and the surrounding microenvironments of these residues

are essential in tuning their redox potential.[140,141] This is true for lignin peroxidase (LiP), a fungal enzyme that plays a key role in the ligninolytic cycles for the degradation of the complex polymer lignin.[142] The surface Trp171 residue of LiP is proposed to be the site of lignin oxidation, where the surrounding negatively charged residues (Asp264, Asp165, Glu168, and Glu250) provide an acidic microenvironment that enhances the oxidation potential of $Trp^{\bullet+}$.[143,144] Taking inspiration from LiP, Smith, Ivancich, and co-workers redesigned *Coprinus cinereus* peroxidase (CiP) by incorporating a surface Trp residue (D179W) along with two negatively charged neighboring residues (R258E and R272D) to impart activity toward veratryl alcohol.[145] More recently, Field et al. created a similar series of C*c*P variants (A193W, Y229W, and A193W/Y229W) with Trp residues near the protein surface to mimic the function of LiPs.[146] The double mutant A193W/Y229W was found to exhibit the highest oxidizing activity, arising from an efficient electron hopping pathway that acted to accelerate oxidation of the aromatic amino acid.

2.3. Rational Design Using Cytochrome *c* as a Scaffold

Cytochrome *c* (C*c*) is an electron transfer protein that contains a six-coordinated Fe heme center with axial ligation by one Met and one His (Figure 9a).[147] The electron provided by C*c* can be utilized by other enzymes, such as cytochrome *c* oxidase (C*c*O), for their functions. Unlike typical peroxidases that harness pentacoordinate heme iron with a vacant distal coordination site for substrate binding, the occupation of the distal coordination site by Met80 in C*c* seems to preclude peroxidase activity. However, C*c*-catalyzed peroxidase reactions still occur despite an initial lag phase that corresponds to the *in situ* conversion of the six-coordinate precatalyst to an active form, which involves permanent displacement of the Met80 ligand from the heme iron.[148] Therefore, the intrinsic peroxidase activity of C*c* is suppressed by the protein matrix in its native Met80-bound state when compared to other peroxidases such as C*c*P and HRP. While the proximal His18 ligation to heme iron in C*c* is very robust, the 70–85 Ω loop (also known as Ω-loop D) is quite flexible,[149,150] contributing to a relatively weak Met80-Fe^{III} bond.[151] Consequently, displacing the Met80 ligand by mutating it to a noncoordinating residue and/or perturbing the unstable Ω-loop D provides a route to converting C*c* into peroxidase-like metalloenzymes. Moreover, the remarkable stability and compact globular protein structure of C*c,* as well as the covalent bound heme group, make it an excellent structural framework for reengineering.

In order to impart peroxidase-like activity in C*c*, the M80V, T67H, and T67H/M80V mutants have been employed to examine the effects of removing the distal Met80 as well as of adding a His residue to the distal pocket.[152] The M80V mutation was made in order to displace the native distal Met80 and generate an open coordination site at the heme iron, while the T67H mutation adds a distal His residue with an N_ε(His67)-to-Fe distance resembling that found in HRP and C*c*P (5.84 and 5.55 Å, respectively). Interestingly, the single mutant T67H C*c* showed the highest peroxidase activity, even higher than that of T67H/M80V C*c,* suggesting that the presence of a distal His residue is more important than eliminating the axial Met ligand for the enhancement of the peroxidase activity in C*c*. Further modeling studies suggest that the additional M80V mutation leads to improper positioning of the His67 side chain, thus negatively impacting its function as an acid–base catalyst in the peroxidase cycle.

In addition to SDM, new routes have been explored to design novel metalloenzymes by replacing a full segment of the template protein, such as a loop, with another segment from a different protein. In C*c*, residues of Ω-loop D (including Met80) constitute the distal coordination environment of the heme iron. Replacing these residues with key protein segments from other heme-containing enzymes that are responsible for substrate recognition and binding offers a great opportunity for protein engineering. In 2011, Ying et al. reported a P450-mimetic system in C*c* by constructing hybrid proteins in which the segment of the coordination loop (residues 78–85) of yeast iso-1 C*c* was substituted by the "substrate recognition sites" (SRSs) of P450 (Figure 9b).[153] Two constructs, HY1 and HY2, which possess SRS-1 and SRS-2 of P450, respectively, were successfully expressed and further exhibited P450-like function by catalyzing the oxidation of styrene while maintaining the high stability of WT-C*c*. In this manner, these hybrids inherited the advantages of both parent proteins. Further enhancement of the peroxidation activity was accomplished by incorporation of the heme pocket of a peroxidase into C*c* by structure-assisted mutagenesis in the distal-ligand-containing loop (Tyr67, Asn70, Pro71, and Met80) of C*c* along with a highly conserved amino acid sequence.[154] The enhanced activities in these variants were primarily ascribed to the stabilization of compound I through the H-bonding interactions involving His and Arg residues. Taken together, these results indicate that loop residues 71–85 are critical for the function of C*c* and that protein engineering targeting this region is a promising strategy for generating novel biocatalysts.

2.4. Rational Design Using *c*-Type Cytochrome Scaffolds

Although peroxidases are ubiquitous enzymes that catalyze the oxidation of many organic compounds, their poor thermal and environmental stability limits their range of practical applications.[157] Therefore, engineering peroxidases with improved thermal stability offers a promising route to broadening their industrial application. In 2008, Watanabe and co-workers presented the first design of a thermally stable artificial peroxidase in cytochrome c_{552} (Cc_{552}) from *Thermus thermophilus* (Figure 10).[158] In these studies, mutations were made to remove the sixth Fe-coordinating ligand (M69A) and to introduce a general acid–base catalyst (V49D). Although V49D/M69A Cc_{552} displayed an increase in peroxidase activity, significant heme degradation prevented this mutant from achieving sustained catalysis over long periods of time. Shortly after, an improved design of this artificial peroxidase was reported by the additional replacement of Tyr45 with phenylalanine (Y45F) or tryptophan (Y45W) in the basal mutant (V49D/M69A), which resulted in both higher peroxidase activity and thermal tolerance.[159] Many class I peroxidases, including C*c*P and APX, contain a Trp residue in the vicinity of the heme iron, acting as a functional receiver of the oxo-ferryl heme-π-cation radical. EPR studies of the V49D/M69A mutant of Cc_{552} indicate weak magnetic coupling between the oxo-ferryl heme and Tyr45 radical. Replacing Tyr45 with Trp or Phe resulted in delocalization of the radical and increased magnetic coupling between the oxo-ferryl heme and the protein radical, which helped to suppress heme degradation while increasing enzymatic activity. These results suggest that engineering proteins from thermophiles could be a promising approach to generating artificial enzymes for practical applications. Moreover, this work demonstrates the importance of fine-tuning the microenvironment of redox active protein residues in improving catalytic performance.

2.5. Rational Design Using Cytochrome P450 as a Scaffold

Cytochrome P450s (P450) have enormous biotechnological potential due to their unparalleled activity and selectivity toward oxidative chemistry. Members of the class VIII subgroup of this superfamily, and particularly its' first discovered member, $P450_{BM3}$, are commonly employed as scaffolds for redesign as they are fused with their complimenting reductase, forgoing the need for purification and assaying of an additional protein component.[161] Furthermore, the high turnover rate and bountiful structural data available for $P450_{BM3}$ have solidified its instrumental role in the advancement of protein engineering using P450 enzymes. Although numerous studies using both rational design and directed evolution approaches have unearthed common residues that can be altered to expand the scope of the reactivity, the amount of structural evidence capable of providing insight into how mutations guide the binding of new substrates or enhance activity is relatively limited. In 2013, Butler et al. reported the crystal structures of A82F and F87V/A82F mutants of $P450_{BM3}$ with and without substrate bound (Figure 11a), showing for the first time how the A82F mutation can serve as a "gatekeeper" to alter the substrate binding pocket toward the nonnative omeprazole substrate.[162] The enhancement of ligand binding affinity in the A82F mutant was attributed to the large change in free energy between the ligand-free and ligand-bound conformations. Notably, the A82F mutation significantly destabilizes the ligand-free state, thus favoring access of the substrate to the binding site.

Engineering efforts in repurposing $P450_{BM3}$ for cyclopropanation reactions have resulted in highly active, *trans* selective enzymes. However, engineering in $P450_{BM3}$ for *cis*-diastereomers has had limited success, requiring a large number of mutations.[163] To access stereoselective cyclopropanation catalysts using simpler variants, Gober et al. applied a strategic mutation, T268A, into a panel of 13 diverse P450 scaffolds and identified T286A $P450_{BM3}$ as having extraordinary *trans*-selectivity.[164] Although the detailed function of this mutation is not well understood, the crystal structure of T286A $P450_{BM3}$ suggests that this mutation has little impact on either secondary or tertiary protein structure but rather serves to alter protein dynamics and/or H-bonding in the active site to disfavor the O_2 binding and enable nitrene/carbene precursor binding[156]

Mutation of the conserved heme ligating Cys residue (Figure 11b) to Ser or His in the PCS has provided a basis for $P450_{BM3}$ variants with substantially increased cyclopropanation activity.[165,166] However, these changes in the PCS can result in the stability of the protein itself being compromised. A complementary route toward engineering P450-based biocatalysts for highly active and selective cyclopropanation reactions is through modulation of the SCS.[167] It has been demonstrated that mutation of the conserved Phe393 residue to His or Ala increased the heme reduction potential and conversion of the cyclopropanation reaction to comparable levels of the PCS mutants without sacrificing protein stability. Structural analysis (Figure 11c) of the Phe393 variants suggests that the F393A and F393H mutations led to the formation of an electron-withdrawing H-bond to the Cys ligand via Gln403 or His393, thus increasing the heme reduction potential, which is the key to increasing catalytic reactivity.

2.6. Development of Heme Enzymes beyond the Primary Coordination Sphere by Directed Evolution

While the rational design of enzymes based on structure and calculations can offer insights into the role of residues beyond the PCS in promoting catalysis, this approach can still be limited by human intuition or computer programs that may not be able to capture or reproduce the functional properties of PCS and SCS features, especially subtle differences of metal ions and weak SCS interactions. Directed evolution of enzymes allows a route of overcoming these limitations to not only improve enzymatic activity but also unveil new structure–function relationships that are not readily intuited from a rational design approach, including residues far away from the PCS. The general approach of directed evolution uses various techniques to generate a random library of protein mutants, which is then screened based on desired activity.[59,130,172] The main requirements for this process to work are (1) starting from an enzyme with nonzero target activity, (2) sufficient stability of the target enzyme to undergo several rounds of mutagenesis, and (3) an effective screening process for assaying the target activity.[173] Several ensuing directed evolution studies focused on the $P450_{BM3}$ enzyme to enhance its substrate or product scope.[174-178] In one variant, the positions of several activity enhancing mutations were found to be surprisingly distant from the active site, with less than half of mutations appearing in the substrate binding region.[174] Notably, mutations that have been employed by rational design were not found in the selection process of these enzymes.[179] Based on activity and binding assays, it was concluded that the electronic environment around the heme binding site was similar to that of the native enzyme. However, despite the directed evolution engineered variant having a higher turnover with native substrate than its native enzyme counterpart, it did not exhibit the same regio- or enantioselectivity, demonstrating the importance of the screening method in acquiring the desired activity.[179] In such cases where the development of an appropriate assay is not possible, rational design can be used complementarily. For example, the addition of an A238V mutation to another engineered variant, 9-10A, results in the positioning of a residue close to the alkane methyl group at the active site, drastically improving the regioselectivity for alkane oxidation.

While directed evolution has successfully tailored a number of enzymes for specific activity with target substrates, the roles of many of the resulting mutations are not particularly well understood. However, based on previous rational design studies, a number of mutations in particular scaffolds can be rationalized. P450 has been particularly thoroughly studied, and the reader is referred to ref 180 for an in-depth discussion of the enzyme itself. For unnatural reaction landscapes explored by directed evolution, the reader is referred to refs 77 and 180-187, which cover the most recent advancements in the field, specifically for heme-enzymes, and also focus on the mechanistic aspect of these unnatural transformations.

2.6.1. Discovery of Noncanonical Reactions for Cytochrome P450.—The main driving force behind the P450 mediated oxidation reaction is the formation of an Fe^{IV}=O− (heme $b^{\bullet+}$) intermediate termed as compound I. The core of this system and the subsequent reduced system termed compound II is isoelectronic with iron carbenes and nitrenes, the former of which is well studied (Figure 12).[188] Inspired by the similarities between synthetic Fe-porphyrin carbene complexes and compound I, Arnold and co-workers employed

$P450_{BM3}$ for the study of carbene transfer reactions, starting with cyclopropanation of styrene.[163]

To identify an optimal starting candidate for further reaction optimization via directed evolution, native $P450_{BM3}$ (Figure 13) and 92 other variants were included in an initial selection pool.[163] Native P450 is capable of catalyzing the cyclopropanation of styrene; albeit, very low yield numbers (TONs) above 100 have been found. Notably, a number of these active variants, including H2A10, H2-5-F10, and H2-4-D4, contain several Ala residues in the active site across positions Leu75, Met177, Leu181, Ile263, Thr268, and Leu437. To elucidate the effects of each, a series of SDM studies with respect to each active site residue was performed on different select variants. As a result, the T268A mutation was identified as the most important factor for modulating cyclopropanation activity, with a 60-fold increase in activity observed for the single mutant relative to WT-$P450_{BM3}$. This residue has also been identified as fundamental in native P450 activity, in which its elimination results in almost complete deactivation.[180] Based on these observations, it can be inferred that one of the main factors in improving selectivity for newly introduced non-native reactivity is the suppression of the native reaction pathway. These findings concluded on the development of a highly reactive and *cis*-selective variant termed $P450_{BM3}$-CIS containing 13 mutations. Next, site saturation mutagenesis (SSM) on the active site residues Leu181, Ile263, Ala328, Leu437, and Thr438 in this variant helped to elucidate the influence of each on reactivity. Out of these residues, only mutations at Ala328 and Thr438 improved the *cis*-selectivity. The A328G, T438A, T438S, and T438P mutations were found to be the most beneficial without significantly reducing TON.[180]

P450 enzymes exhibit redox switching behavior in which the Fe^{III}/Fe^{II} potential is decreased upon binding of substrate. Importantly, this behavior only enables reduction of the heme cofactor (and subsequent O_2 binding) in the presence of substrate, helping to mitigate the generation of reactive oxygen species (ROS) which could potentially degrade the enzyme or waste reductant via direct formation of compound I or by peroxide-to-water reduction (the oxidase and peroxide shunts, which have been extensively studied).[190-192] In ArMs, however, this redox switch is no longer intrinsically present, requiring both stronger reductants to effectively reduce ferric heme and raising potential concerns regarding both inefficiency and protein degradation. Therefore, in the absence of such a mechanism, practical applications of designed P450 mimics as carbene and nitrene transfer catalysts would be limited.

To overcome this barrier, a series of varying proximal ligands in P450 were assayed to optimize activity under *in vivo* conditions in which C400H and C400S variants were found to be the most active. The latter resulted in a shift of the Soret band for the ferrous-CO bound state to 411 nm, and therefore, the C400S $P450_{BM3}$ variant is referred to as $P411_{BM3}$.[165] The increased activity of this variant was attributed to an increase in the Fe^{III}/Fe^{II} redox potential of the active site and subsequent stabilization of the carbene intermediate. Interestingly, this also drastically increases the *cis*-selectivity of the enzyme, which could allude to enhanced bond rigidity of the carbene intermediate. Based on these findings, other groups utilized the T268A and C400S mutations on homologous P450 enzymes to achieve similar reactivity with other substrates.[193]

Combining chemical intuition with directed evolution has proven fruitful for advancing the reaction landscape of these developed enzymes. Wang et al. developed a new $P450_{BM3}$ cyclopropanation variant with only five mutations relative to the wild-type enzyme (C400H, T268A, L437W, V78M, and L181V) capable of reacting with *N,N*-diethyl-2-phenylacrylamide in very high yields, as well as high enantio- and diastereoselectivity.[194] This showcases the importance of the evolution pathway in reaction optimization.[77] In contrast to $P450_{BM3}$-CIS, this variant was able to achieve higher reactivity with only five mutations, albeit with different substrates. Furthermore, this variant has shown wide alkene selectivity.[166]

Direct evolution has also been used to expand the substrate scope of cyclopropanation. Brandenberg et al. developed two sets of new variants, P411-VAC_{cis} and P411-VAC_{trans}, which were optimized for the catalysis of *N*-vinylphthalimide cyclopropanate to *cis*- and *trans*-cyclopropanes, respectively.[195] Previous studies have demonstrated the activity of P450 variants toward N-H insertion,[196] and this work further highlighted the challenges involved in designing enzymes with new reactivity while suppressing possible side reactions. Interestingly, the P411-VAC_{cis} and P411-VAC_{trans} constructs were also capable of catalyzing O- and S-vinyl compounds, albeit with one additional mutation. The substrate scope of this system was further diversified by the development of a new $P411_{BM3}$ variant capable of accepting nonaromatic substrates for cyclopropanation,[197] and a subsequent study found additional new variants capable of catalyzing C_3 or C_2 selective pyrrole alkylation of indoles and cyclopropanate cyclic hydrocarbons.[198] The key to enabling reactivity has been the utilization of two generations of directed evolution, initially for the development of indole reactivity and subsequently for diversification toward either hydrocarbons or pyrroles.

Directed evolution has also been used to develop $P411_{BM3}$ into a C-H insertion carbene transfer enzyme.[199] Specifically, P411-CHF was developed by directed evolution of $P411_{BM3}$ and shown capable of sp^3 C-H activation with aromatic substrates with high enantio- and regioselectivity for α-carbon over aryl or allylic carbons in alkene substrates. It was also found to be highly selective for C-H insertion over cyclopropanation. Further development of P411-CHF also led to selectivity for highly fluorinated alkanes.[200]

The scope of the insertion activity of P450 has also been expanded further to include tandem cyclopropanation of bicyclobutanes.[201] Previously developed variants of P411 and other heme proteins with nitrene insertion activity were screened for carbene transfer activity with alkyne substrate to provide a stepping stone for subsequent directed evolution of the most active construct (P411-E10). Structural analysis suggested the Trp263 acted to obscure the active site, inhibiting its ability to perform tandem cyclopropanation. Additionally, a second $P411_{BM3}$ variant was separately developed for cycloprenation catalysis, starting from a less reactive alkyne substrate. The mutations incorporated to achieve this reactivity, however, have not been rationalized. In another study, cyclopropene formation was developed further to incorporate less reactive internal alkynes.[202]

In most studies of P450-based carbene transfer activity, the carbene precursor, with a few exceptions,[198-200] has been ethyl diazoacetate (EDA). Recently, a new P411-CIS variant

has been developed which binds α-diazo lactone rather than EDA to perform enantio- and diastereoselective cyclopropanation reactions as well as S—H bond insertion with aromatic substrates.[203] The activity of this precursor with the S400C variant (reinsertion of the native Cys ligand) has been studied as well, demonstrating that the proximal ligand affects reaction TON but not selectivity. This reaction has also been independently studied using another variant of $P411_{BM3}$, which was also capable of binding the same lactone and performing enantioselective C—C bond formation.[204]

Nitrene transfer reactivity has also been explored using the same strategy employed for carbene transfer, and the same mutants optimized for cyclopropanation also exhibit activity toward intramolecular amination.[205] To this end, $P411_{BM3}$ variants have been commonly employed, including one based on the CIS variant[163] and another a double mutant of $P411_{BM3}$.[205] A similar cyclization study performed by Singh et al. showcased the radical character of the aziridation reaction.[206] In this study, different stereoisomers reacted with the enzyme to yield the same product, indicating a common intermediate and ruling out a concerted insertion mechanism. Furthermore, comparison of the kinetic isotope effect (KIE) for the cleaved C—H bonds to those of known, concerted, C—H insertion reactions and the correlation of the reaction rate with the C—H bond strength further suggested an intramolecular hydrogen abstraction by the nitrene as the rate-limiting step. Comparisons with previous research[207] and analysis of undesired side products demonstrated that the main side reaction for the putative nitrene intermediate is an enzyme mediated reduction similar to native hydroxylation reactions.

In 2016, Arnold and co-workers utilized the sigmatropic rearrangement of allylic sulfimides to form an N—C bond following the initial enzyme-catalyzed nitrene transfer to the sulfur atom.[208] The finalized variant, developed through five rounds of SSM, was capable of reacting with a variety of different phenyl thioethers. The developed mutant (P5) was developed to target allylic substrates and was also found to react with nonallylic substrates with high enantioselectivity and TON.

The first enzymatic olefin aziridation catalyst was constructed by Farwell et al. based on P411-CIS, which produced significant quantities of amido-alcohol products due to the styrene-based skeleton of the substrate.[209] In 2017, one of the first cases of C-H amination by $P411_{BM3}$ variants was reported.[210] In this variant, SSM of the previously developed P411-CIS variant culminated in a variant termed P411-CHA This variant contains a “reversal” of Phe263 to Leu in addition to three other mutations which activate the enzyme toward enantioselective reactions with different aromatic substrates. Using this approach, Brandenberg and co-workers engineered a $P411_{BM3}$ variant capable of selective indole amination.[211] Initial rounds of SSM revealed a variant capable of [3 + 2] cycloaddition reaction, showcasing the possibility of substrate binding without nitrene generation. Interestingly, this behavior was enabled by a W1046F mutation at the C-terminus of the enzyme. The motivation behind including this region for SSM was to reduce the rate of substrate reduction, and it was initially attempted by truncating the enzyme after its reduction domain to leave only the P450 region. After observing the adverse effects of truncation, SSM of the NADPH binding site was attempted. As Trp1046 stacks on top of the

NADPH ring, the mutation to Phe was speculated to disrupt binding, which is supported by the resulting 10-fold decrease in electron transfer rate.

Another study in 2020 expanded the substrate scope to allylic and benzylic amines.[212] The nitrene precursor has been changed from tosylazide to pivaloylhydroxyamine, which was based on a previous study[213] inspired by the findings of Tsutsumi et al.[214] and Morandi et al.[215] This serves to disable the direct reduction of the substrate and provides a final primary amine as the product instead of a secondary tosylamine. For benzylic amines, P411-BPA has been engineered, which acts with high selectivity toward them. Another variant, termed P411-APA, has been found to be successful at allylic aminations. The difference between these variants is the addition of two mutations at N395R and S438A.

In 2021, Athavale et al. reported a P411 variant developed through nine rounds of directed evolution which is capable of nitrene transfer of pivaloxyl-amides.[216] In contrast to the P411 enzymes designed for tosylazide as the substrate, the rate-determining step (RDS) in this variant is not C-H activation but nitrene formation as shown by KIE studies. These variants extend the substrate scope of the benzylic amines while also increasing the TON compared to that of P411-BPA.

As discussed *vide supra,* the redox switch mechanism is not intrinsically present in engineered enzymes, the O_2 binding capacity has been drastically altered via numerous mutations, and the active intermediate formation and substrate binding steps can be at least partially uncoupled. As a result, for the carbene intermediate, side reactions with nearby residues are one of the main factors limiting the enzyme turnover number (TON).[217] For nitrene transfer, the main barrier has been the reduction of the nitrene intermediate to its corresponding amine prior to reaction with the substrate. These side reactions could be potentially suppressed by either mutation of the residues responsible for the side reaction or optimization of the enzyme reactivity to increase the reaction rate of the generated compound one-like intermediate.[218]

2.6.2. Myoglobin as a Scaffold.—One of the first reports of directed evolution in a heme protein was presented by Wan et al., who enhanced the peroxidase activity of Mb 25-fold through a quadruple mutant without sacrificing the O_2-binding affinity.[219] This same mutant was later used as a basis for the development of Mb variants active toward carbene and nitrene transfer. Several key amino acids that define the distal pocket in Mb significantly influence the activity and selectivity of this artificial biocatalyst in carbene- or nitrene transfer reactions.[124-127,131] In particular, mutations at the “gating” residue His64 lead to a general activity enhancement for many carbene-mediated reactions. SSM at the active residues Leu29, Phe43, His64, Val68, and Ile107 (Figure 14a) has proven to be a valuable strategy in generating biocatalysts with high proficiency and superior selectivity.

By screening the active site mutation landscape library, in which active positions are subject to substitution by all other possible 19 amino acids, two triple mutants of Mb, L29A/H64V/V68A and F43A/H64W/V68F, were developed that displayed high but complementary stereoselectivity toward intramolecular cyclopropanation (Figure 14).[220] Although detailed structural evidence for this stereodivergence is currently lacking, it is clear from mapping

these mutations onto the Mb structure that the active site configurations of these two mutants are distinct; smaller residues in positions 29 and 68 in L29A/H64V/V68A render an expanded cavity in the upper side of ring A/D of the heme, while increased steric bulk in the F43A/H64W/V68F variant enlarged the cavity at the opposite side of the cofactor (Figure 14b). Therefore, by fine-tuning the distribution and expansion of the distal heme pocket by active site mutagenesis, one can modulate the stereoselectivity of Mb-based biocatalysts.

The active site of Mb has also been configured using directed evolution to enhance opposite enantioselectivities for intramolecular cyclopropanation via the quadruple mutants F43L/H64A/V68G/I107V Mb and F43Y (or F43H)/H64A/V68G/I107F Mb.[221] Notably, *R*-selectivity was achieved by increasing the steric bulk at position 107 (I107F) together with addition of an aromatic group with hydrogen bonding abilities (F43Y or F43H) at position 43. In contrast, *S*-selectivity could be made favorable by reduced the steric bulk at both positions 43 and 107 (F43L and I107V). To expand the substrate scope to more sterically demanding intramolecular cyclopropanation reactions, SSM was used to target active site residues to further expand the distal heme pocket, resulting in an optimized F43Y/H64V/V68A/I107V Mb mutant.[222] These results also supported that positions Phe43 and Ile107 are especially critical for the stereoinduction of substrate when large (i.e., aryl) substituents on the olefinic group are present.

Inspired by previous work investigating mutations at His64 and Val68 to tune the stereoselectivity of the cyclopropanation reactions,[124,135] Hernandez et al. mutated the analogous residues (T45 and Q49) in *B. subtilis* truncated globin to one of three nonpolar residues (Leu, Phe, and Ala) in an effort to enhance the performance toward cyclopropanation.[223] The double mutant T45A/Q49A exhibited high selectivity, possibly due to the increased volume of the active site.

It is notable that the structure-guided rational design and directed evolution methods are not alone in guiding protein engineering for developing artificial metalloenzymes. Although these two approaches have provided fruitful results, both methods are time consuming and labor intensive. The efficiency of protein engineering can be significantly improved by employing calculations to identify promising target residues and mutations. Thanks to advances in computational tools, calculation-guided methods have emerged as effective comple-mentary tools for protein engineering. For the practical use of artificial enzymes, protein stabilization against thermal and chemical denaturation is a long-standing goal in enzyme engineering. In 2017, Moore et al. reported the development of a Rosetta-guided protein design to optimize protein stability for better performance in enzymatic catalysis.[224] Starting from the H64V/V68A Mb construct, which has been found to perform carbene-mediated cyclopropanation reactions with enhanced activity and high diastereo- and enantioselectivities, the authors utilized the Rosetta enzyme design framework to identify the optimal positions for incorporating a thioether covalent staple to improve its robustness for synthetic applications, obtaining nine designs that were further examined for stability and catalytic activity in cyclopropanation reactions. This methodology allowed them to uncover stabilized variants with superior catalytic performance compared to the parent enzyme when exposed to organic solvents.

2.6.3. *Rma* Cytochrome *c* as a Scaffold.—Protein machinery promiscuity is observed not only in the P450 enzymes but also in bacterial cytochrome *c* from *Rhodothermus marinus* (*Rma*-C*c*, Figure 15a), which is an electron transfer protein and has no catalytic functions in living systems. However, Arnold and co-workers have uncovered activity in *Rma*-C*c* toward carbene-mediated C—Si bond formation and thereafter pursued the laboratory evolution of *Rma*-C*c* variants to perform many new-to-nature functions with high activity and selectivity.[225]

In 2018, Kan et al. generated a triple mutant, V75T/M100D/M103E (TDE-*Rma*-C*c*), by SSM at three positions near the distal heme pocket to perturb the distal ligand (M100) and the two residues that are close to the heme iron (Val75 and Met103).[226] The evolved variant catalyzed the C—Si bond formation with more than 15-fold higher turnover than state-of-art synthetic catalysts and extremely high enantioselectivity (>99% ee). In 2018, Lewis and co-workers resolved the high-resolution crystal structure of the TDE-*Rma*-C*c* mutant, which revealed a mutation-generated pocket in the distal side of the heme.[226] Molecular dynamics (MD) simulations indicated that the front loop (Thr98-Glu103) of the active site is quite flexible, adopting an “open” conformation which favors the accessibility of substrate to the iron porphyrin carbene (IPC) intermediate with pro-*R* facial selectivity. The more recently solved high resolution crystal structure of carbene-bound TDE-*Rma*-C*c* reveals how the laboratory-evolved enzyme achieved perfect carbene transfer by holding the iron porphyrin carbene in a single orientation (Figure 15b).[226]

In addition to C—Si bond formation, the *Rma*-C*c*-based biocatalyst has been evolved for C—B bond formation by multiple rounds of SSM.[227] By incorporating different substitutions at Val75 and Met103, the borylation reactivity was directed to diverse diazo ester substituents. The substrate scope of these biocatalysts was later expanded to perform C—B bond-forming chemistry with more rigid, cyclic, lactone-based carbenes by creating a V75R/M99/M100D/T101Y/M103V mutant (BOR^{LAC}).228

Encouraged by the beneficial mutations targeting the active site front loop, Cho et al. continued to explore the new-to-nature functions of the thermostable *Rma*-C*c* platform by generating a biocatalyst for enantioselective aminohydroxylation of styrenyl olefins.[213] Apart from the SSM targeted residues (Thr98, Met99, Thr101, and Met103) within the same loop as the Met100 ligand, mutations at Met76 and Tyr44, which are relatively far from the active site, also improved the catalytic performance. Similarly, a Y44I mutation enhanced the borylation activity and enantioselectivity of an *Rma*-C*c*-based biocatalyst for the synthesis of chiral α-CF_3 organoboranes.[229] MD simulations revealed that the -CF_3 group pointed toward the active site, whereas the bulkier phenyl group lay between the side chains of the M103D and Y44I substituted residues, implying that the primary roles of these mutations were to facilitate the binding of the diazo substrate. Therefore, residue 44 could be a key to modulating substrate selectivity in this artificial enzyme.

The TDE-*Rma*-C*c* mutant was revisited in 2021 by Garcia-Borràs et al. to study the origin of the chemoselectivity of this variant toward C—Si over C—N bond formation.[231] A combination of computational and experimental methods suggests that the protein front loop conformation and dynamics dictate silane binding, which is a major contributor to the

rate-limiting step. The more favorable silane binding affinity in the TDE-*Rma*-C*c* mutant may result from the increased flexibility of the front loop, induced by the hydrophilicity of the Asp100 and Glu103 side chains. Redesign of several mutations in the front loop led to the generation of a new protein (N80F/M99P/E103I TD-*Rma*-C*c*) in which chemoselectivity was switched from silylation to amination.

2.7. DNA as a Scaffold for Heme-Based Biosynthetic Models

While proteins have long been known to serve enzymatic functions, it has also been discovered in recent decades that both RNA and DNA can function as enzymes.[232-234] Naturally occurring oligonucleotides are composed of a much narrower range of building blocks in comparison to proteins, and therefore, recruiting metallocofactors such as heme can help oligonucleotides to expand their enzymatic capabilities. Based on this hypothesis, Li, Geyer, and Sen used *in vitro* selection to obtain single-stranded DNA aptamers that specifically bound *N*-methylmesoporphyrin IX (NMM), a stable transition-state analogue for porphyrin-metalation reactions.[235] A library of 1.8×10^{15} DNA molecules was screened for NMM binding affinity using NMM-bound acrylic beads through HPLC, subjected to both positive and negative selection in 12 rounds. In the DNA aptamers that bound strongly, sequence analysis revealed a common guanine-rich motif. Further characterization of the resulting DNA aptamers showed that hemin could form complexes with guanine-rich, short single-stranded DNA molecules with submicromolar affinities. The authors presented spectroscopic evidence that this complex more closely resembled a peroxidase than it did uncoordinated hemin, consistent with the observed increase in peroxidase activity from the hemin/DNA complex when compared to hemin alone.[236]

Shortly thereafter, the electron paramagnetic resonance (EPR) and UV/visible spectra of a folded guanine-rich oligonucleotide and hemin complex (wholly referred to as PS2.M-hemin) were shown to be similar to the spectra observed for high-spin ferric heme with axial symmetry, as observed with myoglobin.[237,238] The DNA component of PSM2.M-hemin was known previously to form a G-quadruplex structure, in which tetrads of guanosine stack atop each other to form a four-stranded supermolecule under physiological salt conditions.[239] The initial work characterizing the peroxidase activity of a G-quadruplex/heme complex used ABTS as a substrate.[236] A little more than a decade later, the G-quadruplex/heme complex was demonstrated to act as an NADH oxidase and NADH peroxidase mimic, oxidizing NADH via O_2 to generate H_2O_2.[240] The complex of G-quadruplexed DNA and heme has since been characterized as a peroxidase-like DNAzyme, able to accommodate ligands in the distal sixth coordination site such as CO, O_2, and imidazole.[241,242] Heme-G-quadruplexed-DNA-zymes, however, have a major difference from protein peroxidases, as they lack a proximal imidazoyl ligand from a histidine amino acid residue.

Ten years after the spectroscopic investigation on PS2.M-hemin, the same complex was shown to catalyze two-electron oxidation reactions with substrates such as thioanisoles, indole, and styrene, and ^{18}O labeling demonstrated that the transferred oxygen atom originates from hydrogen peroxide through what is presumably a ferryl moiety.[243] Docking simulations of heme to a G-quadruplex structure suggested a lack of a structured environment distal to the heme, and it was suggested this is linked to the lack of

enantioselectivity observed with oxidation reactions catalyzed by PS2.M-hemin, as the oxygen transfer reaction to thioanisole produces a racemic mixture and indole oxidation yields several products.[243]

Although no additional complexes of oligonucleotides with heme have been reported since, several other interactions do exist with other porphyrin molecules in complex with DNA.[244] In G-quadruplex DNA formed from the repeating human telomere sequence d(TTAGGG), ferrous heme binds to the 3′-terminal G-quartet through $\pi-\pi$ stacking interactions.[245-247] Chemical modifications of the heme in the d(TTAGGG)-heme complex to form different electron densities at the catalytic iron site altered the peroxidase activity of the complex, with decreasing peroxidase activity observed with decreasing ρ_{Fe}.[248] Resonance Raman spectroscopy has revealed that the vibrational feature ν_{CO} for the $[d(TTAGGG)]_4$-heme complex with a bound CO adduct appears at a lower frequency than in myoglobin, suggesting a weaker donor strength of the proximal ligand and slightly longer Fe—C bond.[248] This agrees well with earlier NMR work of chemically modified hemes in complex with G-quadruplex DNA, where the fifth (proximal) ligand appears to be a water molecule.[247]

In 2019, a different G-quadruplex/heme complex (called G4) was shown to work as a catalyst for carbene insertion into styrene, expanding the range of heme-DNAzymes beyond oxygen transfer reactions.[249] As the heme molecule is situated above the 3′ G-quartet, the 3′ end of the oligonucleotide is free to interact with the cofactor—the authors report that the presence of 3′-terminal AAA or TTT results in indistinguishable effects upon carbene insertion, while AAA shows higher oxidation rates relative to TTT.[249] The addition of multiple pendant nucleotides shows increasing stereoselectivity compared to porphyrin/DNAzymes that do not possess nucleotides on the distal side of the porphyrin. Figure 16 shows the “active site” of the heme-DNAzymes studied. Reactions were limited to oxene and carbene insertions, but they are mechanistically distinct from the Fe^{IV}-based, radical-dependent mechanism of heme monooxygenases.[183]

While there is a lack of crystal structure data for a G-quadruplex/hemin complex, efforts from the Mergny and Petitjean groups produced a planar Pt^{II} complex that binds in the same proposed position where hemin binds atop the G-tetrads at the 3′ end.[250] This serves as a good structural model for the heme binding position on G-complexes in general, but the Pt/DNA complex does not display the proximal water ligand that has been demonstrated in peroxidase-type heme/DNAzymes.

3. CATALYSIS BEYOND THE PRIMARY COORDINATION SPHERE BY DESIGNED NON-HEME IRON ENZYMES

Non-heme Fe enzymes constitute a broad class of proteins that bind Fe to promote a variety of reactions, many of which parallel those of heme enzymes. Many non-heme Fe enzymes employ mono- or dinuclear Fe sites to promote O_2 activation and incorporation into organic substrates.[251,252] Additionally, non-heme Fe enzymes have been found to promote reactions including nitric oxide reduction, the reversible of oxidation of H_2, and even the reduction of atmospheric nitrogen to ammonia.[56,253-256] In many O_2-activating mononuclear

non-heme Fe enzymes, the active site is composed of a $(His)_2$-carboxylate binding motif arranged to facially coordinate Fe^{II}, commonly referred to as the “facial triad”, with one or two labile ligands (such as H_2O) that allow facile binding of O_2.[257-260] Dinuclear non-heme Fe enzymes that serve to activate O_2 or reduce NO typically exhibit mixed His and carboxylate-coordinated active sites, often with one or more carboxylates (Asp or Glu) bridging the two irons that can appear in both the terminal and bridging positions and additional non-amino acid coordinating atoms such as H_2O, OH^-, or O^{2-}.[252,261] Further non-heme Fe enzymes may offer more exotic coordination environments, such as the 5,10-methlenetetrahydromethanopterin cofactor in Fe hydrogenase (H_2ase),[262] the bridging dithiolate/pendant amine cofactor and CO/CN^- ligands of FeFe H_2ase,[263] and hetero iron-sulfur-based clusters of nitrogenases and carbon monoxide dehydrogenase (CODH).[264-267]

The broad nature of non-heme iron systems naturally affords a high degree of modularity in the PCS and SCS. We have organized our discussion of these systems first in terms of mononuclear vs dinuclear systems and then further between approaches toward the active site, namely, (1) the use of amino acid residues to provide the PCSs of metal centers, (2) those which employ unnatural amino acids for metal coordination and those which incorporate a guest organometallic complex in a host protein scaffold (also referred to as the “Trojan horse” approach) using (3) covalent interactions and (4) supra-molecular interactions.

3.1. Design of Mononuclear Non-heme Iron Proteins

3.1.1. Design Using Natural Amino Acids.—One of the earliest studies to rationally design a catalytically active mononuclear non-heme Fe site into a non-native protein scaffold was performed by Pinto, Hellinga, and Caradonna.[268] Utilizing the scaffold thioredoxin (Trx), a facial triad binding site was designed with the assistance of the program DEZYMER via Leu7His, Phe27Asp, Ile60His, and Asn63His mutations (Figure 17). Fe binding was observed via the appearance of a new absorption feature at 350 nm, assigned to a His $\rightarrow Fe^{III}$ ligand-to-metal charge transfer transition. When tested via colorimetric assay, the Fe-Trx ArM exhibited significant superoxide dismutase (SOD) activity, with a dismutation reaction rate of $k \sim 10^5\ M^{-1}\ s^{-1}$.

Azurin (Az) has also served as an effective scaffold for the design of low-coordinate mononuclear non-heme Fe binding sites. Az is a type 1 copper metalloprotein but has garnered attention for protein engineering efforts due to its stability and ease of expression. The use of Az to bind Fe was first demonstrated by Holland and co-workers,[270] who were able to incorporate Fe^{II} into both WT-Az and the M121A Az variant. Surprisingly, WT-Fe^{II}-Az appeared to resist oxidation and reduction by a variety of redox agents, suggesting that the accessible iron reduction potentials are outside the physiological potential range from approximately −1 to + 1 V vs SHE. Characterization by a combination of ^1H NMR and ^{57}Fe Mossbauer spectroscopies strongly indicates that there is little structural difference between WT-Fe^{II}-Az and M121A Fe^{II}-Az, implying the absence of Met121 does not significantly affect the coordination geometry. X-ray crystallography reveals clear coordination of Fe by His46, Cys112, and His117 and likely Gly45 as well. Further N_3^- binding experiments reveal that replacement of Met121 for Ala opens an additional binding pocket without

perturbing metal binding. Additional binding experiments demonstrated the ability of CN^- to coordinate Fe but that alternative ligands such as *N*-methylformamide, hydrazine, and CO are incapable of binding.

Following the initial discovery of Fe binding in Az, the Liu group further engineered the binding pocket to impart superoxide reductase activity via a M121E substitution (Figure 18b).[271] Fe^{II} incorporation into M121E Az was supported by a combination of absorption spectroscopy, inductively coupled plasma (ICP) analysis, and electrospray ionization mass spectrometry (ESI-MS). Successful crystallization of M121E Fe^{II}-Az allowed structural determination at 2.0 Å resolution. Interestingly, M121E Fe^{II}-Az crystallizes as a tetramer of two heterodimers, with subunits A and C in conformation **1** and subunits B and D in conformation **2**. No observable occupancy was found in conformation **1**, while 100% occupancy was found in conformation **2**. In addition to Gly45, His46, C112, and His117, Glu121 was found to coordinate Fe^{II} through the extended carboxylate side chain. Unlike WT-Fe^{II}-Az or M121A Fe^{II}-Az, the $Fe^{II} \rightarrow Fe^{III}$ redox couple of M121E Fe^{II}-Az was found to be readily accessible, with a reduction potential of +0.327 V. Further testing for superoxide reductase (SOR) activity using the Fridovich method[273] revealed an SOR activity, with a reduction rate of $k = 1.8 \times 10^4\ M^{-1}\ s^{-1}$. Based on observations for native SOR, a second substitution was made exchanging Met44 for Lys. In the native system, it is believed this SCS residue aids in guiding superoxide to the metal center or even potentially stabilizes binding of the negatively charged superoxo via its positively charged side chain. This rational modification further only slightly lowered the Fe^{II}/Fe^{III} redox couple to +0.320 V but boosted the SOR activity of M121E/M44L Fe^{II}-Az by 2 orders of magnitude to $1.1 \times 10^6\ M^{-1}\ s^{-1}$ relative to M121E Fe^{II}-Az, supporting the importance of this SCS interaction in promoting the SOR activity.

More recently, the Lu group has further utilized Az to engineer the formation of a dinitrosyl iron complex (DNIC).[274] Nitric oxide (NO) plays an important role in numerous processes ranging from cellular signaling to immune defense, and understanding how these processes are regulated by non-heme Fe proteins remains an intense subject of investigation. Note that in the following we will use Enemark–Feltham notation, $\{MNO\}^n$, to describe the overall oxidation state of NO-bound metal (M) systems, where n denotes the number of valence electrons (metal d plus NO π^* electrons).[275] Using the M121H/H46E Az scaffold previously developed for Cu^{II} binding aimed at *S*-nitrosylation[276] (Figure 18c), Fe^{II} binding was observed via a combination of absorption and ^{57}Fe Mössbauer spectroscopy. Further addition of 1 equiv of NO produced significant spectroscopic changes in the absorption spectrum, as well as the appearance of a new $S = 3/2$ signal as observed by EPR, indicative of $\{FeNO\}^7$ formation. This new $S = 3/2$ species was actually a convolution of two signals with unique zero-field splitting (ZFS) properties, representing two different conformations of the $\{FeNO\}^7$ species at low temperature, with one slightly more axial and the second more rhombic. By combining EPR and field-dependent ^{57}Fe Mössbauer spectroscopic measurements with density functional theory (DFT) calculations, it was proposed that these species represented two different PCSs. Specifically, the more axial species was proposed to arise from $\{FeNO\}^7$(His)(Glu)(Cys) coordination, while the more rhombic from $\{Fe\text{-}NO\}^7(His)_2(Glu)$. Interestingly, room temperature resonance Raman (rR) measurements

revealed a single set of Fe-NO and NO vibrations, indicating that the appearance of two conformers as observed by EPR and ^{57}Fe Mössbauer spectroscopy may only arise at low temperatures.

Exposure of M121H/H46E {FeNO}^{7}-Az to an excess of NO produced a new novel species, which exhibited an axial $S = 1/2$ signal as observed by EPR. Using ^{14}N/^{15}N Q-band electron double nuclear resonance (ENDOR) spectroscopy, two isotope-dependent signals with relatively weak hyperfine interactions (3.6 and ~ 7 MHz in ^{15}NO) were observed, supporting the formation of a {Fe(NO)$_2$}^{9} DNIC species. This hypothesis was further bolstered by the presence of two unique sets of Fe-NO/NO stretching frequencies as observed by Fourier transform infrared (FT-IR) and rR spectroscopies. Further ^{1}H Q-band ENDOR measurements supported Cys coordination, and by combining these results with ^{57}Fe Mössbauer measurements and DFT calculations, a {Fe(NO)$_2$}^{9}(His)(Cys) coordination environment was proposed. Finally, investigation of the mechanism of {Fe(NO)$_2$}^{9} formation from {FeNO}^{7} revealed the presence of an additional $S = 1$ intermediate species assigned as {FeNO}^{8}. Single-value decomposition of time-dependent absorption measurements shows this species is on-path to {Fe(NO)$_2$}^{9} formation, and researchers further propose this species to be {FeNO}^{8}(His)(Glu)(Cys) coordinated based again on ^{57}Fe Mössbauer measurements and DFT calculations. This study not only provides insight into the stepwise nitrosylation of Fe in a protein scaffold and the resulting coordination environments but strongly illustrates the deep structural insight that can be obtained by applying a combination of multiple orthogonal spectroscopic and computational methods.

In addition to Az, reengineering of rubredoxin (Rd) has also allowed for successful {FeNO}^{7} formation. Rd is a low-molecular-weight electron transfer protein which natively binds Fe through the coordination of 4Cys (Figure 19). Substituting either Cys8 or Cys41 for Ala in *Clostridium pasteurianum* (*Cp*) Rd it has been shown to open a binding site, forming Fe(Cys)$_3$(OH) coordination.[278] Using this approach, Lin and He were able to generate an open binding site for Fe^{III} in Rd from *Pyrococcus furiosus* (*Pf*) and subsequently bind NO following reduction with sodium dithionite (DT) to form an air-stable C9A {FeNO}^{7}-Rb (and equivalently C41A {FeNO}^{7}-Rb).[272] The dominant $S = 3/2$ species was characterized by EPR and absorption spectroscopies; interestingly, an additional $S = 1/2$ signal was also observed and assigned to a nonspecifically bound {FeNO}^{7} species. Irradiation with red light (625–650 nm) resulted in the stoichiometric release of NO from both C8A {FeNO}^{7}-Rb and C41A {FeNO}^{7}-Rb systems under either aerobic or anaerobic conditions. Under anaerobic conditions, photolysis of NO resulted in the Fe^{II} precursor, and further air exposure produced the starting Fe^{III} complex, which in turn was capable of binding NO to reform the {FeNO}^{7} complex. Meanwhile, photolysis of C8A {FeNO}^{7}-Rb under aerobic conditions showed similar properties to the Fe^{III} starting material, but with a ~16 Da increased molecular weight. Based on this difference in molecular weight, it was hypothesized that oxygenation of either a binding Cys or Fe itself may occur. This species further decomposed to C8A Fe^{III}-Rd, which then could be used to also reform the {FeNO}^{7} complex. Further incubation with plasmid pBR322 DNA demonstrated photolysis of C8A {FeNO}^{7}-Rb promoted DNA cleavage, demonstrating the practical biological applications of this system.

3.1.2. Design Using Unnatural Amino Acids.—One of the first examples utilizing an unnatural amino acid (UAA) to generate a biosynthetic non-heme iron binding pocket was accomplished by Schultz and co-workers, who genetically encoded *E. coli* to incorporate (2,2′-bipyridin-5-yl)alanine (Ala_{Bpy}) into the sequence of a DNA-binding protein).[279,280] Earlier studies have shown that incorporation of Fe^{II}-EDTA in DNA binding enzymes at the DNA interface induces oxidative cleavage at deoxyribose,[281,282] which has inspired efforts to directly bind Fe^{II} using bipyridyl as a high-affinity ligator. The homodimeric catabolite activator protein (CAP) was chosen as a scaffold due to its specificity for a 2-fold symmetric 22 base pair binding site. Inspired by the crystal structure of the CAP-DNA complex,[283,284] Lys26 was chosen for substitution to form the $L26A_{Bpy}$ CAP variant (Figure 20a). Determination of the K_d of $L26A_{Bpy}$ CAP vs WT-CAP for a 50 base pair DNA strand containing the 22 base pair binding site revealed similar affinities for both proteins, demonstrating that incorporation of Ala_{Bpy} did not significantly perturb the CAP-DNA interaction. Incubation of $L26A_{Bpy}$ CAP with the same sequence in the presence of Fe^{II}, cyclic adenosine monophosphate (cAMP), and a reducing agent such as ascorbic acid or 3-mercaptopropionic acid resulted in DNA cleavage. Analysis of the products revealed cleavage primarily at either end of the recognition sequence, near the anticipated location of the Ala_{Bpy}. As cleavage was not observed in the absence of either Ala_{Bpy} or Fe^{II} (or equivalently Cu^{II}), it was inferred that the formation of an Fe^{II}-Bpy complex was necessary for activity. Continuing their work in DNA binding and regulation, Schultz and co-workers utilized the Zif268 transcription factor protein to design a novel Fe^{II} binding site, again using Ala_{Bpy} as a chelating ligand.[285] Zif268 is a zinc finger protein, which uses Zn^{II} to stabilize the protein fold through $Zn^{II}(Cys)_2(His)_2$ coordination (Figure 20b). While Zif268 natively binds a specific nine base pair double-stranded DNA sequence, modification of the finger domain can lead to binding of both alternative sequences and other metals. Following successful incorporation of Ala_{Bpy} into Zif268 at three different positions (26, 28, and 29), it was found that all three mutants were capable of binding DNA with comparable affinities and with the same site specificity as WT-Zif268. Furthermore, substitution of Ala_{Bpy} for Ala_{Bph} (Bph = biphenyl) eliminated DNA binding affinity, as did the presence of EDTA, together demonstrating a requirement for both Ala_{Bpy} and a metal ion. Using a combination of ESI-MS along with absorption and EPR spectroscopies, it was elucidated that DNA binding by Zif268 Ala_{Bpy} is Fe^{II}-dependent. Comparison of the rR spectra from Fe^{II}-Zif268 Ala_{Bpy} and $[Fe^{II}(bpy)(CN)_4]$ was indicative of Fe^{II}-bpy coordination. Further ^{57}Fe Mössbauer measurements revealed a single species with d = +0.41 mm/s and $|\Delta E_Q|$ = 0.34 mm/s, consistent with low-spin Fe^{II}. This result was further corroborated by temperature-dependent magnetic circular dichroism (VT-MCD) measurements, where the similarity of the low- and high-temperature spectra revealed a diamagnetic (S = 0) system. Together, these results support that incorporation of the UAA Ala_{Bpy} to Zif268 results in a similar fold to WT-Zif268, but with alternative metal selectivity.

Incorporation of UAAs has also been used to design metal binding sites for radical intermediate stabilization. Continuing from their previous work using a Ala_{Bpy}-incorporated lactococcal multidrug resistance regulator (M89X LmrR) protein (Figure 20c and d), Roelfes and co-workers probed the influence of varying the surrounding AA residues on the binding affinity for 3d transition metals ranging from Mn^{II} to Zn^{II}.[286,287] In order to bind Fe^{II} (as

evidenced by the appearance of a 310 nm LMCT absorption band), additional substitutions of F93D and V15G were required, evidencing the need for available carboxyl ligands to induce Fe^{II} binding to bpy. Furthermore, Fe^{II} was found to bind and stabilize 3,5-di-*tert*-butylsemiquinone (DTB-SQ).

A significant challenge in designing competent metal catalysts in non-native scaffolds is understanding how each substitution will impact both structure and function. This problem can be even greater when employing unnatural amino acids, as most studies have focused around the use of natural AAs. Using the program Rosetta,[290,291] Baker and co-workers computationally designed a series of potential divalent metal binding sites utilizing Ala_{Bpy}, with the goal of forming a catalytic site mimicking catechol dioxygenase.[289] Potential models were screened around a PCS involving Ala_{Bpy} and dopamine (a catechol). Genes for the best 13 candidates were synthesized and expressed in *E. coli,* of which five successfully produced soluble protein and two (CB_02 and CB_12) were capable of binding Fe^{II}. A successful crystallization of CB_02, a scaffold based on bacterial sialidase, revealed the Ala_{Bpy} side chain to be oriented outward toward solvent rather than aiding formation of a well-organized metal binding site. To overcome this, a second round of computational design was undertaken with a more constrained metal binding site geometry involving Ala_{Bpy}, Asp, Glu, and His, as well as two H_2O molecules replacing the catechol moiety. Of the 28 designs investigated, eight appeared to bind Fe^{II} in a buried fashion. Model MB_07 (based on indole-3-glycerolphosphate synthase) was successfully crystallized with both bound Co^{II} and Ni^{II} (Figure 20e and f) showing good homology with the respective computational designs. Although Fe^{II}-MB_07 could not be crystallized for direct comparisons, this pioneering work demonstrates the power of computational approaches in rationally designing PCS and SCS interactions to form novel metal binding sites.

3.1.3. Design via Covalent Interactions.—In addition to direct natural AA or UAA coordination, protein–metal binding sites can be generated via direct incorporation of an exogeneous organometallic complex into a host scaffold, commonly referred to as the “Trojan horse” method. Early applications of this approach were pioneered in the late 1990s by Distefano and co-workers by incorporation of a metal-binding 1,10-phenanthroline and pyridoxamine derivatives into adipocyte lipid binding protein.[292-295] This method is less commonly used to investigate the function of natural metalloenzymes and instead imparts altogether new catalytic activity. Here, the protein serves to impart SCS effects, such as controlling solvent access and hydrophilicity/hydrophobicity, charge screening, hydrogen bonding, enforcing conformers, and even imparting stability. Anchoring of these complexes can be accomplished either directly through covalent linking or via supramolecular interactions.

Maleimide reacts facilely with thiols via Michael addition to form thiosuccinimide under very mild basic conditions (pH ~ 7.5), providing an excellent route to forming a covalent linkage with Cys side chains (Scheme 2). Although use of this route requires careful consideration of cysteine accessibility, it offers a powerful tool for the incorporation of guest complexes into a wide range of protein scaffolds.

Banse and co-workers prepared one of the first examples of a mononuclear nonheme Fe site generated using a thiosuccini-mide anchor by incorporation of $[Fe^{II}(L_5{}^2{}_{maleimide})Cl]^+$ into isoform B of bovine β-lactoglobulin (β-LG, Figure 21a) ($L_5{}^2{}_{maleimide}$ = 1-(2-{[2-(Bis-pyridin-2-ylmethylamino)ethyl]-pyridin-2-ylmethylamino}ethyl)pyrrole-2,5-dione)).[296] The $[Fe^{II}(L_5{}^2{}_{maleimide})Cl]^+$ complex was specifically chosen based on its reactivity with thioanisole and H_2O_2 to form phenyl-methylsulfoxide. Interestingly, incorporation into β-LG resulted in a 5-fold *decrease* in reactivity while simultaneously producing a 20% enantiomeric excess (*ee*). In the absence of thioanisole substrate, time-dependent absorption measurements revealed a transient signal at 660 nm maximizing around 4 min; further EPR measurements of the reaction mixture revealed this to be an $S = 1/2$ species, consistent with the formation of a low-spin Fe^{III} intermediate. Based on the energy of the 660 nm transition, this intermediate was further proposed to be $Fe^{III}(H_2O_2)$ at room temperature, undergoing an acid/base equilibrium to form $Fe^{III}(OOH)$ at low temperatures.

Further work by Jarvis and co-workers looked to utilize the oxidizing power of iron-peroxo to attack the β-O-4 linkage of lignin, a notoriously difficult to process material with important consequences as a potential renewable resource.[299] A series of organic ligands were designed to enable both iron binding and covalent linkage via thiosuccinimide formation to the A100C variant of steroid carrier protein 2L (SCP-2L, Figure 21b). Of the explored organometallic complexes, only the maleimide-substituted tris(2-pyridylmethyl)amine exhibited activity to activate a lignin model complex via hydroxide to ketone conversion, which was improved by incorporation of the complex into SCP-2L. In an attempt to further stabilize the metal site (via either hydrogen bonding or direct dative bonding), F94E and F94H substitutions were introduced on the basis of MD simulations. While no effect was observed with histidine, glutamate resulted in improved conversion and yield. It is still uncertain whether direct coordination of Fe by Glu occurs, but it is possible the carboxylate side chain serves to stabilize the Fe center.

Counter to the pyridyl-based complexes used to impart oxygenase activity in studies with β-LG and SCP-2L, Mahy and co-workers combined the S212C variant of xylanase (Ser212Cys Xln, Figure 21c) with a maleimide Knölker's Fe complex to generate a biohybrid with hydrogenation activity.[301] Using Rosetta,[290,291] the backbone perturbations arising from Michael addition of the maleimide-Knölker complex at S212C were modeled using a combination of MD and normal-mode analysis (NMA) which indicated some conformational rearrangement may be necessary for favorable binding to occur. However, successful incorporation was achieved, and hydrogenation of trifluoroacetophenone (TFAC) to its alcohol complement was boosted approximately 2.5-fold relative to Knölker's complex in ethanol solution.

3.1.4. Design via Supramolecular Interactions.—While covalent attachment is one method of inserting a guest complex into a host scaffold, supramolecular interactions provide an equally powerful approach. Several systems have been employed to generate mononuclear non-heme Fe active sites via, for example, salt bridge, hydrogen bonding, and/or π-stacking interactions.

Ménage and co-workers have extensively employed the protein scaffold NikA (nickel-binding periplasmic protein, Figure 22a) to incorporate mononuclear non-heme Fe organometallic complexes to study the impact of the surrounding protein scaffold on oxygenation and hydroxylation activity. NikA natively serves as a Ni^{II} transporter protein which is essential for the maturation of a variety of microbial energy-converting enzymes.[303] Interestingly, initial studies reinvestigating the structure of recombinantly expressed NikA resulted in the unexpected coordination of $[Fe^{III}EDTA(H_2O)]^-$ (EDTA = ethylenediaminetetraacetic acid).[304] Binding of this complex was proposed to be stabilized through several possible salt bridges, most importantly via Arg137 to the apical carboxylate of EDTA. Spurred on by these results, Ménage and co-workers generated an EDTA-inspired organometallic ligand **L0** (**L0** = *N*-benzyl-*N*′-(2-hydroxybenzyl)-*N,N*′-ethylenediaminediacetic acid, Scheme 3) as a mimic of Fe oxygenase and further incorporated the Fe^{III}**L0** complex into the NikA scaffold to form Fe^{III}**L0**-NikA.[302] Crystallography revealed stabilization via the previously observed carboxylate-Arg137 salt bridge and further π-stacking between an equatorial phenol and Trp398 (Figure 22b). Exposure of Fe^{III}**L**-NikA crystals to dithiothreitol (DTT) induced a transformation of the equatorial ligand phenol → catechol and of benzyl → phenol, and further exposure to O_2 intramolecular resulted in dihydroxylation of the **L0** scaffold. Further combination of crystallography and rR allowed the characterization of two O_2-bound intermediates, leading to the proposal that homolytic O_2 cleavage occurs to form an Fe^{IV}═O/Fe^{III}—$O^{\bullet}$ intermediate (Figure 22c-f).

While the dioxygenase activity of Fe^{III}**L0**-NikA is promising, the dihydroxylated product results in coordination of Fe by the newly formed phenol, hindering any further turnover.[302] This inspired further efforts to deter the intramolecular reaction via two approaches. Under the first approach, substitutions on the benzyl and phenol groups of **L0** inhibit the intramolecular reaction, while the second employed organic ligand was modified to provide N_2Py_2 coordination (N = substituted amine, Py = pyridyl).

To inhibit intramolecular hydroxylation, Cavazza, Ménage, and co-workers modified the origin **L** ligand by blocking the sites of aromatic hydroxylation observed previously.[302,305] To do so, a thiomethyl substituent was introduced at the *para* position of the benzyl group (complex **L1,** Scheme 3), and an additional methoxy substituent was placed at the *meta* position of the phenol (complex **L2**). Crystal structures were obtained for the Fe^{III}**LY**-NikA and Fe^{II}**LY**-NikA systems (**Y** = 1, 2), as well as Fe^{II}**LY**-NikA following exposure to O_2 (Fe**LY**-NikA-O_2). This structural characterization revealed that, in addition to the previously observed Arg137 salt bridge, H-bonding from Tyr402 and π-stacking from Trp398 provide important stabilizing interactions with Fe^{III}**LY**-NikA. Upon reduction to form Fe^{II}**LY**-NikA, the conformational change resulting from rotation at the thiomethyl-substituted benzylic group results in substitution of H_2O for thioether coordination and the formation of a new salt bridge with Arg97. While O_2 exposure of Fe^{II}**L1**-NikA resulted in intramolecular hydrogenation to form a catechol, Fe^{II}**L2**-NikA appeared unimpacted. Through this process, products of both still preserve an open coordination site. Activity studies demonstrated some monooxygenase activity in Fe**LY**-NikA, which was also greatly improved by cross-linking NikA to form enzymatic crystals (CLECs).[305]

To explore N_2Py_2 coordination, a series of Fe-EDTA derivatives Fe**LX** (**X** = 3–7) were generated with pyridyl-substituted amines and a varying number of carboxylate groups, and their interactions with NikA were subsequently investigated (Scheme 3).[308] The presence of a carboxylate moiety was found to be necessary for binding, and the affinity was significantly boosted by the presence of two carboxylates. Addition of steric hindrance by substitution of the 1,2-diaminoethane backbone for 1,2-diaminocyclohexane additionally decreased the binding affinity. Comparing complex charges, it was found that binding was also influenced by charge screening, where negatively charged complexes generally exhibited higher affinity. This effect was partially overcome in complexes that were capable of forming CH/π interactions. Further catalytic studies for these complexes were performed to probe their oxygenase activities toward sulfide complexes.[309] Substrates were screened using molecular docking calculations and chosen on the basis of probing the presence/absence of H-bonding interactions with Glu247 and Gln385 residues. With a select substrate, the activities for sulfoxidation in the presence of NaOCl were monitored, demonstrating that the presence of the NikA host around Fe**LX**-NikA is critical for catalysis. To further boost the catalytic capabilities of the NikA-hosted N_2Py_2 coordination complexes, CLECs of NikA were grown and substituted with Fe**LX**-NikA (**X** = 8, 9) containing *ortho* methyl substituents on either pyridyl group.[310] The sulfoxidation activity was significantly improved in the Fe**LX**-NikA/CLEC system relative to solution Fe**LX**-NikA, promoting both higher yields and significantly greater turnover numbers (TONs). The harsh conditions used in the sulfoxidation reaction (including the presence of NaOCl as oxidant) were suggested to degrade the catalyst and protein during turnover, and the stability imparted by the CLEC likely mitigates this issue to some degree.

Ménage and co-workers have also explored sulfoxidation via incorporation of a Fe-N_2Py_2 complex in human serum albumin (HSA) by taking advantage of this protein's ibuprofen recognition site.[306] An ibuprofen-substituted *N,N′*-bis(2-pyridylmethyl)-*N*-methyl-1,2-ethanediamine complex (**L$_{ibu}$**) was used to coordinate $Fe^{II}Cl_2$, forming the Fe^{II}**L$_{ibu}$**Cl_2 complex, which was further successfully incorporated into HSA as supported by ICP, absorption, and fluorescence measurements (Figure 23). While Fe^{II}**L$_{ibu}$**Cl_2 was found to completely oxidize thioanisole to sulfone in the presence of H_2O_2, product formation was limited predominately to sulfoxide in the Fe^{II}**L$_{ibu}$**-HSA complex. Significant activity was also observed for HSA alone, although both selectivity and TON were improved by the presence of Fe^{II}**L$_{ibu}$**.

In addition to NikA and HSA, the streptavidin (Sav)-biotin system has been effectively used to generate a wide range of artificial metalloenzymes, including several examples of mononuclear non-heme Fe sites. The first example incorporating a biotinylated Fe complex into Sav comes from Renaud, Ward, and co-workers, who utilized a series of modified Knölker's complexes to promote the enantioselective hydrogenation activity (Figure 24).[311] While most exhibited low catalytic activity, the use of an intermediate length linker was found to promote ketone hydrogenation with 26% conversion and 34% *ee.* Ward and co-workers have also incorporated a biotinylated Fe-TAML complex (Fe-TAML$_{biot}$, TAML = tetraamido macrocyclic ligand) into Sav to impart hydroxylation activity into the scaffold.[312] While the Fe-TAML$_{biot}$ exhibits similar activity independently of the Sav

scaffold, incorporation of a S112R mutation resulted in >40% *ee* in the conversion of ethylbenzene to 1-phenylethanol, favoring the *R* enantiomer. Meanwhile, the L121R and S112R/L121E variants favored formation of the (*S*)-1-phenylethanol enantiomer. Structural characterization via crystallography of the S112R Sav and S112R/L121E Sav variants revealed salt bridge formation between Arg112 and the TAML ligand, forcing the Fe-TAML complex into a conformation allowing for Lys121 of the neighboring subunit (Lys121′) to bind Fe. In the S112R/L121E variant, the Arg112 side chain is turned away from TAML, with the side chain of Glu121′ coordinating Fe in an h^2 conformation. These changes in coordination are believed to impact the resulting product distribution and *ee* of these systems.

The Sav-biotin system has also been employed to simulate the classic facial triad present in many mononuclear non-heme Fe enzymes. To accomplish such a binding site, Borovik and co-workers designed a biotinylated bis(2-pyridylmethyl)amine (dpa) which was bound to a reengineered Sav scaffold with S112E, L121A, and E101Q mutations (2xm-S112E-Sav), each respectively intended to provide direct metal coordination, reduce sterics, and prevent exogeneous metal binding.[313] The crystal structure of Fe^{II}dpa-(2xm-S112E-Sav) revealed an unusual binding mode in which only one of the two pyridines of dpa coordinates Fe^{II}, resulting in N_2O_3 coordination (Figure 25). Meanwhile, structural characterization of Fe^{II}dpa-(2xm-S112E-Sav) showed facial coordination of all three N-donors of dpa, forming an N_3O_3 coordination set. In both Fe^{II}- and Fe^{III}dpa-(2xm-S112E-Sav), Glu121 serves to coordinate Fe in a k^1 fashion.

3.2. Designed Dinuclear Non-heme Iron Enzymes

Catalytic nonheme diiron enzymes can be broadly separated into two categories based on the nature of their bridging moieties, namely, those involving μ-carboxylate and those involving μ-thiolate. The former represents a large family with a diverse array of functionality, including methane and toluene monooxygenases, ribonucleotide reductases, flavodiiron nitric oxide reductases, rubrerythrin, and stearyl-ACP desaturase, to name a few. Meanwhile, the primary example of a catalytic (μ-thiolato)diiron site is FeFe hydrogenase (FeFe H_2ase).

Despite the ubiquitous nature of natural (μ-carboxylato)-diiron enzymes, there are few examples of incorporating such an active site into an ArM due to the difficulty involved in tailoring a binding environment for not one but two metal centers. The *de novo* Due Ferri (DF) scaffold designed by Lombardi, DeGrado, and co-workers has proven to be extremely valuable for the generation and study of such active sites and is discussed in depth by Pecoraro and co-workers.[314-316] Recently, the Sav-biotin system was reengineered to form a unique (μ-carboxylato)diiron binding site, employing a combination of Trojan Horse and direct AA coordination approaches.[317] To do so, Borovik and co-workers took advantage of the quaternary structure of Sav, which positions two biotin-binding sites in close proximity and with an intermediary pocket. Utilizing variants of biot-et-dpa, a series of ligands (biot-x-dpa) with varying linker length (x = ethyl, propyl, and butyl) were cross-correlated with a series of Sav variants, namely, WT, S112Y, L121Y, and L121A/L124Y.[313] Tyr was chosen due to the intense CT absorption feature that arises from Fe^{III}-O_{Tyr} coordination,[318] which allowed for the design of a visual assay testing for

Fe—O coordination. Successful binding was observed when employing a combination of the biot-bu-dpa ligand (bu = butyl) with the L121A/L124Y Sav variant. Using a combination of crystallography, ^{57}Fe Mössbauer spectroscopy, and DFT calculations, it was demonstrated that the newly formed site contained a [Fe^{III}-(μ-OH)-Fe^{III}] core with a labile proximal position at either Fe (Figure 26). Interestingly, an unusually long Fe—Fe distance of 3.96 Å and a small O_{Tyr}—Fe—$O_{\mu\text{-OH}}$ angle of 65° were observed, presumedly due to the strain imposed by the rigid Sav host, serving as an example of how deeply the SCS structure can impact the PCS.

Although (μ-thiolato)diiron enzymes are found in a much smaller family of enzymes, the most prominent member, [FeFe] H_2ase, has been the subject of intense interest for several decades due to its ability to efficiently and reversibly catalyze the production of H_2. The catalytic H-cluster of [FeFe] H_2ase, [$Fe_2(CO)_3(CN)_2$(adt)] (adt = $^-SCH_2NHCH_2S^-$), is unto itself an organometallic complex covalently tethered to a neighboring [Fe_4S_4] cluster via a cysteine-thiol bridge, making it an attractive target for incorporation in biosynthetic designs.

Given the H-cluster is a stable entity unto its own, one of the critical questions posed for the development of biologically inspired H_2ase catalysts is the extent of the SCS influence on H_2 production. As a result, many studies have utilized minimal oligopeptide maquettes to either form or bind H-cluster mimics. One of the first attempts was made by Jones et al., who incorporated a [$Fe(CO)_3$-(μ-S_{Cys})$_2$-$Fe(CO)_3$] complex via a CXXC motif in a single-stranded 36-mer oligopeptide maquette.[319] Based on this work, Hayashi and co-workers provided one of the first examples attempting to incorporate an H-cluster mimic into a non-native protein scaffold.[320] Inspired by the success of Jones et al., apo-cytochrome *c* (apo-C*c*) was chosen due to its native CXXC motif (Figure 27a and b). Formation of a [$Fe(CO)_3$-(μ-S_{Cys})$_2$-$Fe(CO)_3$] complex in apo-C*c* to form H-apo-C*c* was evidenced by a combination of ESI-TOF MS, absorption spectroscopy, and IR spectroscopy. Addition of the photosensitizer [$Ru(bpy)_3$]$^{2+}$ and excess ascorbate to H-apo-C*c* led to visible light-controlled H_2 formation, with a TON reaching ~80 after 3 h. The drop in efficiency observed with decreasing amounts of [$Ru(bpy)_3$]$^{2+}$ inspired further investigation of an alternative scaffold that could prospectively also bind a photosensitizer close in proximity to the CXXC motif. Using a single-stranded α-helical octadecapeptide maquette (Pep18) based on the sequence of cytochrome c_{556}, a CXXCH motif was employed (Figure 27c and d).[321] Similar to the case of C*c*, ESI-TOF MS, absorption spectroscopy, and IR spectroscopy were used to evidence both formation of [$Fe(CO)_3$-(μ-S_{Cys})$_2$-$Fe(CO)_3$] and binding of [$Ru(bpy)_3$]$^{2+}$ via His. Importantly, this maquette was able to evolve H_2 in the presence of light and excess ascorbate, which was otherwise not found without datively tethered [$Ru(bpy)_3$]$^{2+}$.

Alternative to the CXXC motif, Ghirlanda and co-workers explored the formation of a [$Fe(CO)_3$-(μ-S_{Cys})$_2$-$Fe(CO)_3$] complex with a single-stranded α-helical maquette using a UAA containing a dithiol side chain (Figure 27e).[322] Interestingly, reaction of this system with [$Ru(bpy)_3$]$^{2+}$, citrate buffer, and light produced a H_2 TON of 84 after 2.3 h, comparable to that observed by Sano et al. in their H-apo-cyt *c* system.[320]

Berggren and co-workers have recently expanded on the maquette-binding H-cluster model by design of a [Fe_4S_4]-binding oligopeptide (FdM) capable of binding

$[Fe_2(CO)_3(CN)_2(adt)]$ via a bridging Cys to generate a more comprehensive H-cluster structural model (Figure 27f).[323] While $[Fe_2(CO)_4(CN)_2(adt)]$ or $[Fe_4S_4]$-FdM was not observed to evolve H_2 as isolated in the presence of methyl viologen, the $[Fe_2(CO)_3(CN)_2(adt)]$-(μ-S_{Cys}-$[Fe_4S_4]$-FdM complex was capable of producing H_2 with a TON = 11 over the course of 1 h. Together with the maquette studies of Hayashi and Ghirlanda,[320-322] these results emphasize the importance of an electron transfer site in the proximity of the H-cluster.

Further studies have incorporated mimics of the H-cluster into larger scaffolds. Hayashi and co-workers have employed the thiosuccinimide-anchor method to generate a covalently bound H_2ase model using a modified nitrobindin (NB) β-barrel peptide scaffold with a Q96C substitution in combination with a maleimide-containing synthetic $[Fe(CO)_3$-(μ-$S)_2$-$Fe(CO)_3]$ complex (Figure 27g).[324] This combination yielded up to a TON of 130 over the course of 6 h in the presence of $[Ru(bpy)_3]^{2+}$, ascorbate, and light. Interestingly, in the absence of NB this complex still is capable of reaching a TON ~ 130 over the course of just 2 h. In this case, it appears that the limitations of $[Ru(bpy)_3]^{2+}$ access to the catalytic site imposed by NB hinder the reaction as opposed to promoting it.

Most recently, Ghirlanda and co-workers have employed the Sav-biotin system to generate a synthetic H_2ase using a biotinylated $[Fe(CO)_3$-(μ-$S)_2$-$Fe(CO)_3]$ complex.[325] Use of $[Ru(bpy)_3]^{2+}$ to drive catalysis in the presence of visible light and ascorbate resulted in slow H_2 production, reaching ~48 TON over the course of 11 h, significantly greater than the TON = 6 found in the absence of the Sav scaffold, demonstrating that the presence of a surrounding protein scaffold significantly improves the catalyst integrity. This hypothesis was further supported by transient absorption measurements, which evidenced an increase in the lifetime of the catalytically competent intermediate in the presence of Sav.

4. ACTIVITY BEYOND THE FIRST COORDINATION SPHERE IN ENGINEERED COPPER ARMS

Like Fe, Cu serves as an important cofactor for a variety of protein functions, including electron transfer (ET) and catalysis.[326-332] These functions can be regulated by tuning both the PCS and SCS. Cu proteins can function as ET proteins using one of two types of copper centers, known as type 1 Cu (T1Cu) (Figure 28a) and copper A (Cu_A) (Figure 28b); structurally homologous proteins (or protein subunits) containing either type of the copper site are referred to as cupredoxins.[333-335] The T1Cu center is coordinated by one cysteine and two histidine residues in a trigonal plane; for many T1Cu cupredoxins, another interaction from the axial position above the trigonal plane can form a distorted tetrahedral geometry that is between the coordination geometries preferred by the Cu^{II} and Cu^{I} states, thus facilitating ET.[336] Meanwhile, the Cu_A center is more complicated, involving a spatially close, electronically delocalized dicopper core bridged by two cysteines together with one histidine and one variable axial ligand on either side.[337,338] The geometry of Cu_A is more rigid than T1Cu with a comparably lower reorganization energy for the $Cu^{1.5+}$-$Cu^{1.5+}$/Cu^{2+}-Cu^{2+} redox pair. Cu_A sites are often found in conjunction with metalloenzymes containing catalytically active sites, including heme-copper oxidase

(HCO),[339] nitrous oxide reductase (N_2OR),[340] and non-heme nitric oxide reductase.[341] In HCO, the Cu_A center serves to transfer electrons from the periplasm to the buried heme-Cu_B site for the reduction of O_2. Meanwhile, the Cu_A site of N_2OR shuttles electrons to the copper Z (Cu_Z) site to catalyze the reduction of N_2O to N_2.[342] A Cu_A center with a unique PCS was recently identified in the protein PmoD.[343,344] Although this protein is related to two copper enzymes, ammonia monooxygenase (AMO) and particulate methane monooxygenase (pMMO), the function of this Cu_A center is not yet well understood.

While the T1Cu and Cu_A sites serve to transfer electrons, type 2 copper (T2Cu) is directly involved in biocatalysis as part of a catalytic active site.[350] The ligand set of T2Cu is typically composed of nitrogen- and oxygen-based ligands and, in special cases, methionine as well. Unlike the trigonal or distorted tetrahedral geometry of the PCS of T1Cu sites, T2Cu is in a distorted square-planar geometry in the Cu^{II} resting state with one or more empty sites allowing for the binding of small molecular oxidants such as O_2 or superoxide and enzyme substrates (Figure 28d). T2Cu-containing enzymes are generally oxidoreductases with vastly different structures, including nitrite reductase (NiR),[351,352] SOD,[353] and numerous O_2-utilizing enzymes known as oxygenases and oxidases.[354-356] Oxygenases function to incorporate an oxygen atom from molecular oxygen into the substrate. For example, lytic polysaccharide monooxygenase (LPMO) catalyzes the hydroxylation of the C—H bond in the glycosidic linkage using molecular O_2.[357,358] Meanwhile, oxidases use O_2 to reoxidize copper in the catalytic cycle without incorporation of O into the substrate. For example, laccase catalyzes the oxidative cross-linking of phenolic substrates while reducing O_2 to water.[359,360] For T2Cu enzymes, secondary coordination sphere (SCS) interactions function to not only tune the copper center but more importantly stabilize and/or activate substrates by hydrophobic interactions or hydrogen bonds or directly participate in the formation of reaction intermediates.

Beyond native functionality, the development of novel reactivity is an important perspective of artificial metalloenzymes. Copper complexes are important catalysts in organometallic chemistry, a topic covered by several in-depth reviews.[361-366] By combining a copper cofactor with a protein, one can take further advantage of the SCS environment imposed by the surrounding scaffold while maintaining the versatile chemistry of the organometallic copper compounds. There have been emerging examples using proteins or peptides as hosts for copper cofactors to achieve nonbiological reactivity, including Diels–Alder coupling,[367] Friedel–Crafts alkylation,[368] the Michael addition reaction,[369] and atom transfer radical polymerization (ATRP).[370] In many of these cases, the interactions between the SCS of the protein and the substrate molecules were shown to have a significant impact on the activity and selectivity.

The following section introduces a series of case studies on the SCS tuning effect of the two essential aspects of copper protein function—the electron transfer properties of T1Cu and Cu_A and the catalytic behaviors of T2Cu sites—in biosynthetic proteins or peptides. This section also covers nonbiological coppers catalysts including protein-fused synthetic copper complexes and the use of natural copper centers to catalyze nonbiological reactions. Due to their scarcity in nature and high complexity, other copper centers, such as type 3 copper (T3Cu)[371-373] and Cu_Z,[349] are rarely studied using biosynthetic models and, therefore, are

not discussed in this section. Despite their significance, the coverage of *de novo* designed copper proteins will be limited in this article, and we refer the reader to the review by Pecoraro and coauthors in this same issue for an in-depth discussion.

4.1. Designed Copper Proteins with Electron Transfer Functionality

The ET functions of T1Cu and Cu_A are essential for many biological processes requiring the transfer of electrons to active sites that are not close in contact with electron donors or acceptors. T1Cu can carry out efficient ET across long (>10 Å) distances, which is rationalized by the optimization of the driving force (ΔG) and reorganization energy (λ) according to Marcus theory.[333,374] Cu_A centers have been reported to perform even faster electron transfer than T1Cu in a comparative study.[375,376] Therefore, tuning the driving force—the reduction potential of copper ($E^{\circ\prime}$)—is essential to understand electron transfer processes in nature and to build better systems with improved ET properties.

To avoid the complexity of many native enzymes, the electron transfer properties of T1Cu have been studied using simple cupredoxins such as Az.[378-381] The $E^{\circ\prime}$ values of the native T1Cu proteins typically exhibit a wide (500 mV) range despite their similar structures.[382-384] Three main factors are considered responsible for such a large variarion in $E^{\circ\prime}$, namely, the identity of the axial ligand, hydrophobicity, and H-bonding (Figure 29). Axial ligation is not conserved among T1Cu proteins, taking varying identities such as Met in Az, Gln in stellacyanin, and a variety of hydrophobic residues in fungal laccases, etc.[385] To exclude other structural variables, the relationship between the axial ligand and $E^{\circ\prime}$ has been demonstrated in Az, in which the native Met has been mutated into nearly every other natural amino acid, as well as a series of unnatural amino acids.[386-391] A positive correlation was found between the hydrophobicity of the axial ligand and the $E^{\circ\prime}$ value of the T1Cu copper site, yet the range of observed potentials (150 mV) was not nearly as high as that observed between natural T1Cu cupredoxins. The influence of hydrophobicity in the T1Cu site SCS environment was examined in another study in which substitution of three more distant residues (Leu33, Met44, and Leu86) with Phe resulted in an increase of the reduction potential by 80 mV, which is additive to the tuning effect established by varying the axial residue.[392] Additionally, Lu and co-workers have demonstrated that the hydrogen bonding network may play a more subtle but equally important role.[377] The F114P mutation disrupts H-bonding between a backbone amide nitrogen and the S(Cys), increasing S-Cu covalency and causing a 110 mV decrease in $E^{\circ\prime}$. The N47S mutation further alters the H-bonding interaction with Cys112, leading to a 140 mV increase in $E^{\circ\prime}$ without significantly changing the PCS. The effects of H-bonding are additive to those from axial ligand modifications, producing a cumulative tuning range of ~800 mV.[377] SCS mutations also play a role in tuning the reorganization energy of the copper center. Interestingly, most of the mutants investigated were found to have lower reorganization energies and, hence, higher intra-molecular electron transfer rates than WT-Az, with the N47S/F114N Az mutant exhibiting the fastest electron transfer rate.[393] A following study of electron transfer in these mutants suggested a Marcus-inverted trend in which a higher reduction potential may lead to slower electron transfer,[394] therefore supporting the hypothesis that maximizing the rate of electron transfer requires optimizing the reduction potential.

Besides homology-based biosynthetic modeling, *de novo* design emerged in the 1990s as a powerful alternative approach to building metal binding sites in simple protein scaffolds.[397,398] Hildebrandt and co-workers reported a series of designed four-helix bundle proteins with Cys and His residues in the core of the protein. The position of these residues was shuffled throughout helices, among which 30 candidates displayed copper binding affinity.[399] The design was improved in a subsequent study by optimization of SCS interactions. By varying core residues with different hydrophobicity and bulkiness, the copper binding site was shown to be between T1Cu and T2Cu based on electronic absorption spectroscopy (color) and EPR ($A_{\parallel}$).[400] A more recent report by Shiga et al. showcased an exact blue T1Cu center in a four-helix protein (Figure 30a).[395,401] The reduction potential of copper was determined to be 328 mV, close to the reduction potential of Az (~280 mV). The Ala residues in the SCS were proposed to be replaceable, allowing for enhanced packing of the core and, thereby, tuning of the configuration of the T1Cu, although this is yet to be experimentally verified. Quaranta, Pecoraro, and co-workers reported a three-helix T1Cu protein with spectral features resembling the red copper nitrosocyanin.[402,403] Recently, the electronic properties of red copper were found to depend on Glu41 in the SCS that lengthens both the Cu—S(Cys) and the Cu—N(His) bonds (Figure 30b).[396,404] This residue was also found to tune the T1Cu reduction potential, as a E41D substitution was shown to increase the reduction potential by 50 mV. Two additional designs were made from the initial red copper construct to mimic the T1Cu center of enzymes such as plastocyanin and nitrite reductase, which are blue and green copper, respectively. The primary difference between these two proteins is the absence or presence of a SCS axial methionine.[404] Interestingly, the reduction potentials of the three mutants did not vary significantly, which opened up opportunities to further study the influence of the SCS in these three helical proteins to tune reduction potential.

The necessity of redox potential tuning has been demonstrated in several T1Cu-containing enzymes, where a fine-tuning of the T1Cu potential can significantly affect the enzymatic activity. Multicopper oxidases (MCOs) are a class of enzymes that catalyze the oxidation of organic substrates while reducing O_2 to H_2O, such as ascorbic oxidase, bilirubin oxidase, copper efflux oxidase, and laccase (Figure 31a).[326,354] Despite the different structures and functionalities, all MCOs require efficient electron transfer from T1Cu to the active site, which is directly dependent on the redox potential of the T1Cu.[410-412] The strategies of redox potential tuning in single T1Cu protein have been applied in MCOs.[413] Mutation of the axial T1Cu ligand from Met to either Leu or Phe in *Bacillus subtilis* laccase resulted in a 100 mV increase in reduction potential, which, in turn, decreased the laccase activity by 2–4-fold in the Leu mutant, with a near complete loss of activity in the Phe mutant (Figure 31b).[414] This trend was corroborated by another study in which mutation of the native axial Phe of *Thapsia villosa* laccase to Met lowered the T1Cu potential by 100 mV.[384] This mutation increased k_{cat} and K_M while shifting the optimal pH to a more basic regime. Kamitaka et al. reported a M467Q mutant of *Myrothecium verrucaria* bilirubin oxidase which lowered the formal potential of T1Cu by 230 mV while improving the kinetics of the electrocatalytic oxygen reduction reaction (Figure 31c).[415] Similar to the case of cupredoxins, introduction of an additional hydrogen bond donor can pose a significant impact on the T1Cu potential in MCO. Kakaota et al. studied the effect of the SCS hydrogen

bonds of the T1Cu in *E. coli* copper efflux oxidase (CueO).[416,417] The conserved Pro444 was mutated to Ala, Leu, or Ile to introduce a second hydrogen bond to Cu-bound S(Cys) (Figure 31d). Similar to its Az counterpart, this modification decreased the covalency of the S(Cys)—Cu bond while increasing the T1Cu reduction potential by 40–70 mV. As a result, k_{cat} was observed to decrease by 40–60% among these mutants. Meanwhile, the P444G mutant showed higher activity than the native enzyme; however, the T1Cu reduction potential in this variant was not reported.

Another study by the same group focused on proton transfer in the SCS between the T1Cu and T2/T3Cu sites in *E. coli* CueO.[409] Mutation of the proton donor Glu506 to Ile resulted in complete loss of activity, whereas a less bulky Ala mutation led to a compensated proton transfer pathway bridged by two water molecules. The E506N mutant also showed no activity, demonstrating the importance of a dissociable proton. The correlation between the T1Cu redox potential and the MCO activity has been previously reviewed[411] and recently demonstrated in a comparative study by Solomon and co-workers.[418] The authors compared the high-potential fungal laccase of *Trametes versicolor* (axial Phe) with the low-potential plant laccase (axial Met) from *Rhus vernicifera.* The higher potential was found to result in an 8 kcal/mol decrease in the intramolecular electron transfer driving force. While electron transfer from T1Cu to the trinuclear Cu active site is the rate-limiting step of fungal laccase, this slow electron transfer is partially offset by the higher reduction potential of the trinuclear center (TNC, the T2Cu and T3Cu sites) due to a more positive protein environment and is still faster than the decay of the native intermediate during catalytic turnover.

In addition to laccases, the tuning of T1Cu and correlation with enzymatic activity have been studied in copper-dependent nitrite reductase (CuNiR), a more complex enzyme that catalyzes the reduction of nitrite (NO_2^-) to nitric oxide (NO), a process essential for denitrification as part of the nitrogen cycle.[422] The reduction of NO_2^- at the T2Cu of CuNiR requires the injection of one electron and two protons, the former of which is mediated by T1Cu through a Cys-His bridge (Figure 32a).[348,423] A subtle balance exists between the two copper centers that their reduction potentials are only slightly different to prevent premature reduction of T2Cu in the rest state.[424] Inspired by the studies on individual cupredoxins, the axial ligands of T1Cu in CuNiR were subjected to mutagenesis. The M144A mutation of the *Alcaligenes xylosoxidans* NiR (AxNir) profoundly increased the reduction potential of the T1Cu from 255 mV to 314 mV and, therefore, reversed electron transfer from the low-potential T2Cu (230 mV) (Figure 32b).[421] An even greater increase of the T1Cu potential was observed in the more hydrophobic M144L mutant (336 mV), whereas incorporation of the hydrophilic M144N mutation decreased the reduction potential to 173 mV.[420] Interestingly, the M144L mutants showed higher NO_2^- reduction activity than the native enzyme while the Gln mutants exhibited no activity, suggesting that an artificially tuned, moderately uphill electron transfer is beneficial to the CuNiR activity (Figure 32c). In another study by Sato et al. the T1Cu binding loop of NiR was replaced with that from amicyanin, which maintains the PCS ligand sets but with a much shorter length (nine residues) (Figure 32d and e).[419] The swap caused a significant increase of 200 mV in the T1Cu reduction potential together with diminishing NiR activity due to the excessively negative driving force of electron transfer. This effect does not appear to corroborate with

the trend observed between the decreased hydrophobicity and redox potential, as indicated by the coordinating water molecule, suggesting a profound but unknown influence from the SCS of the binding loop.

Likewise, Cu_A has been studied in both native cupredoxins and biosynthetic models using similar tuning strategies as employed to study the electron transfer properties of T1Cu. For example, mutation of the axial Met227 to Ile in *Paracoccus denitrificans* cytochrome *c* oxidase (C*c*O), was shown to result in the loss of electron delocalization in the Cu-Cu core and impair electron transfer to heme *a*.[429] A study of *Rhodobacter sphaeroides* C*c*O showed that the M263L mutation maintained the electron delocalization between the copper atoms but caused a 120 mV increase in the reduction potential and, correspondingly, a 2.5-fold decrease in the electron transfer rate and 90% diminishment of the C*c*O enzyme activity.[430,431] Other studies have investigated Cu_A by truncating native proteins, effectively separating the electron transfer and catalytic components.[346] In a series of studies on the Cu_A domain of *Thermus thermophilus* cytochrome *ba3* oxidase (*Tt*Cu_A), the weakly bound axial Met160 was mutated to Glu and Gln (Figure 33b).[432] In both cases, the mutated axial residues showed strong interactions with Cu possessing features similar to the PCS residues. Early EPR studies suggested an elongated Cu—Cu distance and change in geometry of the Cu_2S_2 core,[433] while recent results from X-ray spectroscopy indicated that the Cu—Cu distance remains mostly unchanged in the M160Q mutant.[428] The M160Q mutation resulted in a change of redox potential by −170 mV at neutral pH, with a Cu—Cu distance nearly identical to that of the wild-type (2.45 Å). An even greater difference of −190 mV was observed in another M160H mutant. Despite similar reduction potentials, the electronic structures of M160H and M160Q were found to differ significantly. The M160Q mutant has a significantly higher energy gap between the two accessible ground states π_u and σ_u^* (900 cm^{-1}, pH = 6.0) than the wild-type (600 cm^{-1}) and the M160H mutant (200 cm^{-1}) (Figure 33f). A broader set of axial mutations were studied by Ledesma et al. with M160S, M160L, and M160Y mutations.[434] The hydrophobic M160Y and M160L mutants exhibited similarly high reduction potentials (348 and 346 mV, +55 and +53 mV vs WT), while the hydrophilic M160S mutant exhibited lower reduction potentials (209 mV, −84 mV vs WT).[434] In a study by Blackburn et al., the axial Met was replaced by Met_{Se}. The electrochemical properties were mostly identical between Met and Met_{Se}, and the EXAFS data indicated very similar geometries at the Cu_A core.[435]

Cu_A centers have also been introduced into the homologous cupredoxins to explore the influence of the SCS. Biosynthetic Cu_A centers have been built in amicyanin[436,437] and Az[438,439] by replacing the original Cu binding loop with a Cu_A binding loop. Similar to studies of T1Cu, the axial Met has been mutated to hydrophilic Asp and Glu and hydrophobic Leu residues, altering the Cu_A redox potential by +16, −5, and −8 eV (Figure 33e).[440] To modulate the H-bonding interaction with Cys112, N47S and E114P mutations were made in Cu_A azurin (Cu_AAz) (Figure 33d), leading to + 30 and −42 mV changes in the Cu_A reduction potential, which are modest in comparison to the + 120 and −46 mV differences seen in T1Cu.[441] Both strategies resulted in a smaller tuning effect compared to the T1Cu counterpart, which was attributed to either the higher robustness of the Cu_A diamond core or the fact that these alterations produced more subtle changes in

the coordination environment, such as the possible presence of a water ligand in M123L Cu_AAz.[442]

The loop replacement strategy has also been applied in the native Cu_A cupredoxins, where the use of different loops allows for the PCS of Cu_A to be kept consistent while modifying the SCS. The three loops of *Tt*Cu_A, referred to as the His loop, entry loop, and ligand loop, were replaced by the loops from the native Cu_A subunits of human or plant C*c*O (Figure 33c). A moderate ±30 mV tuning of the reduction potential was observed in the loop-exchanged mutants compared to wild-type *Tt*Cu_A.[427] Other electronic properties, including the ground state (π_u/σ_u^*) energy and delocalized spin density on axial Met, were also tuned by the loop replacements.[443,444]

In addition to cupredoxins, Cu_A has been constructed in both natural nonhomologous proteins and *de novo* designed proteins. Mirts et al. designed a Cu_A site in a cytochrome *c* peroxidase (C*c*P) scaffold (Figure 34).[446] The new CuA center resides in the buried α-helical pocket where the heme is docked in the unmodified C*c*P. The reduction potential of the Cu_A center was found to be 251 mV as measured by redox titration, comparable to the case of Cu_A in native C*c*O (240 mV). Electron transfer between this Cu_AC*c*P protein and cytochrome *c* was observed, albeit at a significantly lower rate compared to the case of native Cu_A (10^{-3} s^{-1} vs 10^5 s^{-1}). Cu_A has also been incorporated into *de novo* designed helical bundles by Hildebrandt and co-workers, as evidenced by EPR, MCD, and UV–vis absorption spectroscopies.[400] A later study by Tanaka and co-workers reported another example of Cu_A in a coiled-coil protein in a rationally designed $Cu_2(Cys)_2(His)_2$ core, exhibiting a Cu—Cu distance of 2.55 Å, longer than in native Cu_A.[445] Unfortunately, no electrochemical characterization was carried out in either of these studies, and the ET activities of these constructs remain unknown. Studies using nonhomologous scaffolds have shown that the Cu_A structure can be well mimicked by transplanting the PCS ligand set. While full functionality is dependent on outer sphere interactions, it can be partially restored in these biosynthetic models.

4.2. Designed T2Cu Proteins with Catalytic Functions

Compared to the electron transfer copper proteins, modeling the catalytic sites of T2Cu proteins requires more detailed consideration. T2Cu proteins are, in general, more complex due to the numerous auxiliary units required to promote native catalytic activity. It is also difficult to achieve functional interactions with the substrates, as well as to stabilize redox-active intermediates during enzymatic turnover, roles which are fulfilled by well-positioned amino acid residues in the native protein. Three approaches, *de novo* design,[83,447-449] incorporation of T2Cu into natural proteins by coordination with amino acid side chains, and bioconjugation of organometallic complexes, have been applied to mimic the active site of catalytic Cu enzymes, and each of these approaches has provided insights into the role of SCS interactions.

The functionalities of several Cu enzymes, such as catechol oxidase (COx),[451] superoxide dismutase (SOD),[452] and nitrite reductase (NiR),[453] have been applied in artificial protein models, among which models of NiR are the most well studied with respect to probing the influence of the SCS. The first functional model of the catalytic T2Cu was reported

by Pecoraro and co-workers.[450,453] A tri-His copper binding site was introduced into the core of the three-helical peptide TRI-W. The NiR activity was observed by generation of N_2O without side reactions, albeit with lower activity than that of native NiR (Figure 35a). The activity was improved by tuning the SCS through electrostatic interactions, for which several solvent-exposed Lys and Glu residues were mutated to their counterparts with opposite charge.[454] A 4-fold increase in the activity was observed between the most positively charged E27K and the most negatively charged K24E mutants. The reduction potential also decreased with increasing negative charge in the SCS by a maximum of 100 mV. Meanwhile, the influence of the steric hindrance was tuned by mutating the Leu residues below or above the active site into Ala or Asp.[455] All variants showed elevated activity, with an increase in reaction rate up to 75-fold. These changes were attributed to an interplay between the coordination geometry of the Cu^I state and the electronic structure of the transition states. Recently, similar designs have been applied to construct Cu-bound α-helical peptides for other activities, including superoxide dismutation[452] and peroxide activation,[456] with the effects beyond the PCS unexplored but promising for future studies.

In addition to *de novo* design, strategies employing natural protein scaffolds have also been reported for NiR. Berry and co-workers have incorporated a His_3 or a His_2Asp site on the surface of Az (AzNiR), producing a system that includes both the T1Cu and T2Cu sites of CuNiR (Figure 35b and c).[457] Both UV–vis and EPR spectra showed a new T2Cu species in addition to the native T1Cu. The incorporated T2Cu is solvent-exposed, leading to a moderately high potential (350 mV), which is between those of the previous model and native NiR, which are both hydrophobically buried. The NiR reaction rate (0.34–0.59 min^{-1}) in this Az model is lower than that of the native NiR yet comparable with those of the previously mentioned *de novo* designed peptides. The native T1Cu site serves as an optional electron donor which may participate in NiR catalysis directly, although the T2Cu was also found to independently catalyze nitrite reduction when the T1 site is blocked by Hg^{2+}.

Similar cupredoxin scaffolds have been adopted to model catalytic Cu sites other than NiR. In Az, the substitution of the chromogenic Cys residue with a hard Asp ligand resulted in a typical $(His)_2Asp$ T2Cu center, with large $A_\parallel$ as measured by EPR and a weak absorption feature at 600 nm.[460,461] Surprisingly, it has been found in a more recent study that further mutation of the axial Met residue to a hydrophobic, noncoordinating Leu, Phe, or Ile residue results in a new type of copper center that resembles neither T1Cu nor T2Cu.[458] The new copper center, called “Type 0 Cu” (T0Cu, Figure 36), showed a weak d—d transition band at 800 nm but no absorption in the visible region. The $A_\parallel$ splitting falls into the low 300 MHz range, which is between the values from T1 (<200 MHz) and T2 Cu (>400 MHz). The reduction potential of T0Cu is higher than that of T2Cu and closer to that of the native T1Cu. The authors mutated the axial ligands to Glu in a following study, which reverted the spectroscopic features back to T2Cu with a comparably high potential (300 mV).[459] The axial Glu exerts only an electrostatic effect and does not bind directly to copper at lower pH. At higher pH (9.0), the H-bonding network in the SCS caused a structural rearrangement of the T2Cu site as indicated by XANES and X-ray crystallography, leading to binding of the deprotonated Glu to Cu and a down-tuning of the reduction potential to 120 mV. Both modified T0Cu and T2Cu possess promising features, such as the low coordination number,

high reduction potential, and flexible coordination pattern, for mimicking the catalytic T2Cu sites in nature.[462]

Starting from the same Az model, the Lu group turned to investigate Cu-mediated post-translational modifications of S(Cys). A report in 2014 demonstrated that the M121G mutation decreased the hydrophobicity of the T1Cu pocket while opening an axial binding site (Figure 37a).[463] Reduction to Cu^{I} enabled the interaction of the T1Cu site with hydrogen peroxide to yield a species with an absorption maximum at 400 nm that decays quickly in air to form the starting Cu^{II}-M121G Az. Further investigation of this intermediate by resonance Raman spectroscopy revealed an S-O vibration which could be attributed to the formation of sulfenic acid (Cys-SOH) formed at the Cys112 as further supported by proteomic analysis. The formation of sulfenic acid was attributed to the Cu-activated H_2O_2 based on ^{18}O-isotope labeling studies. A computational study suggested the SCS served to stabilize the sulfenate by removing a negatively oriented dipole near Cu. This study was one of the first to demonstrate metal-sulfenate coordination in an artificial metalloenzyme system, whose natural presence was considered essential for the activity of nitrile hydratase and thiocyanate hydrolase. Although this process was accomplished using a different metal cofactor, this Az model demonstrated a plausible reaction mechanism for this post-translational modification in nature. Furthermore, the Lu group investigated the intramolecular nitrosylation of the Cys residue to form nitrosothiol (Cys-SNO), which serves as one of the most important biological reactions in NO regulation.[276] To accomplish this, a H46E/M121H Az mutant was created to mimic the T1Cu of nitrosocyanin (Figure 37b). An additional F114P SCS mutation was introduced to eliminate H-bonding with S(Cys) and decrease the Cu potential. Under anoxic conditions, the T1Cu of the triple mutant catalyzed the formation of a Cu-Cys-SNO species on the ligating Cys residue, while a facile and complete release of NO could be achieved in vacuum or air. The Cu-mediated nitrosylation reaction displayed rapid kinetics ($k = 6.7 \times 10^5\ M^{-1}\ s^{-1}$), high yields (>90%), and efficient scavenging of NO at micromolar concentration.

Ward and co-workers have also designed a copper peroxidase using 6-phosphogluconolactonase, a natural hydrolase scaffold, that has a potential $(His)_2Asp$ copper binding motif discovered by the STAMPS algorithm (Figure 38).[464] The protein was expressed and cocrystallized with $CuSO_4$, showing that the two predicted His residues bound Cu as anticipated, although the third ligand was found to be H_2O stabilized by H-bonding with a side chain carbonyl moiety rather than the anticipated Asp131 residue. The peroxidase activity was found through the Cu-catalyzed oxidation of *o*-dianisidine using *tert*-butyl-hydroperoxide (*t*-BuOOH) as oxidant, with a maximum turnover number of ~25 achieved over the course of 1 h. Computational docking simulations revealed a possible hydrogen bond between the substrate and residues Asp131 and Tyr69, leading to the arrangement of the aromatic rings in-plane with the copper ion. A mutagenesis study of these two residues did not result in a significant change of catalytic efficiency when varied, although one mutant, Y69L, showed a 3-fold increase in turnover frequency.

In addition to natural proteins, Borovik and co-workers have used the Sav scaffold together with a biotinylated CuN_3 synthetic complex to study Cu-H_2O_2 interactions (Figure 39),[465] a similar strategy previously adopted to create a T1Cu in the same scaffold.[466] The protein/

copper complex was used to model lytic polysaccharide monooxygenase (LPMO), an enzyme with a special Cu-His-brace active site to catalyze the oxidative degradation of long-chain polysaccharides.[358,467] The SCS of LPMO is known to stabilize the transient Cu-hydroperoxo (Cu-OOH) complexes but eventually lead to the cleavage of the O—O bond and the oxidation of the substrate.[468,469] Such interaction was mimicked by this Sav-Cu model but resulted in a room-temperature-stable Cu-OOH complex. Upon addition of hydrogen peroxide, an intense shoulder around 380 nm was observed and attributed as an $^{-}$OOH → Cu LMCT transition. The Sav-Cu protein crystal was soaked in H_2O_2-containing buffer, and the structure was determined with X-ray crystallography. The structure showed an electron density of two oxygen atoms on the axial site of copper, which was assigned as the axial hydroperoxo ligand. A hydrogen bond network was depicted in the crystal structure. The distal oxygen of the hydroperoxo anion formed a hydrogen bond with the amide nitrogen of the Asn49 residue. The proximal oxygen was involved in a more complicated hydrogen bond network consisting of Ala86, Ser112, Lys121, and two water molecules. The latter interaction was proposed to be important for the stability of the Cu-OOH complex as it offsets the push–pull effect from the distal hydrogen bond and avoids breaking the O—O bond, similar to the His-O_2 interaction in myoglobin.[470] The study provided key insight into how a well-positioned hydrogen bond alters the stabilization or activation of a Cu-oxygen adduct.

Aside from the α-helical bundle proteins mentioned previously, another type of *de novo* designed peptides was reported by Rufo et al. as copper-based oxidases (Figure 40). These β-sheet peptides self-assemble to form an amyloid fibril, serving as robust heterogeneous biocatalysts. A tri-His motif was built on the outer face between the β-strands to bind metals such as Zn and Cu.[471] These solvent-exposed metal binding sites may be able to interact with substrates that are incompatible with hydrophobic environments in common enzymes. A report in 2016 showed that such amyloid assembly catalyzed the oxidative C—C coupling of 2,6-dimethoxyphenol using molecular oxygen.[472] In a following study, the Cu-amyloid assembly showed versatile activities, catalyzing the cascade hydrolysis and oxidation of 2′,7′-dichlorofluorescin diacetate (DCFH-DA).[473] It also showed that pure hydrolase activity could be achieved by catalyzing the hydrolysis and detoxification of paraoxon, a toxic organophosphate insecticide.

4.3. Designed Copper Enzymes with New-to-Nature Activities

The concept to combine artificial organometallic complexes with protein scaffolds was first raised in the 1970s by Whitesides, Kaiser, and co-workers.[474,475] Not limited by the natural amino acid ligand set, this bioconjugation-based strategy takes advantage of the non-natural reactivities of artificial cofactors while using the outer coordination spheres imposed by the surrounding protein matrix to impart unique properties on reactions, including enhanced rates, yields, stability, and selectivity. Various transformations have been reported in the past decades and reviewed extensively.[69,476] This section will focus on the protein-conjugated copper catalysts that specifically utilize the outer coordination spheres of the protein hosts.

Copper, known for its Lewis acidity, has been used as a catalyst for the Diels–Alder (D-A) reaction since the 1960s.[486] To mimic this reactivity, Reetz et al. used commercially

available Cu-phthalocyanine imbedded in serum albumin (SA).[487] The Cu macrocycle was proposed to be noncovalently anchored in the IB subdomain, analogous to the natural hemin. Among a series of substrates, an *endo/exo* product ratio of up to 95:5 with an *ee* value up to 98% could be accomplished. The high enantioselectivity was not experimentally probed beyond product analysis, but it was proposed that protonation and/or hydrogen bonding with the substrate nitrogen atom was relevant. A later study by the same group created a Cu-$(His)_2$Asp facial triad site in a β-barrel core of the tHisF protein (Figure 41a), which was found to catalyze the D—A reaction on the same set of substrates but with lower enantioselectivity.[477] The same Cu-$(His)_2$Asp core was later adopted and improved by Ghattas et al. in a 1-aminocyclopropane carboxylic acid oxidase (ACAO) scaffold by substituting the native Fe center with Cu (Figure 41b).[478] Yields over 85% for all substrates were accomplished, with a maximum *endo/exo* ratio of 99:1 and *ee* of 95%. A computational docking study indicated that the substrate is flanked and orientated by Lys158 and Ile184, while Phe250 packs with the substrate from the noncoordinating side. These SCS restraints only enable one possible direction for the attack by cyclopentadiene, explaining why such high enantioselectivity was achievable.

Meanwhile, a series of artificial enzymes were reported using covalently fused Cu-phenanthroline or Cu-dipyridine compounds and scaffolds including polynucleotides,[480,488] LmrR,[367,489] αRep A3,[481] neocarzinostatin,[482] FhuA,[483] aponitrobindin,[484] adipocyte lipid binding protein, and human adenosine receptor (Figure 41c-j).[485] Most of these examples adopt a hydrophobic SCS, either inside the protein or formed between dimer surfaces, to stabilize the aromatic copper complex, facilitate substrate binding, and accelerate the reaction. Another strategy using amino acid residues as ligands has also been adopted to design a Diels–Alderase in bovine-pancreatic polypeptide (BPP)[369] (Figure 41k), LmrR[490] and mTFP.[479] Nonetheless, many of the enzymes in these early works have slow catalytic rates and relatively low conversion. This issue was addressed in a very recent study by Basler et al.[491] An α-helical protein binding Zn (a structural analogue of Cu with different acidity) was designed and developed through several rounds of directed evolution. The catalytic efficiency of this construct was improved by over 10^5-fold between the starting and final designs. The final design, DA7, has a catalytic efficiency of 2.9×10^{10} M^{-1}, a TON of 10^4, and >99% endo selectivity. Examination of the crystal structure and a docking model revealed the alignment of the diene substrate by the hydrogen bond donor Arg28 from the carboxylate side and by Gln31, Gln80, and Tyr84 from the pyridyl side. The dienophile substrate was packed underneath the diene by the aromatic ring of Trp68 with the two dienedienophile moieties closely facing each other. The precise orientation of the substrate explained how these high numbers were accomplished, the most efficient currently reported for a Diels–Alderase.

Another application of Cu-protein hybrid catalysts is the Friedel–Crafts (F-C) alkylation reaction. To this end, the Roelfes group used a LmrR protein that forms a homodimer with a large hydrophobic pocket.[368] The two Trp residues at the interface exert strong π-π stacking to allow tight binding to an aromatic Cu^{II}-phenanthroline (Cu^{II}(phen)) or Cu^{II}-2,2′-bipyridine (Cu^{II}(bpy)) complex with micromolar affinity (Figure 42a). These artificial metalloenzymes catalyzed the site selective alkylation of an indole substrate with near full conversion and *ee* up to 93%. Interestingly, the reactivity of this artificial enzyme

could be tuned by mutation of two SCS residues. The A92E mutation altered the side chain orientation toward an outer Asn14 residue, enhancing binding of the Cu^{II}(phen) cofactor between the two Trp residues according to MD simulations and eliminating the minor reactivity of the tandem F-C alkylation/enantioselective protonation reaction (FC-EP).[492] Removal of the packing Trp96 residue, however, switched the reactivity toward the FC-EP reaction with moderate enantioselectivity due to the binding dynamics of the cofactor. The hybrid catalyst was further applied in whole-cell biocatalysis, and directed evolution was applied to the outer sphere residues to enhance the yield and selectivity.[494] A similar noncovalent cofactor docking method has also been applied in other proteins from the TetR family to catalyze the same Friedel–Crafts reaction (Figure 42b).[493] An alternative strategy of genetic unnatural amino acid incorporation was adopted by the same group to introduce the Ala_{Bpy} unnatural amino acid residue as Cu ligand.[490] Mutation of three SCS residues, Asn19, His86, and Phe93, had a moderate impact on the conversion rate, enantioselectivity, and substrate preference, which was attributed to π-stacking interactions and the steric freedom of the hydrophobic pocket. This Ala_{Bpy} LmrR mutant was further used to stabilize a semiquinone radical (Figure 42c), reminiscent of the chemistry of COx.[286]

The Michael addition reaction, another type of C—C bond formation reaction, can be catalyzed by artificial copper enzymes. In the late 2000s, Roelfes and co-workers reported the enantioselective catalysis of the Michael addition reaction by a Cu binding oligonucleotide[488] and bovine pancreatic peptide scaffold,[369] respectively. Recently, the group expanded the previously mentioned Cu^{II}(phen)-Trp docking strategy with an unnatural adjacent *p*-aminophenylalanine (pAF) residue.[495] The two active centers work in a synergistic manner, in which Cu binds and activates the Michael donor while the pAF residue activates the Michael acceptor substrate by forming a Schiff base (Figure 43a). An improved yield (36%) and *ee* (86%) were observed in the dual-functional catalyst versus controls. The M8L mutation provided moderately improved activity and selectivity (99%), which were correlated to a hydrophobic interaction with Trp96, as described in a previous study *vide supra.* The Itoh group has reported a cupin-based catalyst using only natural amino acids (Figure 43b).[496] Starting from a natural $(His)_4$ binding motif, a ligand set library was screened by decreasing numbers of His residues. Both the tris-His mutant H52A (*S* product) and the bis-His mutant H54A/H58A (*R* product) were found capable of catalyzing the Michael addition reaction with both high yield and selectivity, but interestingly, their enantioselectivities were reversed relative to one another. A docking study revealed that the hydrogen bond from Cys106 (sulfinic acid form) may swing to the *Si*-face of the azachalcone substrate in the H52A mutant, favoring the attack by nitromethane from this side. On the other hand, the H54A/H58A mutant appeared to have an open *Re*-face with the Phe104 residue blocking the *Si*-face, and as a result the Cys106 swings to the *Re*-face to enable attack from the *Re* side. This effect was supported by a subsequent mutagenesis study, in which the H52A/C106A or H52A/C106S mutation removes or disori-entates the H-bond and reduces the *Si* selectivity, whereas the H54A/H58A/F104W mutation enhances the steric hindrance from residue 104 to increase the *Re* selectivity. Another recent study by Rimoldi et al. used two simple peptides derived from the methionine-rich motif in hCtr-1 transporter to catalyze the Michael addition reaction.[497] The yield was comparable to those

of previous studies with a relatively lower enantioselectivity, possibly due to the absence of the SCS interactions of more complex proteins.

Artificial Cu enzymes have also been reported for hydration reactions and small molecule polymerization. Both covalent conjugation and noncanonical amino acid incorporation strategies were used in two studies to introduce phenanthroline or Ala_{Bpy} Cu complexes into the LmrR scaffold (Figure 44).[498,499] Hydration of α,β-unsaturated ketone substrates was achieved in both cases with moderate enantioselectivity (60–80%). Two residues, Phe93 and Asp100, were found to serve as important SCS residues in both cases. The Phe residue provided a $\pi-\pi$ stacking interaction to support binding of aromatic copper complexes, while the Asp residue acts as a general Lewis base, forming hydrogen bonds and activating the water substrate. In the latter case (Cu-Ala_{Bpy}), adding an alternative general base such as V15E significantly increased both the conversion rate and enantioselectivity due to better positioning of the carboxylate. As for polymerization, the Bruns group reported a protein cage nanoreactor system using thermosome (THS).[370] This protein is a group II archaea chaperonin with a large (130 nm^3) cavity, that was used to confine the Cu complex and substrate, as well as wide pores, to release polymeric products. The nanoreactor produced poly(*N*-isopropyl acrylamide) by ATRP with an average molecular weight of 1500 g/mol and a polydispersity index of 1.11. Other catalysts, such as horseradish peroxidase, have also been used in this nanoreactor system.[500]

5. CATALYSIS BEYOND THE PRIMARY COORDINATION SPHERE BY RATIONALLY DESIGNED MULTINUCLEAR METALLOENZYMES CONTAINING HEME

By incorporating another metallocofactor next to the heme, nature evolved a number of multinuclear metalloenzymes to fulfill different and more challenging functions. One example is manganese peroxidase (MnP), in which a Mn^{II}-binding site next to the heme macrocycle can oxidize Mn^{II} to Mn^{III} upon reaction with H_2O_2. The generated Mn^{III} is then used to oxidize other organic substrates, in some instances.[501] On the other hand, heme-copper oxidase (HCO) consists of a heme-Cu_B heteronuclear center. It functions as a terminal oxidase catalyzing the reduction of O_2 to water to generate the transmembrane proton gradient required for ATP synthesis.[41,502] Interestingly, bacterial nitric oxide reductase (NOR) has a non-heme iron center (Fe_B site) at the corresponding Cu_B position of HCO and catalyzes the one-step, two-electron reduction of NO into N_2O, which is an important step in denitrification.[422,503] Dissimilatory sulfite reductase (SiR) catalyzes a six-electron reduction of sulfite into sulfide using a combination of a heme macrocycle (siroheme) and a [4Fe-4S] cluster as cofactor. It makes up one of the important steps in sulfate respiration in sulfate-reducing bacteria.[504] In order to elucidate how nature evolved these different multinuclear heme-containing metalloenzymes to catalyze different reactions, efforts have been made using synthetic[505] and biosynthetic models[69,476,506] to provide more insights. Moreover, inspired by the water-bridged homodinuclear magnesium mechanism for some natural nucleases,[507] an artificial nuclease was made by the design of a Mg^{2+}-heme heteronuclear Mb system.[508] In this section, we will focus on how SCS affects the performance of these multinuclear heme-containing ArMs.

5.1. Manganese Peroxidase Using Cytochrome *c* Peroxidase as a Scaffold

To engineer a functional mimic of MnP, the Lu group successfully designed a Mn binding site into C*c*P through the introduction of G41E, V45E, and H181D mutations (Figure 45a and b).[509] The resulting triple mutant (MnC*c*P) could oxidize Fe^{II} at least five times more efficiently than the native C*c*P. A deeper structural analysis and comparison of the secondary coordination spheres of C*c*P and MnP uncovered two residues of interest, namely Trp51 and Trp191 of C*c*P, which sit in the same positions occupied by Phe in MnP (Figure 45c and d). Hence, the W51F and W191F mutations were made to further tune the reactivity of MnC*c*P. While no significant change in activity on Mn^{II} oxidation was observed for W191F MnC*c*P, W51F MnC*c*P was found to have a 4.3-fold increase in V_{max} compared to MnC*c*P, and the W51F/W191F MnC*c*P double mutant displayed a further 14.3-fold increase in V_{max} over that of W191F MnC*c*P. This compounding effect may be rationalized if one assumes there is an equilibrium between the $Fe^{III}Trp^{+\cdot}$ state (the radical of compound I in C*c*P is believed to preside on Trp191 rather than the porphyrin ring, as Trp is readily oxidized) and the ferryl state of C*c*P compound II. Both Trp51 and Trp191 are capable of stabilizing compound II, with either Trp51 through H-bonding to the ferryl oxygen or Trp191 through the proposed equilibrium. Although W191F MnC*c*P cannot stabilize compound II through radical delocalization, it can still be stabilized by H-bonding interactions with Trp51; therefore, no increase in activity is observed. For W51F MnC*c*P, the delocalization from Trp191 can stabilize compound II, but the H-bonding interaction is missing, so an increase in activity is observed. By mutating both Trp to Phe, both stabilizing effects are removed, producing the largest increase in activity.[510,511] The resonance Raman spectra of these mutants also reveal that the W51F mutant lacks the H-bonding interactions between tryptophan and a weakly bound distal water. The loosening of this water may lead to quicker formation of compound I and an increase in activity.[512] However, all the MnC*c*P and its mutant mentioned did not match the activity of native MnP. The k_{cat}/K_M for W51F/W191F MnC*c*P was 0.599 s^{-1} mM^{-1}, while the one for native MnP was 3952 s^{-1} mM^{-1}.[510]

To enhance the activity of MnC*c*P and investigate the roles of other secondary sphere residues, MnC*c*P was further redesigned by replacing Asp181 with Glu, reverting the G41E mutation, and further mutating Asp37 to Glu. The resulting construct is referred to here as MnC*c*P.1. MnC*c*P.1 was found to have a 2.5-fold higher catalytic efficiency (k_{cat}/K_M) than MnC*c*P.[514] Based on MnC*c*P.1, several additional alterations to the secondary coordination sphere were made to further tune its activity.[515]

First, comparison of the crystal structures of MnP and MnC*c*P revealed that Glu39 in MnP is very flexible and can adapt different rotamers. As a result, binding of Mn^{II} can occur with a relatively short distance of 2.10 Å. Meanwhile, the correspond-ing Glu45 of Mnc*c*P.1 is rather rigid, retaining its position in either Mn^{II}-free form or Mn^{II}-bound form with a distance of 3.94 Å in the latter. This results in a different metal center geometry and may be responsible for the different Mn^{II} binding affinities and MnP activities. Tyr36 was found to be within H-bonding distance of the carboxylate group of Glu45 in MnC*c*P.1 (Figure 46), an interaction that is otherwise missing in MnP. This H-bond may compete with Mn^{II} coordination by stabilizing rotamers that are unfavorable for coordination. To address this, a

Y36F mutation was introduced into Mnc*c*P.1 and was found to have a 2.8-fold improvement of K_M, indicating the binding affinity of Mn^{II} was increased.

Second, residues Glu37 and Glu181 were found to closely neighbor Mn^{II} in MnC*c*P.1, with distances of 3.23 Å and 4.08 Å, respectively. However, these distances are considerably longer than the corresponding coordination bonds of Mn^{II}—Glu35 and Mn^{II}—Asp179 in MnP, which are 2.4 Å and 2.41 Å, respectively. A structure-based sequence alignment of MnPs from different organisms revealed that a conserved Arg was located below Glu35 in MnP. Bearing in mind that this arginine might play a key role in the positioning of Glu35 and Asp179 in MnP through the formation of a salt bridge, a K179R mutation was made in MnC*c*P.1 (Figure 46). MD simulations showed that Arg179 moved farther from Glu181, causing a reorientation of Glu181 and, consequently, reducing the interatomic distance of the carboxylate side chain to Mn^{II} by nearly 2 Å. Activity assays showed that, as a result, a 2.6-fold improvement in K_M was observed.

Additionally, it was discovered that Ile40 in MnC*c*P.1 may sterically clash with Glu37 in Mnc*c*P.1, causing the Glu side chain to reorient away from the Mn^{II} center. In most MnPs, the corresponding position is occupied by glycine, and therefore, an I40G mutation was introduced in MnC*c*P.1 (Figure 46). The corresponding MD simulations showed a decrease in bond length between the ligands and Mn^{II}. That for Glu37 decreased from 3.23 Å to 2.54 Å, and that for Glu45 decreased from 3.94 Å to 2.34 Å. This resulted in a 3.6-fold improvement for K_M. For this mutant, a 2.4-fold increase for k_{cat} is also observed and resulted in an overall 8.6-fold increase in catalytic efficiency.

5.2. Heme-Copper Oxidase Using Myoglobin as a Scaffold

5.2.1. Design Using Natural Amino Acids.—

The practical application of enzymes such as HCO outside of the cellular environment is often challenging due to their large size and complexity. Therefore, designing ArMs based on small and robust protein scaffolds is an attractive solution to this problem.

While Mb contains a single heme center, HCOs contain a high-spin heme-Cu_B center and a low-spin heme dinuclear center (Figure 47). As a subclass of HCO, C*c*O also possesses a dinuclear Cu center called Cu_A.[331] To understand the role of the Cu_B site for the function of HCOs, Lu and co-workers reported their first design of the HCO biomimetic system using the Mb scaffold in 2000.[518] To accomplish this, a Cu-binding site (Cu_B site) was engineered in the vicinity of the heme Fe by introduction of two His residues, L29H and F43H, in the distal pocket of the heme site, closely resembling the heterobinuclear active site found in HCOs (Figure 47c). Herein, the L29H/F43H Mb mutant is referred to as Cu_BMb. Initial studies on Cu_BMb suggest that the copper ion in the Cu_B center is essential for the O_2 reduction activity.[519] However, Cu_BMb generates verdoheme, instead of ferryl-heme, during the O_2 reduction due to the lack of the H-bonding network that delivers protons to promote the heterolytic O—O cleavage. Since the Tyr residue in the active site of HCOs has been thought to be critical to the enzymatic functions,[520] Miner et al. later found that introduction of Tyr to the active site of Cu_BMb (F33Y-Cu_BMb and G65Y-Cu_BMb) enabled this artificial enzyme to convert O_2 to water with minimal release of reactive oxygen species (ROS), which in turn prevented the degradation of heme to verdoheme

(Figure 48).[517] Repositioning of Tyr in the G65Y Cu_BMb construct further improved the rate of H_2O production relative to that of F33Y Cu_BMb, illustrating for the first time that the positioning of the Tyr is critical for modulating the catalytic rate. Moreover, the crystal structure of apo-F33Y Cu_BMb revealed additional water molecules in the distal heme pocket, suggesting that Tyr may be involved in the H-bonding network that activates the ferric-superoxo intermediate for water generation. Two years later, Yu et al. reported the direct observation of the Tyr33 radical in F33Y Cu_BMb by EPR (Figure 48b), providing firm support for the presence of a Tyr radical and the role of Tyr as an electron and proton donor in the enzymatic mechanism of HCO.[521] Moreover, in 2016, the EPR spectra of cryoreduced oxy-F33Y Cu_BMb and the crystal structure (Figure 48c) of this mutant provided further direct evidence of the importance of H-bonding networks in activating the enzyme to reduce O_2 to water.[522]

Taking advantage of the enhanced O_2-reduction activity of G65Y Cu_BMb, Mukherjee et al. reported the Mb-based biosynthetic model C*c*O, capable of electrochemically catalyzing O_2 reduction with a reaction rate higher than that of either any known synthetic analogue or the native C*c*O.[524] The electrons required for the O_2 reduction reaction were directly injected into the heme cofactor via tethering by click reaction of the functionalized hemin-yne to azide terminated thiols bound to a gold electrode. This approach to direct electron transfer circumvents the rate-limiting dissociation of ferric hydroxide and the presence of the protecting Tyr65, resulting in an O_2 reduction activity that is an order of magnitude faster than that of C*c*O fixed by immobilization on an electrode.

In 2015, Yu et al. further developed a Mb variant (D44K/D60K/E85K) based on the G65Y-Cu_BMb platform by incorporating residues to promote favorable surface electrostatic interactions with the native redox partner of HCO, cyt b_5 (Figure 49).[525] Using this approach increased the activity of the Cu_BMb model to a level comparable to that of the native enzyme.

In addition to serving as functional models of HCOs, engineered Mb oxidases have also proven to be excellent models for studying the relationship between the reduction potential and O_2-reducing activity. In 2014, Bhagi-Damodaran et al. introduced an S92A mutation to F33Y-Cu_BMb, aiming to remove the H-bonding interactions between Ser92, the proximal His ligand, and a heme propionate as well as increasing the hydrophobicity in the heme pocket (Figure 50).[527] The S92A mutation led to an increase in the reduction potential by about 30 mV, resulting in a higher driving force and faster O_2 reduction.

In 2018, Mukherjee et al. incorporated one or two proton transfer glutamate residues (V68E and V68E/I107E) in Cu_BMb to mimic the proton donor acidic residues in HCOs (Figure 51a).[524,528] Although V68E and V68E/I107E-Cu_BMb showed O_2 reduction rates comparable to that of G65Y-Cu_BMb, which does not contain a glutamate residue in the active site, the presence of Glu resulted in a significantly reduced solvent kinetic isotope effect (SKIE), with V68E/I107E-Cu_BMb bearing the lowest SKIE of ~2.4 (Figure 51b). The dramatic difference in SKIE indicates a change in the rate-limiting step in the reaction mechanisms, with Glu mutations presumably providing a preorganized proton transfer channel that speeds up proton translocation.

The crucial role of the active site Glu residue in regulating oxidase activity was further reinforced by Petrik et al. in 2021.[530] An I107E mutation not only promoted the O_2 reduction rate but almost completely eradicated ROS formation. A combination of crystallographic and EPR studies revealed an extensive H-bonding network involving glutamate-facilitated reaction intermediate protonation (Figure 51).

5.2.2. Design Using Unnatural Amino Acids.—Although the Tyr-His cross-link is a well-established feature in native HCOs (Figure 52a), the mechanistic role of this cross-link is still unclear.[531] To better understand the impact of this feature in HCOs, Liu et al. reported the genetic incorporation of an UAA, imiTyr, into Cu_BMb at position 33 to mimic the Tyr-His cross-link of HCOs (Figure 52b).[532] Compared to the F33Y Cu_BMb mutant, the Mb model bearing imiTyr exhibited an 8-fold increase in selectivity and 3-fold increase in catalytic turnover (Figure 52c). It was postulated that the decrease in the pK_a of the phenol in imiTyr is key to facilitating proton delivery and Tyr radical formation.

Since Tyr has been suggested to function as both a proton and electron donor in the enzymatic cycle of HCOs, both the pK_a and reduction potential of Tyr can potentially affect its role in modulating the enzymatic activity. To analyze the correlations between these factors and the oxidase activity, Yu and co-workers established a linear relationship between the pK_a of the phenol group at position 33 and the O_2 reduction activity using a series of unnatural analogues of Tyr with varying pK_a values of the phenol ring (Figure 52d).[533] However, the dependence of the oxidase activity on the reduction potential of Tyr is convoluted, since the pK_a and the reduction potential of Tyr are closely correlated. To tackle this problem, Yu et al. incorporated a Tyr analog, 3-methoxy tyrosine (OMeY), that has a comparable pK_a to that of Tyr but a lower reduction potential (Figure 52e).[534] The F33OMeY Cu_BMb exhibited a higher O_2 consumption rate with a lower generation of ROS compared to the case of F33Y Cu_BMb. In this manner, they demonstrated that the electron donating ability of Tyr in the active site is a critical factor for the function of HCOs.

5.3. Bacterial Nitric Oxide Reductase Using Myoglobin as a Scaffold

NOR is structurally homologous to the largest subunit of HCO; rather than a three-histidine-coordinated Cu_B site in the distal position of the heme, the Fe_B site is incorporated into this position instead. Aside from the three His residues, two additional Glu residues were found to be essential for NOR activity. To mimic the structure and activity of NOR, the Lu group engineered a three His/one Glu site in the distal pocket of swMb, successfully established NOR activity.[535] To make this model more similar to the native NOR and to investigate the role of the second Glu, the second Glu was introduced into Fe_BMb by a I107E mutation. The resulting crystal structure showed a bridging water molecule between the OE2 atom of Glu107 and the non-heme iron center (Figure 53). The NO reduction activity of Fe^{II}-I107E Fe_BMb was found to be higher than that of Fe^{II}-Fe_BMb, with ~24% N_2O for the former and ~10% for the latter over the course of ~20 h under single-turnover conditions. This suggests that unlike the initial three His residues and one Glu, which directly coordinate to the Fe_B site, the second Glu may potentially play a role in the proton transfer pathway during the reduction of NO.[529] This hypothesis was further supported by making a I107F mutation in Fe_BMb, which inhibited N_2O formation.[536]

By utilizing this model Fe_BMb NOR enzyme, an important question as to why Cu is preferred over Fe for O_2 activation and reduction in HCO was resolved. The role of different metal ions in the distal pocket was explored by titration of the non-heme Fe_B center with Cu^I (Cu^I-Fe_BMb, mimic of HCO), Fe^{II} (Fe^{II}-Fe_BMb, mimic of NOR), and Zn^{II} (Zn^{II}-Fe_BMb, control).[537] While the redox potential values of the heme center were similar (−64 ± 4 mV, − 58 ± 3 mV, and − 45 ± 2 mV, respectively), the redox potential values of the non-heme metal center were different, with +259 ± 20 mV for non-heme Fe^{III}/Fe^{II} and +387 ± 25 mV for Cu^{II}/Cu^I. Resonance Raman (rR) spectroscopy showed that, in the O_2-bound form, Zn^{II}-Fe_BMb exhibited a stronger Fe—O_2 bond, which, in turn, implies greater O—O bond activation compared to that of Fe_BMb in the absence of a distal metal ion. DFT calculations indicated that the O—O bond in Fe-Fe_BMb was longer than that in Zn-Fe_BMb and even longer in Cu-Fe_BMb. One possible explanation for this behavior is that Fe^{II} and Cu^I are redox active and capable of electron donation to O_2. Additionally, Cu^{II} may provide a higher degree of *d*-electron density (d^9) than Fe^{III} (d^5) to O_2 through d_π-p_π backbonding, further weakening the O—O bond. In fact, copper is the only 3*d* transition metal that is redox active and have maximum number of *d*-electrons for O_2 activation.[537]

The redox potential of heme can play an important role in tuning NOR reactivity. Bhagi-Damodaran et al. tuned Fe_BMb by exchanging heme *b* for monoformyl (MF-) or diformyl (DF-) heme, as well as by mutating Leu89, a residue close to the proximal His, into Ser. The exchange of heme increased the redox potential of heme center, while the mutation increased the hydrophilicity around heme and lowered the redox potential by stabilizing the higher oxidation states. This work found that a lower redox potential facilitated fast NO binding and subsequent decay of dinitrosyl species, while higher redox potentials facilitate faster electron transfer. Accomplishing multiple turnovers of NOR reactivity requires balancing optimizing the redox potential to balance these two factors.[538]

5.4. Sulfite Reductase (SiR) Using Cytochrome *c* Peroxidase as a Scaffold

In 2018, the Lu group successfully engineered a [4Fe-4S] binding site into C*c*P using six mutations (H175C, T180C, W191C, L232C, M230A, and D235V), which will be referred to as SiRC*c*P.1, with the purpose of creating a biosynthetic model of SiR.[539] Following incorporation of heme *b* and the [4Fe-4S] cluster into SiRC*c*P.1, the resulting heme-FeS-SiRC*c*P.1 exhibited notable sulfite reducing activity, forming a basis for further work tuning the SCS to enhance its activity. A series of mutations were incorporated to form a positively charged cavity reminiscent of native SiR, including W51K, H52R, and P145K, mimicking Lys217, Arg153, and Lys215 in native SiR. The position of native Arg48 in C*c*P is similar to that of Arg83 in native SiR (Figure 54a). This W51K/H52R/P145K-SiRC*c*P.1 variant exhibited a 5.3-fold increase in activity over that of SiRC*c*P.1. Residue Asn481 in native SiR was oriented towards the iron sulfur cluster and may increase activity. Therefore, a D235N mutation at a similar position as SiR Asn481 was made to replace the original D235V mutation, with the resulting construct named SiRC*c*P.2 (Figure 54b). This new SiRC*c*P.2 construct was found to be 17-fold more active than SiRC*c*P.1. Further exchange of residue 235 for Cys in the D235C variant (SiRC*c*P.3) (Figure 54b) resulted in even higher activity. In combination with the W51K/H52R/P145K substitutions, W51K/H52R/P145K-SiRC*c*P.3

displayed a 63-fold increase in activity relative to the original SiRC*c*P.1 construct, achieving ~18% of the activity observed for native SiR from *Mycobacterium tuberculosis*.[539]

5.5. An Artificial Nuclease Using Myoglobin as a Scaffold

By incorporating a Mg^{2+} into L29E Mb, an efficient artificial nuclease Mg^{2+}-L29E Mb was made. Through molecular docking simulations of double-stranded B-DNA with the enzyme (Figure 55), it was determined that the distal Arg45 can interact with the sugar/phosphate group of DNA through H-bonding interactions. This basic residue was found to be conserved in the native nuclease, possibly enhancing the DNA binding affinity and further promoting cleavage. Introduction of a R45S mutation was introduced to eliminate the interaction and the DNA cleavage, and it was found to successfully inhibit nuclease activity by ~55–60%.[508]

6. BEYOND FE AND CU: INSIGHTS INTO THE SECONDARY COORDINATION SPHERE OF ENGINEERED METALLOENZYMES INCORPORATING NON-NATIVE METAL IONS

6.1. Replacement of Native Metal Ions and Metallocofactors

Besides mimicking the diverse array of metalloenzymes found in nature, the protein reengineering approach can be used to generate novel active sites to impart new reactivity with non-native metal ions and cofactors. However, doing so presents its own unique challenges, particularly in finding a scaffold capable of tightly binding the desired metal center or organometallic complex. To solve this problem, noncovalent, single-point covalent attachments, and dual covalent anchoring strategies can be employed. The Watanabe group has demonstrated that enantioselective enzymatic sulfoxidation can be regulated by unnatural metal complexes in a redesigned protein active site.[540] Oxidative Cr^{III} and Mn^{III} Schiff base catalysts were inserted to Mb using His93 as an anchor, forming a metal–His93 dative bond. In addition to the noncovalent interactions, including π-stacking between the benzene ring of the salophen ligand and the Phe43 side chain, and C-H/π-interactions between the side chains of Leu89 and Ile99 and the ligand (Figure 56a), the two methyl groups of the salophen ligand were found to interact with Ile107, allowing the Mn complex to be inserted deep in the pocket (Figure 56b). The rate of sulfoxidation catalyzed by these complexes was accelerated by inserting into apo-Mb, and Cr^{III}-Mb and Mn^{III}-Mb exhibited 15- and 6-fold higher reactivities than that of the Cr^{III} Schiff base complex in buffer, respectively. Further modification of the ligand sterics regulated the position of the inserted synthetic metal complex, helping to tune the enantioselectivity, and additional mutation of H64D increased the substrate accessibility, enabling a larger substrate scope.

To further enhance both the rate and enantioselectivity of the sulfoxidation reaction, the Lu group constructed an artificial metalloenzyme by incorporating manganese salen complex into Mb using a dual covalent anchoring approach, generating MnSalen-Mb(T39C/L72C) (Figure 57).[541,542] Mb(T39C/L72C) was found to exclusively catalyze the formation of sulfoxide. To account for such high chemoselectivity, it was hypothesized that the polarity of the residue near the entrance of the protein pocket may play an important role in regulating

substrate access. A single mutation, A71S, near the entrance of the protein pocket was made to increase hydrophilicity and, as a result, led to the further oxidized product sulfone. This demonstrates the delicate balance of the secondary coordination sphere in tuning selectivity.

To further enhance reactivity, the distal His64 residue was modulated by substitution with Phe to remove the H-bonding interaction with the active Mn-hydroperoxo species.[543] Such mutation did not increase in the turnover numbers; however, substitution of His64 with Arg resulted in increased oxidation activity. This observation strongly suggested that the distal ligand His64 plays a key role in tuning the reactivity of the Mn-salen complex through H-bonding interactions.

Superoxide dismutases (SODs) serve to detoxify superoxides produced by aerobic metabolism and by the mammalian immune system in response to infection.[544] Different SOD families are defined by the cofactor they utilize, including Ni SODs, Cu and Zn SODs, and Mn or Fe SODs. All members of the most common Mn/Fe-dependent SODs are related in sequence. They exhibit identical protein folds and have identical ligands coordinating the metal ion. Therefore, it is unclear why some enzymes require exclusively Mn for catalysis (MnSOD), while others require Fe (FeSOD) and yet others, such as camSOD, show metal cofactor flexibility.

The metal ion reduction midpoint potential (E_m) plays a critical role in which reactions an enzyme can participate and, therefore, must be carefully controlled. Miller and co-workers successfully tuned Fe- and Mn-containing SODs, generating FeSOD variants with E_m values spanning 900 mV (Figure 58a).[545] The protonation state of the coordinated solvent accounted for the significant differences observed in both the redox potential and metal ion specificity. It was postulated that protonation of the coordinated solvent was suppressed in MnSOD by a strong H-bonding interaction with Gln69, leading to drastic differences in the E_m values relative to FeSOD (Figure 58b). Mutations Q69H and Q69E in FeSOD were designed to decrease the strength of this H-bond interaction with the coordinated solvent (Q69H) or to reverse the polarity of the H-bond (Q69E). The E_m was observed to increase moving from WT-FeSOD to Q69H to Q69E, supporting this hypothesis (Figure 58).

To further explain the metal specificity of MnSOD and camSOD, Waldron and co-workers identified three residues (19, 159, and 160) that are spatially close to the metal binding site and vary between MnSOD and camSOD (Figure 59).[546] Modification of position 159 in the G159L MnSOD increased its Fe-dependent activity while decreasing its Mn-dependent activity by ~2-fold. On the contrary, camSOD L159G diminished its Fe-dependent activity by >10-fold while increasing its Mn-dependent activity by >3-fold. Interconversion of activity and metal specificity could also be achieved by varying position 160, although alterations at position 19 seemed to have little impact on these properties. Surprisingly, although mutations at these positions change the metal specificity, there are essentially no changes observable in the protein backbone structure, at least within the resolution of the crystal structures. The primary coordination spheres, substrate access channels, and H-bonding networks all appear otherwise identical. However, such mutations had direct effects on the electronic properties of the Mn center, as demonstrated by high-field EPR. Different reactivities toward auto-oxidation and dithionite reduction suggested that each of

the two WT-SODs have different redox potentials. These differences were inverted in the double mutants (MnSOD G159L/L160F and camSOD L159G/F160L), correlating also to an inversion of the Mn-dependent activity in these variants. Together, these results provide important insight into the role of secondary coordination sphere residues in modulating SODs and the factors that contribute to both altered metal specificity and reduction potential.

Cobalamin-dependent methionine synthase (MS) catalyzes the conversion of homocysteine to methionine in most mammals and bacteria. This large, modular protein (ca. 146 Da) consists of four distinct functional domains. Two kinds of methyl group transfers occur during the catalytic cycle. Namely, *N*-methyl tetrahydrofolate first acts as a methyl group donor to methylate cobalamin. This methyl-cobalamin is then used for methionine synthesis from homocysteine. Mechanistic studies of the native enzyme are challenging due to the structural complexities and the dynamic conformational changes that occur in MS during the reaction.[548] Despite the importance of this enzyme, the number of protein model systems developed to investigate how MS initiates the S_{n2}-like transmethylation reaction and stabilizes reaction intermediates is limited.[548] Using Mb reconstituted with a Co tetrahydrocorrin derivate (Co(TDHC)Mb), Hayashi and co-workers investigated the reaction catalyzed by methionine synthase.[549] It was found that Co^{I}(TDHC)Mb could react with methyl iodide to form a methylated cobalt complex, a process that did not efficiently proceed for Co^{I}(TDHC) in organic solvents. These initial results highlight the importance of the heme pocket of Mb, which may serve to enhance the nucleophilicity of the Co^{I} species while simultaneously stabilizing the methylated Co^{III} species. Interestingly, transmethylation from the methylated cobalt complex to one of the nitrogen atoms of the His64 imidazole ring was observed. DFT calculations exploring this process supported a reduced barrier for His64 methylation together with significant stabilization of the methylated His product through the dielectric effect of the surrounding protein environment. In the crystal structure, the N_{δ} atom of His64 was found to be hydrogen bonded to a water molecule (Figure 60), suggesting barriers can be further reduced by the partial or full deprotonation of the methylated histidine.

Ghirlanda and co-workers have also investigated the influence of the protein second coordination sphere on Mb substituted with cobalt-protoporphyrin XI (CoMb) (Figure 61).[551] Compared to free cobalt-protoporphyrin IX (CoPP(IX)), a 4-fold increase in the photoinduced hydrogen production activity was observed for CoMb. Substitution of the distal His residues in the engineered H64A/H97A CoMb mutant displayed a 2.5-fold higher reactivity relative to that of CoMb. It is hypothesized that the H64A substitution removes a slightly positive charge from His at physiological pH as well as a potential competitor for proton binding in the proximity of the CoPP(IX) active site. A hydrogen bond formed between His97 and one of the propionic acid groups of CoPP(IX) was also observed based on analysis of the crystal structure. Meanwhile, the H97A mutation was found to destabilize binding of CoPP(XI), alter the steric constraints on the porphyrin, and increase the degree of freedom between the scaffold and the CoPP(XI), effectively lowering the catalytic ability. However, the H97A substitution also increased the solvent accessibility of the active site, which may favor interaction between the photosensitizer and CoPP(XI), as the TON of H64A/H97A was found to be higher than that of the H64A mutant.

In 2016, Hartwig and co-workers constructed an artificial metalloenzyme (ArM) by incorporation of an Ir(Me)-heme cofactor into myoglobin (IrMb), capable of carbene insertion activity with up to 50% yields for a model reaction,[553] Unlike many other anchoring strategies, the Ir(Me)-heme cofactor is embedded within the protein cavity, allowing SCS interactions to be readily employed to tune reactivity.[554] Directed evolution of this IrMb was conducted by mutating a variety of residues, including the axial ligand and those in the substrate-binding region, to achieve substrate specificity. Aside from the axial and proximal ligands (His64 and His93, respectively), Phe43 and Val68 were mutated into hydrophobic or uncharged residues to maintain the hydrophobicity of the porphyrin/substrate binding site. Four additional residues around the active site (Leu32, Phe33, His97, and Ile99) were also investigated (Figure 62a). Different selectivities and yields were achieved for varying carbene insertion reactions across the range of designed mutants, with selectivities reaching up to a 92:8 enantiomeric ratio, yields up to 97%, and TONs up to 7260.[553] The Ir(Me)-heme catalyst was also incorporated into the CYP119 scaffold (a variant of P450 enzymes), producing an ArM with better thermal stability and reactivity toward carbene insertion,[555] cyclopropanation,[556] and (sp^3)C-H site selective functionalization reactions.[557] Upon directed evolution of the residues near the active site, the authors achieved ArMs with improved yields, enantiomeric excess, chemoselectivity, total turnovers and turnover frequencies relative to those of IrMb. These mutations mainly focused around varying the heme axial residue (Cys317), residues lining the substrate binding pocket (Leu69, Ala209, Thr213, and Val254), and residues toward the distal side of the substrate binding site (Ala152, Leu155, Phe310, and Leu318) (Figure 62b).

6.2. Design of New Metal Binding Sites

Nickel is intimately involved at the active sites of several important energy-converting enzymes, including NiFe H_2ases, carbon monoxide dehydrogenase (CODH), and acetyl coenzyme-A synthetase (ACS), all of which coordinate Ni in a S-rich environment. To better understand the nature of these enzymes and to mimic their unique activities, a number of protein reengineering efforts have been put forth.

Chakraborty and co-workers reported the rational redesign of a copper storage protein (Csp1) into a nickel binding protein as a novel mimic of [NiFe] H_2ase (Figure 63).[560] The native active site of NiFe employs two Fe-bridging and two terminal Cys residues to coordinate Ni, making the already thiol-rich Csp1 an intuitive starting point. The 13 Cys residues along the central helical core of native Csp1 are capable of binding a total of 13 equiv of Cu^I. The Cu4 binding site (Cys26/62/87/113), which already enables tetrathiolate ligation, was chosen as the target location for the formation of a $Ni(Cys)_4$ site. During the redesign process, seven Cys residues away from the Cu4 site were mutated to Ala due to the similar side chain size of these residues in an effort to maintain a compact structure. Additionally, two bulky hydrophobic residues, Val (Cys94) and Leu (Cys103), were introduced to provide hydrophobic interactions at the exposed ends of the protein, aiding in folding. Spectroscopic and computational data supported Ni binding to occur in this redesigned construct, adapting a distorted square planar geometry. More strikingly, the Ni^{II}-incorporated protein was found to catalyze proton reduction to H_2 under photochemical

and electrochemical conditions, with a TOF of ~210 under photochemical conditions, comparable to those of reported biomolecular catalysts.[561]

Also taking advantage of a naturally Cys-rich scaffold, the Shafaat group has developed a nickel-substituted rubredoxin (NiRd) and further probed the secondary coordination sphere of this construct to shed light on how the secondary sphere can modulate the hydrogenase activity.[563] A rationally designed library of 30 mutants were generated in the metal-binding loops of Rd targeting residues V08, V34, and V37 (Figure 64), which exhibit H-bonding interactions with the Ni-coordinated cysteines through the amide backbone. By varying the identity of these residues, it was found that the strength of these H-bonding interactions is reflected in changes of the $Ni^{III/II}$ reduction potential, in which stronger hydrogen bonds between the amide proton and sulfur atom of Cys were correlated with higher reduction potentials, likely due to the increased electronic delocalization and stabilization of the reduced state. Further-more, it was found that the steric constraints imposed by certain side chain residues are capable of influencing both H-bonding with the amide backbone and solvent accessibility. Solvent accessibility is a key factor in proton-dependent H_2 evolution reactions. Specifically, the greatest increases in activity correlated with mutations of the V08 residue. The TOF and solvent accessibility of V08X mutants increased relative to WT-NiRd due to the rotation of side chains away from Cys35, improving the solvent accessibility of the active site. Meanwhile, the solvent accessibility and catalytic performance of V34X mutants were comparable to those of WT-NiRd, with the exceptions of V34G and V34H, which reduced the degree of H-bonding between the amide backbone and nearby Cys32 due to substantial movement of the backbone. The dependence of the TOF on pH was found to correlate with secondary sphere perturbations as well. The V34H mutant showed a logarithmic dependence of reactivity on pH. MD simulations demonstrated that protonation of His34 at low pH resulted in a rotation of the His side chain away from the metal binding site, enabling direct access of water to the active site. This extensive work from the Shafaat group with a simple NiRd scaffold demonstrates the impact of the secondary coordination sphere in tuning both catalysis and reaction mechanism.[563]

Besides H_2ase mimics, the Shafaat group recently reconstructed ferrodoxin using a $[NiFe_3S_4]$ cluster to form a protein model of CODH.[564] While native ferrodoxin is capable of binding CN^-, only the $[NiFe_3S_4]$ reconstituted enzyme was found capable of binding CO, as supported by an extensive spectroscopy study. Further systematic studies of the PCS and SCS residues of surrounding this ferredoxin-based model system will provide even greater insights into the mechanism of native CO_2 reduction by CODH.

The Baker lab has also successfully redesigned a mononuclear Zn metalloenzyme for organophosphate hydrolysis with the assistance of applied computational tools.[565] Starting from an adenosine deaminase scaffold (PT3), eight mutations were introduced to help establish a Zn coordination site as well as stabilize a postulated transition state geometry for hydrolysis based on an extracted set of mononuclear Zn enzyme scaffolds. Based on these calculations, residue Glu217 was suggested to be crucial for proton shuttling in the deamination reaction. These calculations were supported by the low activity observed for the E217Q variant, highlighting the importance of Glu217 for organophosphate hydrolysis, which was suggested to aid in fine-tuning substrate alignment at the active

site. Directed evolution was further performed to enhance the hydrolysis reactivity toward organophosphate substrates, resulting in the develop-ment of variant PT3.1, with approximately 2500-fold higher reactivity than the initial PT3 variant. Based on these results, it was postulated that substitutions in the vicinity of Glu217, such as V218F and Q58V, may increase the hydrophobicity around the putative catalytic base Glu217 (Figure 65). A change in pH of 1.6 accounts for the catalytic increase observed in PT3.1, containing V218F mutation relative to PT3, which suggests that the basicity of Glu217 is related to the activity enhancement obtained through the directed evolution pathway.

6.3. Design Using Strong Noncovalent Interactions

The biotin–avidin interaction is known to be one of the strongest noncovalent interactions in nature,[566] and the use of this strong interaction to construct ArMs by connecting avidin-based protein scaffolds with biotin-substituted artificial metal-locofactors can be dated back to the last century.[475,567] In 2003, the Ward group reported an artificial metalloenzyme (ArM) using Sav and a Rh complex with a biotinylated amino-diphosphine ligand **Biot-1** ([Rh(COD)(**Biot-1**)]$^+$⊂Sav, Scheme 4, bottom) capable of achieving 92% *ee* (*R*) when catalyzing the enantioselective hydrogenation of α-acetamidoacrylic acid (Scheme 4, top). When mutating the Ser112 of the L7,8 loop of Sav (Figure 66), which is in the proximity of the metal active center, into glycine, an increase in enantioselectivity for the ArM [Rh(COD)(**Biot-1**)]$^+$⊂Sav S112G to 96% (*R*) was observed.[568] In addition to S112G, the group also studied the V47G, K80G, and P64G mutations. Val47 forms a close contact with Ser45, which interacts with the H-N group of biotin through H-bonding. Meanwhile, Lys80 is a neighboring residue of Trp79, which is a SCS residue of biotin, forming a hydrogen bond with Thr90, which further interacts with the thioether of biotin (Figure 66). Although Pro64 is located on a loop that is relatively remote from the biotin, mutations at this residue may have an impact on the loop geometry. It was found that mutations closer to the active site (V47G and S112G) had a more significant effect on the enantioselectivity compared to those that are relatively remote (K80G and P64G).[569] Site saturation mutagenesis (SSM) on Ser112 in the same ArM system catalyzing α-acetamidoacrylic acid or α-acetamidophenylacrylic acid provided more insights into this site. Generally, the ArMs having S112A and S112G mutations more heavily favor the *R* products, while those with S112H, S112K, and S112R mutations favor producing *S* products. By modifying the artificial cofactor itself, a further increase in the *ee* of both *R* and *S* products was achieved. The authors speculated that the cationic side chains of residue 112 can interact with the carboxylate moiety of the substrate through hydrogen bonds, making one of the prochiral faces of the substrate more favorable for coordination.[570] A directed evolution approach using the same **Biot-1** ArM system for catalysis of the α-acetamidoacrylic acid ester substrate found that several residues ~4–6 Å away from the metal center can change the *ee* to favor either *R* or *S* isomers, possibly by directly affecting the conformation of the catalyst or catalyst/substrate complex. Among these, N49V increased the *ee* from 23% (*R*) to 65% (*R*), and N49H/L124F decreased the *ee* from 23% (*R*) to −7% (*S*).[571]

Incorporation of a racemic biotinylated three-legged d^5/d^6-piano stool complex (Scheme 5) into Sav enabled the formation of a series of artificial transfer hydrogenases (ATHases). Starting from the Ru d^6-piano stool complex, several mutations were made to study

the influence of the secondary coordination sphere on ketone hydrogenation. S112G, a mutation close to the catalytic site, resulted in the highest conversion (90%) but lowest enantioselectivity (28% *ee* (*R*)). P64G, a mutation at a relatively remote site, has the greatest enhancement on enantioselectivity (72% *ee* (*R*)) but moderate conversion (54%). The double mutant P64G/S112G combined the positive effects of both single mutants, resulting in excellent conversion (95%) and reasonable enantioselectivity (58% *ee* (*R*)).[573] Later, a series of alternative d^5/d^6-piano stool complexes coordinating Rh, Ru, and Ir, respectively, were screened for activity toward the reduction of ketones or cyclic imines. Select complexes were further developed by SSM to generate more advanced ArMs. Variants of Sav containing cationic residues at position 112 (S112R and S112K) generally have higher S-enantioselectivity. It was also found that the introduction of aromatic residues (i.e., S112F and S112Y) or using small amino acids at the same site (i.e., S112G and S112A) leads to higher *R*-enantioselectivity.[574,575] Based on the S112A and S112K mutations, a follow-up study was performed focusing on the SSM of the Lys121 and Leu124 sites. Sav is a homotetrameric protein, in which the Lys121 of one monomer interacts with the η^6-arene ring of the complex, while the Lys121 from the adjacent monomer interacts with the incoming substrate (Figure 67a). Therefore, this residue may play a role in favoring certain prochiral substrate interactions. Leu124 may influence the biotinylated catalyst slightly because its methyl group is in close proximity (3.53 Å) with the sulfone group of the catalyst. Overall, SSM of Lys121 proved to be more effective for the optimization of enantioselectivity than when applied to Leu124.[576] The crystal structure of S112K Sav containing Ru-cofactor clearly showed interaction between Lys112 and Leu124. Also, several other residues close to the active site, including Thr114 and Pro64, were investigated, where mutation of either to Gly was found beneficial in enhancing the enantioselectivity. Thr114 is close to the η^6-arene ring, while Pro64 is located in the L4,5 loop, which neighbors the L7,8 loop from another monomer, the latter of which is close to the catalytic metal center (Figure 67a). Mutation of the Pro64 to Gly hypothetically perturbs the location of the L4,5 loop, which in turn should influence the positioning of the L7,8 loop and further influence the Ru complex.[577]

There are also some ATHases that have been constructed based on similar Sav-bound biotinylated Ir complexes. Several cationic and anionic residues around the metal complex were investigated using imine reduction as a model reaction. Both S112A/K121A and S112A/K121L displayed excellent catalytic efficiency (k_{cat}/K_M). An additional D67V mutation to the S112A/K121L construct was made to remove a negative charge near the catalytic site, resulting in a lowering of the catalytic efficiency due to a lower k_{cat}. A possible explanation for this effect is that the reduction of imine may proceed through an iminium ion intermediate, and removal of the cationic residue (K121A or K121L) next to the catalytic site would help with the catalytic process. The presence of an anionic residue (Asp67) would stabilize the cationic transition state and increase the k_{cat}.[578]

To further modulate the ATHase activity in the Ir-complex-based Sav, an additional 24-residue helix-turn-helix motif (FPD) was incorporated into the L7,8 loop and combined with other previously investigated point mutations to tune the catalytic performance of the ArM. The two best-performing mutants found for the reduction of a quinolium substrate were S112A/K121P Ir-Sav-FPD and S112V/K121A Ir-Sav-FPD. The crystal structure of

S112V/K121A Ir-Sav-FPD revealed that the L4,5 loop was shifted 5.6 Å compared with that of Sav S112A, and the directionality of the L7,8 loop had rearranged to point toward the Ir cofactor, although the FPD-loop was not resolvable (Figure 67b). The cofactor occupancy for S112V/K121A Sav-FPD was also found to increase relative to that for S112V/K121A Sav (from 50% to 80%, indicating that the FPD-loop shielded the biotin-binding vestibule and helped the binding of the complex.[579] Since Sav is a tetramer hypothetically capable of binding up to four biotinylated cofactors, the roles for different monomeric units were also investigated. To this end, two Sav subunits were fused together and mutated separately at the respective Ser112 and Lys121 positions. It was found that mutations made in the first subunit (Sav_A) had a greater impact on both substrate conversion and product enantioselectivity. Meanwhile, those made in the second subunit (Sav_B) do not show a clear trend for the influence on the reactivity; however, these residues do still appear to play a role in fine-tuning substrate interactions, as well as conversion and enantioselectivity. This likely arises from different conformations of the Ir complex in each subunit, with Sav_A serving as the predominately active form.[580]

The $[Cp^*RhCl_2]_2$ (Cp^* = pentamethylcyclopentadienyl) complex is a versatile catalyst for electrophilic aromatic C-H activation.[581] With the aim of introducing asymmetric activity and improving conversion, Hyster et al. synthesized a biotinylated $[Cp^*RhCl_2]_2$ complex ($[Cp^*RhCl_2]_2$-biot) and successfully incorporated the complex into Sav.[582] The low activity observed in the resulting ($[Cp^*RhCl_2]_2$-biot)-Sav construct inspired further modification of the secondary coordination sphere based on molecular docking simulations. Initial efforts introduced a basic residue in the vicinity of the metal center through S112E and K121E mutations. Similar to previous reports,[570,574,575] both of these variants exhibited low conversion for the reaction (10% and 7%, respectively). However, mutation of K121 to Asp resulted in a significantly improved reaction conversion of up to 89%, demonstrating that both the presence of a carboxylate *and* its precise positioning can significantly impact aromatic C-H activation. Inspired by these results, the authors further added a N118K mutation to K121E ($[Cp^*RhCl_2]_2$-biot)-Sav (Asn118 is adjacent to Lys121), and they observed a further increase in conversion to 99%, as well as an excellent regioisomeric ratio (rr) (15:1) and enantiomeric ratio (er) (82:18). By screening different mutations at the Ser112 site, S112Y was found to have the best enantioselectivity, with an er of 88:12. The synergistic effect of combining S112Y and K121E mutations also led to a total conversion of up to 95%, rr of 19:1, and er of 91:9. Through kinetic isotope effect (KIE) and competition studies, the authors found that the introduction of the carboxylate had the most dominant effect on improving the activity and selectivity.[582]

Further expanding the scope of the biotin-Sav guest–host scaffold, Ward and co-workers incorporated a biotinylated second-generation Hoveyda–Grubbs catalyst into Sav to generate a novel artificial metathase. Importantly, this ArM system was developed to function in whole cells as a catalyst for *in cellulo* abiotic transformations. Directed evolution was applied to enhance the activity of this ArM, and a quintuple mutant (V47A/N49K/T114Q/A119G/K121R) was found to increase the cell-specific activity by 5.4-fold. According to the *B* factors associated with the crystal structures of the wild-type and quintuple mutant, the biotin-vestibule loop of the quintuple mutant exhibited greater flexibility, with mutations T114Q, A119G, and V47A serving as the key mutations for this enhanced flexibility.[583]

Ward and co-workers further explored the use of ArMs as *in vivo* new-to-nature catalysts by developing a method for displaying Sav on the surface of *E. coli.* It was reasoned that a surface display would more readily bind designed biotinylated metallocofactors, as diffusion of the complex through the periplasm is not required. A biotinylated CpRu (2-quinoline-carboxylate) complex was successfully incorporated into surface-displayed Sav with the intention of catalyzing the uncaging of allylcarbamate-protected substrates, generating a functional allylic deallylase. SSM at positions in close proximity to the Ru complex (S112 and K121, *vide supra*) revealed two double mutants, S112Y/K121S and S112M/K121A, with activities 25- and 24-fold higher than that of the wild-type, respectively. The crystal structure of the S112M/K121A mutant showed that the aromatic quinoline ring was stabilized by a methionine CH_3/π-interaction in S112M. Also, the carbonyl groups from K121A and Ser122 helped the binding of the quinoline ligand.[584]

Beyond Ru, Rh, and Ir, the biotin–avidin method has also been used to create ArMs with many other different metal complexes, including Pd for asymmetric allylic alkylation[585] and Suzuki-Miyaura cross-coupling,[586] Au for hydroamination and hydroarylation,[587] and OsO_4 for *cis*-dihydroxylation of olefins.[588] Mutagenesis investigations have been conducted for all of the examples illustrated above, focusing predominately on varying residues Ser112 and Lys121. In the Suzuki-ase ArM generated by incorporation of a Pd complex (Scheme 6) into Sav, the crystal structure of the S112Y/K121E mutant was acquired, revealing that S112Y provided a significant steric barrier on the lower face of Pd, likely accounting for the modest improvement observed in the enantioselectivity. Additionally, an H-bonding interaction was found between Tyr112 and Glu121, further locking the conformation of Tyr.[586]

Aside from the strong biotin–avidin interaction for constructing ArMs, vanadium pentahydrate was found to interact with the Sav host in acidic media through H-bonding with H-donor residues that are also critical for biotin binding (e.g., Asn23, Ser27, Ser45, and Asp128). An ArM catalyzing enantioselective sulfoxidation reaction was, hence, constructed (Figure 68), and this artificially generated vanadyl enzyme successfully catalyzed the oxidation of prochiral sulfides with good enantioselectivities of up to 93% *ee*.[589]

6.4. Engineered Metalloenzymes by Covalent Attachment of Metallocofactors

In addition to the noncovalent anchoring approaches of scaffolds, such as the biotin–avidin method, ArMs can also be generated through covalent anchoring of synthetic catalysts. For example, azide-alkyne cycloaddition (the classic “click” reaction) has been employed to anchor an alkyne-bearing dirhodium complex in propyl oligopeptidase containing the UAA 4-azidophenylalanine (POP-Z). Although initial reactions of otherwise unmodified POP-Z failed to incorporate the cofactor, mutations aimed at reducing the sterics at the end of the β-barrel were found to enable bioconjugation in POP-ZA_4. Further mutations of residues 99 and 594 to Phe, which neighbor the distal Rh based on homology modeling, were found to increase the yields from 61% to 74% and the *ee* from 85% to 92%,[590] despite later crystal structures that showed the Phe99 was not positioned as suggested by homology modeling.[591] Random mutagenesis was also applied to POP-ZA_4 to generate several mutations which improved the enzymatic activity. Among these, only three mutations, G99S/S301G/Y326H (1-SGH-POP-ZA_4), were required to reach optimal selectivity. Based on crystallographic

analysis of 1-SGH-POP-ZA_4, Ser99 and His326 were found in the active site while Gly301 was farther away.[591] 1-SGH-POP-ZA_4 was further subjected to directed evolution targeted at improving the catalytic performance of diazo coupling cascade reactions. Site saturating mutations were introduced in the β-strand across from the putative Rh-binding His to examine mutations that could significantly impact the product yield and selectivity. From this effort, mutations Q98P and S99H were identified, and a further combination of combinatorial codon mutagenesis across 25 active site residues followed by another round of SSM identified residues V71G and E283G to generate a final mutant with product yields as high as 76%.[592]

Thiol-maleimide bioconjugation has also been used to generate 4*d*/5*d* metal containing ArMs. C96 nitrobindin was employed to generate an ArM capable of C(sp^2)—H bond functionalization via concerted metalation deprotonation (CMD) with 15% yield and 92:8 regioselectivity through the covalent binding of a maleimide-tagged Rh complex. Carboxylates are known to facilitate the CMD-type C(sp^2)—H bond functionalization, and therefore, glutamate residues were introduced near the active site in a L100E/A125E mutant, which increased the yields to 40% with similar regioselectivity (90/10).[593] Directed evolution was later applied to this system, and the T98H/L100K/K127E mutant was identified to increase the activity 2.2-fold. Interestingly, MD simulations suggested that all three of these residues are located opposite to the Rh metal center.[594]

Human carbonic anhydrase II (hCA II) exhibits a high binding affinity toward *para*-substituted aryl-sulfonamides at the Zn binding site, providing another tool for the development of ArMs. An $\{IrCp^*\}^{2+}$ moiety was introduced into hCA II to generate a novel ATHase. Structural analysis based on the resulting X-ray structure showed that Ile91 and Lys170 occupy a potential substrate-binding site. Therefore, I91A and K170A mutations were incorporated, with the former showing some increased activity for specific substrates; however, the apparent low occupancy of the catalytic complex precluded significant improvements.[595] Computational redesign using the program Rosetta was applied to tackle the problem of low cofactor occupancy.[596] It was speculated that the active site of WT-hCA II was not well defined toward the Ir complex. To solve this problem, a variety of hydrophobic residues were introduced to tune the shape of the binding site and optimize the packing interactions between the protein and cofactor. N67W, E69Y, and Q92F mutations were made to β-strands 2 and 3 to allow interactions between the biaryl and phenylsulfonamide groups. An L140 M substitution on β-strand 5 and L197 M on loop 7,8 were also made to pack against the coplanar biaryl moiety of the ligand, and several additional mutations were made to stabilize the protein backbone. L60V on β-strand 1 was introduced for stabilization, A65T was made on β-strand 2 to enable H-bonding with the carbonyl oxygen of Phe95, and C205S was introduced at the end of loop 7,8 to add rigidity to the loop via H-bonding with the carbonyl oxygen of Val134, maintaining the orientation of the cofactor (Figure 69). Based on these mutations, one of the variants **d3** (containing L60V, A65T, N67W, E69Y, Q92F, L197M, and C205S) displayed a 64-fold increase in binding affinity for the Ir cofactor. Reverting selected residues such as E69Y (**d2**) or L197 M (**d1**) resulted in some reduction in the binding affinity, although still higher than that in the WT. All three mutants (**d1, d2,** and **d3**) showed improved *ee* and higher TONs than with

the wild-type protein.[597] This ArM system was later applied to another similar IrCp cofactor using a dual-anchoring system to further increase the occupancy and stabilize the geometric configuration.

Directed evolution based on the dual-anchoring mutant I91C was conducted at the Leu60, Asn62, Asn67, Glu69, and Gln92 sites, all of which neighbor the terminal chloride of the Ir complex. All mutations at Gln92 led to decreases in activity, possibly due to the elimination of an optimal H-bonding interaction between Gln92 and the amide oxygen of the cofactor, which serves a crucial role in fixing the Ir cofactor in the active site and maintaining the pyridine–sulfonamide linkage. For purified protein, N67G/E69R/I91C displayed the highest activity toward the *R*-enantioselectivity of the substrate with a TON of 451 and *ee* of 96%. For *S*-enantioselectivity, N67L/E69Y/I91C and L60W/N67L/E69Y/I91C reached moderate *ee* values of −62% and −49%, respectively (TONs 458 and 221, respectively). In comparison, the starting I91C construct exhibited a TON of 265 and *ee* of −39%. The L60W/N67L/E69Y variant alone enhanced the activity by 4.3-fold as well as improved the *S*-enantioselectivity to 59% *ee*. From the crystal structures of N67G/E69R/I91C and I91C, it was surmised that N67G provided more space for the substrate, allowing a more facile approach to Ir-H, while E69R may serve to introduce a cation–π interaction between the residue and the substrate. As a result, the above two mutations together may aid in substrate binding to the active site, leading to the increase of the TON and enantioselectivity.[598]

The HaloTag (HT) protein utilizes a reactive aspartic acid in its binding pocket to react with haloalkanes, forming a covalent linkage. Taking advantage of this, Fischer and co-workers developed a metathase by linking a Ru complex to HT, which was shown to exhibit enhanced TONs when compared to the catalyst alone. Directed evolution was applied to residues around the binding pocket; however, no significant improve-ments in the activity were observed. This is likely due to the long distance between the cofactor and the protein scaffold caused by the length of the linker or possibly due to the minimal interactions between the SCS and the catalytic cofactor transition state.[599]

7. SUMMARY AND OUTLOOK

In this review, we have showcased how catalysis can be modulated in a wide range of designed ArMs by focusing on the roles of the environment beyond the PCS. While we have covered many examples involving the generation of ArMs through the redesign of existing PCSs or the introduction of a new PCS into a native protein scaffold, most of these ArMs display much lower activities in comparison to their native enzyme counterparts. The most impressive examples with high catalytic activities, including several that approach or exceed those of native enzymes, have arisen from those that have further employed SCS modifications to optimize properties such as the reactivity and substrate selectivity.

Throughout this review, we have seen both rational design and directed evolution used as effective tools to impart and enhance new reactivities in ArMs. At face value, the ethoses of rational design and directed evolution appear at odds, in-so-far as the first insists on the question “How?”, while the second avoids it. However, these two strategies can be powerfully used to complement one another and overcome their own respective limitations.

In particular, the further optimization of rationally designed ArMs by directed evolution can uncover subtle SCS roles that may otherwise be easily overlooked. Likewise, the use of rational design to analyze ArMs directed by evolution can provide new insight to overcome barriers associated with limitations in screening methods and to design smaller, higher quality libraries.[600] When synergized with computational methods, particularly those available for initial scaffold design, such as Rosetta[61,62] and AlphaFold,[63,64] and those for analysis, such as QM/MM methods, both our understanding of the roles of SCS residues and the practical development of ArMs can be greatly advanced. Doing so may not only enable further development of the systems discussed in the present review but also open doors to the design of ArMs modeling metalloenzymatic systems with more complex cofactors and more challenging reactions, such as photosystem II, nitrogenases, and methane monooxygenase.

Due to the prevalence, long history of study, and biological significance of heme enzymes, heme-based ArMs represent one of the most thoroughly studied classes in this review, particularly regarding the roles of SCS residues. Engineered heme ArMs generally fall into one of two groups: (1) nonenzymatic native scaffolds, such as Mb and C*c,* that are engineered to generate new activities and (2) enzymatic scaffolds modified to exhibit activity toward non-native substrates or non-native functions. Additionally, three strategies have been employed to study and enhance catalysis in these systems. The first approach is to mimic the structural features of a desired native enzyme, such as the His-Arg pair or the positioning of the distal His in peroxidases.[101,122] The second is to employ SDM at SCS residues surrounding the active site to vary structural features such as sterics, polarization, and H-bonding to tune the activity. The third entails using directed evolution to repurpose a native heme protein for new, non-native functions. This is often accomplished through SDM of residues identified as “hot spots” near the active site, although it is worthwhile to note that directed evolution is also effective at identifying beneficial mutations that are surprisingly remote.[569,573] These strategies have resulted in the generation of several highly competent catalytic heme ArMs, with some of them approaching,[539] rivaling,[525] or even exceeding[524] those of native enzymes. Through this process, we have learned not only how the presence of SCS features, such as H-bonding, influences catalysis but also how the positioning of the same SCS residue in different scaffolds (e.g., distal His in Mb and CcP) can play a key role in both conferring and fine-tuning activity. However, the practical development of these enzymes would benefit from further developments in terms of scaffold stability, and further optimization of these systems for varying activity stands to benefit from the more extensive application of computationally aided design and screening.

It is interesting that DNA has been used as an alternative scaffold for designing artificial heme enzymes. However, current DNA models do not support proximal ligation to the heme by the scaffold molecule, which limits the reactivity of heme/DNAzymes compared to heme enzymes. Extending the oligonucleotide beyond the G-quartet/heme interface provides a structure analogous to the active site of heme proteins;[249] however, the much more disordered distal environment of a G-quadruplex scaffold is very different from typical protein scaffolds. This provides an opportunity for developing an active site *de novo*—importantly, as the DNA scaffold can be developed by *in vitro* selection, active sites made from pendant nucleotides can be selected against one another without the issues of

expression or purification that can otherwise arise when employing directed evolution for proteins.

The PCSs of native mononuclear non-heme Fe enzymes predominately utilize the facial $(His)_2$-carboxylate triad, which has served as the major inspiration for initial designs of non-heme Fe ArMs. However, despite their prevalence in nature, relatively few non-heme Fe ArMs have been designed which employ natural amino acid side chains/protein backbone for metal ion coordination,[268,246-248,274] at least when compared to those for other metals such as Cu, Ni, and Zn. As a result, the study of SCS interactions in non-heme Fe ArMs has not advanced to the extent discussed in some other sections, underlining the need for continued developments in this field, particularly toward mono- and dioxygenase activity. Similarly, the employment of the UAA Ala_{Bpy} has been effective in forming Fe^{II} binding sites (especially when combined with computational design), but UAA-based systems have yet to be turned into efficient catalysts.[255-258,286,287] Meanwhile, non-heme Fe ArMs formed using a protein scaffold to host an organometallic cofactor have proven to be the most well-characterized in terms of catalytic competence, particularly through the efforts of Ménage and co-workers.[302,305,306,308] In these systems, SCS residues have primarily been investigated to support fixation and positioning of the organometallic scaffold through π-stacking and salt bridge interactions to enhance the specificity and selectivity. Lastly, the development of dinuclear non-heme Fe sites in native scaffold-based ArMs has largely been inspired by FeFe H_2ase,[291-295] although little further development has been made in these systems to understand the role of the peptide scaffold beyond the PCS. Borovik and co-workers have developed a notable exception, forming a non-heme diiron site via bridging of Sav active sites that is reminiscent of native oxygenases, although further catalytic studies are yet to be presented.[317] Taken together, non-heme Fe ArMs present a promising field for continued study, particularly through more expansive investigations of the roles of SCS residues in modulating the properties of Fe.

Cu proteins serve diverse roles in nature, including ET and various catalytic roles. Two types of Cu sites natively serve in ET (T1Cu and Cu_A), both of which have been studied by the development of cupredoxin units that are isolated from native ET systems, as well as by incorporation into nonhomologous scaffolds. By modulating the SCS to vary factors such as hydrophobicity and hydrogen bonding, the ET properties of these centers can be effectively optimized by balancing $E°$ with reorganization energy.[349-355,392,393] The next development of these centers requires consideration of how to effectively couple these ET active proteins with catalytic ArMs to enhance enzymatic activity, including the realization of specific surface interactions. Additionally, SCS development optimizing pathways for long-range electron transfer offer a tantalizing challenge, requiring not only a well-balanced electrochemical gradient but also possible involvement of proton donor/acceptors.

Catalytic Cu centers mimicking natural reactivities present a greater challenge. Several reactions with small inorganic molecules have been demonstrated in Cu-based ArMs, including nitrite reduction,[457] superoxide dismutation,[452] S(Cys) peroxidation,[456,464] and S-nitrosylation.[276] In these examples, studies of the SCS have allowed the electrostatic environment and $E°$ of the Cu active site to be tuned. The oxidation of organic substrates has also been reported, where SCS interactions have been employed to control protein–

substrate interactions. Furthermore, artificial Cu proteins have been repurposed to catalyze a number of unnatural reactions including the D-A reaction,[478,487] F-C alkylation,[368] Michael addition,[497] and alkene hydration.[468] In these cases, the SCS has been employed to enforce product selectivity via substrate–SCS interactions. It is worth noting that Cu centers have often been treated as Lewis acids, and their natural roles as oxidoreductases are surprisingly less studied. In particular, oxidative reactivity has been more difficult to achieve than reductive chemistry (in large part due to the damage that can occur to the protein scaffold from ROSs), despite numerous examples of Cu-based oxidases and oxygenases in nature. Therefore, much remains to be explored in the area of Cu ArMs by further consideration of SCS effects.

In addition to Fe and Cu metalloenzymes, there are many ArMs that have employed other biologically relevant metal cofactors, such as V,[589] Cr,[540] Mn,[540,541,547] Co,[549,551] Ni,[560,563] Zn,[565] and Mg,[508] as well as those with abiological metal centers, including Ru,[577] Rh,[568,581,590,594] Pd,[586] Os,[588] Ir,[558,559,579,597] and Au.[587] These studies can be divided into two categories, namely those that target understanding native metalloenzyme functionality and those that aim to utilize the ArM scaffold to enhance the catalytic properties of organometallic complexes. The role of the SCS is key to both of these aims, functioning both to tune the metal site and control substrate–metal interactions through varying factors including H-bonding, steric hindrance, hydrophobicity, and pK_a. Future studies using directed evolution to investigate the SCSs of novel ArMs could benefit from more thorough structural and mechanistic studies of the evolved enzymes to rationalize the specific influence of varying residues on ArM performance for each sequential round of selection. By tracing the evolutionary path, greater insight could be gained on how to further engineer ArMs with enhanced performance through tuning the environment beyond the PCS.

SCS interactions are often weak and difficult to pinpoint, with many effects remaining nonobvious even for experienced ArM designers and too subtle to be reliably predicted by current computational methods. To overcome these limitations, the study and development of ArMs stand to benefit from machine learning approaches. To achieve such goals, a large and well-defined set of structural and activity data for each target metalloenzyme is required. Since it is much easier to produce these data sets using ArMs, designed ArMs can play a key role in advancing this field. Given the rapid progress made in data collection and improvement of machine learning algorithms, it would be possible to routinely incorporate the best combinations of PCS and SCS features to design any metalloenzyme with desired activity.

ACKNOWLEDGMENTS

The research in the Lu group was supported by grants from the National Science Foundation (CHE-2108837) and the National Institutes of Health (GM141931). We also thank the Robert A. Welch Foundation (Grant F-0020) for support of the Lu group research program at the University of Texas at Austin.

Biographies

Casey Van Stappen completed his B.Sc. (2011) and M.Sc. (2013) degrees in Chemistry at the University of Minnesota, Duluth, under the supervision of Prof. Viktor Nemykin. Following several years of postgraduate study at the University ofMichigan, Ann Arbor, under the advisement of Profs. Nicolai Lehnert and Vincent Pecoraro, he transferred his studies to the Max Planck Institute for Chemical Energy Conversion (MPI-CEC, 2015), as a member of the IMPRS-RECHARGE, and completed his D.Sc. (2019) in Chemistry via enrollment at Ruhr-Universität Bochum under the advisement of Prof. Dr. Serena DeBeer, Dr. Eckhard Bill, and Prof. Dr. Frank Neese. Following a short period as a postdoctoral research associate, also at the MPI-CEC, he joined the group of Prof. Yi Lu at the University of Texas at Austin as a postdoctoral research fellow. His research interests lie in combining spectroscopic, biochemical, and computational methods to investigate small molecule activation and catalysis, particularly in biological and biologically inspired systems.

Yunling Deng grew up in Changchun, China, and received her B.Sc. (2014) in Chemistry from Nankai University, China (2014). She completed her Ph.D. (2020) in Bioinorganic Chemistry at Dartmouth College investigating the effects of heme propionates on the structural and redox properties of *c*-type cytochromes under the guidance of Prof. Ekaterina Pletneva. She next moved to the University of Illinois at Urbana-Champaign (and recently to the University of Texas at Austin) as a postdoctoral research fellow to work with Prof. Yi Lu, working on developing artificial metalloenzymes for CO_2 reduction.

Yiwei Liu was born in Zhengzhou, China, and received his B.Sc. (2018) from Peking University, China, under the supervision of Prof. Jun-Long Zhang. He joined Prof. Yi Lu's lab at the University of Illinois at Urbana-Champaign (now at the University of Texas at Austin) in the same year. As a Ph.D. candidate in Inorganic Chemistry, his research focuses on engineering simple, noncatalytic proteins such as cupredoxins into artificial metalloenzymes to mimic the coordination chemistry and reactivity of natural enzymes.

Hirbod Heidari was born in Hamedan, Iran, and completed his Chemistry B.Sc. (2018) under the supervision of Prof. Sirus Jamali at the Sharif University of Technology, Tehran, Iran, along with a minor degree in Physics. In 2017, he conducted a summer-long internship under the supervision of Prof. Truhlar and the late Dr. Steven Mielke on Molecular Partition Function Computations. In 2019, he joined the lab of Prof. Yi Lu at the University of Illinois at Urbana-Champaign (now at the University of Texas at Austin) as a Ph.D. candidate. His research interests lie at the interface of computational chemistry and artificial protein engineering.

Jing-Xiang Wang obtained his B.Sc. (2019) from Peking University, Beijing, China, under the supervision of Prof. Jun-Long Zhang. After he joined Dr. Yi Lu's lab at the University of Illinois at Urbana-Champaign in the same year, he moved to the University of Texas at Austin in 2021 with Dr. Yi Lu, continuing to pursuit his doctorate degree. His research interests lie in metalloprotein engineering and constructing artificial metalloenzymes.

His current research is focusing on enhancing activities for metalloenzymes for further applications.

Yu Zhou was born in Jiangxi, China. He received his B.Sc. degree (2019) from Zhiyuan College, Shanghai Jiao Tong University, under the supervision of Prof. Xiaomin Xie and Prof. Zhaoguo Zhang and conducted a half-year internship with Prof. David Sarlah in 2018 (University of Illinois at Urbana-Champaign, UIUC) as a visiting undergraduate. After a three-year undergraduate research experience in copper- and palladium-catalyzed organic reaction development, he decided to join Prof. Yi Lu's lab at UIUC (now at the University of Texas at Austin) and study biocatalysis. His current research aims at designing novel, efficient, and highly selective biocatalytic systems and metabolic networks.

Aaron P. Ledray received a B.S. (2015) in Biotechnology and Biomedical Sciences from the University of Central Florida under the supervision of Prof. Stephen J. King, where he studied neuro-degenerative disease. He completed his Ph.D. (2021) in Biological Sciences from the University of California, Irvine, investigating reactive heme intermediates under the advisement of Prof. Michael T. Green. He joined Prof. Yi Lu's group at the University of Texas at Austin as a postdoctoral research fellow in 2021, shortly after completing his doctorate. Aaron's research interests include bioinorganic chemistry, enzyme design, and mechanisms of human disease.

Yi Lu received his B.S. degree from Peking University in 1986 and his Ph.D. degree from the University of California at Los Angeles in 1992. After two years of postdoctoral research in Professor Harry B. Gray's group at Caltech, Dr. Lu started his own independent career in the Department of Chemistry at the University of Illinois at Urbana-Champaign in 1994. He was promoted to Associate Professor with tenure in 2000, full Professor in 2004, and endowed Jay and Ann Schenck Professor in 2010. In August of 2021, Dr. Lu moved to the University of Texas at Austin, becoming the Robert J. V. Johnson-Welch Regents Chair in Chemistry. Dr. Lu's research interests lie at the interface between chemistry and biology. Specific areas of current interest include (a) design and engineering of functional metalloproteins as environmentally benign catalysts in renewable energy generation and pharmaceuticals; (b) fundamental understanding of DNAzymes and their applications in environmental monitoring, medical diagnostics, and targeted drug delivery; (c) employing principles from biology for directed assembly of nanomaterials with controlled morphologies and its applications in imaging and medicine and (d) engineer biocatalysts to address challenges in synthetic organic chemistry and applications of novel biocatalysts in synthetic biology for biomass conversion, valuable products generation in high yield and good selectivity.

ABBREVIATIONS

AA	natural amino acid
ABTS	2,2′-azino-bis(3-ethylbenzothiazoline-6-sulfonic acid diammonium salt
ACCO	1-aminocyclopropane-1-carboxylate oxidase

ACS	coenzyme-A synthetase
adt	-SCH_2NHCH_2S-
Ala_{Bpy}	(2,2′-bipyridin-5-yl)alanine
AMO	ammonia monooxygenase
apo-C*c*	apo-cytochrome *c*
APX	ascorbate peroxidase
ArM	artificial metalloenzyme
ATHase	artificial transfer hydrogenase
ATRP	atom transfer radical polymerization
AxNiR	*Alcaligenes xylosoxidans* nitrite reductase
Az	azurin
β-LG	β-lactoglobulin
biot	biotin
Bph	biphenyl
BPP	bovine-pancreatic polypeptide
bpy	bipyridine
CA	carbonic anhydrase
cAMP	cyclic adenosine monophosphate
camSOD	cofactor-flexible superoxide dismutase
CAP	catabolite activator protein
C*c*	cytochrome *c*
Cc_{552}	cytochrome c_{552}
C*c*P	cytochrome *c* peroxidase
C*c*O	cytochrome *c* oxidase
CiP	*Coprinus cinereus* peroxidase
CLEC	cross-linked enzymatic crystal
ClTyr	3-chlorotyrosine
CMD	concerted metalation deprotonation
CODH	carbon monoxide dehydrogenase

CoPP(IX)	cobalt-protoporphyrin IX
COx	catechol oxidase
Cp	*Clostridium pasteurianum*
Csp1	copper storage protein
Cu_AAz	Cu_A azurin
Cu_BMb	myoglobin containing a designed Cu_B binding site
CueO	copper efflux oxidase
CuNiR	copper-dependent nitrite reductase
Cgb	cytoglobin
D-A	Diels–Alder reaction
DF	diformyl
DFT	density functional theory
DCFH-DA	2′,7′-dichlorofluorescin diacetate
DHP	dehaloperoxidase
DNA	DNA
DNIC	dinitrosyl iron complex
dpa	bis(2-pyridylmethyl)amine
DTB-SQ	3,5-di-*tert*-butylsemiquinone
DTT	dithiothreitol
DyP	decolorizing peroxidases
***E*°′**	reduction potential
EDA	ethyl diazoacetate
EDTA	ethylenediaminetetraacetic acid
ee	enantiomeric excess
E **m**	midpoint potential
ENDOR	electron double nuclear resonance spectroscopy
ESI-MS	electrospray ionization mass spectrometry
ET	electron transfer
EXAFS	extended X-ray absorption fine structure

EPR	electron paramagnetic resonance spectroscopy
F2Tyr	3,5-difluorotyrosine
F3Tyr	2,3,5-trifluorotyrosine
F-C	Friedel–Crafts alkylation
FdM	$[Fe_4S_4]$-binding oligopeptide
FeSOD	iron superoxide dismutase
FT-IR	Fourier transform infrared spectroscopy
GQ	G-quadruplex
H-bonding	hydrogen bonding
H-cluster	$[Fe_2(CO)_3(CN)_2(adt)]$
H_2ase	hydrogenase
hCA II	Human carbonic anhydrase II
HCO	heme-copper oxidase
HRP	horseradish peroxidase
HSA	human serum albumin
HT	HaloTag
IR	infrared
ICP	inductively coupled plasma
imiTyr	Tyr-His cross-link
IrMb	myoglobin containing the Ir(Me)-heme cofactor
KIE	kinetic isotope effect
L0	*N*-benzyl-*N*′- (2-hydroxybenzyl)-*N,N*′-ethylenediaminediacetic acid
L_5^2 maleimide	1-(2-{[2-(bispyridin-2-ylmethylamino)ethyl]-pyridin-2-ylmethylamino}ethyl)pyrrole-2,5-dione
L ibu	*N,N*′-bis(2-pyridylmethyl)-*N*-methyl-1,2-ethanediamine complex
LiP	lignin peroxidase
LMCT	ligand-to-metal charge transfer
LmrR	Lactococcal multidrug resistance regulator

LPMO	lytic polysaccharide monooxygenase
Mb	myoglobin
MCO	multicopper oxidase
MD	molecular dynamics
MF	monoformyl
MG	malachite green
MnC*c*P	Mn-bound cytochrome *c* peroxidase
MnP	manganese peroxidase
MnSOD	manganese superoxide dismutase
MtTyr	2-amino-3-(4-hydroxy-3-(methylthio)phenyl)-propanoic acid
N_2OR	nitrous oxide reductase
NB	nitrobindin
Ngb	neuroglobin
NiR	nitrite reductase
NiRd	nickel rubredoxin
NMM	*N*-methylmesoporphyrin IX
NMR	nuclear magnetic resonance
NO	nitric oxide
NOR	nitric oxide reductase
OMeY	3-methoxytyrosine
P411	cytochrome P411
P450	cytochrome P450
Pf	*Pyrococcus furiosus*
pMMO	particulate methane monooxygenase
pAF	*p*-aminophenylalanine
phen	phenylalanine
PT3	adenosine deaminase protein scaffold
POP	propyl oligopeptidase

POP-Z	propyl oligopeptidase containing the UAA 4-azidophenylalanine
PCS	primary coordination sphere
RDS	rate-determining step
Rma*-C*c	bacterial cytochrome *c* from *Rhodothermus marinus*
Rd	rubredoxin
ROS	reactive oxygen species
RMSD	root mean squared deviation
RNA	ribonucleic acid
rR	resonance Raman spectroscopy
SA	serum albumin
Sav	streptavidin
SCP-2L	steroid carrier protein 2L
SCS	secondary coordination sphere
SDM	side-directed mutagenesis
SHE	standard hydrogen electrode
SKIE	solvent kinetic isotope effect
SNO	nitrosothiol
SOD	superoxide dismutase
SOH	sulfenic acid
SOR	superoxide reductase
SRS	substrate recognition site
SSM	site-saturation mutagenesis
STAMPS	synchronous, transactional, and asynchronous multiprocessing
swMb	sperm whale myoglobin
***t*-BuOOH**	*t*-butyl-hydroperoxide
TAML	tetraamido macrocyclic ligand
TCP	2,4,6-trichlorophenol

TDHC	tetrahydrocorrin
TFAC	trifluoroacetophenone
THS	thermosome
TOF	turnover frequency
TOF MS	time-of-flight mass spectrometry
TON	turnover number
Trx	thioredoxin
TvNiR	*T. nitratireducens* cytochrome *c* nitrite reductase
T*t*Cu$_A$	*Thermus thermophilus* cytochrome *ba3* oxidase
UAA	unnatural amino acid
UV	ultraviolet
VT-MCD	variable temperature magnetic circular dichroism
WT	wild-type
XANES	X-ray absorption near-edge spectroscopy
Xln	xylanase
ZFS	zero-field splitting

REFERENCES

(1). Andreini C; Bertini I; Cavallaro G; Holliday GL; Thornton JM Metal Ions in Biological Catalysis: From Enzyme Databases to General Principles. JBIC, J. Biol. Inorg. Chem 2008, 13, 1205–1218. [PubMed: 18604568]

(2). Cvetkovic A; Menon AL; Thorgersen MP; Scott JW; Poole FL II; Jenney FE Jr.; Lancaster WA; Praissman JL; Shanmukh S; Vaccaro BJ; et al. Microbial Metalloproteomes Are Largely Uncharacterized. Nature 2010, 466, 779–782. [PubMed: 20639861]

(3). Encyclopedia of Geobiology; Reitner J, Thiel V, Eds.; Encyclopedia of Earth Sciences Series; Springer Netherlands: Dordrecht, 2011; pp 558–562.

(4). Rajakovich LJ; Balskus EP Metabolic Functions of the Human Gut Microbiota: The Role of Metalloenzymes. Nat. Prod. Rep 2019, 36, 593–625. [PubMed: 30452039]

(5). Nitschke W; McGlynn SE; Milner-White EJ; Russell MJ On the Antiquity of Metalloenzymes and Their Substrates in Bioenergetics. Biochim. Biophys. Acta, Bioenerg 2013, 1827, 871–881.

(6). Froese DS; Fowler B; Baumgartner MR Vitamin B_{12} Folate, and the Methionine Remethylation Cycle—Biochemistry, Pathways, and Regulation. J. Inherited Metab. Dis 2019, 42, 673–685. [PubMed: 30693532]

(7). Persson B; Hedlund J; Jörnvall H Medium- and Short-Chain Dehydrogenase/Reductase Gene and Protein Families. Cell. Mol. Life Sci 2008, 65, 3879. [PubMed: 19011751]

(8). Gonzalez FJ; Gelboin HV Human Cytochromes P450: Evolution and CDNA-Directed Expression. Environ. Health Perspect 1992, 98, 81–85. [PubMed: 1486867]

(9). Danielson PB The Cytochrome P450 Superfamily: Biochemistry, Evolution and Drug Metabolism in Humans. Curr. Drug. Metab 2002, 3, 561–597. [PubMed: 12369887]

(10). Nelson DR Cytochrome P450 Diversity in the Tree of Life. Biochim. Biophys. Acta, Proteins Proteomics 2018, 1866, 141–154. [PubMed: 28502748]

(11). Adam PS; Borrel G; Gribaldo S Evolutionary History of Carbon Monoxide Dehydrogenase/ Acetyl-CoA Synthase, One of the Oldest Enzymatic Complexes. Proc. Natl. Acad. Sci. U.S.A 2018, 115, No. E1166–E1173. [PubMed: 29358391]

(12). Can M; Armstrong FA; Ragsdale SW Structure, Function, and Mechanism of the Nickel Metalloenzymes, CO Dehydrogenase, and Acetyl-CoA Synthase. Chem. Rev 2014, 114, 4149–4174. [PubMed: 24521136]

(13). Kumar M; Lu W-P; Smith A; Ragsdale SW; McCracken J Azide Binding to Carbon Monoxide Dehydrogenase from Clostridium Thermoaceticum. J. Am. Chem. Soc 1995, 117, 2939–2940.

(14). Wittenborn EC; Cohen SE; Merrouch M; Léger C; Fourmond V; Dementin S; Drennan CL Structural Insight into Metallocofactor Maturation in Carbon Monoxide Dehydrogenase. J. Biol. Chem 2019, 294, 13017–13026. [PubMed: 31296570]

(15). Eklund H; Uhlin U; Färnegårdh M; Logan DT; Nordlund P Structure and Function of the Radical Enzyme Ribonucleotide Reductase. Prog. Biophys. Mol. Biol 2001, 77, 177–268. [PubMed: 11796141]

(16). Nordlund P; Reichard P Ribonucleotide Reductases. Annu. Rev. Biochem 2006, 75, 681–706. [PubMed: 16756507]

(17). Hofer A; Crona M; Logan DT; Sjöberg B-M DNA Building Blocks: Keeping Control of Manufacture. Crit. Rev. Biochem. Mol. Biol 2012, 47, 50–63. [PubMed: 22050358]

(18). Jordan A; Reichard P Ribonucleotide Reductases. Annu. Rev. Biochem 1998, 67, 71–98. [PubMed: 9759483]

(19). Vinyard DJ; Ananyev GM; Charles Dismukes G Photosystem II: The Reaction Center of Oxygenic Photosynthesis. Annu. Rev. Biochem 2013, 82, 577–606. [PubMed: 23527694]

(20). McEvoy JP; Brudvig GW Water-Splitting Chemistry of Photosystem II. Chem. Rev 2006, 106, 4455–4483. [PubMed: 17091926]

(21). Boyd ES; Anbar AD; Miller S; Hamilton TL; Lavin M; Peters JW A Late Methanogen Origin for Molybdenum-Dependent Nitrogenase. Geobiology 2011, 9, 221–232. [PubMed: 21504537]

(22). Bulen WA; LeComte JR The Nitrogenase System from Azotobacter: Two-Enzyme Requirement for N_2 Reduction, ATP-Dependent H_2 Evolution, and ATP Hydrolysis. Proc. Natl. Acad. Sci. U.S.A 1966, 56, 979–986. [PubMed: 5230193]

(23). Dervartanian DV; Shethna YI; Beinert H Purification and Properties of Two Iron-Sulfur Proteins from *Azotobacter vinelandii*. Biochim. Biophys. Acta, Protein Struct 1969, 194, 548–563.

(24). Burns RC; Holsten RD; Hardy RWF Isolation by Crystallization of the Mo-Fe Protein of *Azotobacter* Nitrogenase. Biochem. Biophys. Res. Commun 1970, 39, 90–99. [PubMed: 5438303]

(25). Crichton RR Biological Ligands for Metal Ions. In Biological Inorganic Chemistry, 2nd ed.; Crichton RR, Ed.; Elsevier: Oxford, 2012; Chapter 4, pp 69–89.

(26). Poulos TL Heme Enzyme Structure and Function. Chem. Rev 2014, 114, 3919–3962. [PubMed: 24400737]

(27). Keller TCS; Lechauve C; Keller AS; Brooks S; Weiss MJ; Columbus L; Ackerman H; Cortese-Krott MM; Isakson BE The Role of Globins in Cardiovascular Physiology. Physiol. Rev 2022, 102, 859–892. [PubMed: 34486392]

(28). Wajcman H; Kiger L; Marden MC Structure and Function Evolution in the Superfamily of Globins. C.R. Biol 2009, 332, 273–282. [PubMed: 19281958]

(29). Lecomte JTJ; Vuletich DA; Lesk AM Structural Divergence and Distant Relationships in Proteins: Evolution of the Globins. Curr. Opin. Struct. Biol 2005, 15, 290–301. [PubMed: 15922591]

(30). Derbyshire ER; Marletta MA Structure and Regulation of Soluble Guanylate Cyclase. Annu. Rev. Biochem 2012, 81, 533–559. [PubMed: 22404633]

(31). Poulos TL Soluble Guanylate Cyclase. Curr. Opin. Struct. Biol 2006, 16, 736–743. [PubMed: 17015012]

(32). Horst BG; Marletta MA Physiological Activation and Deactivation of Soluble Guanylate Cyclase. Nitric Oxide 2018, 77, 65–74. [PubMed: 29704567]

(33). Shuvalov VA Composition and Function of Cytochrome b559 in Reaction Centers of Photosystem II of Green Plants. J. Bioenerg. Biomembr 1994, 26, 619–626. [PubMed: 7721723]

(34). Pospíšil P Enzymatic Function of Cytochrome b559 in Photosystem II. J. Photochem. Photobiol. B 2011, 104, 341–347. [PubMed: 21377371]

(35). Shinopoulos KE; Brudvig GW Cytochrome b559 and Cyclic Electron Transfer within Photosystem II. Biochim. Biophys. Acta, Bioenerg 2012, 1817, 66–75.

(36). Maté MJ; Murshudov G; Bravo J; Melik-Adamyan W; Loewen PC; Fita I Heme-Catalases. In Handbook of Metalloproteins; John Wiley & Sons, Ltd, 2006; pp 1–17.

(37). Yuan F; Yin S; Xu Y; Xiang L; Wang H; Li Z; Fan K; Pan G The Richness and Diversity of Catalases in Bacteria. Front. Microbiol 2021, 12, 645477. [PubMed: 33815333]

(38). Díaz A; Loewen PC; Fita I; Carpena X Thirty Years of Heme Catalases Structural Biology. Arch. Biochem. Biophys 2012, 525, 102–110. [PubMed: 22209752]

(39). Vlasits J; Jakopitsch C; Bernroitner M; Zamocky M; Furtmüller PG; Obinger C Mechanisms of Catalase Activity of Heme Peroxidases. Arch. Biochem. Biophys 2010, 500, 74–81. [PubMed: 20434429]

(40). Anjum NA; Sharma P; Gill SS; Hasanuzzaman M; Khan EA; Kachhap K; Mohamed AA; Thangavel P; Devi GD; Vasudhevan P; et al. Catalase and Ascorbate Peroxidase-Representative H_2O_2-Detoxifying Heme Enzymes in Plants. Environ. Sci. Pollut. Res. Int 2016, 23, 19002–19029. [PubMed: 27549233]

(41). García-Horsman JA; Barquera B; Rumbley J; Ma J; Gennis RB The Superfamily of Heme-Copper Respiratory Oxidases. J. Bacteriol 1994, 176, 5587–5600. [PubMed: 8083153]

(42). van der Oost J; De Boer APN; de Gier J-WL; Zumft WG; Stouthamer AH; Van Spanning RJM The Heme-Copper Oxidase Family Consists of Three Distinct Types of Terminal Oxidases and Is Related to Nitric Oxide Reductase. FEMS Microbiol. Lett 1994, 121, 1–9. [PubMed: 8082820]

(43). Ortiz de Montellano PR The Mechanism of Heme Oxygenase. Curr. Opin. Chem. Biol 2000, 4, 221–227. [PubMed: 10742194]

(44). Kikuchi G; Yoshida T; Noguchi M Heme Oxygenase and Heme Degradation. Biochem. Biophys. Res. Commun 2005, 338, 558–567. [PubMed: 16115609]

(45). Gozzelino R; Jeney V; Soares MP Mechanisms of Cell Protection by Heme Oxygenase-1. Annu. Rev. Pharmacol. Toxicol 2010, 50, 323–354. [PubMed: 20055707]

(46). Poulos TL Thirty Years of Heme Peroxidase Structural Biology. Arch. Biochem. Biophys 2010, 500, 3–12. [PubMed: 20206121]

(47). Davies MJ; Hawkins CL; Pattison DI; Rees MD Mammalian Heme Peroxidases: From Molecular Mechanisms to Health Implications. Antioxid. Redox. Signal 2008, 10, 1199–1234. [PubMed: 18331199]

(48). Smith AT; Veitch NC Substrate Binding and Catalysis in Heme Peroxidases. Curr. Opin. Chem. Biol 1998, 2, 269–278. [PubMed: 9667928]

(49). Watmough NJ; Field SJ; Hughes RJL; Richardson DJ The Bacterial Respiratory Nitric Oxide Reductase. Biochem. Soc. Trans 2009, 37, 392–399. [PubMed: 19290869]

(50). Daiber A; Shoun H; Ullrich V Nitric Oxide Reductase (P450nor) from *Fusarium oxysporum*. J. Inorg. Biochem 2005, 99, 185–193. [PubMed: 15598501]

(51). Zumft WG Nitric Oxide Reductases of Prokaryotes with Emphasis on the Respiratory, Heme-Copper Oxidase Type. J. Inorg. Biochem 2005, 99, 194–215. [PubMed: 15598502]

(52). Murphy MJ; Siegel LM Siroheme and Sirohydrochlorin: The Basis for a New Type of Porphyrin-Related Prosthetic Group common to Both Assimilatory and Dissimilatory Sulfite Reductases. J. Biol. Chem 1973, 248, 6911–6919. [PubMed: 4583265]

(53). Trüper HG [29] Reverse Siroheme Sulfite Reductase from Thiobacillus denitrificans. In Inorganic Microbial Sulfur Metabolism; Methods in Enzymology, Vol. 243; Abelson JN, Simon MI, Peck HD Jr., LeGall J, Eds.; Academic Press, 1994; pp 422–426.

(54). Nakayama M; Akashi T; Hase T Plant Sulfite Reductase: Molecular Structure, Catalytic Function and Interaction with Ferredoxin. J. Inorg. Biochem 2000, 82, 27–32. [PubMed: 11132635]

(55). Van Stappen C; Decamps L; Cutsail GE; Bjornsson R; Henthorn JT; Birrell JA; DeBeer S The Spectroscopy of Nitrogenases. Chem. Rev 2020, 120, 5005–5081. [PubMed: 32237739]

(56). Lubitz W; Ogata H; Rüdiger O; Reijerse E Hydrogenases. Chem. Rev 2014, 114, 4081–4148. [PubMed: 24655035]

(57). Feynman R What I cannot create I do not understand. https://archives.caltech.edu/pictures/1.10-29.jpg (accessed 2022-02-07).

(58). Hibbert EG; Dalby PA Directed Evolution Strategies for Improved Enzymatic Performance. Microb. Cell Fact 2005, 4, 29. [PubMed: 16212665]

(59). Cobb RE; Chao R; Zhao H Directed Evolution: Past, Present, and Future. AIChE J 2013, 59, 1432–1440. [PubMed: 25733775]

(60). Voigt CA; Kauffman S; Wang ZG Rational Evolutionary Design: The Theory of in Vitro Protein Evolution. Adv. Protein Chem 2000, 55, 79–160. [PubMed: 11050933]

(61). Das R; Baker D Macromolecular Modeling with Rosetta. Annu. Rev. Biochem 2008, 77, 363–382. [PubMed: 18410248]

(62). Leaver-Fay A; Tyka M; Lewis SM; Lange OF; Thompson J; Jacak R; Kaufman K; Renfrew PD; Smith CA; Sheffler W; et al. ROSETTA3: An Object-Oriented Software Suite for the Simulation and Design of Macromolecules. Methods Enzymol. 2011, 487, 545–574. [PubMed: 21187238]

(63). Senior AW; Evans R; Jumper J; Kirkpatrick J; Sifre L; Green T; Qin C; Žídek A; Nelson AWR; Bridgland A; et al. Improved Protein Structure Prediction Using Potentials from Deep Learning. Nature 2020, 577, 706–710. [PubMed: 31942072]

(64). Jumper J; Evans R; Pritzel A; Green T; Figurnov M; Ronneberger O; Tunyasuvunakool K; Bates R; Žídek A; Potapenko A; et al. Highly Accurate Protein Structure Prediction with AlphaFold. Nature 2021, 596, 583–589. [PubMed: 34265844]

(65). Korendovych IV; DeGrado WF De Novo Protein Design, a Retrospective. Q. Rev. Biophys 2020, 53, No. e3. [PubMed: 32041676]

(66). Huang P-S; Boyken SE; Baker D The Coming of Age of De Novo Protein Design. Nature 2016, 537, 320–327. [PubMed: 27629638]

(67). Chalkley MJ; Mann SI; DeGrado WF De Novo Metalloprotein Design. Nat. Rev. Chem 2022, 6, 31–50. [PubMed: 35811759]

(68). Pinter TBJ; Koebke KJ; Pecoraro VL Catalysis and Electron Transfer in De Novo Designed Helical Scaffolds. Angew. Chem., Int. Ed. Engl 2020, 59, 7678–7699. [PubMed: 31441170]

(69). Schwizer F; Okamoto Y; Heinisch T; Gu Y; Pellizzoni MM; Lebrun V; Reuter R; Köhler V; Lewis JC; Ward TR Artificial Metalloenzymes: Reaction Scope and Optimization Strategies. Chem. Rev 2018, 118, 142–231. [PubMed: 28714313]

(70). Steinreiber J; Ward TR Artificial Metalloenzymes as Selective Catalysts in Aqueous Media. Coord. Chem. Rev 2008, 252, 751–766.

(71). Mao J; Ward TR Artificial Metalloenzymes for Enantiose-lective Catalysis Based on the Biotin-Avidin Technology. CHIMIA International Journal for Chemistry 2008, 62, 956–961.

(72). Creus M; Ward TR Designed Evolution of Artificial Metalloenzymes: Protein Catalysts Made to Order. Org. Biomol. Chem 2007, 5, 1835–1844. [PubMed: 17551630]

(73). Thomas CM; Ward TR Artificial Metalloenzymes: Proteins as Hosts for Enantioselective Catalysis. Chem. Soc. Rev 2005, 34, 337–346. [PubMed: 15778767]

(74). Creus M; Ward TR Design and Evolution of Artificial Metalloenzymes: Biomimetic Aspects. In Progress in Inorganic Chemistrty, Vol. 4; Karlin KD, Ed.; John Wiley & Sons, Ltd, 2011; Chapter 4, pp 203–253.

(75). Nastri F; D'Alonzo D; Leone L; Zambrano G; Pavone V; Lombardi A Engineering Metalloprotein Functions in Designed and Native Scaffolds. Trends Biochem. Sci 2019, 44, 1022–1040. [PubMed: 31307903]

(76). Bos J; Roelfes G Artificial Metalloenzymes for Enantioselective Catalysis. Curr. Opin. Chem. Biol 2014, 19, 135–143. [PubMed: 24608083]

(77). Leveson-Gower RB; Mayer C; Roelfes G The Importance of Catalytic Promiscuity for Enzyme Design and Evolution. Nat. Rev. Chem 2019, 3, 687–705.

(78). Springer BA; Sligar SG; Olson JS; Phillips GN Jr. Mechanisms of Ligand Recognition in Myoglobin. Chem. Rev 1994, 94, 699–714.

(79). Antonini E; Brunori M Hemoglobin and Myoglobin in Their Reactions with Ligands. In Frontiers of Biology, Vol. 21; North-Holland, 1971; pp 296.

(80). Lin Y; Wang J; Lu Y Functional Tuning and Expanding of Myoglobin by Rational Protein Design. Sci. China: Chem 2014, 57, 346–355.

(81). Bhagi-Damodaran A; Petrik I; Lu Y Using Biosynthetic Models of Heme-Copper Oxidase and Nitric Oxide Reductase in Myoglobin to Elucidate Structural Features Responsible for Enzymatic Activities. Isr. J. Chem 2016, 56, 773–790. [PubMed: 27994254]

(82). Lin Y-W Rational Design of Heme Enzymes for Biodegradation of Pollutants toward a Green Future. Biotechnol. Appl. Biochem 2020, 67, 484–494. [PubMed: 31175692]

(83). Rittle J; Field MJ; Green MT; Tezcan FA An Efficient, Step-Economical Strategy for the Design of Functional Metalloproteins. Nat. Chem 2019, 11, 434–441. [PubMed: 30778140]

(84). Lu Y; Berry SM; Pfister TD Engineering Novel Metalloproteins: Design of Metal-Binding Sites into Native Protein Scaffolds. Chem. Rev 2001, 101, 3047–3080. [PubMed: 11710062]

(85). Ozaki S; Matsui T; Roach MP; Watanabe Y Rational Molecular Design of a Catalytic Site: Engineering of Catalytic Functions to the Myoglobin Active Site Framework. Coord. Chem. Rev 2000, 198, 39–59.

(86). Hayashi T; Hisaeda Y New Functionalization of Myoglobin by Chemical Modification of Heme-Propionates. Acc. Chem. Res 2002, 35, 35–43. [PubMed: 11790087]

(87). Lu Y Design and Engineering of Metalloproteins Containing Unnatural Amino Acids or Non-Native Metal-Containing Cofactors. Curr. Opin. Chem. Biol 2005, 9, 118–126. [PubMed: 15811795]

(88). Lu Y Biosynthetic Inorganic Chemistry. Angew. Chem., Int. Ed. Engl 2006, 45, 5588–5601. [PubMed: 16900547]

(89). Isogai Y; Imamura H; Nakae S; Sumi T; Takahashi K; Nakagawa T; Tsuneshige A; Shirai T Tracing Whale Myoglobin Evolution by Resurrecting Ancient Proteins. Sci. Rep 2018, 8, 16883. [PubMed: 30442991]

(90). Bonagura CA; Bhaskar B; Shimizu H; Li H; Sundaramoorthy M; McRee DE; Goodin DB; Poulos TL High-Resolution Crystal Structures and Spectroscopy of Native and Compound I Cytochrome c Peroxidase. Biochemistry 2003, 42, 5600–5608. [PubMed: 12741816]

(91). Patterson WR; Poulos TL Crystal Structure of Recombinant Pea Cytosolic Ascorbate Peroxidase. Biochemistry 1995, 34, 4331–4341. [PubMed: 7703247]

(92). LaCount MW; Zhang E; Chen YP; Han K; Whitton MM; Lincoln DE; Woodin SA; Lebioda L The Crystal Structure and Amino Acid Sequence of Dehaloperoxidase from *Amphitrite ornata* Indicate Common Ancestry with Globins. J. Biol. Chem 2000, 275, 18712–18716. [PubMed: 10751397]

(93). Ortiz de Montellano PR; Catalano CE Epoxidation of Styrene by Hemoglobin and Myoglobin. Transfer of Oxidizing Equivalents to the Protein Surface. J. Biol. Chem 1985, 260, 9265–9271. [PubMed: 4019473]

(94). Rao SI; Wilks A; Ortiz de Montellano PR The Roles of His-64, Tyr-103, Tyr-146, and Tyr-151 in the Epoxidation of Styrene and Beta-Methylstyrene by Recombinant Sperm Whale Myoglobin. J. Biol. Chem 1993, 268, 803–809. [PubMed: 8419357]

(95). Adachi S; Nagano S; Ishimori K; Watanabe Y; Morishima I; Egawa T; Kitagawa T; Makino R Roles of Proximal Ligand in Heme Proteins: Replacement of Proximal Histidine of Human Myoglobin with Cysteine and Tyrosine by Site-Directed Mutagenesis as Models for P-450, Chloroperoxidase, and Catalase. Biochemistry 1993, 32, 241–252. [PubMed: 8380334]

(96). Yonetani T; Schleyer H Studies on Cytochrome *c* Peroxidase. J. Biol. Chem 1967, 242, 1974–1979. [PubMed: 4290448]

(97). Finzel BC; Poulos TL; Kraut J Crystal Structure of Yeast Cytochrome *c* Peroxidase Refined at 1.7-Å Resolution. J. Biol. Chem 1984, 259, 13027–13036. [PubMed: 6092361]

(98). Gajhede M; Schuller DJ; Henriksen A; Smith AT; Poulos TL Crystal Structure of Horseradish Peroxidase C at 2.15 Å Resolution. Nat. Struct. Mol. Biol 1997, 4, 1032–1038.

(99). Matsui T; Ozaki S; Watanabe Y On the Formation and Reactivity of Compound I of the His-64 Myoglobin Mutants. J. Biol. Chem 1997, 272, 32735–32738. [PubMed: 9407045]

(100). Ozaki S; Matsui T; Watanabe Y Conversion of Myoglobin into a Highly Stereo- Specific Peroxygenase by the L29H/H64L Mutation. J. Am. Chem. Soc 1996, 118, 9784–9785.

(101). Wu L-B; Du K-J; Nie C-M; Gao S-Q; Wen G-B; Tan X; Lin Y-W Peroxidase Activity Enhancement of Myoglobin by Two Cooperative Distal Histidines and a Channel to the Heme Pocket. J. Mol. Cat. B: Enzym 2016, 134, 367–371.

(102). Matsui T; Ozaki S; Liong E; Phillips GN; Watanabe Y Effects of the Location of Distal Histidine in the Reaction of Myoglobin with Hydrogen Peroxide. J. Biol. Chem 1999, 274, 2838–2844. [PubMed: 9915818]

(103). Poulos TL; Finzel BC; Howard AJ High-Resolution Crystal Structure of Cytochrome P450cam. J. Mol. Biol 1987, 195, 687–700. [PubMed: 3656428]

(104). Hara I; Ueno T; Ozaki S; Itoh S; Lee K; Ueyama N; Watanabe Y Oxidative Modification of Tryptophan 43 in the Heme Vicinity of the F43W/H64L Myoglobin Mutant. J. Biol. Chem 2001, 276, 36067–36070. [PubMed: 11481319]

(105). Quillin ML; Li T; Olson JS; Phillips GN Jr; Duo Y; Ikeda-Saito M; Regan R; Carlson M; Gibson QH; Li H; et al. Structural and Functional Effects of Apolar Mutations of the Distal Valine in Myoglobin. J. Mol. Biol 1995, 245, 416–436. [PubMed: 7837273]

(106). Yang H-J; Matsui T; Ozaki S; Kato S; Ueno T; Phillips GN; Fukuzumi S; Watanabe Y Molecular Engineering of Myoglobin: Influence of Residue 68 on the Rate and the Enantioselectivity of Oxidation Reactions Catalyzed by H64D/V68X Myoglobin. Biochemistry 2003, 42, 10174–10181. [PubMed: 12939145]

(107). Quillin ML; Arduini RM; Olson JS; Phillips GN High-Resolution Crystal Structures of Distal Histidine Mutants of Sperm Whale Myoglobin. J. Mol. Biol 1993, 234, 140–155. [PubMed: 8230194]

(108). Tiso M; Tejero J; Basu S; Azarov I; Wang X; Simplaceanu V; Frizzell S; Jayaraman T; Geary L; Shapiro C; et al. Human Neuroglobin Functions as a Redox-Regulated Nitrite Reductase. J. Biol. Chem 2011, 286, 18277–18289. [PubMed: 21296891]

(109). Beckerson P; Reeder BJ; Wilson MT Coupling of Disulfide Bond and Distal Histidine Dissociation in Human Ferrous Cytoglobin Regulates Ligand Binding. FEBS Lett. 2015, 589, 507–512. [PubMed: 25601563]

(110). Wu L-B; Yuan H; Zhou H; Gao S-Q; Nie C-M; Tan X; Wen G-B; Lin Y-W An Intramolecular Disulfide Bond Designed in Myoglobin Fine-Tunes Both Protein Structure and Peroxidase Activity. Arch. Biochem. Biophys 2016, 600, 47–55. [PubMed: 27117233]

(111). Yin L-L; Yuan H; Du K-J; He B; Gao S-Q; Wen G-B; Tan X; Lin Y-W Regulation of Both the Structure and Function by a De Novo Designed Disulfide Bond: A Case Study of Heme Proteins in Myoglobin. Chem. Commun 2018, 54, 4356–4359.

(112). Chen YP; Woodin SA; Lincoln DE; Lovell CR An Unusual Dehalogenating Peroxidase from the Marine Terebellid Polychaete *Amphitrite ornata*. J. Biol. Chem 1996, 271, 4609–4612. [PubMed: 8617721]

(113). Osborne RL; Taylor LO; Han KP; Ely B; Dawson J *Amphitrite ornata* Dehaloperoxidase: Enhanced Activity for the Catalytically Active Globin Using MCPBA. Biochem. Biophys. Res. Commun 2004, 324, 1194. [PubMed: 15504340]

(114). Du J; Huang X; Sun S; Wang C; Lebioda L; Dawson JH Amphitrite Ornata Dehaloperoxidase (DHP): Investigations of Structural Factors That Influence the Mechanism of Halophenol Dehalogenation Using “Peroxidase-like” Myoglobin Mutants and “Myoglobin-like” DHP Mutants. Biochemistry 2011, 50, 8172–8180. [PubMed: 21800850]

(115). Yan D-J; Li W; Xiang Y; Wen G-B; Lin Y-W; Tan X A Novel Tyrosine-Heme C-O Covalent Linkage in F43Y Myoglobin: A New Post-Translational Modification of Heme Proteins. ChemBioChem 2015, 16, 47–50. [PubMed: 25392956]

(116). Liao F; He B; Du K-J; Gao S-Q; Wen G-B; Lin Y-W Enhanced Dehaloperoxidase Activity of F43Y Myoglobin with a Novel Thyrosine-Heme Crosslink. Chem. Lett 2016, 45, 1087–1089.

(117). Li L-L; Yuan H; Liao F; He B; Gao S-Q; Wen G-B; Tan X; Lin Y-W Rational Design of Artificial Dye-Decolorizing Peroxidases Using Myoglobin by Engineering Tyr/Trp in the Heme Center. Dalton Trans. 2017, 46, 11230–11238. [PubMed: 28795725]

(118). Yin L; Yuan H; Liu C; He B; Gao S-Q; Wen G-B; Tan X; Lin Y-W A Rationally Designed Myoglobin Exhibits a Catalytic Dehalogenation Efficiency More than 1000-Fold That of a Native Dehaloperoxidase. ACS Catal. 2018, 8, 9619–9624.

(119). Sundaramoorthy M; Terner J; Poulos TL The Crystal Structure of Chloroperoxidase: A Heme Peroxidase-Cytochrome P450 Functional Hybrid. Structure 1995, 3, 1367–1378. [PubMed: 8747463]

(120). Matsui T; Ozaki S; Watanabe Y Formation and Catalytic Roles of Compound I in the Hydrogen Peroxide-Dependent Oxidations by His64 Myoglobin Mutants. J. Am. Chem. Soc 1999, 121, 9952–9957.

(121). Liu C; Xu J; Gao S-Q; He B; Wei C-W; Wang X-J; Wang Z; Lin Y-W Green and Efficient Biosynthesis of Indigo from Indole by Engineered Myoglobins. RSC Adv. 2018, 8, 33325–33330. [PubMed: 35548150]

(122). Liao F; Xu J-K; Luo J; Gao S-Q; Wang X-J; Lin Y-W Bioinspired Design of an Artificial Peroxidase: Introducing Key Residues of Native Peroxidases into F43Y Myoglobin with a Tyr-Heme Cross-Link. Dalton Trans. 2020, 49, 5029–5033. [PubMed: 32236202]

(123). Xiang H-F; Xu J-K; Liu J; Yang X-Z; Gao S-Q; Wen G-B; Lin Y-W Efficient Biodegradation of Malachite Green by an Artificial Enzyme Designed in Myoglobin. RSC Adv. 2021, 11, 16090–16095. [PubMed: 35481174]

(124). Bordeaux M; Tyagi V; Fasan R Highly Diastereoselective and Enantioselective Olefin Cyclopropanation Using Engineered Myoglobin-Based Catalysts. Angew. Chem., Int. Ed 2015, 54, 1744–1748.

(125). Tyagi V; Bonn RB; Fasan R Intermolecular Carbene S-H Insertion Catalysed by Engineered Myoglobin-Based Catalysts. Chem. Sci 2015, 6, 2488–2494. [PubMed: 26101581]

(126). Tyagi V; Sreenilayam G; Bajaj P; Tinoco A; Fasan R Biocatalytic Synthesis of Allylic and Allenyl Sulfides through a Myoglobin-Catalyzed Doyle-Kirmse Reaction. Angew. Chem., Int. Ed 2016, 55, 13562–13566.

(127). Tinoco A; Steck V; Tyagi V; Fasan R Highly Diastereo- and Enantioselective Synthesis of Trifluoromethyl-Substituted Cyclopropanes via Myoglobin-Catalyzed Transfer of Trifluoromethylcarbene. J. Am. Chem. Soc 2017, 139, 5293–5296. [PubMed: 28366001]

(128). Tyagi V; Fasan R Myoglobin-Catalyzed Olefination of Aldehydes. Angew. Chem., Int. Ed 2016, 55, 2512–2516.

(129). Bourissou D; Guerret O; Gabbaï FP; Bertrand G Stable Carbenes. Chem. Rev 2000, 100, 39–92. [PubMed: 11749234]

(130). Wang Y; Xue P; Cao M; Yu T; Lane ST; Zhao H Directed Evolution: Methodologies and Applications. Chem. Rev 2021, 121, 12384–12444. [PubMed: 34297541]

(131). Sreenilayam G; Fasan R Myoglobin-Catalyzed Intermolecular Carbene N-H Insertion with Arylamine Substrates. Chem. Commun 2015, 51, 1532–1534.

(132). Vargas DA; Tinoco A; Tyagi V; Fasan R Myoglobin-Catalyzed C-H Functionalization of Unprotected Indoles. Angew. Chem., Int. Ed 2018, 57, 9911–9915.

(133). Vargas DA; Khade RL; Zhang Y; Fasan R Biocatalytic Strategy for Highly Diastereo- and Enantioselective Synthesis of 2,3-Dihydrobenzofuran-Based Tricyclic Scaffolds. Angew. Chem., Int. Ed 2019, 58, 10148–10152.

(134). Nam D; Steck V; Potenzino RJ; Fasan R A Diverse Library of Chiral Cyclopropane Scaffolds via Chemoenzymatic Assembly and Diversification of Cyclopropyl Ketones. J. Am. Chem. Soc 2021, 143, 2221–2231. [PubMed: 33497207]

(135). Tinoco A; Wei Y; Bacik J-P; Carminati DM; Moore EJ; Ando N; Zhang Y; Fasan R Origin of High Stereocontrol in Olefin Cyclopropanation Catalyzed by an Engineered Carbene Transferase. ACS Catal. 2019, 9, 1514–1524. [PubMed: 31134138]

(136). Zhou Q; Hu M; Zhang W; Jiang L; Perrett S; Zhou J; Wang J Probing the Function of the Tyr-Cys Cross-Link in Metalloenzymes by the Genetic Incorporation of 3-Methylthiotyrosine. Angew. Chem., Int. Ed 2013, 52, 1203–1207.

(137). Meharenna YT; Oertel P; Bhaskar B; Poulos TL Engineering Ascorbate Peroxidase Activity into Cytochrome *c* Peroxidase. Biochemistry 2008, 47, 10324–10332. [PubMed: 18771292]

(138). Erman JE; Kilheeney H; Bidwai AK; Ayala CE; Vitello LB Peroxygenase Activity of Cytochrome *c* Peroxidase and Three Apolar Distal Heme Pocket Mutants: Hydroxylation of 1-Methoxynaphthalene. BMC Biochemistry 2013, 14, 19. [PubMed: 23895311]

(139). Wang J; Mauro JM; Edwards SL; Oatley SJ; Fishel LA; Ashford VA; Xuong NH; Kraut J X-Ray Structures of Recombinant Yeast Cytochrome *c* Peroxidase and Three Heme-Cleft Mutants Prepared by Site-Directed Mutagenesis. Biochemistry 1990, 29, 7160–7173. [PubMed: 2169873]

(140). Stubbe J; van der Donk WA Protein Radicals in Enzyme Catalysis. Chem. Rev 1998, 98, 705–762. [PubMed: 11848913]

(141). Seyedsayamdost MR; Yee CS; Reece SY; Nocera DG; Stubbe J pH Rate Profiles of F_nY_{356}-R2s (n = 2, 3, 4) in *Escherichia coli* Ribonucleotide Reductase: Evidence That Y_{356} Is a Redox-Active Amino Acid along the Radical Propagation Pathway. J. Am. Chem. Soc 2006, 128, 1562–1568. [PubMed: 16448127]

(142). Schoemaker HE; Piontek K On the Interaction of Lignin Peroxidase with Lignin. Pure Appl. Chem 1996, 68, 2089–2096.

(143). Choinowski T; Blodig W; Winterhalter KH; Piontek K The Crystal Structure of Lignin Peroxidase at 1.70 Å Resolution Reveals a Hydroxy Group on the C^{β} of Tryptophan 171: A Novel Radical Site Formed during the Redox Cycle. J. Mol. Biol 1999, 286, 809–827. [PubMed: 10024453]

(144). Blodig W; Smith AT; Doyle WA; Piontek K Crystal Structures of Pristine and Oxidatively Processed Lignin Peroxidase Expressed in Escherichia Coli and of the W171F Variant That Eliminates the Redox Active Tryptophan 171. Implications for the Reaction Mechanism. J. Mol. Biol 2001, 305, 851–861. [PubMed: 11162097]

(145). Smith AT; Doyle WA; Dorlet P; Ivancich A Spectroscopic Evidence for an Engineered, Catalytically Active Trp Radical That Creates the Unique Reactivity of Lignin Peroxidase. Proc. Natl. Acad. Sci. U.S.A 2009, 106, 16084–16089. [PubMed: 19805263]

(146). Field MJ; Bains RK; Warren JJ Using an Artificial Tryptophan “Wire” in Cytochrome *c* Peroxidase for Oxidation of Organic Substrates. Dalton Trans. 2017, 46, 11078–11083. [PubMed: 28792039]

(147). Berghuis AM; Brayer GD Oxidation State-Dependent Conformational Changes in Cytochrome *c*. J. Mol. Biol 1992, 223, 959–976. [PubMed: 1311391]

(148). Yin V; Shaw GS; Konermann L Cytochrome *c* as a Peroxidase: Activation of the Precatalytic Native State by H_2O_2-Induced Covalent Modifications. J. Am. Chem. Soc 2017, 139, 15701–15709. [PubMed: 29048162]

(149). Xu Y; Mayne L; Englander SW Evidence for an Unfolding and Refolding Pathway in Cytochrome c. Nat. Struct. Biol 1998, 5, 774–778. [PubMed: 9731770]

(150). Krishna MMG; Maity H; Rumbley JN; Lin Y; Englander SW Order of Steps in the Cytochrome *c* Folding Pathway: Evidence for a Sequential Stabilization Mechanism. J. Mol. Biol 2006, 359, 1410–1419. [PubMed: 16690080]

(151). Tezcan FA; Winkler JR; Gray HB Effects of Ligation and Folding on Reduction Potentials of Heme Proteins. J. Am. Chem. Soc 1998, 120, 13383–13388.

(152). Wang Z-H; Lin Y-W; Rosell FI; Ni F-Y; Lu H-J; Yang P-Y; Tan X-S; Li X-Y; Huang Z-X; Mauk AG Converting Cytochrome *c* into a Peroxidase-like Metalloenzyme by Molecular Design. ChemBioChem 2007, 8, 607–609. [PubMed: 17328023]

(153). Ying T; Zhong F; Wang Z-H; Li W; Tan X; Huang Z-X A Route to Novel Functional Metalloproteins via Hybrids of Cytochrome P450 and Cytochrome *c*. ChemBioChem 2011, 12, 707–710. [PubMed: 21404414]

(154). Ying T; Zhong F; Wang Z-H; Xie J; Tan X; Huang Z-X Generation of Novel Functional Metalloproteins via Hybrids of Cytochrome *c* and Peroxidase. Protein Eng., Des. Sel 2013, 26, 401–407. [PubMed: 23515371]

(155). Wester MR; Yano JK; Schoch GA; Yang C; Griffin KJ; Stout CD; Johnson EF The Structure of Human Cytochrome P450 2C9 Complexed with Flurbiprofen at 2.0-A Resolution. J. Biol. Chem 2004, 279, 35630–35637. [PubMed: 15181000]

(156). Nair PC; McKinnon RA; Miners JO Cytochrome P450 Structure-Function: Insights from Molecular Dynamics Simulations. Drug Metab. Rev 2016, 48, 434–452. [PubMed: 27167388]

(157). Ayala M; Verdin J; Vazquez-Duhalt R The Prospects for Peroxidase-Based Biorefining of Petroleum Fuels. Biocatal. Biotrans 2007, 25, 114–129.

(158). Nakajima H; Ichikawa Y; Satake Y; Takatani N; Manna SK; Rajbongshi J; Mazumdar S; Watanabe Y Engineering of Thermus Thermophilus Cytochrome C552: Thermally Tolerant Artificial Peroxidase. ChemBioChem 2008, 9, 2954–2957. [PubMed: 19006152]

(159). Nakajima H; Ramanathan K; Kawaba N; Watanabe Y Rational Engineering of Thermus Thermophilus Cytochrome C552 to a Thermally Tolerant Artificial Peroxidase. Dalton Trans. 2010, 39, 3105–3114. [PubMed: 20221545]

(160). Than ME; Hof P; Huber R; Bourenkov GP; Bartunik HD; Buse G; Soulimane T *Thermus thermophilus* Cytochrome c_{552}: A New Highly Thermostable Cytochrome *c* Structure Obtained by MAD Phasing. J. Mol. Biol 1997, 271, 629–644. [PubMed: 9281430]

(161). Finnigan JD; Young C; Cook DJ; Charnock SJ; Black GW Cytochromes P450 (P450s): A Review of the Class System with a Focus on Prokaryotic P450s. In Advances in Protein Chemistry and Structural Biology, Vol. 122; Karabencheva-Christova T, Christov C, Eds.; Academic Press, 2020; Chapter 9, pp 289–320. [PubMed: 32951814]

(162). Butler CF; Peet C; Mason AE; Voice MW; Leys D; Munro AW Key Mutations Alter the Cytochrome P450 BM3 Conformational Landscape and Remove Inherent Substrate Bias. J. Biol. Chem 2013, 288, 25387–25399. [PubMed: 23828198]

(163). Coelho PS; Brustad EM; Kannan A; Arnold FH Olefin Cyclopropanation via Carbene Transfer Catalyzed by Engineered Cytochrome P450 Enzymes. Science 2013, 339, 307–310. [PubMed: 23258409]

(164). Gober JG; Rydeen AE; Gibson-O'Grady EJ; Leuthaeuser JB; Fetrow JS; Brustad EM Mutating a Highly Conserved Residue in Diverse Cytochrome P450s Facilitates Diastereoselective Olefin Cyclopropanation. ChemBioChem 2016, 17, 394–397. [PubMed: 26690878]

(165). Coelho PS; Wang ZJ; Ener ME; Baril SA; Kannan A; Arnold FH; Brustad EM A Serine-Substituted P450 Catalyzes Highly Efficient Carbene Transfer to Olefins in Vivo. Nat. Chem. Biol 2013, 9, 485–487. [PubMed: 23792734]

(166). Renata H; Wang ZJ; Kitto RZ; Arnold FH P450-Catalyzed Asymmetric Cyclopropanation of Electron-Deficient Olefins under Aerobic Conditions. Catal. Sci. Technol 2014, 4, 3640–3643. [PubMed: 25221671]

(167). Gober JG; Rydeen AE; Schwochert TD; Gibson-O'Grady EJ; Brustad EM Enhancing Cytochrome P450-Mediated Non-Natural Cyclopropanation by Mutation of a Conserved Second-Shell Residue. Biotechnol. Bioeng 2018, 115, 1416–1426. [PubMed: 29460311]

(168). Girvan HM; Seward HE; Toogood HS; Cheesman MR; Leys D; Munro AW Structural and Spectroscopic Characterization of P450 BM3 Mutants with Unprecedented P450 Heme Iron Ligand Sets: New Heme Ligation States Influence Conformational Equilibria in P450 BM3. J. Biol. Chem 2007, 282, 564–572. [PubMed: 17077084]

(169). Sevrioukova IF; Li H; Zhang H; Peterson JA; Poulos TL Structure of a Cytochrome P450-Redox Partner Electron-Transfer Complex. Proc. Natl. Acad. Sci. U.S.A 1999, 96, 1863–1868. [PubMed: 10051560]

(170). Ost TWB; Clark J; Mowat CG; Miles CS; Walkinshaw MD; Reid GA; Chapman SK; Daff S Oxygen Activation and Electron Transfer in Flavocytochrome P450 BM3. J. Am. Chem. Soc 2003, 125, 15010–15020. [PubMed: 14653735]

(171). Ost TWB; Munro AW; Mowat CG; Taylor PR; Pesseguiero A; Fulco AJ; Cho AK; Cheesman MA; Walkinshaw MD; Chapman SK Structural and Spectroscopic Analysis of the F393H Mutant of Flavocytochrome P450 BM3. Biochemistry 2001, 40, 13430–13438. [PubMed: 11695889]

(172). Behrendorff JBYH; Huang W; Gillam EMJ Directed Evolution of Cytochrome P450 Enzymes for Biocatalysis: Exploiting the Catalytic Versatility of Enzymes with Relaxed Substrate Specificity. Biochem. J 2015, 467, 1–15. [PubMed: 25793416]

(173). Arnold FH Design by Directed Evolution. Acc. Chem. Res 1998, 31, 125–131.

(174). Glieder A; Farinas ET; Arnold FH Laboratory Evolution of a Soluble, Self-Sufficient, Highly Active Alkane Hydroxylase. Nat. Biotechnol 2002, 20, 1135–1139. [PubMed: 12368811]

(175). Peters MW; Meinhold P; Glieder A; Arnold FH Regio- and Enantioselective Alkane Hydroxylation with Engineered Cytochromes P450 BM-3. J. Am. Chem. Soc 2003, 125, 13442–13450. [PubMed: 14583039]

(176). Farinas ET; Alcalde M; Arnold F Alkene Epoxidation Catalyzed by Cytochrome P450 BM-3 139–3. Tetrahedron 2004, 60, 525–528.

(177). Li QS; Schwaneberg U; Fischer P; Schmid RD Directed Evolution of the Fatty-Acid Hydroxylase P450 BM-3 into an Indole-Hydroxylating Catalyst. Chemistry 2000, 6, 1531–1536. [PubMed: 10839169]

(178). Quéméneur E; Moutiez M; Charbonnier J-B; Menez A Engineering Cyclophilin into a Proline-Specific Endopeptidase. Nature 1998, 391, 301–304. [PubMed: 9440697]

(179). Appel D; Lutz-Wahl S; Fischer P; Schwaneberg U; Schmid RD A P450 BM-3 Mutant Hydroxylates Alkanes, Cycloalkanes, Arenes and Heteroarenes. J. Biotechnol 2001, 88, 167–171. [PubMed: 11403851]

(180). Whitehouse CJC; Bell SG; Wong L-L $P450_{BM3}$ (CYP102A1): Connecting the Dots. Chem. Soc. Rev 2012, 41, 1218–1260. [PubMed: 22008827]

(181). Kaur P; Tyagi V Recent Advances in Iron-Catalyzed Chemical and Enzymatic Carbene-Transfer Reactions. Adv. Synth. Catal 2021, 363, 877–905.

(182). Coin G; Latour J-M Nitrene Transfers Mediated by Natural and Artificial Iron Enzymes. J. Inorg. Biochem 2021, 225, 111613. [PubMed: 34634542]

(183). Wei Y; Tinoco A; Steck V; Fasan R; Zhang Y Cyclopropanations via Heme Carbenes: Basic Mechanism and Effects of Carbene Substituent, Protein Axial Ligand, and Porphyrin Substitution. J. Am. Chem. Soc 2018, 140, 1649–1662. [PubMed: 29268614]

(184). Su H; Ma G; Liu Y Theoretical Insights into the Mechanism and Stereoselectivity of Olefin Cyclopropanation Catalyzed by Two Engineered Cytochrome P450 Enzymes. Inorg. Chem 2018, 57, 11738–11745. [PubMed: 30156099]

(185). Hammer SC; Knight AM; Arnold FH Design and Evolution of Enzymes for Non-Natural Chemistry. Curr. Opin Green Sustainable Chem 2017, 7, 23–30.

(186). Yang Y; Arnold FH Navigating the Unnatural Reaction Space: Directed Evolution of Heme Proteins for Selective Carbene and Nitrene Transfer. Acc. Chem. Res 2021, 54, 1209–1225. [PubMed: 33491448]

(187). Miller DC; Athavale SV; Arnold FH Combining Chemistry and Protein Engineering for New-to-Nature Biocatalysis. Nat. Synth 2022, 1, 18–23. [PubMed: 35415721]

(188). Batista VF; Pinto DCGA; Silva AMS Iron: A Worthy Contender in Metal Carbene Chemistry. ACS Catal. 2020, 10, 10096–10116.

(189). Geronimo I; Denning CA; Rogers WE; Othman T; Huxford T; Heidary DK; Glazer EC; Payne CM Effect of Mutation and Substrate Binding on the Stability of Cytochrome $P450_{BM3}$ Variants. Biochemistry 2016, 55, 3594–3606. [PubMed: 27267136]

(190). Denisov IG; Makris TM; Sligar SG; Schlichting I Structure and Chemistry of Cytochrome P450. Chem. Rev 2005, 105, 2253–2278. [PubMed: 15941214]

(191). Shaik S; Kumar D; de Visser SP; Altun A; Thiel W Theoretical Perspective on the Structure and Mechanism of Cytochrome P450 Enzymes. Chem. Rev 2005, 105, 2279–2328. [PubMed: 15941215]

(192). Luthra A; Denisov IG; Sligar SG Spectroscopic Features of Cytochrome P450 Reaction Intermediates. Arch. Biochem. Biophys 2011, 507, 26–35. [PubMed: 21167809]

(193). Gober JG; Ghodge SV; Bogart JW; Wever WJ; Watkins RR; Brustad EM; Bowers AA P450-Mediated Non-Natural Cyclopropanation of Dehydroalanine-Containing Thiopeptides. ACS Chem. Biol 2017, 12, 1726–1731. [PubMed: 28535034]

(194). Wang ZJ; Renata H; Peck NE; Farwell CC; Coelho PS; Arnold FH Improved Cyclopropanation Activity of Histidine-Ligated Cytochrome P450 Enables the Enantioselective Formal Synthesis of Levomilnacipran. Angew. Chem., Int. Ed 2014, 53, 6810–6813.

(195). Brandenberg OF; Prier CK; Chen K; Knight AM; Wu Z; Arnold FH Stereoselective Enzymatic Synthesis of Heteroatom-Substituted Cyclopropanes. ACS Catal. 2018, 8, 2629–2634.

(196). Wang ZJ; Peck NE; Renata H; Arnold FH Cytochrome P450-Catalyzed Insertion of Carbenoids into N-H Bonds. Chem. Sci 2014, 5, 598–601. [PubMed: 24490022]

(197). Knight AM; Kan SBJ; Lewis RD; Brandenberg OF; Chen K; Arnold FH Diverse Engineered Heme Proteins Enable Stereodivergent Cyclopropanation of Unactivated Alkenes. ACS Cent. Sci 2018, 4, 372–377. [PubMed: 29632883]

(198). Brandenberg OF; Chen K; Arnold FH Directed Evolution of a Cytochrome P450 Carbene Transferase for Selective Functionalization of Cyclic Compounds. J. Am. Chem. Soc 2019, 141, 8989–8995. [PubMed: 31070908]

(199). Zhang RK; Chen K; Huang X; Wohlschlager L; Renata H; Arnold FH Enzymatic Assembly of Carbon-Carbon Bonds via Iron-Catalysed sp^3 C-H Functionalization. Nature 2019, 565, 67–72. [PubMed: 30568304]

(200). Zhang J; Huang X; Zhang RK; Arnold FH Enantiodivergent α-Amino C-H Fluoroalkylation Catalyzed by Engineered Cytochrome P450s. J. Am. Chem. Soc 2019, 141, 9798–9802. [PubMed: 31187993]

(201). Chen K; Huang X; Kan SBJ; Zhang RK; Arnold FH Enzymatic Construction of Highly Strained Carbocycles. Science 2018, 360, 71–75. [PubMed: 29622650]

(202). Chen K; Arnold FH Engineering Cytochrome P450s for Enantioselective Cyclopropenation of Internal Alkynes. J. Am. Chem. Soc 2020, 142, 6891–6895. [PubMed: 32223130]

(203). Chen K; Zhang S-Q; Brandenberg OF; Hong X; Arnold FH Alternate Heme Ligation Steers Activity and Selectivity in Engineered Cytochrome P450-Catalyzed Carbene-Transfer Reactions. J. Am. Chem. Soc 2018, 140, 16402–16407. [PubMed: 30372623]

(204). Zhou AZ; Chen K; Arnold FH Enzymatic Lactone-Carbene C-H Insertion to Build Contiguous Chiral Centers. ACS Catal. 2020, 10, 5393–5398.

(205). Hyster TK; Farwell CC; Buller AR; McIntosh JA; Arnold FH Enzyme-Controlled Nitrogen-Atom Transfer Enables Regiodivergent C-H Amination. J. Am. Chem. Soc 2014, 136, 15505–15508. [PubMed: 25325618]

(206). Singh R; Kolev JN; Sutera PA; Fasan R Enzymatic C(sp^3)-H Amination: P450-Catalyzed Conversion of Carbonazidates into Oxazolidinones. ACS Catal. 2015, 5, 1685–1691. [PubMed: 25954592]

(207). Farwell CC; McIntosh JA; Hyster TK; Wang ZJ; Arnold FH Enantioselective Imidation of Sulfides via Enzyme-Catalyzed Intermolecular Nitrogen-Atom Transfer. J. Am. Chem. Soc 2014, 136, 8766–8771. [PubMed: 24901646]

(208). Prier CK; Hyster TK; Farwell CC; Huang A; Arnold FH Asymmetric Enzymatic Synthesis of Allylic Amines: A Sigmatropic Rearrangement Strategy. Angew. Chem., Int. Ed 2016, 128, 4789–4793.

(209). Farwell CC; Zhang RK; McIntosh JA; Hyster TK; Arnold FH Enantioselective Enzyme-Catalyzed Aziridination Enabled by Active-Site Evolution of a Cytochrome P450. ACS Cent. Sci 2015, 1, 89–93. [PubMed: 26405689]

(210). Prier CK; Zhang RK; Buller AR; Brinkmann-Chen S; Arnold FH Enantioselective, Intermolecular Benzylic C-H Amination Catalysed by an Engineered Iron-Haem Enzyme. Nat. Chem 2017, 9, 629–634. [PubMed: 28644476]

(211). Brandenberg OF; Miller DC; Markel U; Ould Chaib A; Arnold FH Engineering Chemoselectivity in Hemoprotein-Catalyzed Indole Amidation. ACS Catal. 2019, 9, 8271–8275. [PubMed: 31938573]

(212). Jia Z-J; Gao S; Arnold FH Enzymatic Primary Amination of Benzylic and Allylic C(sp^3)-H Bonds. J. Am. Chem. Soc 2020, 142, 10279–10283. [PubMed: 32450692]

(213). Cho I; Prier CK; Jia Z-J; Zhang RK; Görbe T; Arnold FH Enantioselective Aminohydroxylation of Styrenyl Olefins Catalyzed by an Engineered Hemoprotein. Angew. Chem., Int. Ed 2019, 58, 3138–3142.

(214). Tsutsumi H; Katsuyama Y; Izumikawa M; Takagi M; Fujie M; Satoh N; Shin-ya K; Ohnishi Y Unprecedented Cyclization Catalyzed by a Cytochrome P450 in Benzastatin Biosynthesis. J. Am. Chem. Soc 2018, 140, 6631–6639. [PubMed: 29716187]

(215). Legnani L; Morandi B Direct Catalytic Synthesis of Unprotected 2-Amino-1-Phenylethanols from Alkenes by Using Iron(II) Phthalocyanine. Angew. Chem., Int. Ed 2016, 55, 2248–2251.

(216). Athavale SV; Gao S; Liu Z; Mallojjala SC; Hirschi JS; Arnold FH Biocatalytic, Intermolecular C-H Bond Functionalization for the Synthesis of Enantioenriched Amides. Angew. Chem., Int. Ed 2021, 60, 24864–24869.

(217). Renata H; Lewis RD; Sweredoski MJ; Moradian A; Hess S; Wang ZJ; Arnold FH Identification of Mechanism-Based Inactivation in P450-Catalyzed Cyclopropanation Facilitates Engineering of Improved Enzymes. J. Am. Chem. Soc 2016, 138, 12527–12533. [PubMed: 27573353]

(218). Brandenberg OF; Fasan R; Arnold FH Exploiting and Engineering Hemoproteins for Abiological Carbene and Nitrene Transfer Reactions. Curr. Opin. Biotechnol 2017, 47, 102–111. [PubMed: 28711855]

(219). Wan L; Twitchett MB; Eltis LD; Mauk AG; Smith M In Vitro Evolution of Horse Heart Myoglobin to Increase Peroxidase Activity. Proc. Natl. Acad. Sci. U.S.A 1998, 95, 12825–12831. [PubMed: 9788999]

(220). Chandgude AL; Ren X; Fasan R Stereodivergent Intramolecular Cyclopropanation Enabled by Engineered Carbene Transferases. J. Am. Chem. Soc 2019, 141, 9145–9150. [PubMed: 31099569]

(221). Ren X; Liu N; Chandgude AL; Fasan R An Enzymatic Platform for the Highly Enantioselective and Stereodivergent Construction of Cyclopropyl-δ-Lactones. Angew. Chem., Int. Ed 2020, 59, 21634–21639.

(222). Ren X; Chandgude AL; Fasan R Highly Stereoselective Synthesis of Fused Cyclopropane-γ-Lactams via Biocatalytic Iron-Catalyzed Intramolecular Cyclopropanation. ACS Catal. 2020, 10, 2308–2313. [PubMed: 32257580]

(223). Hernandez KE; Renata H; Lewis RD; Kan SBJ; Zhang C; Forte J; Rozzell D; McIntosh JA; Arnold FH Highly Stereoselective Biocatalytic Synthesis of Key Cyclopropane Inter-mediate to Ticagrelor. ACS Catal. 2016, 6, 7810–7813. [PubMed: 28286694]

(224). Moore EJ; Zorine D; Hansen WA; Khare SD; Fasan R Enzyme Stabilization via Computationally Guided Protein Stapling. Proc. Natl. Acad. Sci. U.S.A 2017, 114, 12472–12477. [PubMed: 29109284]

(225). Kan SBJ; Lewis RD; Chen K; Arnold FH Directed Evolution of Cytochrome *c* for Carbon-Silicon Bond Formation: Bringing Silicon to Life. Science 2016, 354, 1048–1051. [PubMed: 27885032]

(226). Lewis RD; Garcia-Borràs M; Chalkley MJ; Buller AR; Houk KN; Kan SBJ; Arnold FH Catalytic Iron-Carbene Intermediate Revealed in a Cytochrome *c* Carbene Transferase. Proc. Natl. Acad. Sci. U.S.A 2018, 115, 7308–7313. [PubMed: 29946033]

(227). Kan SBJ; Huang X; Gumulya Y; Chen K; Arnold FH Genetically Programmed Chiral Organoborane Synthesis. Nature 2017, 552, 132–136. [PubMed: 29186119]

(228). Chen K; Huang X; Zhang S-Q; Zhou AZ; Kan SBJ; Hong X; Arnold FH Engineered Cytochrome *c*-Catalyzed Lactone-Carbene B-H Insertion. Synlett. 2019, 30, 378–382. [PubMed: 30930550]

(229). Huang X; Garcia-Borràs M; Miao K; Kan SBJ; Zutshi A; Houk KN; Arnold FH A Biocatalytic Platform for Synthesis of Chiral α-Trifluoromethylated Organoborons. ACS Cent. Sci 2019, 5, 270–276. [PubMed: 30834315]

(230). Stelter M; Melo AMP; Pereira MM; Gomes CM; Hreggvidsson GO; Hjorleifsdottir S; Saraiva LM; Teixeira M; Archer M A Novel Type of Monoheme Cytochrome *c*: Biochemical and Structural Characterization at 1.23 Å Resolution of *Rhodothermus marinus* Cytochrome *c*. Biochemistry 2008, 47, 11953–11963. [PubMed: 18855424]

(231). Garcia-Borràs M; Kan SBJ; Lewis RD; Tang A; Jimenez-Osés G; Arnold FH; Houk KN Origin and Control of Chemoselectivity in Cytochrome *c* Catalyzed Carbene Transfer into Si-H and N-H Bonds. J. Am. Chem. Soc 2021, 143, 7114–7123. [PubMed: 33909977]

(232). Cech TR; Zaug AJ; Grabowski PJ *In Vitro* Splicing of the Ribosomal RNA Precursor of Tetrahymena: Involvement of a Guanosine Nucleotide in the Excision of the Intervening Sequence. Cell 1981, 27, 487–496. [PubMed: 6101203]

(233). Breaker RR; Joyce GF A DNA Enzyme That Cleaves RNA. Chem. Biol 1994, 1, 223–229. [PubMed: 9383394]

(234). Altman S The Road to RNase P. Nat. Struct. Biol 2000, 7, 827–828. [PubMed: 11017184]

(235). Li Y; Geyer R; Sen D Recognition of Anionic Porphyrins by DNA Aptamers. Biochemistry 1996, 35, 6911–6922. [PubMed: 8639643]

(236). Travascio P; Li Y; Sen D DNA-Enhanced Peroxidase Activity of a DNA Aptamer-Hemin Complex. Chem. Biol 1998, 5, 505–517. [PubMed: 9751647]

(237). Travascio P; Witting PK; Mauk AG; Sen D The Peroxidase Activity of a Hemin-DNA Oligonucleotide Complex: Free Radical Damage to Specific Guanine Bases of the DNA. J. Am. Chem. Soc 2001, 123, 1337–1348. [PubMed: 11456705]

(238). Mikuma T; Terui N; Yamamoto Y; Hori H A Novel Heme-DNA Coordination Complex and Its Stability. Nucleic Acids Symp. Ser 2002, 2, 285–286.

(239). Sen D; Gilbert W Formation of Parallel Four-Stranded Complexes by Guanine-Rich Motifs in DNA and Its Implications for Meiosis. Nature 1988, 334, 364–366. [PubMed: 3393228]

(240). Golub E; Freeman R; Willner I A Hemin/G-Quadruplex Acts as an NADDH Oxidase and NADH Peroxidase Mimicking DNAzyme. Angew. Chem., Int. Ed 2011, 50, 11710–11714.

(241). Ohyama T; Kato Y; Mita H; Nagatomo S; Yamamoto Y Structural and Functional Characterization of Novel G-Quadruplexed DNA-Heme Coordination Complex. Nucleic Acids Symp. Ser 2005, 49, 245–246.

(242). Saito K; Nakano Y; Tai H; Nagatomo S; Hemmi H; Mita H; Yamamoto Y Characterization of Heme Coordination Structure in Heme-DNA Complex Possessing Gaseous Molecule as an Exogenous Ligand. Nucleic Acids Symp. Ser 2009, 53, 241–242.

(243). Poon LC-H; Methot SP; Morabi-Pazooki W; Pio F; Bennet AJ; Sen D Guanine-Rich RNAs and DNAs That Bind Heme Robustly Catalyze Oxygen Transfer Reactions. J. Am. Chem. Soc 2011, 133, 1877–1884. [PubMed: 21265562]

(244). Pratviel G Porphyrins in Complex with DNA: Modes of Interaction and Oxidation Reactions. Coord. Chem. Rev 2016, 308, 460–477.

(245). Saito K; Tai H; Fukaya M; Shibata T; Nishimura R; Neya S; Yamamoto Y Structural Characterization of a Carbon Monoxide Adduct of a Heme-DNA Complex. JBIC, J. Biol. Inorg. Chem 2012, 17, 437–445. [PubMed: 22203450]

(246). Shibata T; Nakayama Y; Katahira Y; Tai H; Moritaka Y; Nakano Y; Yamamoto Y Characterization of the Interaction Between Heme and a Parallel G-Quadruplex DNA Formed from d(TTGAGG). Biochim. Biophys. Acta, General Subj 2017, 1861, 1264–1270.

(247). Yamamoto Y; Kinoshita M; Katahira Y; Shimizu H; Di Y; Shibata T; Tai H; Suzuki A; Neya S Characterization of Heme-DNA Complexes Composed of Some Chemically Modified Hemes and Parallel G-Quadruplex DNAs. Biochemistry 2015, 54, 7168–7177. [PubMed: 26595799]

(248). Shinomiya R; Katahira Y; Araki H; Shibata T; Momotake A; Yanagisawa S; Ogura T; Suzuki A; Neya S; Yamamoto Y Characterization of Catalytic Activities and Heme Coordination Structures of Heme-DNA Complexes Composed of Some Chemically Modified Hemes and an All Parallel-Stranded Tetrameric G-Quadruplex DNA Formed from d(TTAGGG). Biochemistry 2018, 57, 5930–5937. [PubMed: 30207701]

(249). Ibrahim H; Mulyk P; Sen D DNA G-Quadruplexes Activate Heme for Robust Catalysis of Carbene Transfer Reactions. ACS Omega 2019, 4, 15280–15288. [PubMed: 31552375]

(250). Miron CE; Staalduinen L; Rangaswamy AM; Chen M; Liang Y; Jia Z; Mergny J; Petitjean A Going Platinum to the Tune of a Remarkable Guanine Quadruplex Binder: Solution- and Solid-State Investigations. Angew. Chem., Int. Ed 2021, 60, 2500–2507.

(251). Feig AL; Lippard SJ Reactions of Non-Heme Iron(II) Centers with Dioxygen in Biology and Chemistry. Chem. Rev 1994, 94, 759–805.

(252). Wallar BJ; Lipscomb JD Dioxygen Activation by Enzymes Containing Binuclear Non-Heme Iron Clusters. Chem. Rev 1996, 96, 2625–2658. [PubMed: 11848839]

(253). Ferousi C; Majer SH; DiMucci IM; Lancaster KM Biological and Bioinspired Inorganic N-N Bond-Forming Reactions. Chem. Rev 2020, 120, 5252–5307. [PubMed: 32108471]

(254). Khatua S; Majumdar A Flavodiiron Nitric Oxide Reductases: Recent Developments in the Mechanistic Study and Model Chemistry for the Catalytic Reduction of NO. J. Inorg. Biochem 2015, 142, 145–153. [PubMed: 25458587]

(255). Gardner AM; Helmick RA; Gardner PR Flavorubredoxin, an Inducible Catalyst for Nitric Oxide Reduction and Detoxification in Escherichia Coli. J. Biol. Chem 2002, 277, 8172–8177. [PubMed: 11751865]

(256). Bulen WA; Burns RC; LeComte JR Nitrogen Fixation: Cell-Free System with Extracts of Azotobacter. Biochem. Biophys. Res. Commun 1964, 17, 265–271. [PubMed: 5862980]

(257). Hegg EL; Que L Jr. The 2-His-1-Carboxylate Facial Triadan Emerging Structural Motif in Mononuclear Non-Heme Iron(II) Enzymes. Eur. J. Biochem 1997, 250, 625–629. [PubMed: 9461283]

(258). Kal S; Que L Dioxygen Activation by Nonheme Iron Enzymes with the 2-His-1-Carboxylate Facial Triad That Generate High-Valent Oxoiron Oxidants. JBIC, J. Biol. Inorg. Chem 2017, 22, 339–365. [PubMed: 28074299]

(259). Que L; Ho RYN Dioxygen Activation by Enzymes with Mononuclear Non-Heme Iron Active Sites. Chem. Rev 1996, 96, 2607–2624. [PubMed: 11848838]

(260). Abu-Omar MM; Loaiza A; Hontzeas N Reaction Mechanisms of Mononuclear Non-Heme Iron Oxygenases. Chem. Rev 2005, 105, 2227–2252. [PubMed: 15941213]

(261). Tshuva EY; Lippard SJ Synthetic Models for Non-Heme Carboxylate-Bridged Diiron Metalloproteins: Strategies and Tactics. Chem. Rev 2004, 104, 987–1012. [PubMed: 14871147]

(262). Shima S; Pilak O; Vogt S; Schick M; Stagni MS; Meyer-Klaucke W; Warkentin E; Thauer RK; Ermler U The Crystal Structure of [Fe]-Hydrogenase Reveals the Geometry of the Active Site. Science 2008, 321, 572–575. [PubMed: 18653896]

(263). Berggren G; Adamska A; Lambertz C; Simmons TR; Esselborn J; Atta M; Gambarelli S; Mouesca J-M; Reijerse E; Lubitz W; Happe T; Artero V; Fontecave M Biomimetic Assembly and Activation of [FeFe]-Hydrogenases. Nature 2013, 499, 66–69. [PubMed: 23803769]

(264). Lancaster KM; Roemelt M; Ettenhuber P; Hu Y; Ribbe MW; Neese F; Bergmann U; DeBeer S X-Ray Emission Spectroscopy Evidences a Central Carbon in the Nitrogenase Iron-Molybdenum Cofactor. Science 2011, 334, 974–977. [PubMed: 22096198]

(265). Spatzal T; Aksoyoglu M; Zhang L; Andrade SLA; Schleicher E; Weber S; Rees DC; Einsle O Evidence for Interstitial Carbon in Nitrogenase FeMo Cofactor. Science 2011, 334, 940. [PubMed: 22096190]

(266). Sippel D; Einsle O The Structure of Vanadium Nitrogenase Reveals an Unusual Bridging Ligand. Nat. Chem. Biol 2017, 13, 956–960. [PubMed: 28692069]

(267). Dobbek H; Svetlitchnyi V; Gremer L; Huber R; Meyer O Crystal Structure of a Carbon Monoxide Dehydrogenase Reveals a [Ni-4Fe-5S] Cluster. Science 2001, 293, 1281–1285. [PubMed: 11509720]

(268). Pinto AL; Hellinga HW; Caradonna JP Construction ofa Catalytically Active Iron Superoxide Dismutase by Rational Protein Design. Proc. Natl. Acad. Sci. U.S.A 1997, 94, 5562–5567. [PubMed: 9159112]

(269). Katti SK; LeMaster DM; Eklund H Crystal Structure of Thioredoxin from *Escherichia coli* at 1.68 Å Resolution. J. Mol. Biol 1990, 212, 167–184. [PubMed: 2181145]

(270). McLaughlin MP; Retegan M; Bill E; Payne TM; Shafaat HS; Peña S; Sudhamsu J; Ensign AA; Crane BR; Neese F; Holland PL Azurin as a Protein Scaffold for a Low-Coordinate Nonheme Iron Site with a Small-Molecule Binding Pocket. J. Am. Chem. Soc 2012, 134, 19746–19757. [PubMed: 23167247]

(271). Liu J; Meier KK; Tian S; Zhang J; Guo H; Schulz CE; Robinson H; Nilges MJ; Münck E; Lu Y Redesigning the Blue Copper Azurin into a Redox-Active Mononuclear Nonheme Iron Protein: Preparation and Study of Fe(II)-M121E Azurin. J. Am. Chem. Soc 2014, 136, 12337–12344. [PubMed: 25082811]

(272). Lin S; He C Development ofNonheme $\{FeNO\}^7$ Complexes Based on the *Pyrococcus furiosus* Rubredoxin for Red-Light-Control-lable Nitric Oxide Release. Inorg. Chem 2021, 60, 14364–14370. [PubMed: 34503329]

(273). Beauchamp C; Fridovich I Superoxide Dismutase: Improved Assays and an Assay Applicable to Acrylamide Gels. Anal. Biochem 1971, 44, 276–287. [PubMed: 4943714]

(274). Tian S; Fan R; Albert T; Khade RL; Dai H; Harnden K ; Hosseinzadeh P; Liu J; Nilges MJ; Zhang Y; Moënne-Loccoz P; Guo Y; Lu Y Stepwise Nitrosylation of the Nonheme Iron Site in an Engineered Azurin and a Molecular Basis for Nitric Oxide Signaling Mediated by Nonheme Iron Proteins. Chem. Sci 2021, 12, 6569–6579. [PubMed: 34040732]

(275). Enemark JH; Feltham RD Principles of Structure, Bonding, and Reactivity for Metal Nitrosyl Complexes. Coord. Chem. Rev 1974, 13, 339–406.

(276). Tian S; Liu J; Cowley RE; Hosseinzadeh P; Marshall NM; Yu Y; Robinson H; Nilges MJ; Blackburn NJ; Solomon EI; et al. Reversible S-Nitrosylation in an Engineered Azurin. Nat. Chem 2016, 8, 670–677. [PubMed: 27325093]

(277). Kurihara K; Tanaka I; Chatake T; Adams MWW; Jenney FE; Moiseeva N; Bau R; Niimura N Neutron Crystallographic Study on Rubredoxin from Pyrococcus Furiosus by BIX-3, a Single-Crystal Diffractometer for Biomacromolecules. Proc. Natl. Acad. Sci. U.S.A 2004, 101, 11215–11220. [PubMed: 15272083]

(278). Cross M; Xiao Z; Maes EM; Czernuszewicz RS; Drew SC; Pilbrow JR; George GN; Wedd AG Removal of a Cysteine Ligand from Rubredoxin: Assembly of Fe_2S_2 and $Fe(S\text{-}Cys)_3(OH)$ Centres. JBIC, J. Biol. Inorg. Chem 2002, 7, 781–790. [PubMed: 12203014]

(279). Xie J; Liu W; Schultz PG A Genetically Encoded Bidentate, Metal-Binding Amino Acid. Angew. Chem., Int. Ed 2007, 46, 9239–9242.

(280). Lee HS; Schultz PG Biosynthesis of a Site-Specific DNA Cleaving Protein. J. Am. Chem. Soc 2008, 130, 13194–13195. [PubMed: 18788806]

(281). Schultz PG; Dervan PB Sequence-Specific Double-Strand Cleavage of DNA by Penta-N-Methylpyrrolecarboxamide-EDTA X Fe(II). Proc. Natl. Acad. Sci. U.S.A 1983, 80, 6834–6837. [PubMed: 6417654]

(282). Sluka JP; Horvath SJ; Bruist MF; Simon MI; Dervan PB Synthesis of a Sequence-Specific DNA-Cleaving Peptide. Science 1987, 238, 1129–1132. [PubMed: 3120311]

(283). Schultz SC; Shields GC; Steitz TA Crystal Structure of a CAP-DNA Complex: The DNA Is Bent by 90 Degrees. Science 1991, 253, 1001–1007. [PubMed: 1653449]

(284). Parkinson G; Wilson C; Gunasekera A; Ebright YW; Ebright RE; Berman HM Structure of the CAP-DNA Complex at 2.5 Å Resolution: A Complete Picture of the Protein-DNA Interface. J. Mol. Biol 1996, 260, 395–408. [PubMed: 8757802]

(285). Kang M; Light K; Ai H; Shen W; Kim CH; Chen PR; Lee HS; Solomon EI; Schultz PG Evolution of Iron(II)-Finger Peptides by Using a Bipyridyl Amino Acid. ChemBioChem 2014, 15, 822–825. [PubMed: 24591102]

(286). Ségaud N; Drienovská I; Chen J; Browne WR; Roelfes G Artificial Metalloproteins for Binding and Stabilization of a Semi-quinone Radical. Inorg. Chem 2017, 56, 13293–13299. [PubMed: 29027794]

(287). Madoori PK; Agustiandari H; Driessen AJM; Thunnissen A-MWH Structure of the Transcriptional Regulator LmrR and Its Mechanism of Multidrug Recognition. EMBO J. 2009, 28, 156–166. [PubMed: 19096365]

(288). Pavletich NP; Pabo CO Zinc Finger-DNA Recognition: Crystal Structure of a Zif268-DNA Complex at 2.1 Å. Science 1991, 252, 809–817. [PubMed: 2028256]

(289). Mills JH; Khare SD; Bolduc JM; Forouhar F; Mulligan VK; Lew S; Seetharaman J; Tong L; Stoddard BL; Baker D Computational Design of an Unnatural Amino Acid Dependent Metalloprotein with Atomic Level Accuracy. J. Am. Chem. Soc 2013, 135, 13393–13399. [PubMed: 23924187]

(290). Kuhlman B; Baker D Native Protein Sequences Are Close to Optimal for Their Structures. Proc. Natl. Acad. Sci. U.S.A 2000, 97, 10383–10388. [PubMed: 10984534]

(291). Zanghellini A; Jiang L; Wollacott AM; Cheng G; Meiler J; Althoff EA; Röthlisberger D; Baker D New Algorithms and an *In Silico* Benchmark for Computational Enzyme Design. Protein Sci. 2006, 15, 2785–2794. [PubMed: 17132862]

(292). Davies RR; Distefano MD A Semisynthetic Metalloenzyme Based on a Protein Cavity That Catalyzes the Enantioselective Hydrolysis of Ester and Amide Substrates. J. Am. Chem. Soc 1997, 119, 11643–11652.

(293). Ory JJ; Mazhary A; Kuang H; Davies RR; Distefano MD; Banaszak LJ Structural Characterization of Two Synthetic Catalysts Based on Adipocyte Lipid-Binding Protein. Protein Eng. Des. Sel 1998, 11, 253–261.

(294). Davies RR; Kuang H; Qi D; Mazhary A; Mayaan E; Distefano MD Artificial Metalloenzymes Based on Protein Cavities: Exploring the Effect ofAltering the Metal Ligand Attachment Position by Site Directed Mutagenesis. Bioorg. Med. Chem. Lett 1999, 9, 79–84. [PubMed: 9990461]

(295). Qi D; Kuang H; Distefano MD Effects of Metal Ions on the Rates and Enantioselectivities of Reactions Catalyzed by a Series of Semisynthetic Transaminases Created by Site Directed Mutagenesis. Bioorg. Med. Chem. Lett 1998, 8, 875–880. [PubMed: 9871558]

(296). Buron C; Sénéchal-David K; Ricoux R; Le Caër J-P; Guérineau V; Méjanelle P; Guillot R; Herrero C; Mahy J-P; Banse F An Artificial Enzyme Made by Covalent Grafting of an Fe^{II} Complex into β-Lactoglobulin: Molecular Chemistry, Oxidation Catalysis, and Reaction-Intermediate Monitoring in a Protein. Chem. Eur. J 2015, 21, 12188–12193. [PubMed: 26178593]

(297). Loch JI; Bonarek P; Polit A; Świątek S; Dziedzicka-Wasylewska M; Lewiński K The Differences in Binding 12-Carbon Aliphatic Ligands by Bovine β-Lactoglobulin Isoform A and B Studied by Isothermal Titration Calorimetry and X-Ray Crystallography. J. Mol. Recog 2013, 26, 357–367.

(298). Doble MV; Obrecht L; Joosten H-J; Lee M; Rozeboom HJ; Branigan E; Naismith JH; Janssen DB; Jarvis AG; et al. Engineering Thermostability in Artificial Metalloenzymes to Increase Catalytic Activity. ACS Catal. 2021, 11, 3620–3627.

(299). Doble MV; Jarvis AG; Ward ACC; Colburn JD; Gotze JP; Buhl M; Kamer PCJ Artificial Metalloenzymes as Catalysts for Oxidative Lignin Degradation. ACS Sustainable Chem. Eng 2018, 6, 15100–15107.

(300). Ducros V; Charnock SJ; Derewenda U; Derewenda ZS; Dauter Z; Dupont C; Shareck F; Morosoli R; Kluepfel D; Davies GJ Substrate Specificity in Glycoside Hydrolase Family 10. Structural and Kinetic Analysis of the *Streptomyces Lividans* Xylanase 10A. J. Biol. Chem 2000, 275, 23020–23026. [PubMed: 10930426]

(301). Kariyawasam K; Ghattas W; De Los Santos YL; Doucet N; Gaillard S; Renaud J-L; Avenier F; Mahy J-P; Ricoux R Artificial Iron Hydrogenase Made by Covalent Grafting of Knölker's Complex into Xylanase: Application in Asymmetric Hydrogenation of an Aryl Ketone in Water. Biotechnol. Appl. Biochem 2020, 67, 563–573. [PubMed: 32134142]

(302). Cavazza C; Bochot C; Rousselot-Pailley P; Carpentier P; Cherrier MV; Martin L; Marchi-Delapierre C; Fontecilla-Camps JC; Menage S Crystallographic Snapshots of the Reaction of Aromatic C-H with O_2 Catalysed by a Protein-Bound Iron Complex. Nat. Chem 2010, 2, 1069–1076. [PubMed: 21107372]

(303). de Pina K; Navarro C; McWalter L; Boxer DH; Price NC; Kelly SM; Mandrand-Berthelot MA; Wu LF Purification and Characterization of the Periplasmic Nickel-Binding Protein NikA of *Escherichia Coli* K12. Eur. J. Biochem 1995, 227, 857–865. [PubMed: 7867647]

(304). Cherrier MV; Martin L; Cavazza C; Jacquamet L; Lemaire D; Gaillard J; Fontecilla-Camps JC Crystallographic and Spectroscopic Evidence for High Affinity Binding of FeEDTA(H2O)$^{-}$ to the Periplasmic Nickel Transporter NikA. J. Am. Chem. Soc 2005, 127, 10075–10082. [PubMed: 16011372]

(305). Lopez S; Rondot L; Leprêtre C; Marchi-Delapierre C; Ménage S; Cavazza C Cross-Linked Artificial Enzyme Crystals as Heterogeneous Catalysts for Oxidation Reactions. J. Am. Chem. Soc 2017, 139, 17994–18002. [PubMed: 29148757]

(306). Rondot L; Girgenti E; Oddon F; Marchi-Delapierre C; Jorge-Robin A; Ménage S Catalysis without a Headache: Modification of Ibuprofen for the Design of Artificial Metalloenzyme for Sulfide Oxidation. J. Mol. Cat. A: Chem 2016, 416, 20–28.

(307). Ghuman J; Zunszain PA; Petitpas I; Bhattacharya AA; Otagiri M; Curry S Structural Basis of the Drug-Binding Specificity of Human Serum Albumin. J. Mol. Biol 2005, 353, 38–52. [PubMed: 16169013]

(308). Cherrier MV; Girgenti E; Amara P; Iannello M; Marchi-Delapierre C; Fontecilla-Camps JC; Ménage S; Cavazza C The Structure of the Periplasmic Nickel-Binding Protein NikA Provides Insights for Artificial Metalloenzyme Design. JBIC, J. Biol. Inorg. Chem 2012, 17, 817–829. [PubMed: 22526565]

(309). Esmieu C; Cherrier MV; Amara P; Girgenti E; Marchi-Delapierre C; Oddon F; Iannello M; Jorge-Robin A; Cavazza C; Ménage S An Artificial Oxygenase Built from Scratch: Substrate Binding Site Identified Using a Docking Approach. Angew. Chem., Int. Ed 2013, 52, 3922–3925.

(310). Lopez S; Marchi-Delapierre C; Cavazza C; Ménage S A Selective Sulfide Oxidation Catalyzed by Heterogeneous Artificial Metalloenzymes Iron@NikA. Chem. Eur. J 2020, 26, 16633–16638. [PubMed: 33079395]

(311). Mérel DS; Gaillard S; Ward TR; Renaud J-L Achiral Cyclopentadienone Iron Tricarbonyl Complexes Embedded in Streptavidin: An Access to Artificial Iron Hydrogenases and Application in Asymmetric Hydrogenation. Catal. Lett 2016, 146, 564–569.

(312). Serrano-Plana J; Rumo C; Rebelein JG; Peterson RL; Barnet M; Ward TR Enantioselective Hydroxylation of Benzylic C(sp^3)-H Bonds by an Artificial Iron Hydroxylase Based on the Biotin-Streptavidin Technology. J. Am. Chem. Soc 2020, 142, 10617–10623. [PubMed: 32450689]

(313). Miller KR; Paretsky JD; Follmer AH; Heinisch T; Mittra K; Gul S; Kim I-S; Fuller FD; Batyuk A; Sutherlin KD; et al. Artificial Iron Proteins: Modeling the Active Sites in Non-Heme Dioxygenases. Inorg. Chem 2020, 59, 6000–6009. [PubMed: 32309932]

(314). Betz SF; Liebman PA; DeGrado WF De Novo Design of Native Proteins: Characterization of Proteins Intended To Fold into Antiparallel, Rop-like, Four-Helix Bundles. Biochemistry 1997, 36, 2450–2458. [PubMed: 9054549]

(315). Kaplan J; DeGrado WF De Novo Design of Catalytic Proteins. Proc. Natl. Acad. Sci. U.S.A 2004, 101, 11566–11570. [PubMed: 15292507]

(316). Faiella M; Andreozzi C; de Rosales RTM; Pavone V; Maglio O; Nastri F; DeGrado WF; Lombardi A An Artificial Di-Iron Oxo-Protein with Phenol Oxidase Activity. Nat. Chem. Biol 2009, 5, 882–884. [PubMed: 19915535]

(317). Miller KR; Biswas S; Jasniewski A; Follmer AH; Biswas A; Albert T; Sabuncu S; Bominaar EL; Hendrich MP; Moënne-Loccoz P; et al. Artificial Metalloproteins with Dinuclear Iron-Hydroxido Centers. J. Am. Chem. Soc 2021, 143, 2384–2393. [PubMed: 33528256]

(318). Que L Metalloproteins with Phenolate Coordination. Coord. Chem. Rev 1983, 50, 73–108.

(319). Jones AK; Lichtenstein BR; Dutta A; Gordon G; Dutton PL Synthetic Hydrogenases: Incorporation of an Iron Carbonyl Thiolate into a Designed Peptide. J. Am. Chem. Soc 2007, 129, 14844–14845. [PubMed: 17997557]

(320). Sano Y; Onoda A; Hayashi T A Hydrogenase Model System Based on the Sequence of Cytochrome *c*: Photochemical Hydrogen Evolution in Aqueous Media. Chem. Commun 2011, 47, 8229–8231.

(321). Sano Y; Onoda A; Hayashi T Photocatalytic Hydrogen Evolution by a Diiron Hydrogenase Model Based on a Peptide Fragment of Cytochrome c_{556} with an Attached Diiron Carbonyl Cluster and an Attached Ruthenium Photosensitizer. J. Inorg. Biochem 2012, 108, 159–162. [PubMed: 22420928]

(322). Roy A; Madden C; Ghirlanda G Photo-Induced Hydrogen Production in a Helical Peptide Incorporating a [FeFe] Hydrogenase Active Site Mimic. Chem. Commun 2012, 48, 9816–9818.

(323). Esmieu C; Guo M; Redman HJ; Lundberg M; Berggren G Synthesis of a Miniaturized [FeFe] Hydrogenase Model System. Dalton Trans. 2019, 48, 2280–2284. [PubMed: 30667428]

(324). Onoda A; Kihara Y; Fukumoto K; Sano Y; Hayashi T Photoinduced Hydrogen Evolution Catalyzed by a Synthetic Diiron Dithiolate Complex Embedded within a Protein Matrix. ACS Catal. 2014, 4, 2645–2648.

(325). Roy A; Vaughn MD; Tomlin J; Booher GJ; Kodis G; Simmons CR; Allen JP; Ghirlanda G Enhanced Photocatalytic Hydrogen Production by Hybrid Streptavidin-Diiron Catalysts. Chemistry 2020, 26, 6240–6246. [PubMed: 32201996]

(326). Solomon EI; Heppner DE; Johnston EM; Ginsbach JW; Cirera J; Qayyum M; Kieber-Emmons MT; Kjaergaard CH; Hadt RG; Tian L Copper Active Sites in Biology. Chem. Rev 2014, 114, 3659–3853. [PubMed: 24588098]

(327). Oka T; Simpson FJ Quercetinase, a Dioxygenase Containing Copper. Biochem. Biophys. Res. Commun 1971, 43, 1–5. [PubMed: 5579942]

(328). Crabbe MJ; Waight RD; Bardsley WG; Barker RW; Kelly ID; Knowles PF Human Placental Diamine Oxidase. Improved Purification and Characterization of a Copper- and Manganese-Containing Amine Oxidase with Novel Substrate Specificity. Biochem. J 1976, 155, 679–687. [PubMed: 182134]

(329). Kosman DJ; Ettinger MJ; Weiner RE; Massaro EJ The Molecular Properties of the Copper Enzyme Galactose Oxidase. Arch. Biochem. Biophys 1974, 165, 456–467. [PubMed: 4441089]

(330). Makino N; McMahill P; Mason HS; Moss TH The Oxidation State of Copper in Resting Tyrosinase. J. Biol. Chem 1974, 249, 6062–6066. [PubMed: 4371447]

(331). Beinert H Copper A of Cytochrome *c* Oxidase, A Novel, Long-Embattled, Biological Electron-Transfer Site. Eur. J. Biochem 1997, 245, 521–532. [PubMed: 9182986]

(332). Malmström BG; Vänngård T Electron Spin Resonance of Copper Proteins and Some Model Complexes. J. Mol. Biol 1960, 2, 118–124.

(333). Rorabacher DB Electron Transfer by Copper Centers. Chem. Rev 2004, 104, 651–698. [PubMed: 14871138]

(334). Solomon EI; Randall DW; Glaser T Electronic Structures of Active Sites in Electron Transfer Metalloproteins: Contributions to Reactivity. Coord. Chem. Rev 2000, 200–202, 595–632.

(335). Dennison C Investigating the Structure and Function of Cupredoxins. Coord. Chem. Rev 2005, 249, 3025–3054.

(336). Gray HB; Malmström BG; Williams RJP Copper Coordination in Blue Proteins. JBIC, J. Biol. Inorg. Chem 2000, 5, 551–559. [PubMed: 11085645]

(337). Malmström BG; Aasa R The Nature of the CuA Center in Cytochrome c Oxidase. FEBS Lett. 1993, 325, 49–52. [PubMed: 8390373]

(338). Savelieff MG; Lu Y CuA Centers and Their Biosynthetic Models in Azurin. JBIC, J. Biol. Inorg. Chem 2010, 15, 461–483. [PubMed: 20169379]

(339). Wikström M Cytochrome *c* Oxidase: 25 Years of the Elusive Proton Pump. Biochim. Biophys. Acta, Bioenerg 2004, 1655, 241–247.

(340). Brown K; Tegoni M; Prudêncio M; Pereira AS; Besson S; Moura JJ; Moura I; Cambillau C A Novel Type of Catalytic Copper Cluster in Nitrous Oxide Reductase. Nat. Struct. Biol 2000, 7, 191–195. [PubMed: 10700275]

(341). Suharti; Strampraad MJF; Schröder I; de Vries S A Novel Copper A Containing Menaquinol NO Reductase from *Bacillus azotoformans*. Biochemistry 2001, 40, 2632–2639. [PubMed: 11327887]

(342). Bertagnolli H; Kaim W The Dinuclear CuA Center in Cytochrome *c* Oxidase and N_2O Reductase–A Metal-Metal Bond in Biology? Angew. Chem, Int. Ed. Engl 1995, 34, 771–773.

(343). Fisher OS; Kenney GE; Ross MO; Ro SY; Lemma BE; Batelu S; Thomas PM; Sosnowski VC; DeHart CJ; Kelleher NL; et al. Characterization of a Long Overlooked Copper Protein from Methane- and Ammonia-Oxidizing Bacteria. Nat. Commun 2018, 9, 4276. [PubMed: 30323281]

(344). Ross MO; Fisher OS; Morgada MN; Krzyaniak MD; Wasielewski MR; Vila AJ; Hoffman BM; Rosenzweig AC Formation and Electronic Structure of an Atypical Cu_A Site. J. Am. Chem. Soc 2019, 141, 4678–4686. [PubMed: 30807125]

(345). Nar H; Messerschmidt A; Huber R; van de Kamp M; Canters GW Crystal Structure Analysis of Oxidized *Pseudomonas aeruginosa* Azurin atpH 5·5 andpH 9·0: ApH-Induced Conformational Transition Involves a Peptide Bond Flip. J. Mol. Biol 1991, 221, 765–772. [PubMed: 1942029]

(346). Williams PA; Blackburn NJ; Sanders D; Bellamy H; Stura EA; Fee JA; McRee DE The CuA Domain of *Thermus thermophilus* Ba3-Type Cytochrome *c* Oxidase at 1.6 Å Resolution. Nat. Struct. Bio 1999, 6, 509–516. [PubMed: 10360350]

(347). Hakulinen N; Kiiskinen L-L; Kruus K; Saloheimo M; Paananen A; Koivula A; Rouvinen J Crystal Structure of a Laccase from *Melanocarpus albomyces* with an Intact Trinuclear Copper Site. Nat. Struct. Mol. Biol 2002, 9, 601–605.

(348). Leferink NGH; Han C; Antonyuk SV; Heyes DJ; Rigby SEJ; Hough MA; Eady RR; Scrutton NS; Hasnain SS Proton-Coupled Electron Transfer in the Catalytic Cycle of *Alcaligenes xylosoxidans* Copper-Dependent Nitrite Reductase. Biochemistry 2011, 50, 4121–4131. [PubMed: 21469743]

(349). Pomowski A; Zumft WG; Kroneck PMH; Einsle O N_2O Binding at a [4Cu:2S] Copper-Sulphur Cluster in Nitrous Oxide Reductase. Nature 2011, 477, 234–237. [PubMed: 21841804]

(350). McGuirl MA; Dooley DM Copper Proteins with Type 2 Sites. In Encyclopedia of Inorganic Chemistry; King RB, Crabtree RH, Lukehart CM, Atwood DA, Scott RA, Eds.; John Wiley & Sons, Ltd: Chichester, UK, 2006; pp 294.

(351). Godden JW; Turley S; Teller DC; ADMAr ET; Liu MY; Payne WJ; Legall J The 2.3 Angstrom X-Ray Structure of Nitrite Reductase from Achromobacter cycloclastes. Science 1991, 253, 438–442. [PubMed: 1862344]

(352). Tavares P; Pereira AS; Moura JJG; Moura I Metalloenzymes of the Denitrification Pathway. J. Inorg. Biochem 2006, 100, 2087–2100. [PubMed: 17070915]

(353). Sheng Y; Abreu IA; Cabelli DE; Maroney MJ; Miller A-F; Teixeira M; Valentine JS Superoxide Dismutases and Superoxide Reductases. Chem. Rev 2014, 114, 3854–3918. [PubMed: 24684599]

(354). Solomon EI; Sundaram UM; Machonkin TE Multicopper Oxidases and Oxygenases. Chem. Rev 1996, 96, 2563–2606. [PubMed: 11848837]

(355). Solomon EI; Chen P; Metz M; Lee S-K; Palmer AE Oxygen Binding, Activation, and Reduction to Water by Copper Proteins. Angew. Chem, Int. Ed 2001, 40, 4570–4590.

(356). Solomon EI; Ginsbach JW; Heppner DE; Kieber-Emmons MT; Kjaergaard CH; Smeets PJ; Tian L; Woertink JS Copper Dioxygen (Bio)Inorganic Chemistry. Faraday Discuss. 2011, 148, 11–39. [PubMed: 21322475]

(357). Hemsworth GR; Johnston EM; Davies GJ; Walton PH Lytic Polysaccharide Monooxygenases in Biomass Conversion. Trends Biotechnol. 2015, 33, 747–761. [PubMed: 26472212]

(358). Ciano L; Davies GJ; Tolman WB; Walton PH Bracing Copper for the Catalytic Oxidation of C-H Bonds. Nat. Catal 2018, 1, 571–577.

(359). Riva S Laccases: Blue Enzymes for Green Chemistry. Trends Biotechnol. 2006, 24, 219–226. [PubMed: 16574262]

(360). Giardina P; Faraco V; Pezzella C; Piscitelli A; Vanhulle S; Sannia G Laccases: A Never-Ending Story. Cell. Mol. Life Sci 2010, 67, 369–385. [PubMed: 19844659]

(361). Monnier F; Taillefer M Catalytic C-C, C-N, and C-O Ullmann-Type Coupling Reactions. Angew. Chem., Int. Ed 2009, 48, 6954–6971.

(362). Alexakis A; Bäckvall JE; Krause N; Pàmies O; Diéguez M Enantioselective Copper-Catalyzed Conjugate Addition and Allylic Substitution Reactions. Chem. Rev 2008, 108, 2796–2823. [PubMed: 18671436]

(363). Wendlandt AE; Suess AM; Stahl SS Copper-Catalyzed Aerobic Oxidative C-H Functionalizations: Trends and Mechanistic Insights. Angew. Chem., Int. Ed 2011, 50, 11062–11087.

(364). Allen SE; Walvoord RR; Padilla-Salinas R; Kozlowski MC Aerobic Copper-Catalyzed Organic Reactions. Chem. Rev 2013, 113, 6234–6458. [PubMed: 23786461]

(365). Guo X-X; Gu D-W; Wu Z; Zhang W Copper-Catalyzed C-H Functionalization Reactions: Efficient Synthesis of Heterocycles. Chem. Rev 2015, 115, 1622–1651. [PubMed: 25531056]

(366). Trammell R; Rajabimoghadam K; Garcia-Bosch I Copper-Promoted Functionalization of Organic Molecules: From Biologically Relevant Cu/O_2 Model Systems to Organometallic Transformations. Chem. Rev 2019, 119, 2954–3031. [PubMed: 30698952]

(367). Bos J; Fusetti F; Driessen AJM; Roelfes G Enantioselective Artificial Metalloenzymes by Creation of a Novel Active Site at the Protein Dimer Interface. Angew. Chem., Int. Ed 2012, 51, 7472–7475.

(368). Bos J; Browne WR; Driessen AJM; Roelfes G Supramolecular Assembly of Artificial Metalloenzymes Based on the Dimeric Protein LmrR as Promiscuous Scaffold. J. Am. Chem. Soc 2015, 137, 9796–9799. [PubMed: 26214343]

(369). Coquière D; Bos J; Beld J; Roelfes G Enantioselective Artificial Metalloenzymes Based on a Bovine Pancreatic Polypeptide Scaffold. Angew. Chem, Int. Ed 2009, 48, 5159–5162.

(370). Renggli K; Nussbaumer MG; Urbani R; Pfohl T; Bruns N A Chaperonin as Protein Nanoreactor for Atom-Transfer Radical Polymerization. Angew. Chem., Int. Ed 2014, 53, 1443–1447.

(371). Magnus KA; Hazes B; Ton-That H; Bonaventura C; Bonaventura J; Hol WGJ Crystallographic Analysis of Oxygenated and Deoxygenated States of Arthropod Hemocyanin Shows Unusual Differences. Proteins 1994, 19, 302–309. [PubMed: 7984626]

(372). Volbeda A; Hol WGJ Crystal Structure of Hexameric Haeqocyanin from *Panulirus interruptus* Refined at 3.2 Å Resolution. J. Mol. Biol 1989, 209, 249–279. [PubMed: 2585484]

(373). Matoba Y; Kumagai T; Yamamoto A; Yoshitsu H; Sugiyama M Crystallographic Evidence That the Dinuclear Copper Center of Tyrosinase Is Flexible during Catalysis. J. Biol. Chem 2006, 281, 8981–8990. [PubMed: 16436386]

(374). Solomon EI; Szilagyi RK; DeBeer George S; Basumallick L Electronic Structures of Metal Sites in Proteins and Models: Contributions to Function in Blue Copper Proteins. Chem. Rev 2004, 104, 419–458. [PubMed: 14871131]

(375). Farver O; Lu Y; Ang MC; Pecht I Enhanced Rate of Intramolecular Electron Transfer in an Engineered Purple Cu_A Azurin. Proc. Natl. Acad. Sci. U.S.A 1999, 96, 899–902. [PubMed: 9927665]

(376). Wilson TD; Yu Y; Lu Y Understanding Copper-Thiolate Containing Electron Transfer Centers by Incorporation of Unnatural Amino Acids and the Cu_A Center into the Type 1 Copper Protein Azurin. Coord. Chem. Rev 2013, 257, 260–276.

(377). Marshall NM; Garner DK; Wilson TD; Gao Y-G; Robinson H; Nilges MJ; Lu Y Rationally Tuning the Reduction Potential of a Single Cupredoxin beyond the Natural Range. Nature 2009, 462, 113–116. [PubMed: 19890331]

(378). Solomon EI; Hadt RG Recent Advances in Understanding Blue Copper Proteins. Coord. Chem. Rev 2011, 255, 774–789.

(379). Liu J; Chakraborty S; Hosseinzadeh P; Yu Y; Tian S; Petrik I; Bhagi A; Lu Y Metalloproteins Containing Cytochrome, Iron-Sulfur, or Copper Redox Centers. Chem. Rev 2014, 114, 4366–4469. [PubMed: 24758379]

(380). Mirts EN; Bhagi-Damodaran A; Lu Y Understanding and Modulating Metalloenzymes with Unnatural Amino Acids, Non-Native Metal Ions, and Non-Native Metallocofactors. Acc. Chem. Res 2019, 52, 935–944. [PubMed: 30912643]

(381). Petrik ID; Liu J; Lu Y Metalloenzyme Design and Engineering through Strategic Modifications of Native Protein Scaffolds. Curr. Opin. Chem. Biol 2014, 19, 67–75. [PubMed: 24513641]

(382). Nersissian AM; Valentine JS; Immoos C; Hill MG; Hart PJ; Williams G; Herrmann RG Uclacyanins, Stellacyanins, and Plantacyanins Are Distinct Subfamilies of Phytocyanins: Plant-Specific Mononuclear Blue Copper Proteins. Protein Sci. 1998, 7, 1915–1929. [PubMed: 9761472]

(383). Lappin AG; Lewis CA; Ingledew WJ Kinetics and Mechanisms of Reduction of Rusticyanin, a Blue Copper Protein from *Thiobacillus ferrooxidans*, by Inorganic Cations. Inorg. Chem 1985, 24, 1446–1450.

(384). Xu F; Palmer AE; Yaver DS; Berka RM; Gambetta GA; Brown SH; Solomon EI Targeted Mutations in a *Trametes villosa* Laccase. J. Biol. Chem 1999, 274, 12372–12375. [PubMed: 10212209]

(385). Hosseinzadeh P; Lu Y Design and Fine-Tuning Redox Potentials of Metalloproteins Involved in Electron Transfer in Bioenergetics. Biochim. Biophys. Acta, Bioenerg 2016, 1857, 557–581.

(386). Karlsson BG; Nordling M; Pascher T; Tsai L-C; Sjolin L; Lundberg LG Cassette Mutagenesis of Met121 in Azurin from *Pseudomonas aeruginosa*. Protein Eng. 1991, 4, 343–349. [PubMed: 1649999]

(387). Kroes SJ; Hoitink CWG; Andrew CR; Ai J; Sanders-Loehr J; Messerschmidt A; Hagen WR; Canters GW The Mutation Met121His Creates a Type-1.5 Copper Site in *Alcaligenes denitrificans* Azurin. Eur. J. Biochem 1996, 240, 342–351. [PubMed: 8841397]

(388). Pascher T; Karlsson BG; Nordling M; Malmstrom BG; Vanngard T Reduction Potentials and Their pH Dependence in Site-Directed-Mutant Forms of Azurin from *Pseudomonas aeruginosa*. Eur. J. Biochem 1993, 212, 289–296. [PubMed: 8383044]

(389). Karlsson BG; Aasa R; Malmström BG; Lundberg LG Rack-Induced Bonding in Blue Copper Proteins: Spectroscopic Properties and Reduction Potential of the Azurin Mutant Met-121 → Leu. FEBS Lett 1989, 253, 99–102.

(390). Murphy LM; Strange RW; Karlsson BG; Lundberg LG; Pascher T; Reinhammar B; Hasnain SS Structural Characterization of Azurin from *Pseudomonas aeruginosa* and Some of Its Methionine-121 Mutants. Biochemistry 1993, 32, 1965–1975. [PubMed: 8383530]

(391). Garner DK; Vaughan MD; Hwang HJ; Savelieff MG; Berry SM; Honek JF; Lu Y Reduction Potential Tuning of the Blue Copper Center in *Pseudomonas aeruginosa* Azurin by the Axial Methionine as Probed by Unnatural Amino Acids. J. Am. Chem. Soc 2006, 128, 15608. [PubMed: 17147368]

(392). Berry SM; Baker MH; Reardon NJ Reduction Potential Variations in Azurin through Secondary Coordination Sphere Phenylalanine Incorporations. J. Inorg. Biochem 2010, 104, 1071–1078. [PubMed: 20615551]

(393). Farver O; Marshall NM; Wherland S; Lu Y; Pecht I Designed Azurins Show Lower Reorganization Free Energies for Intraprotein Electron Transfer. Proc. Natl. Acad. Sci. U.S.A 2013, 110, 10536–10540. [PubMed: 23759745]

(394). Farver O; Hosseinzadeh P; Marshall NM; Wherland S; Lu Y; Pecht I Long-Range Electron Transfer in Engineered Azurins Exhibits Marcus Inverted Region Behavior. J. Phys. Chem. Lett 2015, 6, 100–105. [PubMed: 26263097]

(395). Shiga D; Nakane D; Inomata T; Funahashi Y; Masuda H; Kikuchi A; Oda M; Noda M; Uchiyama S; Fukui K; et al. Creation of a Type 1 Blue Copper Site within a de Novo Coiled-Coil Protein Scaffold. J. Am. Chem. Soc 2010, 132, 18191–18198. [PubMed: 21126081]

(396). Koebke KJ; Ruckthong L; Meagher JL; Mathieu E; Harland J; Deb A; Lehnert N; Policar C; Tard C; Penner-Hahn J; et al. Clarifying the Copper Coordination Environment in a *De Novo* Designed Red Copper Protein. Inorg. Chem 2018, 57, 12291–12302. [PubMed: 30226758]

(397). Lovejoy B; Choe S; Cascio D; McRorie DK; DeGrado WC; Eisenberg D Crystal Structure of a Synthetic Triple-Stranded Ac-Helical Bundle. Science 1993, 259, 1288–1293. [PubMed: 8446897]

(398). Woolfson DN A Brief History of De Novo Protein Design: Minimal, Rational, and Computational. J. Mol. Biol 2021, 433, 167160. [PubMed: 34298061]

(399). Schnepf R; Horth P; Bill E; Wieghardt K; Hildebrandt P; Haehnel W *De Novo* Design and Characterization of Copper Centers in Synthetic Four-Helix-Bundle Proteins. J.Am. Chem. Soc 2001, 123, 2186–2195. [PubMed: 11456864]

(400). Schnepf R; Haehnel W; Wieghardt K; Hildebrandt P Spectroscopic Identification of Different Types of Copper Centers Generated in Synthetic Four-Helix Bundle Proteins. J. Am. Chem. Soc 2004, 126, 14389–14399. [PubMed: 15521758]

(401). Shiga D; Hamano Y; Kamei M; Funahashi Y; Masuda H; Sakaguchi M; Ogura T; Tanaka T Tuning the Geometries of a De Novo Blue Copper Protein by Axial Interactions. JBIC, J. Biol. Inorg. Chem 2012, 17, 1025–1031. [PubMed: 22752182]

(402). Plegaria JS; Duca M; Tard C; Friedlander TJ; Deb A; Penner-Hahn JE; Pecoraro VL De Novo Design and Characterization of Copper Metallopeptides Inspired by Native Cupredoxins. Inorg. Chem 2015, 54, 9470–9482. [PubMed: 26381361]

(403). Plegaria JS; Herrero C; Quaranta A; Pecoraro VL Electron Transfer Activity of a De Novo Designed Copper Center in a Three-Helix Bundle Fold. Biochim. Biophys. Acta, Bioenerg 2016, 1857, 522–530.

(404). Koebke KJ; Alfaro VS; Pinter TBJ; Deb A; Lehnert N; Tard C; Penner-Hahn JE; Pecoraro VL Traversing the Red-Green-Blue Color Spectrum in Rationally Designed Cupredoxins. J. Am. Chem. Soc 2020, 142, 15282–15294. [PubMed: 32786767]

(405). Enguita FJ; Martins LO; Henriques AO; Carrondo MA Crystal Structure of a Bacterial Endospore Coat Component: A Laccase with Enhanced Thermostability Properties. J. Biol. Chem 2003, 278, 19416–19425. [PubMed: 12637519]

(406). Pettersen EF; Goddard TD; Huang CC; Couch GS; Greenblatt DM; Meng EC; Ferrin TE UCSF Chimera-a Visualization System for Exploratory Research and Analysis. J. Comput. Chem 2004, 25, 1605–1612. [PubMed: 15264254]

(407). Akter M; Tokiwa T; Shoji M; Nishikawa K; Shigeta Y; Sakurai T; Higuchi Y; Kataoka K; Shibata N Redox Potential-Dependent Formation of an Unusual His-Trp Bond in Bilirubin Oxidase. Chem. Eur. J 2018, 24, 18052–18058. [PubMed: 30156345]

(408). Roberts SA; Weichsel A; Grass G; Thakali K; Hazzard JT; Tollin G; Rensing C; Montfort WR Crystal Structure and Electron Transfer Kinetics of CueO, a Multicopper Oxidase Required for Copper Homeostasis in Escherichia coli. Proc. Natl. Acad. Sci. U.S.A 2002, 99, 2766. [PubMed: 11867755]

(409). Kajikawa T; Kataoka K; Sakurai T Modifications on the Hydrogen Bond Network by Mutations of *Escherichia coli* Copper Efflux Oxidase Affect the Process of Proton Transfer to Dioxygen Leading to Alterations of Enzymatic Activities. Biochem. Biophy. Res. Comm 2012, 422, 152–156.

(410). Sakurai T; Kataoka K Structure and Function of Type I Copper in Multicopper Oxidases. Cell. Mol. Life Sci 2007, 64, 2642–2656. [PubMed: 17639274]

(411). Jones SM; Solomon EI Electron Transfer and Reaction Mechanism of Laccases. Cell. Mol. Life Sci 2015, 72, 869–883. [PubMed: 25572295]

(412). Vilbert AC; Liu Y; Dai H; Lu Y Recent Advances in Tuning Redox Properties of Electron Transfer Centers in Metal-loenzymes Catalyzing the Oxygen Reduction Reaction and H_2 Oxidation Important for Fuel Cell Design. Curr. Opin. Electrochem 2021, 30, 100780. [PubMed: 34435160]

(413). Pardo I; Camarero S Laccase Engineering by Rational and Evolutionary Design. Cell. Mol. Life Sci 2015, 72, 897–910. [PubMed: 25586560]

(414). Durão P; Bento I; Fernandes AT; Melo EP; Lindley P; Martins LO Perturbations of the T1 Copper Site in the CotA Laccase from *Bacillus subtilis*: Structural, Biochemical, Enzymatic and Stability Studies. J. Biol. Inorg. Chem 2006, 11, 514–526. [PubMed: 16680453]

(415). Kamitaka Y; Tsujimura S; Kataoka K; Sakurai T; Ikeda T; Kano K Effects of Axial Ligand Mutation of the Type I Copper Site in Bilirubin Oxidase on Direct Electron Transfer-Type Bioelectrocatalytic Reduction of Dioxygen. J. Electroanal. Chem 2007, 601, 119–124.

(416). Kataoka K; Hirota S; Maeda Y; Kogi H; Shinohara N; Sekimoto M; Sakurai T Enhancement ofLaccase Activity through the Construction and Breakdown of a Hydrogen Bond at the Type I Copper Center in *Escherichia coli* CueO and the Deletion Mutant Δα5—7 CueO. Biochemistry 2011, 50, 558–565. [PubMed: 21142169]

(417). Kataoka K; Kogi H; Tsujimura S; Sakurai T Modifications of Laccase Activities of Copper Efflux Oxidase, CueO by Synergistic Mutations in the First and Second Coordination Spheres of the Type I Copper Center. Biochem. Biophys. Res. Commun 2013, 431, 393–397. [PubMed: 23337502]

(418). Sekretaryova A; Jones SM; Solomon EI O_2 Reduction to Water by High Potential Multicopper Oxidases: Contributions of the T1 Copper Site Potential and the Local Environment of the Trinuclear Copper Cluster. J. Am. Chem. Soc 2019, 141, 11304–11314. [PubMed: 31260290]

(419). Sato K; Firbank SJ; Li C; Banfield MJ; Dennison C The Importance of the Long Type 1 Copper-Binding Loop of Nitrite Reductase for Structure and Function. Chem. Eur. J 2008, 14, 5820–5828. [PubMed: 18491346]

(420). Hough MA; Ellis MJ; Antonyuk S; Strange RW; Sawers G; Eady RR; Samar Hasnain S High Resolution Structural Studies of Mutants Provide Insights into Catalysis and Electron Transfer Processes in Copper Nitrite Reductase. J. Mol. Biol 2005, 350, 300–309. [PubMed: 15927201]

(421). Ellis MJ; Prudâncio M; Dodd FE; Strange RW; Sawers G; Eady RR; Hasnain SS Biochemical and Crystallographic Studies of the Met144Ala, Asp92Asn and His254Phe Mutants of the Nitrite Reductase from *Alcaligenes xylosoxidans* Provide Insight into the Enzyme Mechanism. J. Mol. Biol 2002, 316, 51–64. [PubMed: 11829502]

(422). Zumft WG Cell Biology and Molecular Basis of Denitrification. Microbiol. Mol. Biol. Rev 1997, 61, 533–616. [PubMed: 9409151]

(423). Horrell S; Kekilli D; Strange RW; Hough MA Recent Structural Insights into the Function of Copper Nitrite Reductases. Metallomics 2017, 9, 1470–1482. [PubMed: 28702572]

(424). Pinho D; Besson S; Brondino CD; de Castro B; Moura I Copper-Containing Nitrite Reductase from *Pseudomonas chlororaphis* DSM 50135. Evidence for Modulation of the Rate of Intramolecular Electron Transfer through Nitrite Binding to the Type 2 Copper Center. Eur. J. Biochem 2004, 271, 2361–2369. [PubMed: 15182351]

(425). Hunsicker-Wang LM; Pacoma RL; Chen Y; Fee JA; Stout CD A Novel Cryoprotection Scheme for Enhancing the Diffraction of Crystals of Recombinant Cytochrome Ba3 Oxidase from *Thermus thermophilus*. Acta Cryst. D 2005, 61, 340–343. [PubMed: 15735345]

(426). Robinson H; Ang MC; Gao Y-G; Hay MT; Lu Y; Wang AH-J Structural Basis of Electron Transfer Modulation in the Purple CuA Center. Biochemistry 1999, 38, 5677–5683. [PubMed: 10231517]

(427). Zitare UA; Szuster J; Santalla MC; Llases ME; Morgada MN; Vila AJ; Murgida DH Fine Tuning of Functional Features of the Cu_A Site by Loop-Directed Mutagenesis. Inorg. Chem 2019, 58, 2149–2157. [PubMed: 30644741]

(428). Leguto AJ; Smith MA; Morgada MN; Zitare UA; Murgida DH; Lancaster KM; Vila AJ Dramatic Electronic Perturbations of Cu_A Centers via Subtle Geometric Changes. J. Am. Chem. Soc 2019, 141, 1373–1381. [PubMed: 30582893]

(429). Zickermann V; Verkhovsky M; Morgan J; Wikstrom M; Anemuller S; Bill E; Steffens GCM; Ludwig B Perturbation ofthe CuA Site in Cytochrome *c* Oxidase of *Paracoccus denitrificans* by Replacement of Met227 with Isoleucine. Eur. J. Biochem 1995, 234, 686–693. [PubMed: 8536720]

(430). Zhen Y; Schmidt B; Kang UG; Antholine W; Ferguson-Miller S Mutants of the Cu_A Site in Cytochrome *c* Oxidase of *Rhodobacter Sphaeroides* : I. Spectral and Functional Properties. Biochemistry 2002, 41, 2288–2297. [PubMed: 11841221]

(431). Wang K; Geren L; Zhen Y; Ma L; Ferguson-Miller S; Durham B; Millett F Mutants of the Cu_A Site in Cytochrome *c* Oxidase of *Rhodobacter Sphaeroides* : II. Rapid Kinetic Analysis of Electron Transfer. Biochemistry 2002, 41, 2298–2304. [PubMed: 11841222]

(432). Slutter CE; Gromov I; Richards JH; Pecht I; Goldfarb D Mutations of the Weak Axial Ligand in the Thermus Cu_A Center Modulates Its Electronic Structure. J. Am. Chem. Soc 1999, 121, 5077–5078.

(433). Slutter CE; Gromov I; Epel B; Pecht I; Richards JH; Goldfarb D Pulsed EPR/ENDOR Characterization of Perturbations of the Cu_A Center Ground State by Axial Methionine Ligand Mutations. J. Am. Chem. Soc 2001, 123, 5325–5336. [PubMed: 11457396]

(434). Ledesma GN; Murgida DH; Ly HK; Wackerbarth H; Ulstrup J; Costa-Filho AJ; Vila AJ The Met Axial Ligand Determines the Redox Potential in CuA Sites. J. Am. Chem. Soc 2007, 129, 11884–11885. [PubMed: 17845037]

(435). Blackburn NJ; Ralle M; Gomez E; Hill MG; Pastuszyn A; Sanders D; Fee JA Selenomethionine-Substituted *Thermus thermophilus* Cytochrome Ba3: Characterization of the Cu_A Site by Se and Cu K-EXAFS. Biochemistry 1999, 38, 7075–7084. [PubMed: 10353818]

(436). Dennison C; Vijgenboom E; de Vries S; van der Oost J; Canters GW Introduction of a Cu_A Site into the Blue Copper Protein Amicyanin from *Thiobacillus versutus*. FEBS Lett. 1995, 365, 92–94. [PubMed: 7774723]

(437). Andrew CR; Lappalainen P; Saraste M; Hay MT; Lu Y; Dennison C; Canters GW; Fee JA; Nakamura N; Sanders-Loehr J Engineered Cupredoxins and Bacterial Cytochrome c Oxidases Have Similar Cu_A Sites: Evidence from Resonance Raman Spectroscopy. J. Am. Chem. Soc 1995, 117, 10759–10760.

(438). Hay M; Richards JH; Lu Y Construction and Characterization of an Azurin Analog for the Purple Copper Site in Cytochrome *c* Oxidase. Proc. Natl. Acad. Sci. U.S.A 1996, 93, 461–464. [PubMed: 8552661]

(439). Hwang HJ; Ang MC; Lu Y Determination of Reduction Potential of an Engineered Cu_A Azurin by Cyclic Voltammetry and Spectrochemical Titrations. JBIC, J. Biol. Inorg. Chem 2004, 9, 489. [PubMed: 15127249]

(440). Hwang HJ; Berry SM; Nilges MJ; Lu Y Axial Methionine Has Much Less Influence on Reduction Potentials in a Cu_A Center than in a Blue Copper Center. J. Am. Chem. Soc 2005, 127, 7274–7275. [PubMed: 15898751]

(441). New SY; Marshall NM; Hor TSA; Xue F; Lu Y Redox Tuning of Two Biological Copper Centers through Non-Covalent Interactions: Same Trend but Different Magnitude. Chem. Commun 2012, 48, 4217.

(442). Tsai M-L; Hadt RG; Marshall NM; Wilson TD; Lu Y; Solomon EI Axial Interactions in the Mixed-Valent Cu_A Active Site and Role of the Axial Methionine in Electron Transfer. Proc. Natl. Acad. Sci. U. S. A 2013, 110, 14658–14663. [PubMed: 23964128]

(443). Morgada MN; Abriata LA; Zitare U; Alvarez-Paggi D; Murgida DH; Vila AJ Control of the Electronic Ground State on an Electron-Transfer Copper Site by Second-Sphere Perturbations. Angew. Chem., Int. Ed 2014, 126, 6302–6306.

(444). Morgada MN; Llases M-E; Giannini E; Castro M-A; Alzari PM; Murgida DH; Lisa M-N; Vila AJ Unexpected Electron Spin Density on the Axial Methionine Ligand in Cu_A Suggests Its Involvement in Electron Pathways. Chem. Commun 2020, 56, 1223–1226.

(445). Shiga D; Funahashi Y; Masuda H; Kikuchi A; Noda M; Uchiyama S; Fukui K; Kanaori K; Tajima K; Takano Y; et al. Creation of a Binuclear Purple Copper Site within a *De Novo* Coiled-Coil Protein. Biochemistry 2012, 51, 7901–7907. [PubMed: 22989113]

(446). Mirts EN; Dikanov SA; Jose A; Solomon EI; Lu Y A Binuclear CuA Center Designed in an All α-Helical Protein Scaffold. J. Am. Chem. Soc 2020, 142, 13779–13794. [PubMed: 32662996]

(447). Peacock AF Incorporating Metals into de Novo Proteins. Curr. Opin. Chem. Biol 2013, 17, 934–939. [PubMed: 24183813]

(448). Rink WM; Thomas F De Novo Designed α-Helical Coiled-Coil Peptides as Scaffolds for Chemical Reactions. Chem. Eur. J 2019, 25, 1665–1677. [PubMed: 30091482]

(449). Boyle AL; Rabe M; Crone NSA; Rhys GG; Soler N; Voskamp P; Pannu NS; Kros A Selective Coordination of Three Transition Metal Ions within a Coiled-Coil Peptide Scaffold. Chem. Sci 2019, 10, 7456–7465. [PubMed: 31489168]

(450). Koebke KJ; Pecoraro VL Development of De Novo Copper Nitrite Reductases: Where We Are and Where We Need To Go. ACS Catal. 2018, 8, 8046–8057. [PubMed: 30294504]

(451). Fujieda N; Hasegawa A; Ishihama K; Itoh S Artificial Dicopper Oxidase: Rational Reprogramming of Bacterial Metallo-β-Lactamase into a Catechol Oxidase. Chem. Asian J 2012, 7, 1203–1207. [PubMed: 22431417]

(452). Mathieu E; Tolbert AE; Koebke KJ; Tard C; Iranzo O; Penner-Hahn JE; Policar C; Pecoraro V Rational De Novo Design of a Cu Metalloenzyme for Superoxide Dismutation. Chem. Eur. J 2020, 26, 249–258. [PubMed: 31710732]

(453). Tegoni M; Yu F; Bersellini M; Penner-Hahn JE; Pecoraro VL Designing a Functional Type 2 Copper Center That Has Nitrite Reductase Activity within α-Helical Coiled Coils. Proc. Natl. Acad. Sci. U.S.A 2012, 109, 21234–21239. [PubMed: 23236170]

(454). Yu F; Penner-Hahn JE; Pecoraro VL De Novo-Designed Metallopeptides with Type 2 Copper Centers: Modulation of Reduction Potentials and Nitrite Reductase Activities. J. Am. Chem. Soc 2013, 135, 18096–18107. [PubMed: 24182361]

(455). Koebke KJ; Yu F; Salerno E; Van Stappen C; Tebo AG; Penner-Hahn JE; Pecoraro VL Modifying the Steric Properties in the Second Coordination Sphere of Designed Peptides Leads to Enhancement of Nitrite Reductase Activity. Angew. Chem., Int. Ed 2018, 57, 3954–3957.

(456). Mitra S; Prakash D; Rajabimoghadam K; Wawrzak Z; Prasad P; Wu T; Misra SK; Sharp JS; Garcia-Bosch I; Chakraborty S De Novo Design of a Self-Assembled Artificial Copper Peptide That Activates and Reduces Peroxide. ACS Catal. 2021, 11, 10267–10278. [PubMed: 36188417]

(457). Berry SM; Strange JN; Bladholm EL; Khatiwada B; Hedstrom CG; Sauer AM Nitrite Reductase Activity in Engineered Azurin Variants. Inorg. Chem 2016, 55, 4233–4247. [PubMed: 27055058]

(458). Lancaster KM; George SD; Yokoyama K; Richards JH; Gray HB Type-Zero Copper Proteins. Nat. Chem 2009, 1, 711–715. [PubMed: 20305734]

(459). Lancaster KM; Sproules S; Palmer JH; Richards JH; Gray HB Outer-Sphere Effects on Reduction Potentials of Copper Sites in Proteins: The Curious Case of High Potential Type 2

C112D/M121E Pseudomonas aeruginosa Azurin. J. Am. Chem. Soc 2010, 132, 14590–14595. [PubMed: 20879734]

(460). Mizoguchi TJ; Di Bilio AJ; Gray HB; Richards JH Blue to Type 2 Binding. Copper(II) and Cobalt(II) Derivatives of a Cys112Asp Mutant of Pseudomonas aeruginosa Azurin. J. Am. Chem. Soc 1992, 114, 10076–10078.

(461). Faham S; Mizoguchi TJ; Adman ET; Gray HB; Richards JH; Rees DC Role of the Active-Site Cysteine of *Pseudomonas aeruginosa* Azurin. Crystal Structure Analysis of the CuII(Cys112Asp) Protein. JBIC, J. Biol. Inorg. Chem 1997, 2, 464–469.

(462). Rosenzweig AC Zeroing in on a New Copper Site. Nat. Chem 2009, 1, 684–685. [PubMed: 21124349]

(463). Sieracki NA; Tian S; Hadt RG; Zhang J-L; Woertink JS; Nilges MJ; Sun F; Solomon EI; Lu Y Copper-Sulfenate Complex from Oxidation of a Cavity Mutant of *Pseudomonas aeruginosa* Azurin. Proc. Natl. Acad. Sci. U.S.A 2014, 111, 924–929. [PubMed: 24390543]

(464). Fujieda N; Schätti J; Stuttfeld E; Ohkubo K; Maier T; Fukuzumi S; Ward TR Enzyme Repurposing of a Hydrolase as an Emergent Peroxidase upon Metal Binding. Chem. Sci 2015, 6, 4060–4065. [PubMed: 29218172]

(465). Mann SI; Heinisch T; Ward TR; Borovik AS Peroxide Activation Regulated by Hydrogen Bonds within Artificial Cu Proteins. J. Am. Chem. Soc 2017, 139, 17289–17292. [PubMed: 29117678]

(466). Mann SI; Heinisch T; Weitz AC; Hendrich MP; Ward TR; Borovik AS Modular Artificial Cupredoxins. J. Am. Chem. Soc 2016, 138, 9073–9076. [PubMed: 27385206]

(467). Vaaje-Kolstad G; Westereng B; Horn SJ; Liu Z; Zhai H; Sørlie M; Eijsink VGH An Oxidative Enzyme Boosting the Enzymatic Conversion of Recalcitrant Polysaccharides. Science 2010, 330, 219–222. [PubMed: 20929773]

(468). Bissaro B; Røhr ÅK; Müller G; Chylenski P; Skaugen M; Forsberg Z; Horn SJ; Vaaje-Kolstad G; Eijsink VGH Oxidative Cleavage of Polysaccharides by Monocopper Enzymes Depends on H_2O_2. Nat. Chem. Biol 2017, 13, 1123–1128. [PubMed: 28846668]

(469). Wang B; Johnston EM; Li P; Shaik S; Davies GJ; Walton PH; Rovira C QM/MM Studies into the H_2O_2-Dependent Activity of Lytic Polysaccharide Monooxygenases: Evidence for the Formation of a Caged Hydroxyl Radical Intermediate. ACS Catal. 2018, 8, 1346–1351.

(470). Brantley RE; Smerdon SJ; Wilkinson AJ; Singleton EW; Olson JS The Mechanism of Autooxidation of Myoglobin. J. Biol. Chem 1993, 268, 6995–7010. [PubMed: 8463233]

(471). Rufo CM; Moroz YS; Moroz OV; Stöhr J; Smith TA; Hu X; DeGrado WF; Korendovych IV Short Peptides Self-Assemble to Produce Catalytic Amyloids. Nat. Chem 2014, 6, 303–309. [PubMed: 24651196]

(472). Makhlynets OV; Gosavi PM; Korendovych IV Short Self-Assembling Peptides Are Able to Bind to Copper and Activate Oxygen. Angew. Chem., Int. Ed 2016, 55, 9017–9020.

(473). Lengyel Z; Rufo CM; Moroz YS; Makhlynets OV; Korendovych IV Copper-Containing Catalytic Amyloids Promote Phosphoester Hydrolysis and Tandem Reactions. ACS Catal. 2018, 8, 59–62. [PubMed: 30319881]

(474). Yamamura K; Kaiser ET Studies on the Oxidase Activity of Copper(II) Carboxypeptidase A. J. Chem. Soc., Chem. Commun 1976, 20, 830–831.

(475). Wilson ME; Whitesides GM Conversion of a Protein to a Homogeneous Asymmetric Hydrogenation Catalyst by Site-Specific Modification with a Diphosphinerhodium(I) Moiety. J. Am. Chem. Soc 1978, 100, 306–307.

(476). Yu F; Cangelosi VM; Zastrow ML; Tegoni M; Plegaria JS; Tebo AG; Mocny CS; Ruckthong L; Qayyum H; Pecoraro VL Protein Design: Toward Functional Metalloenzymes. Chem. Rev 2014, 114, 3495–3578. [PubMed: 24661096]

(477). Podtetenieff J; Taglieber A; Bill E; Reijerse EJ; Reetz MT An Artificial Metalloenzyme: Creation of a Designed Copper Binding Site in a Thermostable Protein. Angew. Chem., Int. Ed 2010, 49, 5151–5155.

(478). Ghattas W; Dubosclard V; Tachon S; Beaumet M; Guillot R; Réglier M; Simaan AJ; Mahy J-P CuII-Containing 1-Aminocyclopropane Carboxylic Acid Oxidase Is an Efficient Stereo-specific Diels-Alderase. Angew. Chem., Int. Ed 2019, 58, 14605–14609.

(479). Fischer J; Renn D; Quitterer F; Radhakrishnan A; Liu M; Makki A; Ghorpade S; Rueping M; Arold ST; Groll M; et al. Robust and Versatile Host Protein for the Design and Evaluation of Artificial Metal Centers. ACS Catal. 2019, 9, 11371–11380.

(480). Rosati F; Roelfes G A Ligand Structure-Activity Study of DNA-Based Catalytic Asymmetric Hydration and Diels-Alder Reactions. ChemCatChem 2011, 3, 973–977.

(481). Di Meo T; Ghattas W; Herrero C; Velours C; Minard P; Mahy J-P; Ricoux R; Urvoas A ARep A3: A Versatile Artificial Scaffold for Metalloenzyme Design. Chem. Eur. J 2017, 23, 10156–10166. [PubMed: 28543753]

(482). Ghattas W; Cotchico-Alonso L; Maréchal J-D; Urvoas A; Rousseau M; Mahy J-P; Ricoux R Artificial Metalloenzymes with the Neocarzinostatin Scaffold: Toward a Biocatalyst for the Diels-Alder Reaction. ChemBioChem 2016, 17, 433–440. [PubMed: 26677011]

(483). Osseili H; Sauer DF; Beckerle K; Arlt M; Himiyama T; Polen T; Onoda A; Schwaneberg U; Hayashi T; Okuda J Artificial Diels-Alderase Based on the Transmembrane Protein FhuA. Beilstein J. Org. Chem 2016, 12, 1314–1321. [PubMed: 27559380]

(484). Himiyama T; Sauer DF; Onoda A; Spaniol TP; Okuda J; Hayashi T Construction of a Hybrid Biocatalyst Containing a Covalently-Linked Terpyridine Metal Complex within a Cavity of Aponitrobindin. J. Inorg. Biochem 2016, 158, 55–61. [PubMed: 26786596]

(485). Ghattas W; Dubosclard V; Wick A; Bendelac A; Guillot R; Ricoux R; Mahy J-P Receptor-Based Artificial Metalloenzymes on Living Human Cells. J. Am. Chem. Soc 2018, 140, 8756–8762. [PubMed: 29909636]

(486). Reymond S; Cossy J Copper-Catalyzed Diels-Alder Reactions. Chem. Rev 2008, 108, 5359–5406. [PubMed: 18942879]

(487). Reetz MT; Jiao N Copper-Phthalocyanine Conjugates of Serum Albumins as Enantioselective Catalysts in Diels-Alder Reactions. Angew. Chem., Int. Ed 2006, 45, 2416–2419.

(488). Boersma AJ; Feringa BL; Roelfes G α,β-Unsaturated 2-Acyl Imidazoles as a Practical Class of Dienophiles for the DNA-Based Catalytic Asymmetric Diels-Alder Reaction in Water. Org. Lett 2007, 9, 3647–3650. [PubMed: 17685624]

(489). Roelfes G LmrR: A Privileged Scaffold for Artificial Metalloenzymes. Acc. Chem. Res 2019, 52, 545–556. [PubMed: 30794372]

(490). Drienovská I; Rioz-Martínez A; Draksharapu A; Roelfes G Novel Artificial Metalloenzymes by *In Vivo* Incorporation of Metal-Binding Unnatural Amino Acids. Chem. Sci 2015, 6, 770–776. [PubMed: 28936318]

(491). Basler S; Studer S; Zou Y; Mori T; Ota Y; Camus A; Bunzel HA; Helgeson RC; Houk KN; Jiménez-Osés G; et al. Efficient Lewis Acid Catalysis of an Abiological Reaction in a de Novo Protein Scaffold. Nat. Chem 2021, 13, 231–235. [PubMed: 33526894]

(492). Villarino L; Chordia S; Alonso-Cotchico L; Reddem E; Zhou Z; Thunnissen AMWH; Maréchal J-D; Roelfes G Cofactor Binding Dynamics Influence the Catalytic Activity and Selectivity of an Artificial Metalloenzyme. ACS Catal. 2020, 10, 11783–11790. [PubMed: 33101759]

(493). Gutiérrez de Souza C; Bersellini M; Roelfes G Artificial Metalloenzymes Based on TetR Proteins and Cu(II) for Enantiose-lective Friedel-Crafts Alkylation Reactions. ChemCatChem 2020, 12, 3190–3194. [PubMed: 32612714]

(494). Chordia S; Narasimhan S; Lucini Paioni A; Baldus M; Roelfes G *In Vivo* Assembly of Artificial Metalloenzymes and Application in Whole-Cell Biocatalysis. Angew. Chem., Int. Ed 2021, 60, 5913–5920.

(495). Zhou Z; Roelfes G Synergistic Catalysis in an Artificial Enzyme by Simultaneous Action of Two Abiological Catalytic Sites. Nat. Catal 2020, 3, 289–294.

(496). Fujieda N; Ichihashi H; Yuasa M; Nishikawa Y; Kurisu G; Itoh S Cupin Variants as a Macromolecular Ligand Library for Stereoselective Michael Addition of Nitroalkanes. Angew. Chem., Int. Ed 2020, 59, 7717–7720.

(497). Rimoldi I; Bucci R; Feni L; Santagostini L; Facchetti G; Pellegrino S Exploring the Copper Binding Ability of Mets7 HCtr-1 Protein Domain and His7 Derivative: An Insight in Michael Addition Catalysis. J. Pept. Sci 2021, 27, No. e3289. [PubMed: 33094563]

(498). Bos J; García-Herraiz A; Roelfes G An Enantioselective Artificial Metallo-Hydratase. Chem. Sci 2013, 4, 3578.

(499). Drienovská I; Alonso-Cotchico L; Vidossich P; Lledós A; Maréchal J-D; Roelfes G Design of an Enantioselective Artificial Metallo-Hydratase Enzyme Containing an Unnatural Metal-Binding Amino Acid. Chem. Sci 2017, 8, 7228–7235. [PubMed: 29081955]

(500). Renggli K; Sauter N; Rother M; Nussbaumer MG; Urbani R; Pfohl T; Bruns N Biocatalytic Atom Transfer Radical Polymerization in a Protein Cage Nanoreactor. Polym. Chem 2017, 8, 2133–2136.

(501). Gold MH; Wariishi H; Valli K Extracellular Peroxidases Involved in Lignin Degradation by the White Rot Basidiomycete Phanerochaete Chrysosporium. In Biocatalysis in Agricultural Biotechnology; ACS Symposium Series, Vol. 389; American Chemical Society, 1989; pp 127–140.

(502). Pereira MM; Santana M; Teixeira M A Novel Scenario for the Evolution of Haem-Copper Oxygen Reductases. Biochim. Biophys. Acta (BBA) - Bioenergetics 2001, 1505, 185–208. [PubMed: 11334784]

(503). Wasser IM; de Vries S; Moënne-Loccoz P; Schröder I; Karlin KD Nitric Oxide in Biological Denitrification: Fe/Cu Metalloenzyme and Metal Complex NO_X Redox Chemistry. Chem. Rev 2002, 102, 1201–1234. [PubMed: 11942794]

(504). Rabus R; Venceslau SS; Wöhlbrand L; Voordouw G; Wall JD; Pereira IAC A Post-Genomic View of the Ecophysiology, Catabolism and Biotechnological Relevance of Sulphate-Reducing Prokaryotes. In Advances in Microbial Physiology, Vol. 66; Poole RK, Ed.; Academic Press, 2015; Chapter 2, pp 55–321. [PubMed: 26210106]

(505). Reed CJ; Lam QN; Mirts EN; Lu Y Molecular Understanding of Heteronuclear Active Sites in Heme-Copper Oxidases, Nitric Oxide Reductases, and Sulfite Reductases through Biomimetic Modelling. Chem. Soc. Rev 2021, 50, 2486–2539. [PubMed: 33475096]

(506). Nastri F; Chino M; Maglio O; Bhagi-Damodaran A; Lu Y; Lombardi A Design and Engineering of Artificial Oxygen-Activating Metalloenzymes. Chem. Soc. Rev 2016, 45, 5020–5054. [PubMed: 27341693]

(507). Schiltz CJ; Lee A; Partlow EA; Hosford CJ; Chappie JS Structural Characterization of Class 2 OLD Family Nucleases Supports a Two-Metal Catalysis Mechanism for Cleavage. Nucleic Acids Res. 2019, 47, 9448–9463. [PubMed: 31400118]

(508). Luo J; Du K-J; Yuan H; Wei C-W; Lang J-J; Wen G-B; Wang Y-H; Lin Y-W Rational Design of an Artificial Nuclease by Engineering a Hetero-Dinuclear Center of Mg-Heme in Myoglobin. ACS Catal. 2020, 10, 14359–14365.

(509). Yeung BKS; Wang X; Sigman JA; Petillo PA; Lu Y Construction and Characterization of a Manganese-Binding Site in Cytochrome *c* Peroxidase: Towards a Novel Manganese Peroxidase. Chem. Biol 1997, 4, 215–221. [PubMed: 9115415]

(510). Gengenbach A; Syn S; Wang X; Lu Y Redesign of Cytochrome c Peroxidase into a Manganese Peroxidase: Role of Tryptophans in Peroxidase Activity. Biochemistry 1999, 38, 11425–11432. [PubMed: 10471293]

(511). Gengenbach A; Wang X; Lu Y Designing a Manganese Peroxidase. In Oxidative Delignification Chemistry: Fundamentals and Catalysis; ACS Symposium Series, Vol. 785; American Chemical Society, 2001; Chapter 31, pp 487–500.

(512). Feng M; Tachikawa H; Wang X; Pfister TD; Gengenbach AJ; Lu Y Resonance Raman Spectroscopy of Cytochrome *c* Peroxidase Variants That Mimic Manganese Peroxidase. JBIC, J. Biol. Inorg. Chem 2003, 8, 699–706. [PubMed: 14505074]

(513). Sundaramoorthy M; Kishi K; Gold MH; Poulos TL Preliminary Crystallographic Analysis of Manganese Peroxidase from Phanerochaete Chrysosporium. J. Mol. Biol 1994, 238, 845–848. [PubMed: 8182752]

(514). Pfister TD; Mirarefi AY; Gengenbach AJ; Zhao X; Danstrom C; Conatser N; Gao Y-G; Robinson H; Zukoski CF; Wang AH-J; Lu Y Kinetic and Crystallographic Studies of a Redesigned Manganese-Binding Site in Cytochrome *c* Peroxidase. JBIC, J. Biol. Inorg. Chem 2006, 12, 126. [PubMed: 17021923]

(515). Hosseinzadeh P; Mirts EN; Pfister TD; Gao Y-G; Mayne C; Robinson H; Tajkhorshid E; Lu Y Enhancing Mn(II)-Binding and Manganese Peroxidase Activity in a Designed Cytochrome

c Peroxidase through Fine-Tuning Secondary-Sphere Interactions. Biochemistry 2016, 55, 1494–1502. [PubMed: 26885726]

(516). Tiefenbrunn T; Liu W; Chen Y; Katritch V; Stout CD; Fee JA; Cherezov V High Resolution Structure of the Ba3 Cytochrome *c* Oxidase from *Thermus thermophilus* in a Lipidic Environment. PLOS ONE 2011, 6, No. e22348. [PubMed: 21814577]

(517). Miner KD; Mukherjee A; Gao Y-G; Null EL; Petrik ID; Zhao X; Yeung N; Robinson H; Lu Y A Designed Functional Metalloenzyme That Reduces O_2 to H_2O with Over One Thousand Turnovers. Angew. Chem., Int. Ed 2012, 51, 5589–5592.

(518). Sigman JA; Kwok BC; Lu Y From Myoglobin to Heme-Copper Oxidase: Design and Engineering of a Cu_B Center into Sperm Whale Myoglobin. J. Am. Chem. Soc 2000, 122, 8192–8196.

(519). Sigman JA; Kim HK; Zhao X; Carey JR; Lu Y The Role of Copper and Protons in Heme-Copper Oxidases: Kinetic Study of an Engineered Heme-Copper Center in Myoglobin. Proc. Natl. Acad. Sci. U.S.A 2003, 100, 3629–3634. [PubMed: 12655052]

(520). Kaila VRI; Verkhovsky MI; Wikström M Proton-Coupled Electron Transfer in Cytochrome Oxidase. Chem. Rev 2010, 110, 7062–7081. [PubMed: 21053971]

(521). Yu Y; Mukherjee A; Nilges MJ; Hosseinzadeh P; Miner KD; Lu Y Direct EPR Observation of a Tyrosyl Radical in a Functional Oxidase Model in Myoglobin During Both H_2O_2 and O_2 Reactions. J. Am. Chem. Soc 2014, 136, 1174–1177. [PubMed: 24383850]

(522). Petrik ID; Davydov R; Ross M; Zhao X; Hoffman B; Lu Y Spectroscopic and Crystallographic Evidence for the Role of a Water-Containing H-Bond Network in Oxidase Activity of an Engineered Myoglobin. J. Am. Chem. Soc 2016, 138, 1134–1137. [PubMed: 26716352]

(523). Vojtěchovský J; Chu K; Berendzen J; Sweet RM; Schlichting I Crystal Structures of Myoglobin-Ligand Complexes at Near-Atomic Resolution. Biophys. J 1999, 77, 2153–2174. [PubMed: 10512835]

(524). Mukherjee S; Mukherjee A; Bhagi-Damodaran A; Mukherjee M; Lu Y; Dey A A Biosynthetic Model of Cytochrome *c* Oxidase as an Electrocatalyst for Oxygen Reduction. Nat. Commun 2015, 6, 8467. [PubMed: 26455726]

(525). Yu Y; Cui C; Liu X; Petrik ID; Wang J; Lu Y A Designed Metalloenzyme Achieving the Catalytic Rate of a Native Enzyme. J. Am. Chem. Soc 2015, 137, 11570–11573. [PubMed: 26318313]

(526). Durley RCE; Mathews FS Refinement and Structural Analysis of Bovine Cytochrome B5 at 1.5 Å Resolution. Acta Cryst. D 1996, 52, 65–76. [PubMed: 15299727]

(527). Bhagi-Damodaran A; Petrik ID; Marshall NM; Robinson H; Lu Y Systematic Tuning of Heme Redox Potentials and Its Effects on O_2 Reduction Rates in a Designed Oxidase in Myoglobin. J. Am. Chem. Soc 2014, 136, 11882–11885. [PubMed: 25076049]

(528). Mukherjee S; Mukherjee M; Mukherjee A; Bhagi-Damodaran A; Lu Y; Dey A O_2 Reduction by Biosynthetic Models of Cytochrome *c* Oxidase: Insights into Role of Proton Transfer Residues from Perturbed Active Sites Models of CcO. ACS Catal. 2018, 8, 8915–8924. [PubMed: 35693844]

(529). Lin Y-W; Yeung N; Gao Y-G; Miner KD; Tian S; Robinson H; Lu Y Roles of Glutamates and Metal Ions in a Rationally Designed Nitric Oxide Reductase Based on Myoglobin. Proc. Natl. Acad. Sci. U.S.A 2010, 107, 8581. [PubMed: 20421510]

(530). Petrik ID; Davydov R; Kahle M; Sandoval B; Dwaraknath S; Ädelroth P; Hoffman B; Lu Y An Engineered Glutamate in Biosynthetic Models of Heme-Copper Oxidases Drives Complete Product Selectivity by Tuning the Hydrogen-Bonding Network. Biochemistry 2021, 60, 346–355. [PubMed: 33464878]

(531). Bu Y; Cukier RI Structural Character and Energetics of Tyrosyl Radical Formation by Electron/Proton Transfers of a Covalently Linked Histidine-Tyrosine: A Model for Cytochrome *c* Oxidase. J. Phys. Chem. B 2005, 109, 22013–22026. [PubMed: 16853859]

(532). Liu X; Yu Y; Hu C; Zhang W; Lu Y; Wang J Significant Increase of Oxidase Activity through the Genetic Incorporation of a Tyrosine-Histidine Cross-Link in a Myoglobin Model of Heme-Copper Oxidase. Angew. Chem., Int. Ed 2012, 51, 4312–4316.

(533). Yu Y; Lv X; Li J; Zhou Q; Cui C; Hosseinzadeh P; Mukherjee A; Nilges MJ; Wang J; Lu Y Defining the Role of Tyrosine and Rational Tuning of Oxidase Activity by Genetic Incorporation of Unnatural Tyrosine Analogs. J. Am. Chem. Soc 2015, 137, 4594–4597. [PubMed: 25672571]

(534). Yu Y; Zhou Q; Wang L; Liu X; Zhang W; Hu M; Dong J; Li J; Lv X; Ouyang H; et al. Significant Improvement of Oxidase Activity through the Genetic Incorporation of a Redox-Active Unnatural Amino Acid. Chem. Sci 2015, 6, 3881–3885. [PubMed: 26417427]

(535). Yeung N; Lin Y-W; Gao Y-G; Zhao X; Russell BS; Lei L; Miner KD; Robinson H; Lu Y Rational Design of a Structural and Functional Nitric Oxide Reductase. Nature 2009, 462, 1079–1082. [PubMed: 19940850]

(536). Matsumura H; Chakraborty S; Reed J; Lu Y; Moënne-Loccoz P Effect of Outer-Sphere Side Chain Substitutions on the Fate of the Trans Iron-Nitrosyl Dimer in Heme/Nonheme Engineered Myoglobins (Fe_BMbs): Insights into the Mechanism of Denitrifying NO Reductases. Biochemistry 2016, 55, 2091–2099. [PubMed: 27003474]

(537). Bhagi-Damodaran A; Michael MA; Zhu Q; Reed J; Sandoval BA; Mirts EN; Chakraborty S; Moënne-Loccoz P; Zhang Y; Lu Y Why Copper Is Preferred over Iron for Oxygen Activation and Reduction in Haem-Copper Oxidases. Nat. Chem 2017, 9, 257–263. [PubMed: 28221360]

(538). Bhagi-Damodaran A; Reed JH; Zhu Q; Shi Y; Hosseinzadeh P; Sandoval BA; Harnden KA; Wang S; Sponholtz MR; Mirts EN; et al. Heme Redox Potentials Hold the Key to Reactivity Differences between Nitric Oxide Reductase and Heme-Copper Oxidase. Proc. Natl. Acad. Sci. U.S.A 2018, 115, 6195. [PubMed: 29802230]

(539). Mirts EN; Petrik ID; Hosseinzadeh P; Nilges MJ; Lu Y A Designed Heme-[4Fe-4S] Metalloenzyme Catalyzes Sulfite Reduction like the Native Enzyme. Science 2018, 361, 1098–1101. [PubMed: 30213908]

(540). Ueno T; Koshiyama T; Ohashi M; Kondo K; Kono M; Suzuki A; Yamane T; Watanabe Y Coordinated Design of Cofactor and Active Site Structures in Development of New Protein Catalysts. J. Am. Chem. Soc 2005, 127, 6556–6562. [PubMed: 15869276]

(541). Carey JR; Ma SK; Pfister TD; Garner DK; Kim HK; Abramite JA; Wang Z; Guo Z; Lu Y A Site-Selective Dual Anchoring Strategy for Artificial Metalloprotein Design. J. Am. Chem. Soc 2004, 126, 10812–10813. [PubMed: 15339144]

(542). Zhang J-L; Garner DK; Liang L; Chen Q; Lu Y Protein Scaffold of a Designed Metalloenzyme Enhances the Chemoselectivity in Sulfoxidation of Thioanisole. Chem. Commun 2008, 14, 1665–1667.

(543). Zhang J-L; Garner DK; Liang L; Barrios DA; Lu Y Noncovalent Modulation of pH-Dependent Reactivity of a Mn-Salen Cofactor in Myoglobin with Hydrogen Peroxide. Chem. Eur. J 2009, 15, 7481–7489. [PubMed: 19557774]

(544). Buvelot H; Posfay-Barbe KM; Linder P; Schrenzel J; Krause K-H *Staphylococcus aureus*, Phagocyte NADPH Oxidase and Chronic Granulomatous Disease. FEMS Microbiol. Rev 2017, 41, 139–157. [PubMed: 27965320]

(545). Miller A-F Redox Tuning over Almost 1 V in a Structurally Conserved Active Site: Lessons from Fe-Containing Superoxide Dismutase. Acc. Chem. Res 2008, 41, 501–510. [PubMed: 18376853]

(546). Barwinska-Sendra A; Garcia YM; Sendra KM; Baslé A; Mackenzie ES; Tarrant E; Card P; Tabares LC; Bicep C; Un S; et al. An Evolutionary Path to Altered Cofactor Specificity in a Metalloenzyme. Nat. Commun 2020, 11, 2738. [PubMed: 32483131]

(547). Barwinska-Sendra A; Baslé A; Waldron KJ; Un S A Charge Polarization Model for the Metal-Specific Activity of Superoxide Dismutases. Phys. Chem. Chem. Phys 2018, 20, 2363–2372. [PubMed: 29308487]

(548). Matthews RG Cobalamin-Dependent Methyltransferases. Acc. Chem. Res 2001, 34, 681–689. [PubMed: 11513576]

(549). Morita Y; Oohora K; Sawada A; Doitomi K; Ohbayashi J; Kamachi T; Yoshizawa K; Hisaeda Y; Hayashi T Intraprotein Transmethylation via a CH_3-Co(III) Species in Myoglobin Reconstituted with a Cobalt Corrinoid Complex. Dalton Trans. 2016, 45, 3277–3284. [PubMed: 26646210]

(550). Hayashi T; Morita Y; Mizohata E; Oohora K; Ohbayashi J; Inoue T; Hisaeda Y Co(II)/Co(I) Reduction-Induced Axial Histidine-Flipping in Myoglobin Reconstituted with a Cobalt Tetradehydrocorrin as a Methionine Synthase Model. Chem. Commun 2014, 50, 12560–12563.

(551). Sommer DJ; Vaughn MD; Ghirlanda G Protein Secondary-Shell Interactions Enhance the Photoinduced Hydrogen Production of Cobalt Protoporphyrin IX. Chem. Commun 2014, 50, 15852–15855.

(552). Brucker EA; Olson JS; Phillips GN; Dou Y; Ikeda-Saito M High Resolution Crystal Structures of the Deoxy, Oxy, and Aquomet Forms of Cobalt Myoglobin. J. Biol. Chem 1996, 271, 25419–25422. [PubMed: 8810310]

(553). Key HM; Dydio P; Clark DS; Hartwig JF Abiological Catalysis by Artificial Haem Proteins Containing Noble Metals in Place of Iron. Nature 2016, 534, 534–537. [PubMed: 27296224]

(554). Ward TR Directed Evolution of Iridium-Substituted Myoglobin Affords Versatile Artificial Metalloenzymes for Enantiose-lective C-C Bond-Forming Reactions. Angew. Chem., Int. Ed 2016, 55, 14909–14911.

(555). Dydio P; Key HM; Nazarenko A; Rha JY-E; Seyedkazemi V; Clark DS; Hartwig JF An Artificial Metalloenzyme with the Kinetics of Native Enzymes. Science 2016, 354, 102–106. [PubMed: 27846500]

(556). Key HM; Dydio P; Liu Z; Rha JY-E; Nazarenko A; Seyedkazemi V; Clark DS; Hartwig JF Beyond Iron: Iridium-Containing P450 Enzymes for Selective Cyclopropanations of Structurally Diverse Alkenes. ACS Cent. Sci 2017, 3, 302–308. [PubMed: 28470047]

(557). Gu Y; Natoli SN; Liu Z; Clark DS; Hartwig JF Site-Selective Functionalization of (sp^3)C-H Bonds Catalyzed by Artificial Metalloenzymes Containing an Iridium-Porphyrin Cofactor. Angew. Chem., Int. Ed 2019, 58, 13954–13960.

(558). Watson HC The Stereochemistry of the Protein Myoglobin. Protein Stereochem. 1969, 4, 299.

(559). Park S-Y; Yamane K; Adachi S; Shiro Y; Weiss KE; Maves SA; Sligar SG Thermophilic Cytochrome P450 (CYP119) from *Sulfolobus solfataricus*: High Resolution Structure and Functional Properties. J. Inorg. Biochem 2002, 91, 491–501. [PubMed: 12237217]

(560). Selvan D; Prasad P; Farquhar ER; Shi Y; Crane S; Zhang Y; Chakraborty S Redesign of a Copper Storage Protein into an Artificial Hydrogenase. ACS Catal. 2019, 9, 5847–5859. [PubMed: 31341700]

(561). Slater JW; Shafaat HS Nickel-Substituted Rubredoxin as a Minimal Enzyme Model for Hydrogenase. J. Phys. Chem. Lett 2015, 6, 3731–3736. [PubMed: 26722748]

(562). Vita N; Platsaki S; Baslé A; Allen SJ; Paterson NG; Crombie AT; Murrell JC; Waldron KJ; Dennison C A Four-Helix Bundle Stores Copper for Methane Oxidation. Nature 2015, 525, 140–143. [PubMed: 26308900]

(563). Slater JW; Marguet SC; Gray ME; Monaco HA; Sotomayor M; Shafaat HS Power of the Secondary Sphere: Modulating Hydrogenase Activity in Nickel-Substituted Rubredoxin. ACS Catal. 2019, 9, 8928–8942.

(564). Lewis LC; Shafaat HS Reversible Electron Transfer and Substrate Binding Support [$NiFe_3S_4$] Ferredoxin as a Protein-Based Model for [NiFe] Carbon Monoxide Dehydrogenase. Inorg. Chem 2021, 60, 13869–13875. [PubMed: 34488341]

(565). Khare SD; Kipnis Y; Greisen PJ; Takeuchi R; Ashani Y; Goldsmith M; Song Y; Gallaher JL; Silman I; Leader H; et al. Computational Redesign of a Mononuclear Zinc Metalloenzyme for Organophosphate Hydrolysis. Nat. Chem. Biol 2012, 8, 294–300. [PubMed: 22306579]

(566). Wilchek M; Bayer EA Introduction to Avidin-Biotin Technology. In Methods in Enzymology; Wilchek M, Bayer EA, Eds.; Academic Press, 1990; Vol. 184, pp 5–13. [PubMed: 2201884]

(567). Lin C-C; Lin C-W; Chan ASC Catalytic Hydrogenation of Itaconic Acid in a Biotinylated Pyrphos-Rhodium(I) System in a Protein Cavity. Tetrahedron: Asymmetry 1999, 10, 1887–1893.

(568). Collot J; Gradinaru J; Humbert N; Skander M; Zocchi A; Ward TR Artificial Metalloenzymes for Enantioselective Catalysis Based on Biotin-Avidin. J. Am. Chem. Soc 2003, 125, 9030–9031. [PubMed: 15369356]

(569). Skander M; Humbert N; Collot J; Gradinaru J; Klein G; Loosli A; Sauser J; Zocchi A; Gilardoni F; Ward TR Artificial Metalloenzymes: (Strept)Avidin as Host for Enantioselective

Hydro-genation by Achiral Biotinylated Rhodium-Diphosphine Complexes. J. Am. Chem. Soc 2004, 126, 14411–14418. [PubMed: 15521760]

(570). Klein G; Humbert N; Gradinaru J; Ivanova A; Gilardoni F; Rusbandi UE; Ward TR Tailoring the Active Site of Chemzymes by Using a Chemogenetic-Optimization Procedure: Towards Substrate-Specific Artificial Hydrogenases Based on the Biotin-Avidin Technology. Angew. Chem., Int. Ed 2005, 44, 7764–7767.

(571). Reetz MT; Peyralans JJ-P; Maichele A; Fu Y; Maywald M Directed Evolution of Hybrid Enzymes: Evolving Enantioselectivity of an Achiral Rh-Complex Anchored to a Protein. Chem. Commun 2006, 41, 4318–4320.

(572). Weber PC; Ohlendorf DH; Wendoloski JJ; Salemme FR Structural Origins of High-Affinity Biotin Binding to Streptavidin. Science 1989, 243, 85–88. [PubMed: 2911722]

(573). Letondor C; Humbert N; Ward TR Artificial Metal-loenzymes Based on Biotin-Avidin Technology for the Enantioselective Reduction of Ketones by Transfer Hydrogenation. Proc. Natl. Acad. Sci. U.S.A 2005, 102, 4683–4687. [PubMed: 15772162]

(574). Letondor C; Pordea A; Humbert N; Ivanova A; Mazurek S; Novic M; Ward TR Artificial Transfer Hydrogenases Based on the Biotin-(Strept)Avidin Technology: Fine Tuning the Selectivity by Saturation Mutagenesis of the Host Protein. J. Am. Chem. Soc 2006, 128, 8320–8328. [PubMed: 16787096]

(575). Dürrenberger M; Heinisch T; Wilson YM; Rossel T; Nogueira E; Knörr L; Mutschler A; Kersten K; Zimbron MJ; Pierron J; et al. Artificial Transfer Hydrogenases for the Enantioselective Reduction of Cyclic Imines. Angew. Chem., Int. Ed 2011, 50, 3026–3029.

(576). Creus M; Pordea A; Rossel T; Sardo A; Letondor C; Ivanova A; LeTrong I; Stenkamp RE; Ward TR X-Ray Structure and Designed Evolution of an Artificial Transfer Hydrogenase. Angew. Chem., Int. Ed 2008, 47, 1400–1404.

(577). Pordea A; Creus M; Letondor C; Ivanova A; Ward TR Improving the Enantioselectivity of Artificial Transfer Hydrogenases Based on the Biotin-Streptavidin Technology by Combinations of Point Mutations. Inorg. Chim. Acta 2010, 363, 601–604.

(578). Schwizer F; Köhler V; Dürrenberger M; Knörr L; Ward TR Genetic Optimization of the Catalytic Efficiency of Artificial Imine Reductases Based on Biotin-Streptavidin Technology. ACS Catal. 2013, 3, 1752–1755.

(579). Zhao J; Rebelein JG; Mallin H; Trindler C; Pellizzoni MM; Ward TR Genetic Engineering of an Artificial Metalloenzyme for Transfer Hydrogenation of a Self-Immolative Substrate in Escherichia Coli's Periplasm. J. Am. Chem. Soc 2018, 140, 13171–13175. [PubMed: 30272972]

(580). Wu S; Zhou Y; Rebelein JG; Kuhn M; Mallin H; Zhao J; Igareta NV; Ward TR Breaking Symmetry: Engineering Single-Chain Dimeric Streptavidin as Host for Artificial Metalloenzymes. J. Am. Chem. Soc 2019, 141, 15869–15878. [PubMed: 31509711]

(581). Satoh T; Miura M Oxidative Coupling of Aromatic Substrates with Alkynes and Alkenes under Rhodium Catalysis. Chem. Eur. J 2010, 16, 11212–11222. [PubMed: 20740508]

(582). Hyster TK; Knörr L; Ward TR; Rovis T Biotinylated Rh(III) Complexes in Engineered Streptavidin for Accelerated Asymmetric C-H Activation. Science 2012, 338, 500–503. [PubMed: 23112327]

(583). Jeschek M; Reuter R; Heinisch T; Trindler C; Klehr J; Panke S; Ward TR Directed Evolution of Artificial Metalloenzymes for in Vivo Metathesis. Nature 2016, 537, 661–665. [PubMed: 27571282]

(584). Heinisch T; Schwizer F; Garabedian B; Csibra E; Jeschek M; Vallapurackal J; Pinheiro VB; Marlière P; Panke S; Ward TR *E. Coli* Surface Display of Streptavidin for Directed Evolution of an Allylic Deallylase. Chem. Sci 2018, 9, 5383–5388. [PubMed: 30079176]

(585). Pierron J; Malan C; Creus M; Gradinaru J; Hafner I; Ivanova A; Sardo A; Ward TR Artificial Metalloenzymes for Asymmetric Allylic Alkylation on the Basis of the Biotin-Avidin Technology. Angew. Chem., Int. Ed 2008, 47, 701–705.

(586). Chatterjee A; Mallin H; Klehr J; Vallapurackal J; Finke AD; Vera L; Marsh M; Ward TR An Enantioselective Artificial Suzukiase Based on the Biotin-Streptavidin Technology. Chem. Sci 2016, 7, 673–677. [PubMed: 29896353]

(587). Vornholt T; Christoffel F; Pellizzoni MM; Panke S; Ward TR; Jeschek M Systematic Engineering of Artificial Metalloenzymes for New-to-Nature Reactions. Sci. Adv 2021, 7, No. eabe4208. [PubMed: 33523952]

(588). Köhler V; Mao J; Heinisch T; Pordea A; Sardo A; Wilson YM; Knörr L; Creus M; Prost J-C; Schirmer T; et al. OsO_4· Streptavidin: A Tunable Hybrid Catalyst for the Enantioselective Cis-Dihydroxylation of Olefins. Angew. Chem., Int. Ed 2011, 50, 10863–10866.

(589). Pordea A; Creus M; Panek J; Duboc C; Mathis D; Novic M; Ward TR Artificial Metalloenzyme for Enantioselective Sulfoxidation Based on Vanadyl-Loaded Streptavidin. J. Am. Chem. Soc 2008, 130, 8085–8088. [PubMed: 18507383]

(590). Srivastava P; Yang H; Ellis-Guardiola K; Lewis JC Engineering a Dirhodium Artificial Metalloenzyme for Selective Olefin Cyclopropanation. Nat. Commun 2015, 6, 7789. [PubMed: 26206238]

(591). Yang H; Swartz AM; Park HJ; Srivastava P; Ellis-Guardiola K; Upp DM; Lee G; Belsare K; Gu Y; Zhang C; et al. Evolving Artificial Metalloenzymes via Random Mutagenesis. Nat. Chem 2018, 10, 318–324. [PubMed: 29461523]

(592). Upp DM; Huang R; Li Y; Bultman MJ; Roux B; Lewis JC Engineering Dirhodium Artificial Metalloenzymes for Diazo Coupling Cascade Reactions. Angew. Chem., Int. Ed 2021, 60, 23672–23677.

(593). Kato S; Onoda A; Grimm AR; Tachikawa K; Schwaneberg U; Hayashi T Incorporation of a Cp*Rh(III)-Dithiophosphate Cofactor with Latent Activity into a Protein Scaffold Generates a Biohybrid Catalyst Promoting C(sp^2)-H Bond Functionalization. Inorg. Chem 2020, 59, 14457–14463. [PubMed: 32914980]

(594). Kato S; Onoda A; Taniguchi N; Schwaneberg U; Hayashi T Directed Evolution of a Cp^*Rh^{III}-Linked Biohybrid Catalyst Based on a Screening Platform with Affinity Purification. ChemBioChem 2021, 22, 679–685. [PubMed: 33026156]

(595). Monnard FW; Nogueira ES; Heinisch T; Schirmer T; Ward TR Human Carbonic Anhydrase II as Host Protein for the Creation of Artificial Metalloenzymes: The Asymmetric Transfer Hydrogenation of Imines. Chem. Sci 2013, 4, 3269.

(596). Fleishman SJ; Leaver-Fay A; Corn JE; Strauch E-M; Khare SD; Koga N; Ashworth J; Murphy P; Richter F; Lemmon G; et al. RosettaScripts: A Scripting Language Interface to the Rosetta Macromolecular Modeling Suite. PLOS ONE 2011, 6, No. e20161. [PubMed: 21731610]

(597). Heinisch T; Pellizzoni M; Dürrenberger M; Tinberg CE; Köhler V; Klehr J; Häussinger D; Baker D; Ward TR Improving the Catalytic Performance of an Artificial Metalloenzyme by Computational Design. J. Am. Chem. Soc 2015, 137, 10414–10419. [PubMed: 26226626]

(598). Stein A; Chen D; Igareta NV; Cotelle Y; Rebelein JG; Ward TR A Dual Anchoring Strategy for the Directed Evolution of Improved Artificial Transfer Hydrogenases Based on Carbonic Anhydrase. ACS Cent. Sci 2021, 7, 1874–1884. [PubMed: 34849402]

(599). Fischer S; Ward TR; Liang AD Engineering a Metathesis-Catalyzing Artificial Metalloenzyme Based on HaloTag. ACS Catal. 2021, 11, 6343–6347. [PubMed: 34055452]

(600). Lutz S Beyond Directed Evolution—Semi-Rational Protein Engineering and Design. Curr. Opin. Biotechnol 2010, 21, 734–743. [PubMed: 20869867]

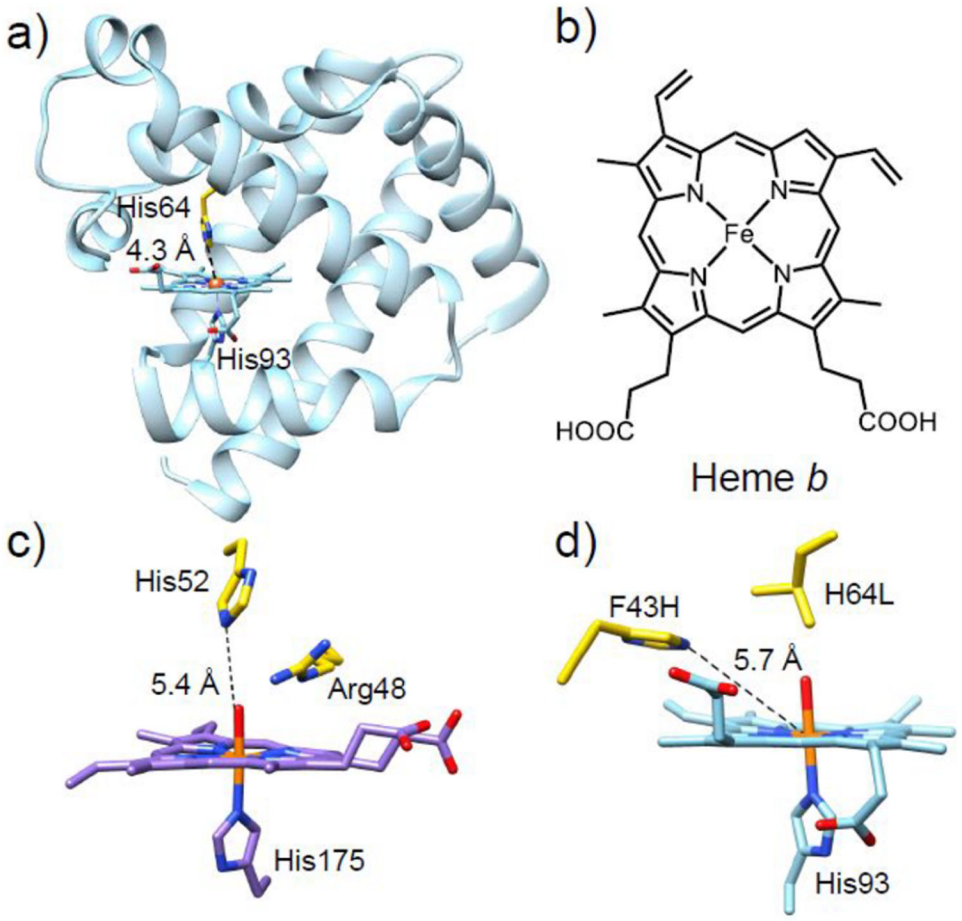

Figure 1.

(a) Crystal structure of WT-sperm whale Mb (swMb) (PDB ID: 5YCE).[89] (b) Chemical structure of heme *b*. (c) Crystal structure of the active site of cytochrome *c* peroxidase (PDB ID: 1ZBY) with the distal His52 and Arg48 residues shown in yellow.[90] (d) Crystal structure of the active site of the F43H/H64L Mb mutant (PDB ID: 1OFK)[102] with the two mutated residues shown in yellow. The distances between the N_ε atom of the distal His residue and the heme iron in each crystal structure are labeled.

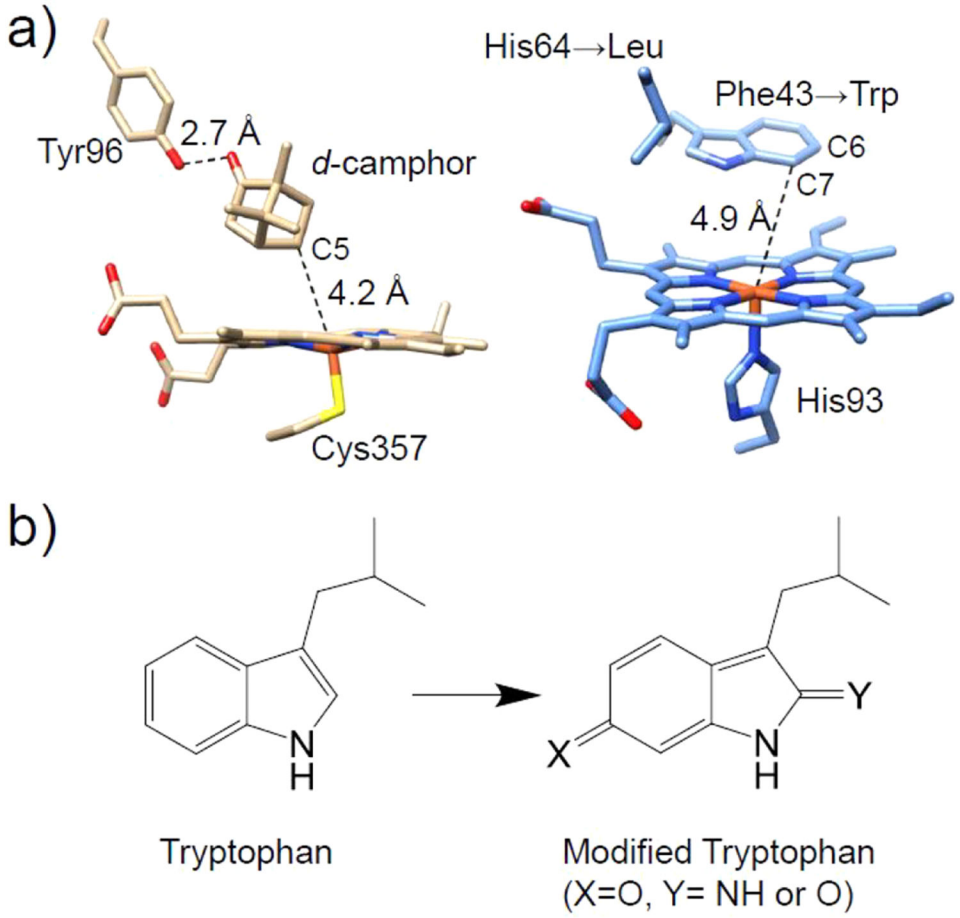

Figure 2.

(a) Crystal structure of $P450_{cam}$ (left, PDB ID: 2CPP)[103] and structural model of F43W/H64L Mb (right). (b) Chemical structures of tryptophan and the six-electron modified tryptophan products.

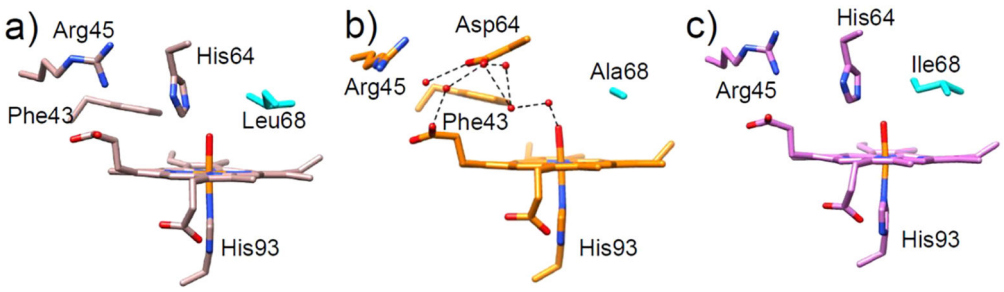

Figure 3.

Crystal structures of the (a) V68L (rose brown, PDB ID: 1MLS),[105] (b) H64D/V68A (orange, PDB ID: 1LUE),[106] and (c) V68I (magenta, PDB ID: 1MLO)[105] Mb variants. Different residues at position 68 are shown in cyan. Water molecules are denoted as red spheres. The hydrogen bonds are represented by black dashed lines.

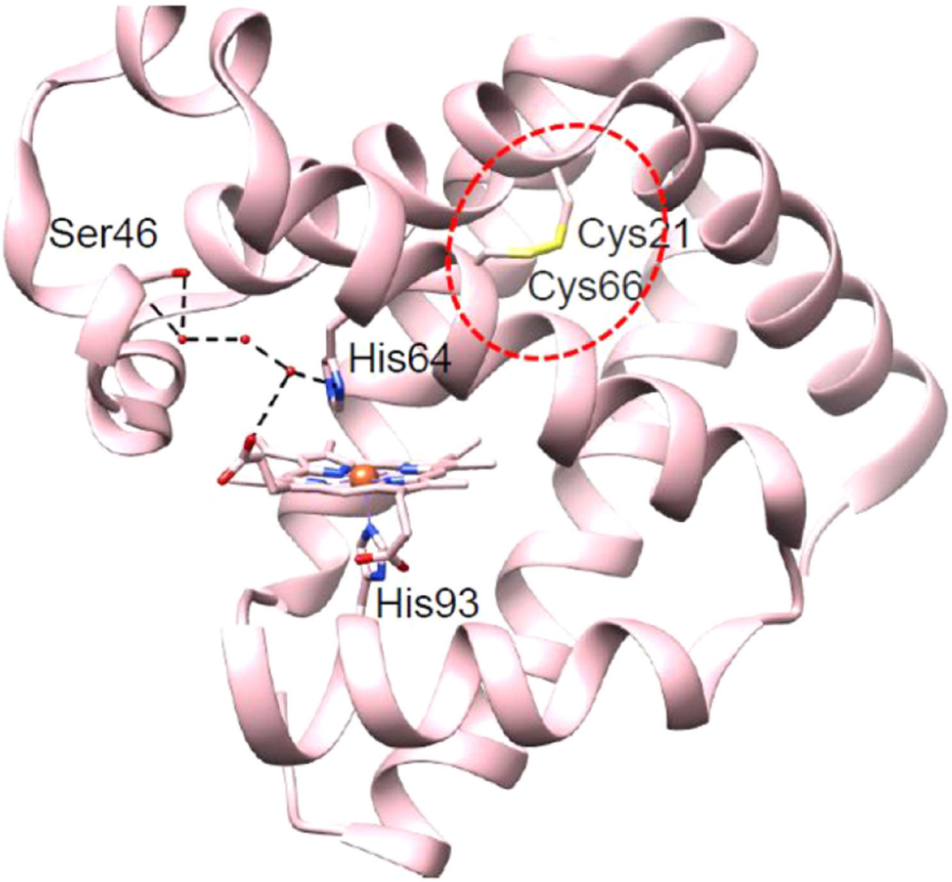

Figure 4.

Crystal structures of the V21C/V66C/F46S Mb variant (PDB ID: 5ZEO).[111] The disulfide bond between the Cys21 and Cys66 residues is highlighted in the red dashed circle. The hydrogen bonds involving the distal His64 and the Ser46 residues are shown by black dashed lines.

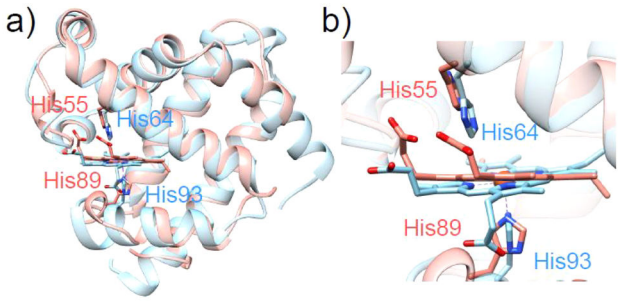

Protein	Fe-Nε(His) distance (Å)
wt-Mb	4.3
G65TMb	4.6
G65I Mb	5.1
wt-DHP	5.4

Figure 5.

(a) Overlay of the crystal structures of native DHP (red, PDB ID: 1EW6)[92] and WT-Mb (blue, PDB ID: 5YCE).[89] (b) Active sites of native DHP and WT-Mb. The distances between the N_{ε} atoms of the distal His residues and the heme irons in DHP, Mb, and the G65T and G65I Mb variants are summarized in the table on the right.

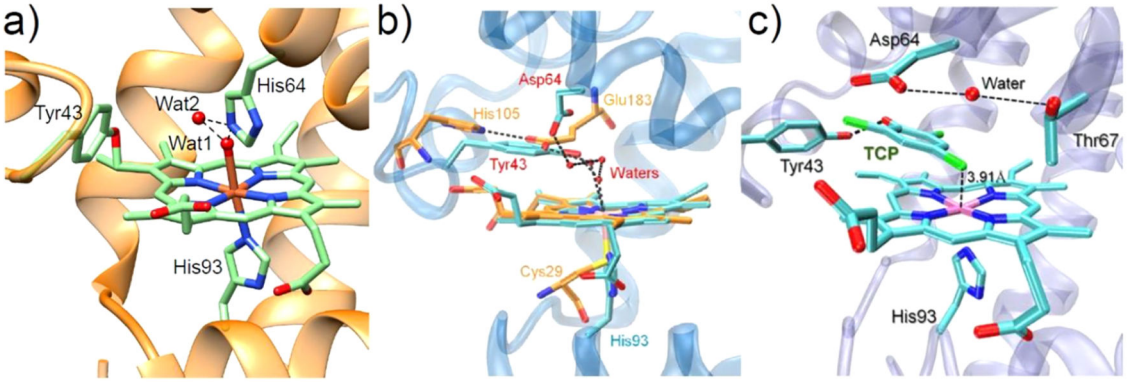

Figure 6.

(a) Crystal structure of F43Y Mb (PDB ID: 4QAU)[115] showing the Tyr-heme covalent C—O bond and two distal water molecules forming H-bonding interactions (dotted lines).[115] (b) Overlay of the crystal structures of ferric F43Y/H64D Mb (blue, PDB ID: 5ZZF)[118] and the heme active site of native chloroperoxidase (orange, PDB ID: 1CPO),[119] showing the H-bonding network. (c) Crystal structure of ferric F43Y/H64D Mb in complex with TCP (PDB ID: 5ZZG),[118] showing the conformation of Tyr43 and TCP and the H-bonding interactions in the heme center. The distance between the Cl4 atom and the heme Fe (3.91 Å) is indicated. Reproduced with permission from ref 118. Copyright 2018 American Chemical Society.

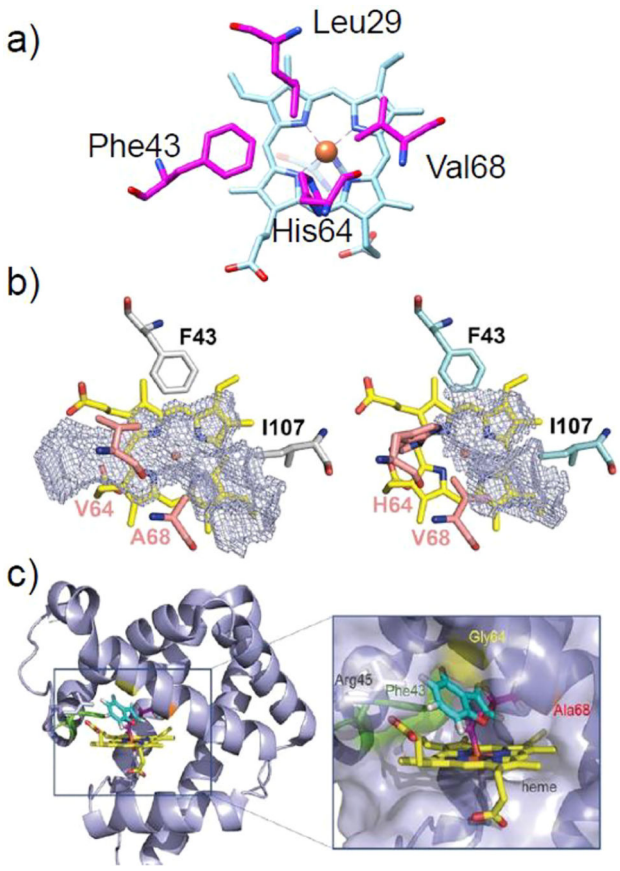

Figure 7.

(a) Top view of the crystal structure of WT-swMb (PDB ID: 5YCE) with the key residues in the distal heme pocket shown in magenta.[89] (b) Pocket cavity space (mesh) above the heme cofactor in H64V/V68A Mb (left) and WT-swMb (right). The pocket volumes were calculated to correspond to 243 and 125 $Å^3$, respectively. Reproduced with permission from ref 135. Copyright 2019 American Chemical Society. (c) Structural model of the carbene-bound transition state (TSO/ins) of H64G/V68A Mb. The benzofuran substrate is shown in cyan. Reproduced with permission from ref 133. Copyright 2019 John Wiley & Sons.

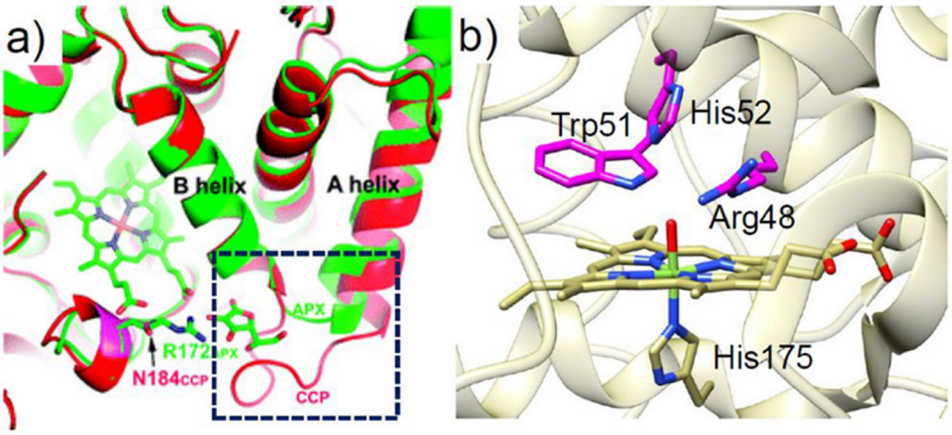

Figure 8.

(a) Overlay of the crystal structures of WT-C*c*P (red) and APX (green). Reproduced with permission from ref 137. Copyright 2008 American Chemical Society. The ascorbate binding site and the corresponding loop in C*c*P are highlighted in the black dashed square. (b) Crystal structure of yeast CcP (PDB ID: 2CCP).[139] Three residues that are mutated to Ala are highlighted in magenta.

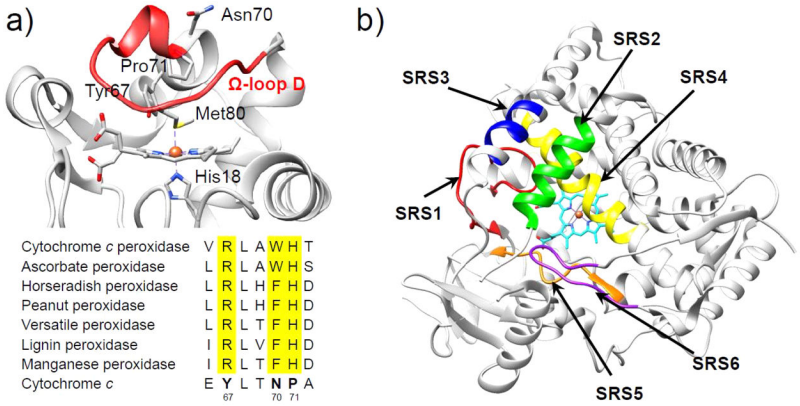

Figure 9.

(a) Crystal structure of yeast *iso*-1 C*c* (top, PDB ID: 2YCC).[147] The flexible coordination loop, Ω-loop D, is colored in red. At the bottom is the multiple sequence alignment of the distal heme region of some classical peroxidases which is compared to the sequence of the distal heme region of yeast iso-1 C*c*.[154] (b) Substrate recognition sites (SRSs) in P450 enzyme (CYP2C9, PDB ID: 1R9O)[155] shown by arrows: SRS1 (red), SRS2 (green), SRS3 (blue), SRS4 (yellow), SRS5 (orange), SRS6 (magenta).[156]

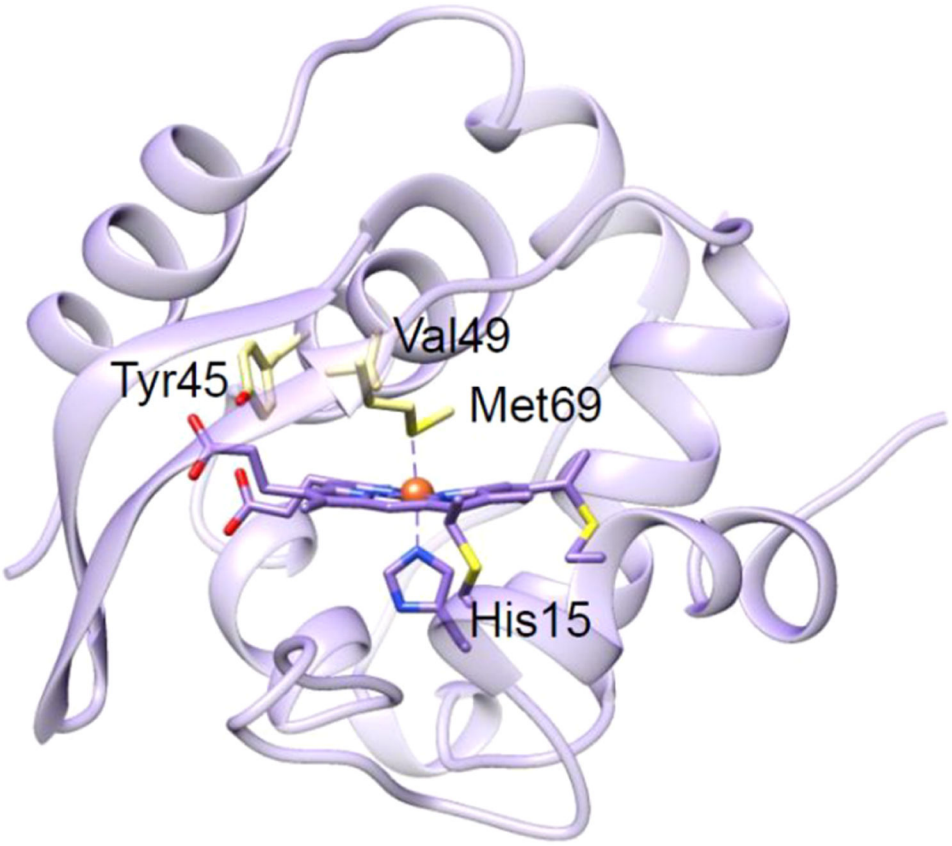

Figure 10.
Crystal structure of Cc_{552} (PDB ID: 1C52).[160] The key residues for mutations are shown in light yellow.

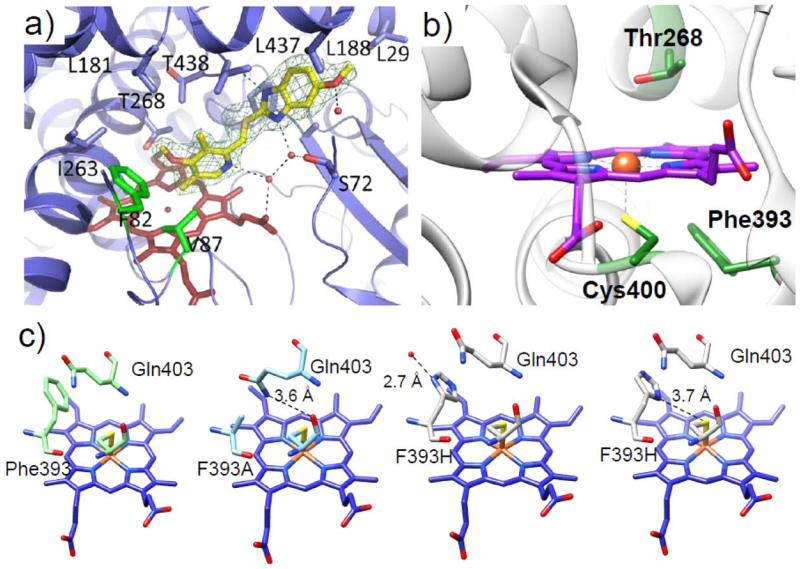

Figure 11.

(a) Mode of binding of omeprazole shown for the F87V/A82F $P450_{BM3}$ double mutant. Reproduced from ref 162 under the Creative Commons CC-BY license. (b) Active site of substrate-free $P450_{BM3}$ (PDB ID: 2IJ2).[168] Conserved residues Thr268, Phe393, and Cys400 are shown in green, and the heme cofactor is shown in purple. (c) From left to right are the crystal structures of WT-$P450_{BM3h}$ (PDB ID: 1BU7),[169] the F393A mutant (PDB ID: 1P0V),[170] and the F393H mutant (PDB ID: 1JME)[171] with the side chain of F393H orienting in two fashions. In the structure of F393A, a hydrogen bond is formed between the side chain amide nitrogen of Q403 and the thiolate of the heme ligating Cys400. For the two orientations of the His side chain in F393H, in one orientation the His side chain hydrogen bonds to an exterior water molecule. In a ring-flipped conformation, the side chain may form a weak hydrogen bond with the axial Cys.[167]

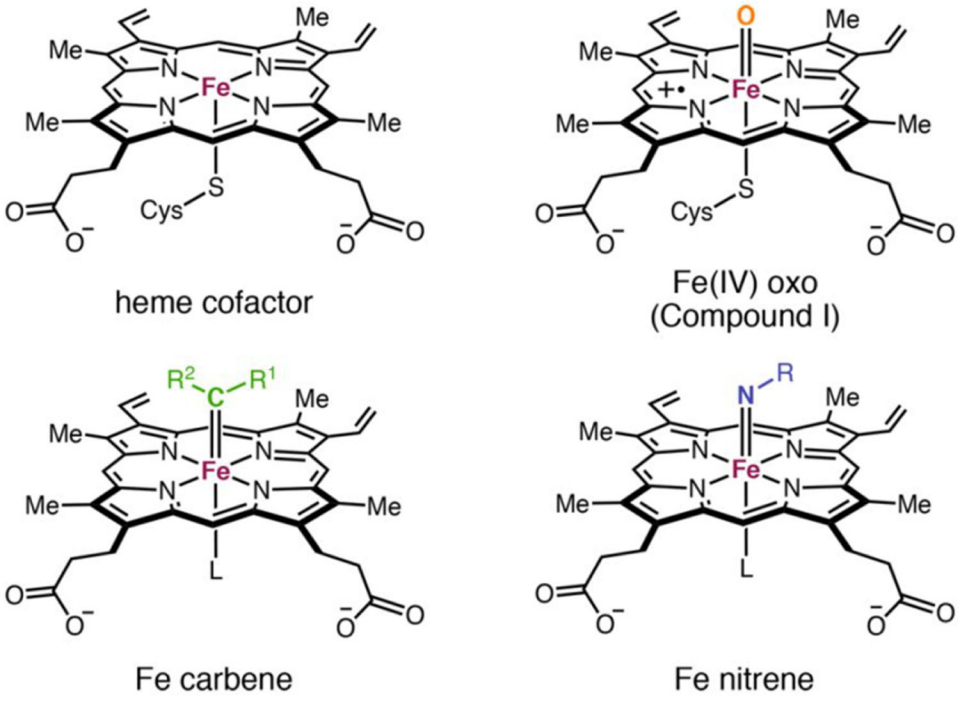

Figure 12.

Structural comparison of the free heme cofactor bound to the cysteine thiolate compared with compound I, iron-carbene, and iron-nitrene intermediates. Reproduced with permission from ref 186. Copyright 2021 American Chemical Society.

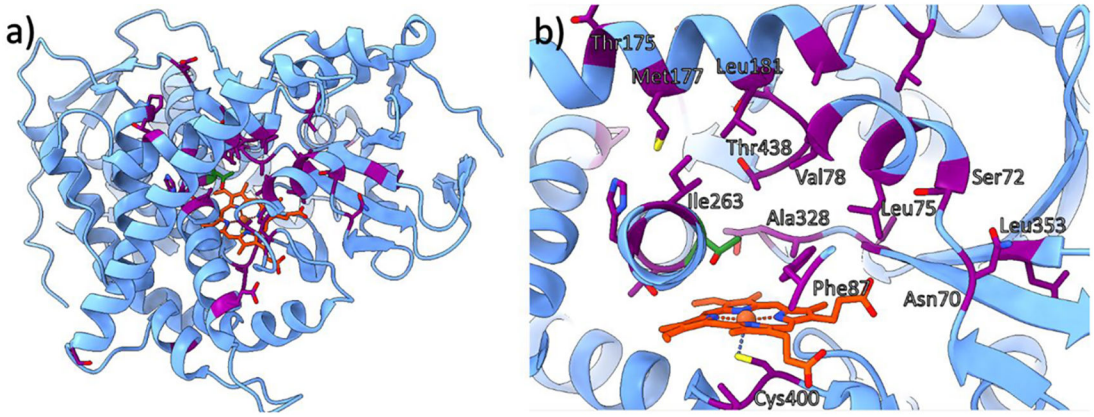

Figure 13.

Structure of the active site of WT-P450$_{BM3}$ (PDB ID: 4ZFA) shown (a) as the full domain and (b) at the enzyme active site.[189] Commonly targeted residues for mutagenesis are highlighted in purple, Thr268 is displayed in green, and heme b is in orange. Some residues are not labeled for clarity.

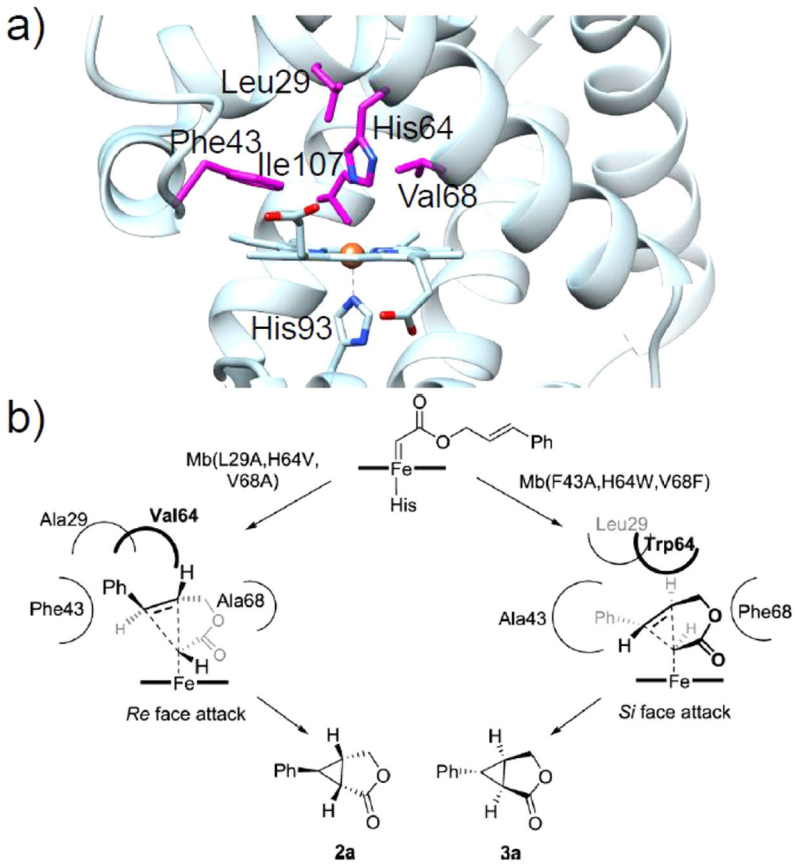

Figure 14.

(a) Crystal structure of WT-swMb (PDB ID: 5YCE)[89] with key residues in the distal heme pocket for directed evolution shown in magenta. (b) Stereochemical model for intramolecular cyclopropanation catalyzed by the stereodivergent Mb variants. Reproduced from ref 220. Copyright 2019 American Chemical Society.

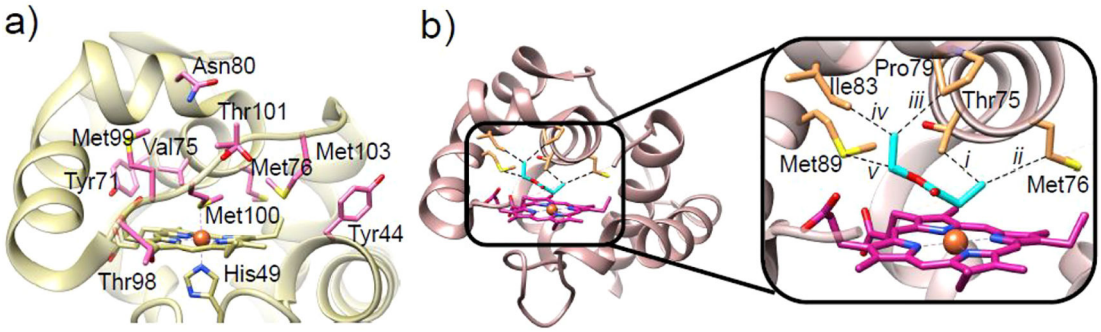

Figure 15.

(a) Crystal structure of WT-*Rma*-C*c* (PDB ID: 3CP5)[230] with the key residues involved in directed evolution shown in purple. (b) Crystal structure of carbene-bound TDE-*Rma*-C*c* (PDB ID: 6CUN) with the carbene species in cyan. (Inset) Interactions between the carbene and amino acid residues are shown with yellow lines: (*i*) Thr75, 3.7 Å; (*ii*) Met76, 4.3 Å; (*iii*) Pro79, 3.5 Å; (*iv*) Ile83, 3.6 Å; (*v*) Met89, 3.5 Å.[226]

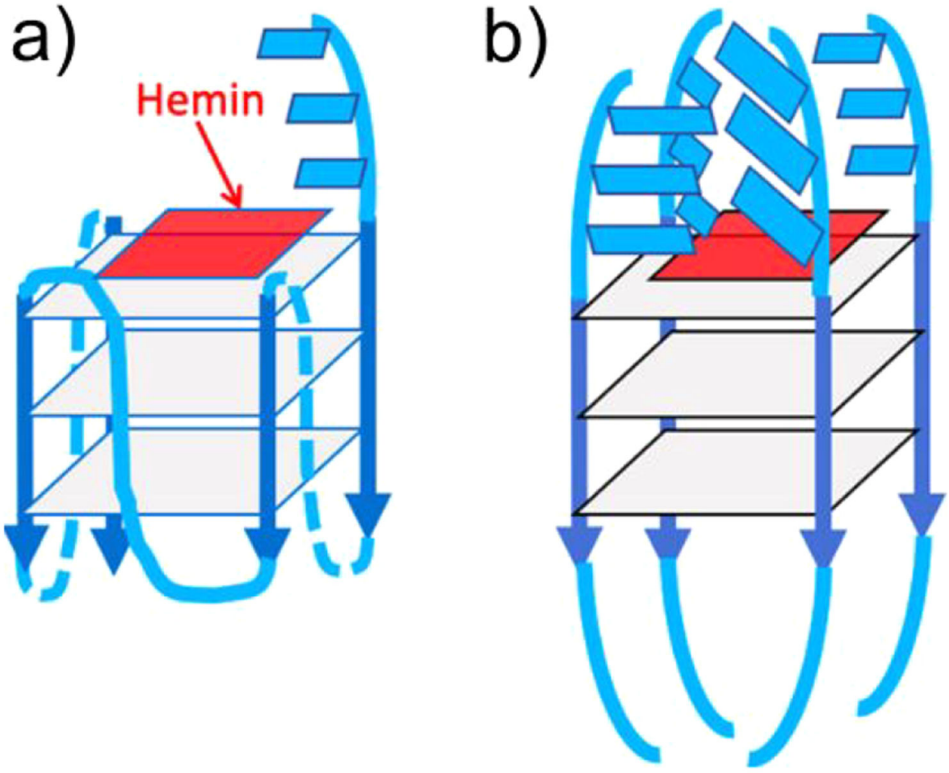

Figure 16.

Active site of heme/DNAzymes (GQ-heme complexes), where the heme end-stacks on the 3′-most guanine-quartet (gray squares): (a) “G4-AAA” and “G4-TTT” oligonucleotides both form intramolecular, propeller looped GQs, with the 3′-terminal AAA or TTT overhanging (shown as blue rectangles). (b) An intermolecularly assembled GQ such as “(dA4G5A4)4” is expected to have a complex “distal” environment above the stacked heme, potentially imparting stereoselectivity to reactions catalyzed by the DNA-bound heme. Reproduced with permission from ref 249. Copyright 2019 American Chemical Society.

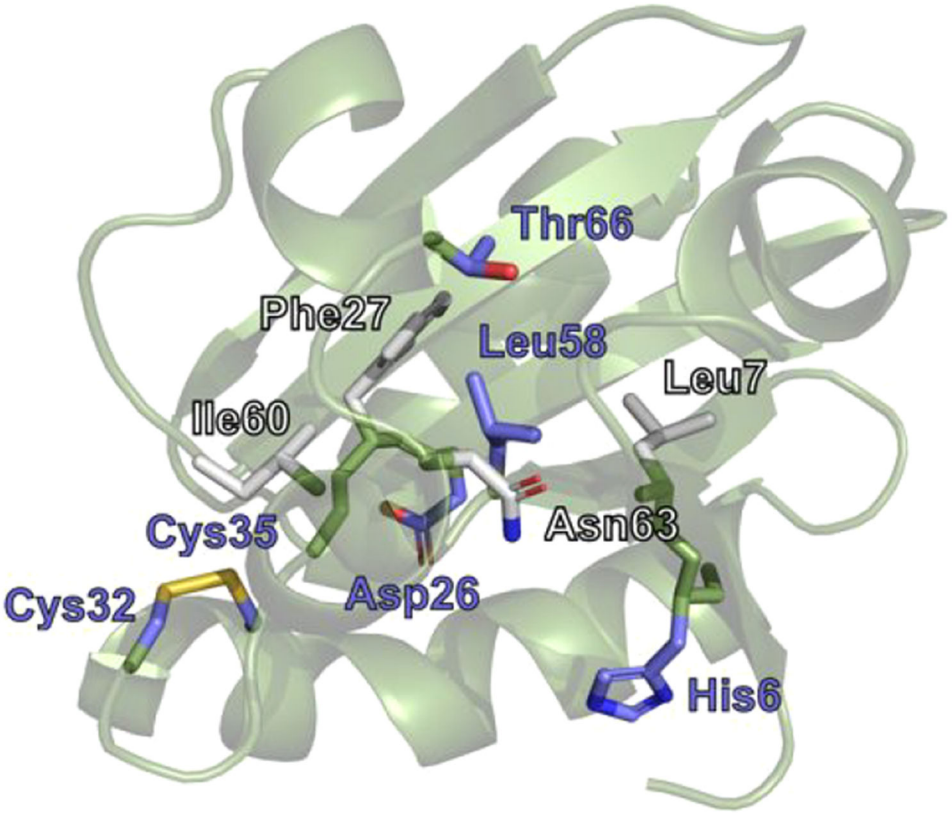

Figure 17.

Crystal structure of Trx from *E. coli* (PDB ID: 2TRX).[269] First coordination residues in designed Trx-SOD were made to residues highlighted in light gray, and SCS mutations are highlighted in blue.[268] Atom coloring: S (yellow); O (red); N (blue).

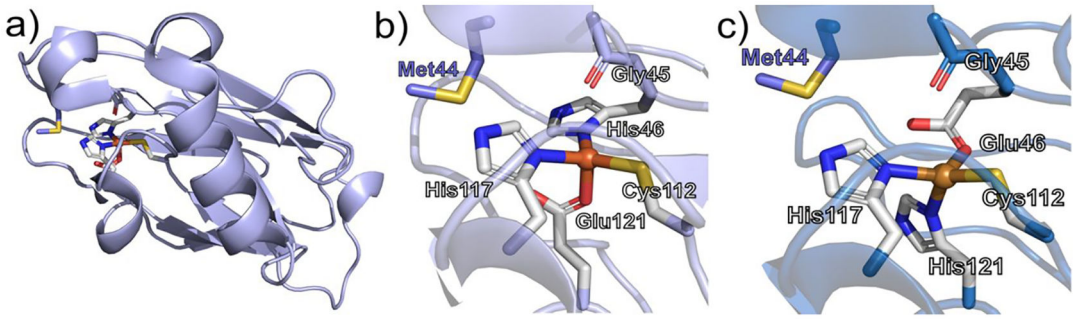

Figure 18.

(a) Crystal structure of M121E Az (PDB ID: 4QLW).[271] (b) Fe-bound metal binding site of M121E Az. (c) Cu-bound metal binding site of M121H/H46GE (PDB ID: 4WKX).[272] PCS atoms are highlighted in light gray, while SCS target residues are highlighted in blue. Atom coloring: S (yellow); O (red); N (blue); Fe (orange); Cu (copper).

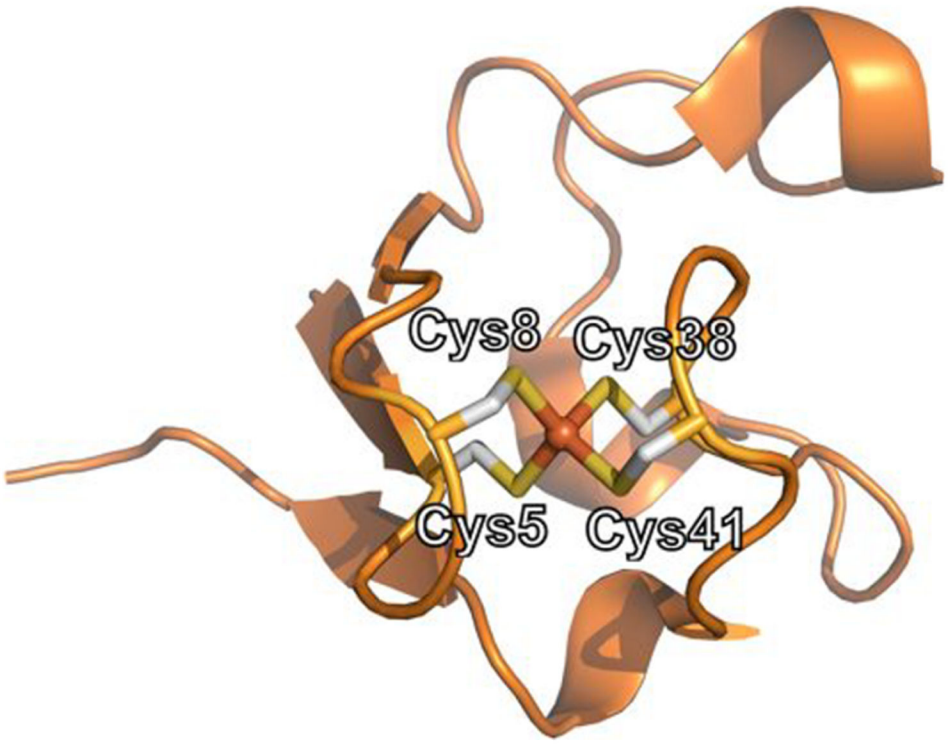

Figure 19.
Crystal structure of *Pf* Rd (PDB ID: 1VCX).[277] Atom coloring: S (yellow); Fe (orange).

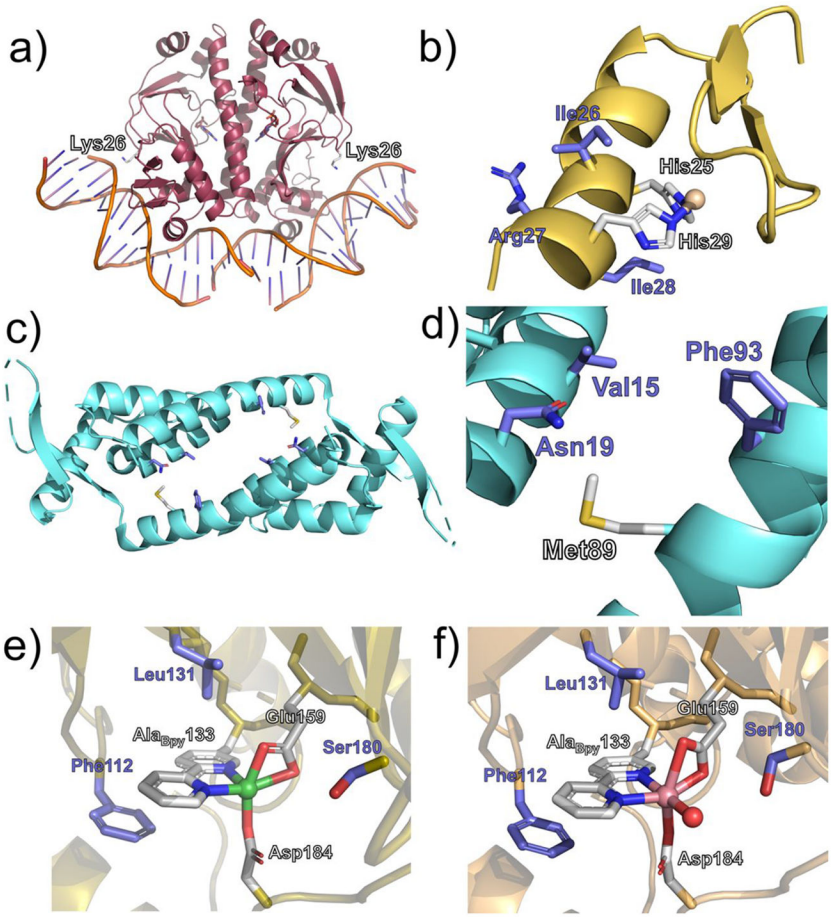

Figure 20.

Crystal structures of target proteins for Ala_{Bpy} incorporation. (a) Catabolite activator protein (CAP) with the Lys26 target location of Ala_{Bpy} incorporation highlighted (PDB ID: 1J59).[280,284] (b) Transcription factor protein Zif268 with target residues for randomization highlighted. Native metal binding residues are highlighted in light gray, while additional target residues are highlighted in blue (PDB ID: 1ZAA).[288,285] (c) LmrR with target residues for Ala_{Bpy} incorporation highlighted (d) in light gray, with additional SCS target residues highlighted in light blue (PDB ID: 3F8B).[286,287] (e) Designed Ala_{Bpy}-incorporated protein scaffold based on indole-3-glycerolphosphate synthase containing bound Ni^{2+} (PDB ID: 4IXO) and (f) Co^{2+} (PDB ID: 4IWW). PCS residues are highlighted in light gray, while SCS target residues are highlighted in light blue.[289] Atom coloring: N (blue); O (red); S (yellow); Fe (orange); Co (salmon); Ni (green).

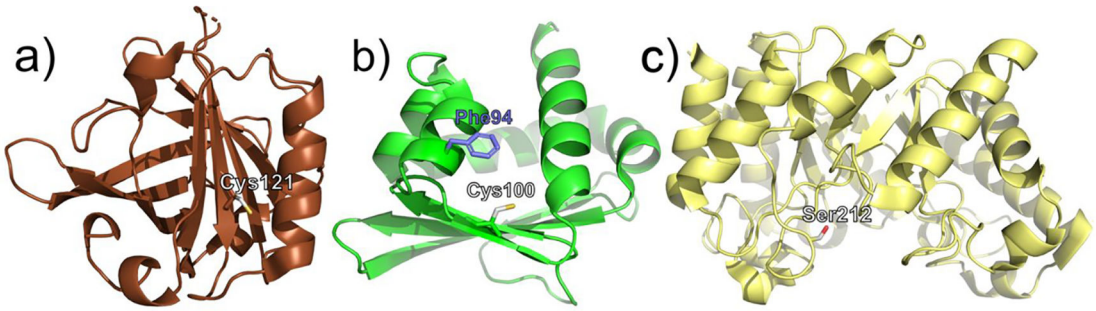

Figure 21.

Crystal structures of target proteins for Cys-maleimide linkages. (a) β-Lactoglobulin isoform B (β-LG) with the target Cys121 for thiosuccinimide formation highlighted in light gray (PDB ID: 4IB9).[296,297] (b) Steroid carrier protein SL (SCP-2L) containing an Ala100Cys mutation as the target for thiosuccinimide formation (highlighted in light gray). An additional target residue, Phe94, targeted for SCS modifications, is highlighted in light blue (PDB ID: 6Z1W).[298,299] (c) Xylanase A (Xln) with target residue for Ser212 (for the Ser212Cys incorporation highlighted in light gray, with additional SCS target residues highlighted in light blue) (PDB ID: 1E0W).[300,301] Atom coloring: O (red); S (yellow).

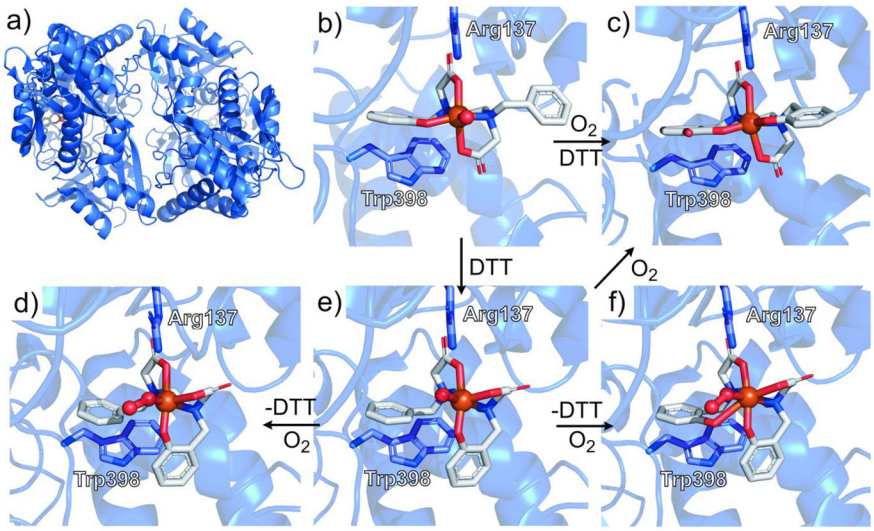

Figure 22.

(a) Crystal structure of NikA with bound $Fe^{III}L0$. (b) $Fe^{III}L0$ binding site of NikA with interacting SCS residues Arg137 and Trp398 highlighted in blue. (c) Dihydroxylated product formed following exposure of NikA/FeL0 to 50 mM DTT and O_2. (d) O_2-bound intermediate formed following four successive back soaks of DTT-reduced NikA/FeL0 in DTT-free mother liquor, followed by O_2 exposure. (e) NikA/FeL0 soaked in 50 mM DTT. (f) Partially hydroxylated O_2-bound intermediate formed following three successive back soaks of DTT-reduced NikA/FeL0 in DTT-free mother liquor, followed by O_2 exposure. Respective PDB IDs for parts a—f: 3MVW, 3MVW, 3MW0, 3MVY, 3MVX, 3MVZ.[302] Atom coloring: N (blue); O (red); Fe (orange).

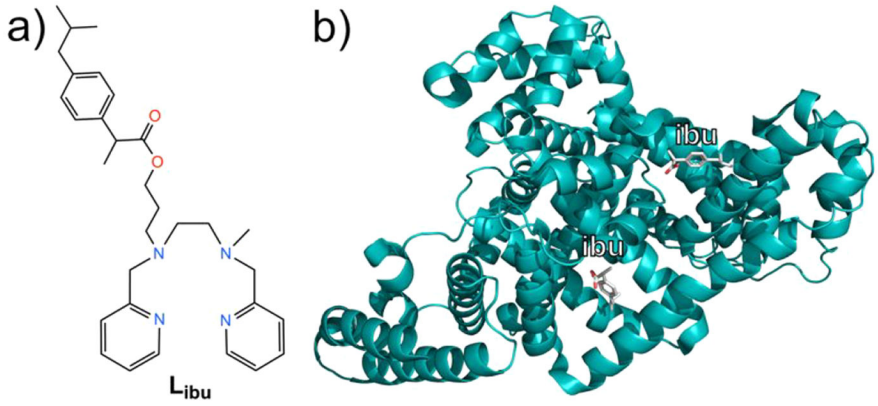

Figure 23.

(a) Fe-chelating complex L_{ibu}.[306] (b) Crystal structure of human serum albumin (HSA) with bound ibuprofen (abbreviated as “ibu”) highlighted in light gray (PDB ID: 2BXG).[307] Atom coloring: N (blue); O (red).

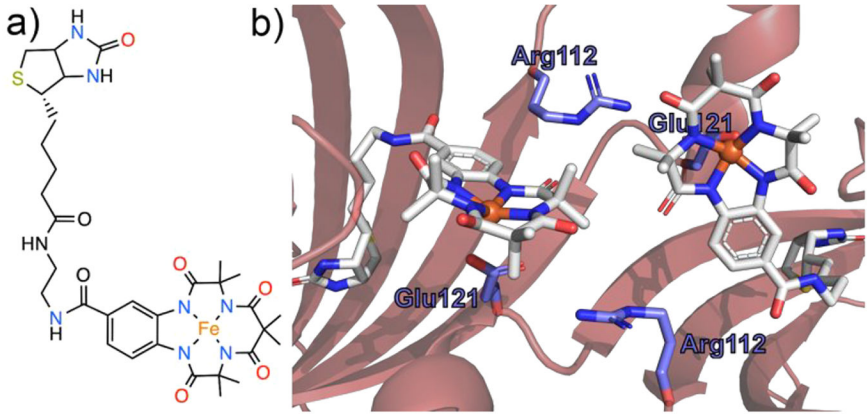

Figure 24.

(a) Fe-TAML$_{biot}$ with a C_4 linker. (b) Fe-TAML$_{biot}$ with a C_4 linker bound in Ser112Arg/Lys121Glu Sav. SCS mutations are highlighted in light blue (PDB ID: 6Y25).[311] Atom coloring: N (blue); O (red); Fe (orange).

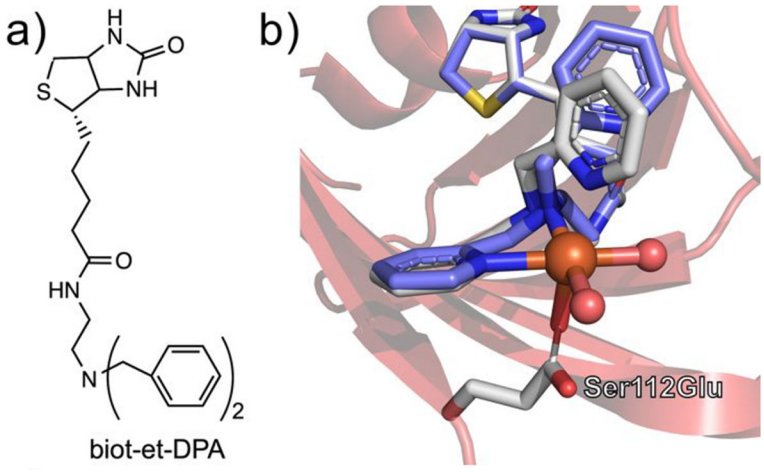

Figure 25.

(a) Fe^{III}-biot-et-dpa. (b) Crystal structure of Ser112Glu Sav-bound Fe^{III}-biot-et-dpa. Two configurations were observed (over-lapping, highlighted as light gray and blue) (PDB ID: 6UIY).[313] Atom coloring: N (blue,) O (red), Fe (orange).

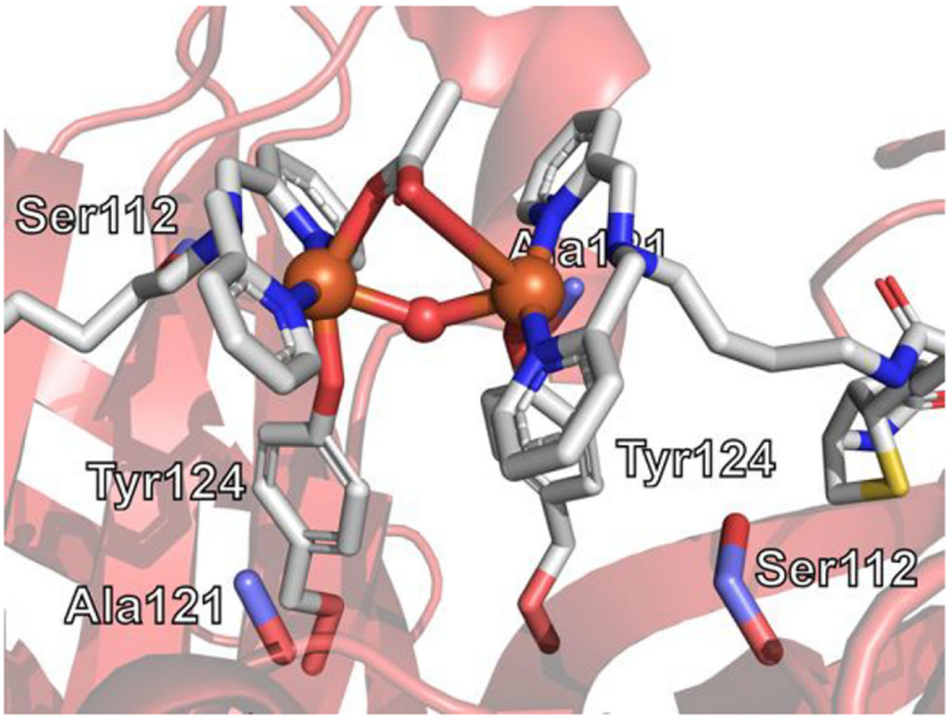

Figure 26.
Fe^{III}-biot-bu-dpa bound in Lys121Ala/Leu124Tyr Sav forming a [Fe^{III}-(μ-OH)-Fe^{III}] core. PCS residues are highlighted as light gray, and SCS in light blue (PDB ID: 6VP1).[317] Atom coloring: N (blue); O (red); S (yellow); Fe (orange).

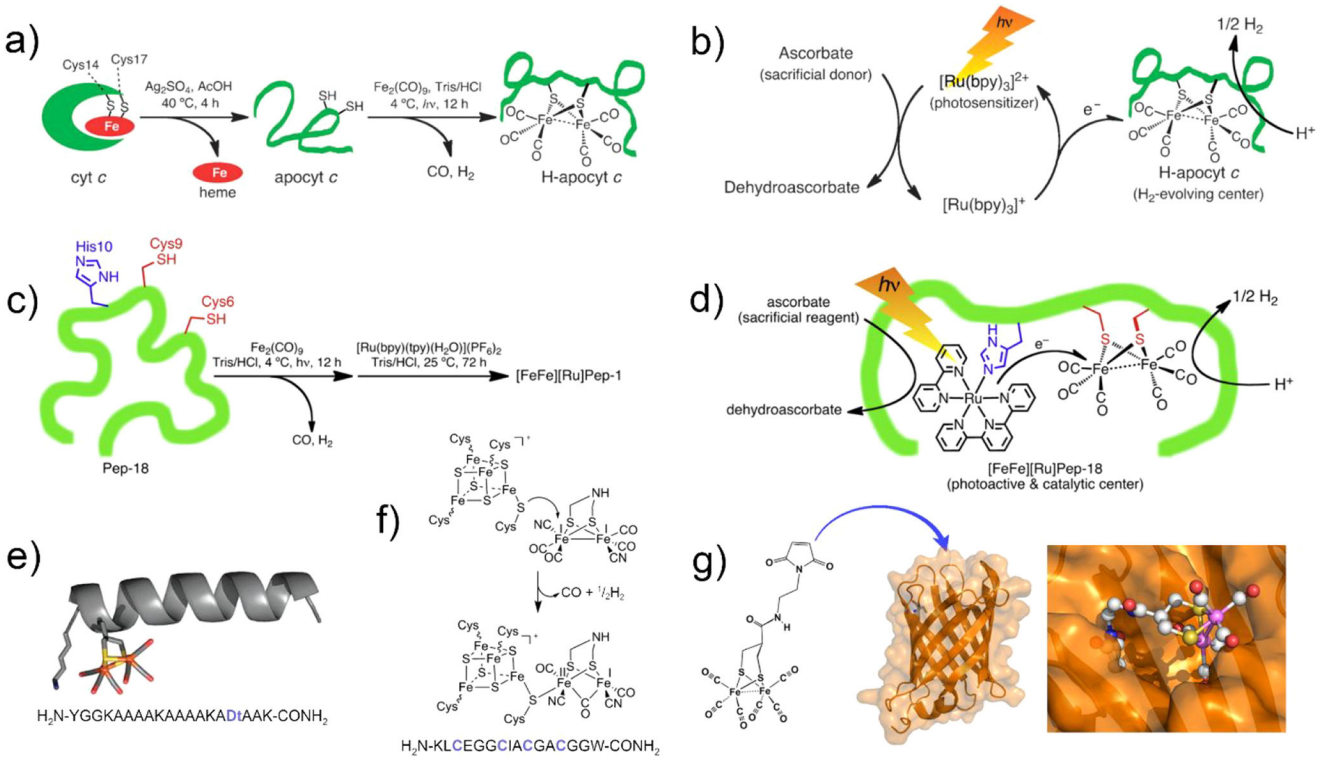

Figure 27.

Summary of H_2ase-inspired (μ-thiolato)diiron enzymes. (a) Synthetic process for the formation of C*c*-bound [$Fe(CO)_3$-(μ-S_{Cys})$_2$-$Fe(CO)_3$] and (b) ensuing H_2 production system.[320] Reproduced with permission from ref 320. Copyright 2011 Royal Society of Chemistry. (c) Synthetic process for the formation of Pep-18 [$Fe(CO)_3$-(μ-S_{Cys})$_2$-$Fe(CO)_3$] with bound $Ru(bpy)_3$ and (d) ensuing H_2 production assay system.[321] Reproduced with permission from ref 321. Copyright 2012 Elsevier. (e) Model of the [$Fe(CO)_3$-(μ-S_{Cys})$_2$-$Fe(CO)_3$] binding single-stranded α-helical maquette containing the dithiol UAA "Dt".[322] Reproduced with permission from ref 322. Copyright 2012 Royal Society of Chemistry. (f) Proposed schematic for [Fe_4S_4]-[$Fe_2(CO)_3(CN)_2$(adt)] bridge formation in the FdM maquette.[323] Reproduced with permission from ref 323. Copyright 2019 Royal Society of Chemistry. (g) Binding of a [$Fe(CO)_3$-(μ-S_{Cys})$_2$-$Fe(CO)_3$]-maleimide complex in the β-barrel protein nitrobindin.[324] Reproduced with permission from ref 324. Copyright 2014 American Chemical Society.

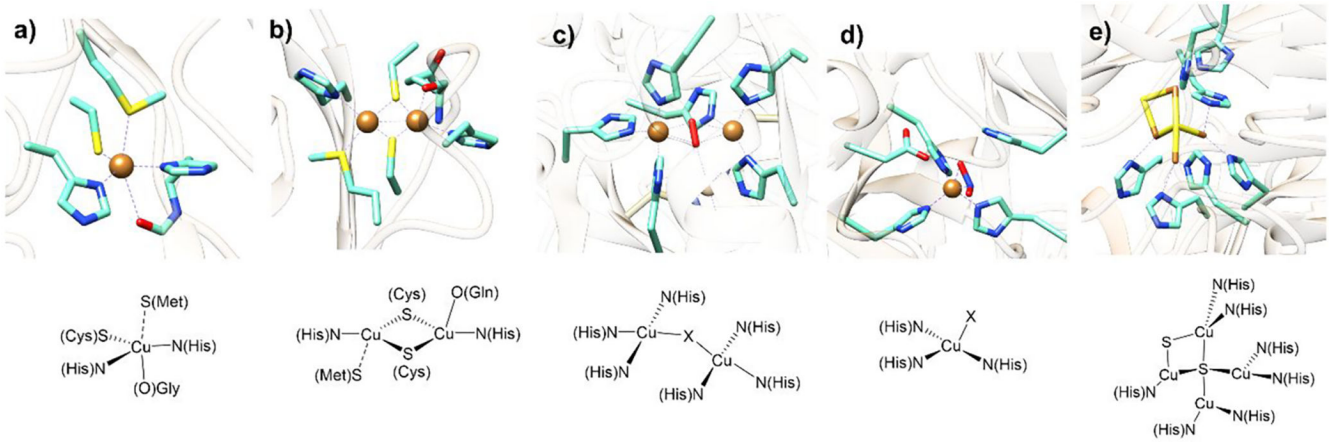

Figure 28.

Active site structures of several representative natural copper binding proteins. (a) T1Cu from *Pseudomonas aeruginosa* (PDB ID: 4AZU).[345] (b) Cu_A site of the cupredoxin domain from *Thermus thermophilus* cytochrome *ba3* oxidase (PDB ID: 2CUA).[346] (c) Substrate-bound (O_2) T3Cu site of laccase from *Melanocarpus albomyces* (PDB ID: 1GW0).[347] (d) Substrate-bound (nitrite) T2Cu site of *Alcaligenes xylosoxidans* nitrite reductase (PDB ID: 2XWZ).[319,348] (e) Cu_z site of the *Pseudomonas stutzeri* N_2OR (PDB ID: 3SBR).[349] Atom coloring: N (blue); C (cyan); O (red); S (yellow); Cu (copper).

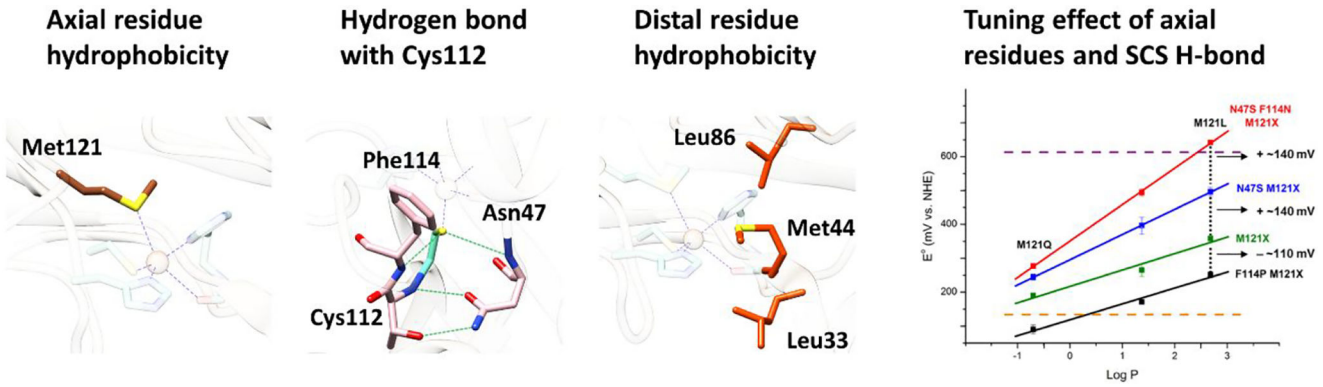

Figure 29.

Three SCS targets of reduction potential tuning in Cu-Az: the axial residue hydrophobicity, hydrogen bonding network, and distal residue hydrophobicity. The plot shows the cumulative effect when different strategies are combined (PDB ID: 4AZU).[345] Reprinted with permission from ref 377. Copyright 2011 Elsevier.

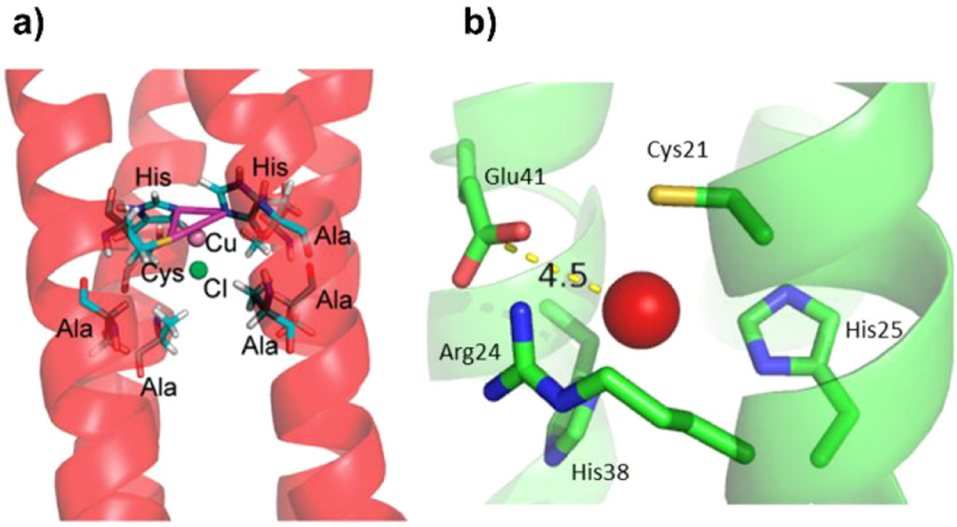

Figure 30.

(a) *De novo* designed T1Cu protein by Shiga et al. with SCS Ala residues. (b) *De novo* designed T1Cu protein by Koebke et al. with an axial Glu residue. Reprinted with permission from refs 395 and 396. Copyright 2010 and 2018 American Chemical Society.

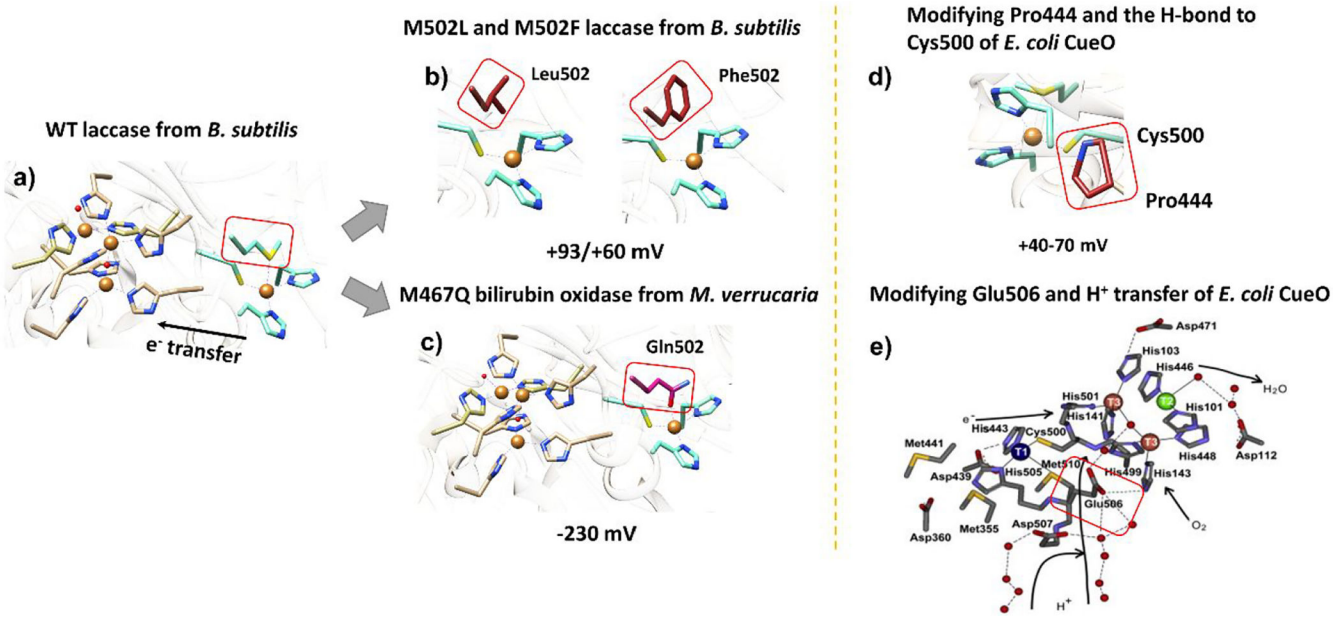

Figure 31.

(a) Structure of wild-type laccase from *B. subtilis* (PDB ID: 1GSK). The black arrow shows the electron transfer from the T1Cu to the T2/T3Cu site to reduce O_2. (b) Axial mutants of *B. subtilis* laccase modeled from the wild-type (PDB ID: 1GSK)[405] using UCSF Chimera.[406] (c) M467Q axial mutant of bilirubin oxidase from *M. verrucaria* (PDB ID: 6IQX).[407] (d) Modifying Pro444, the H-bond donor to the Cys residue of T1Cu in *E. coli* CueO (PDB ID: 1KV7).[408] (e) Modifying Glu506, a proton transfer mediator residue in *E. coli* CueO. Reprinted with permission from ref 409. Copyright 2012 Elsevier.

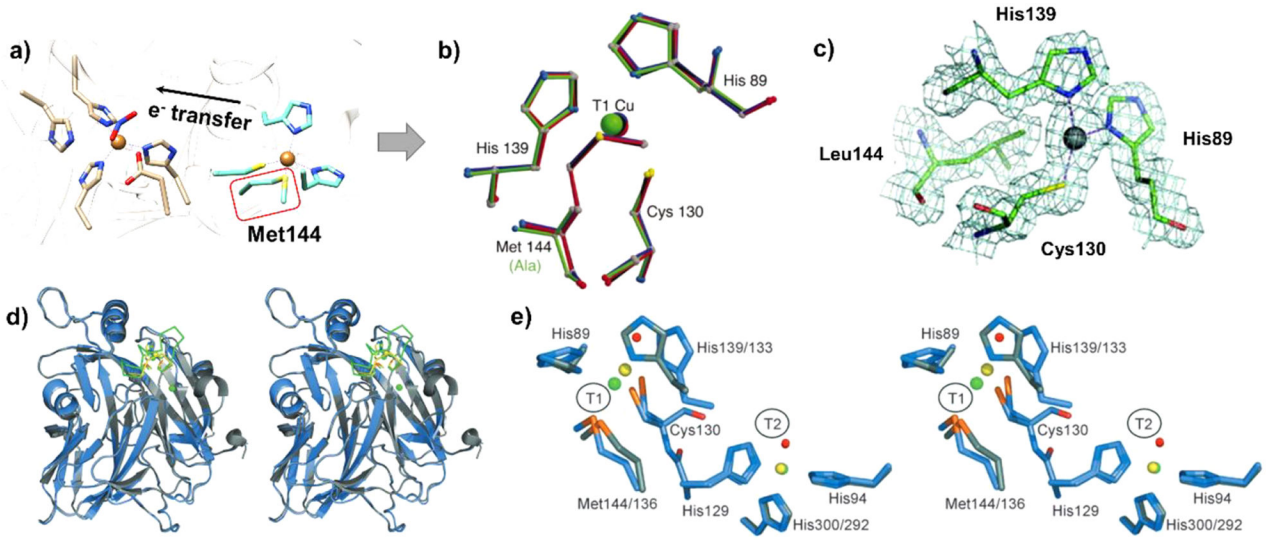

Figure 32.

(a) Structure of the T1Cu (right, cyan) and the T2Cu (left, tan) of AxNiR (PDB ID: 2XWZ).[348] (b and c) Axial residue engineering of the T1Cu in AxNiR. (d and e) NiR with the T1Cu loop exchanged with the loop from amicyanin. Reprinted with permission from refs 419-421. Copyright 2008, 2005, and 2002 Wiley-VCH, Elsevier, and Elsevier.

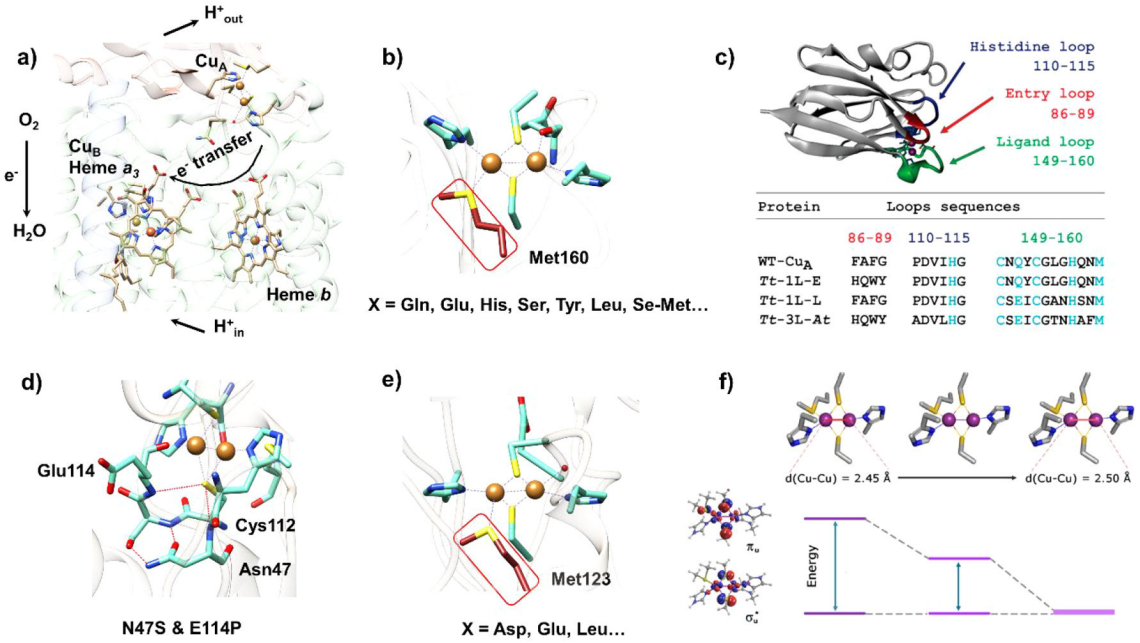

Figure 33.

(a) Schematic of the O_2 reduction reaction catalyzed by heme-copper oxidase (cytochrome *ba3* oxidase of *T. thermophilus*, PDB ID: 1XME).[425] The electron transfer from Cu_A through heme *b* to heme *a*3 and the proton pumping pathway are shown with black arrows. (b) Mutation of the axial Met of the Cu_A from *T. thermophilus* cytochrome *ba3* oxidase (PDB ID: 2CUA).[346,426] (c) Loop swapping strategy to tune the Cu_A center.[427] (d) Hydrogen bonding network surrounding the artificial Cu_A site in engineered azurin. (e) Mutation of the axial Met of the artificial Cu_A in engineered azurin (PDB ID: 1CC3).[426] (f) Tuning of the π_u and $<_u$* energy gap by axial ligand mutation of *T. thermophilus* Cu_A cupredoxin.[428] Parts c and f were reprinted with permission from ref 428. Copyright 2019 American Chemical Society.

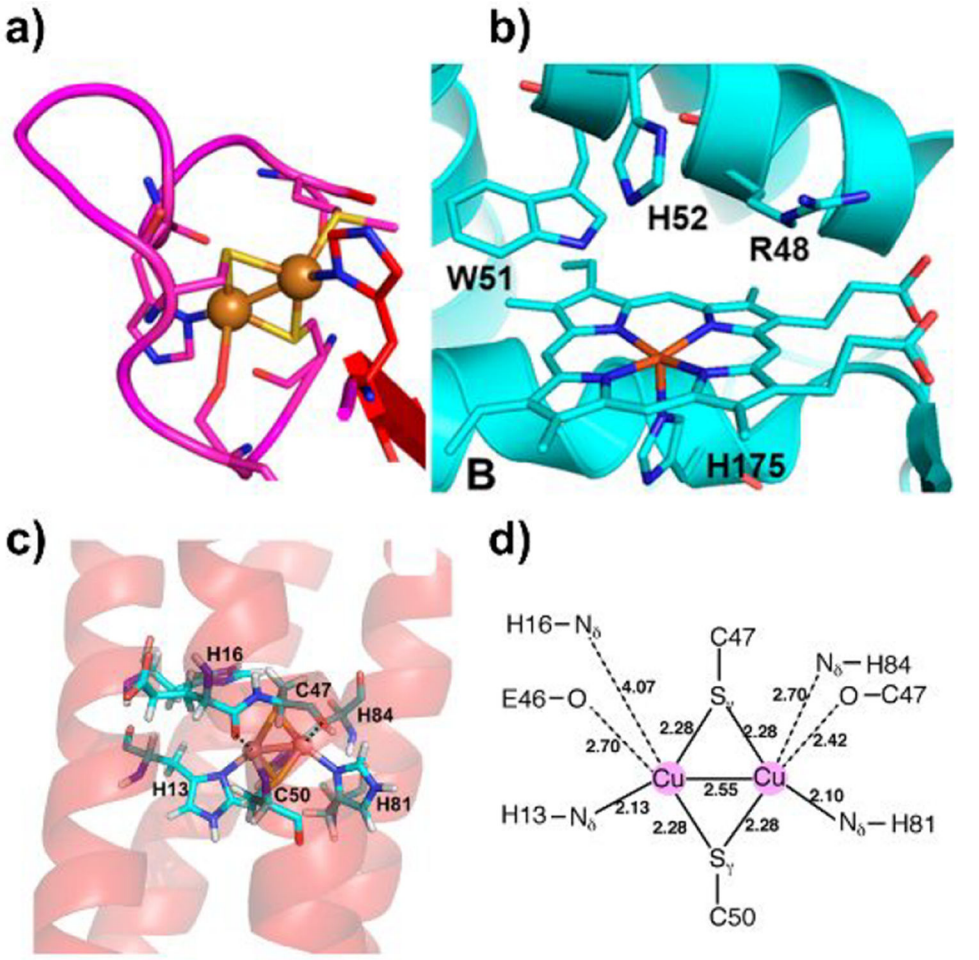

Figure 34.

(a) Cu_A site of *Tt*Cu_A. (b) Original heme pocket of C*c*P. The three residues Trp51, His52, and Arg48 were engineered as the PCS core for Cu_A. (c) *De novo* designed Cu_A protein and (d) Cu_A structure. Reprinted with permission from references 445 and 446. Copyright 2012 and 2020 American Chemical Society.

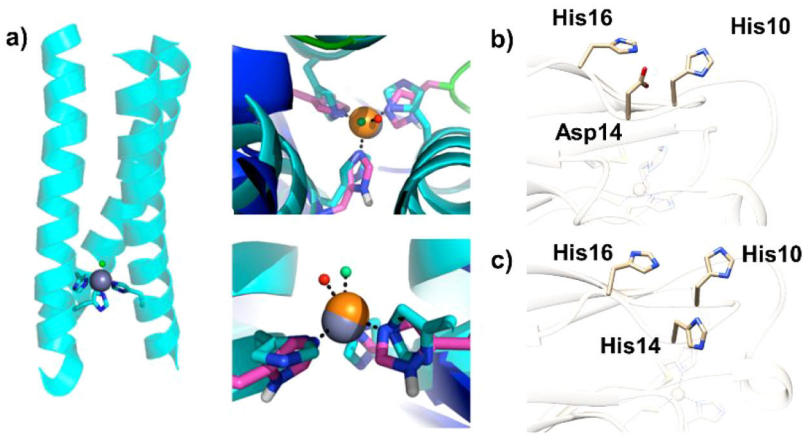

Figure 35.

(a) *De novo* designed NiR peptide and the active site structure. Reprinted with permission from ref 450. Copyright 2018 American Chemical Society. (b and c) Structures of two AzNiR mutants modeled by UCSF Chimera using PDB ID 4AZU.[345,406]

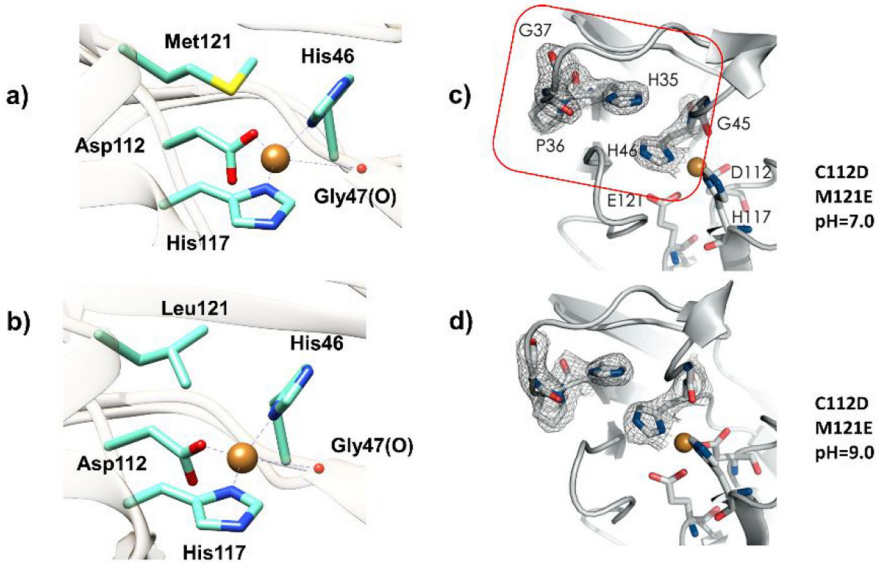

Figure 36.

(a) C112D Az (PDB ID: 3FQY). (b) C112D/M121L Az (PDB ID: 3FPY).[458] (c) C112D/M121E Az at neutral pH. The SCS residues enforcing the binding configuration of the T0Cu site are circled in red. (d) C112D/M121E Az crystallized at basic pH. Reprinted with permission from ref 459. Copyright 2010 American Chemical Society.

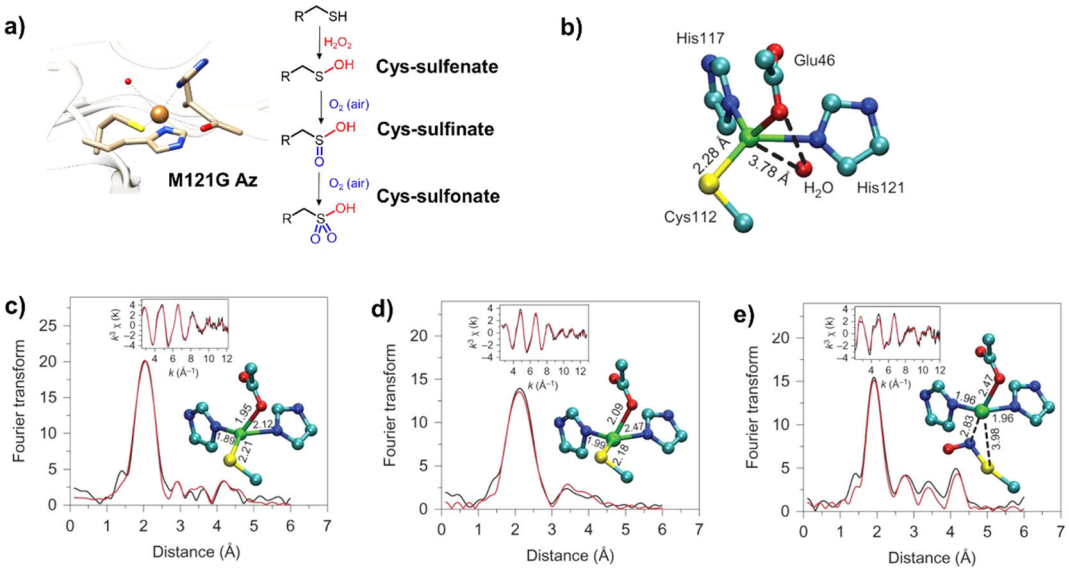

Figure 37.

(a) M121G azurin and the oxidative modification (PDB ID: 4MFH).[103] The first step could only be achieved by H_2O_2 supported by the experiment with isotope labeled agents. The sulfenate could no longer be oxidized by H_2O_2, but further oxidation by O_2 from air was observed. (b) Active site structure of H46E/F114P Cu^{II}-Az. (c–e) EXAFS results for (c) M121H/H46E/F114P Cu^{II}-Az, (d) M121H/H46E/F114P Cu^{I}-Az, and (e) NO-treated M121H/H46E/F114P Cu^{II}-Az. Reprinted with permission from ref 276. Copyright 2016 Springer Nature.

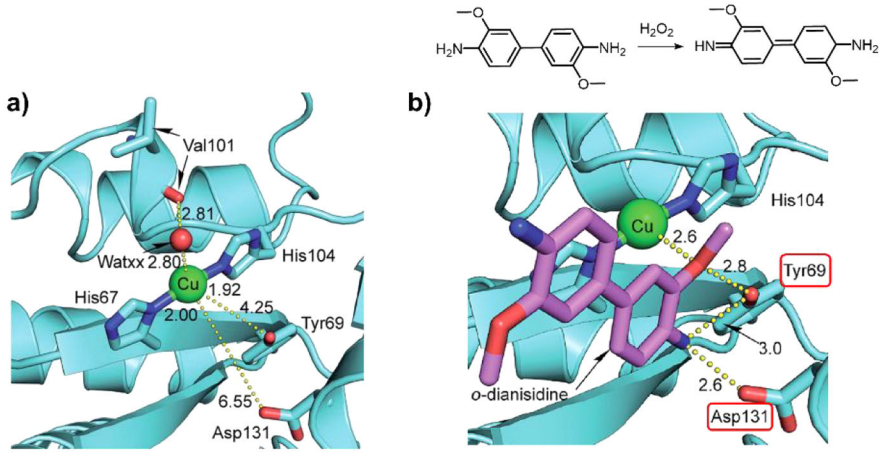

Figure 38.

(a) Copper binding form of engineered 6-phosphogluconolactonase (PDB ID: 4TM8).[464] (b) Peroxidation of o-dianisidine catalyzed by the Cu enzyme and the computationally docked substrate in the active site. The Asp131 and Tyr69 residues were believed to align the substrate. Reprinted with permission from ref 464. Copyright 2015 Royal Society of Chemistry.

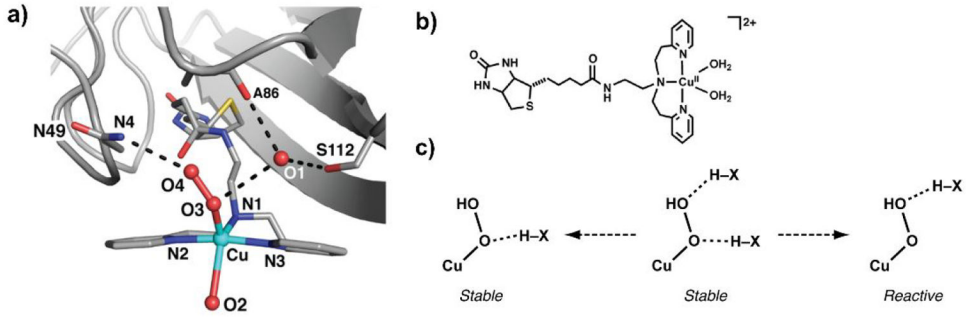

Figure 39.

(a) Crystal structure of the H_2O_2-bound Sav-Cu protein (PDB ID: 6ANX). (b) Structure of the copper complex conjugated to Sav. (c) Proposed mechanism to control Cu-OOH stability by different positioning of hydrogen bonds. Reprinted with permission from ref 465. Copyright 2017 American Chemical Society.

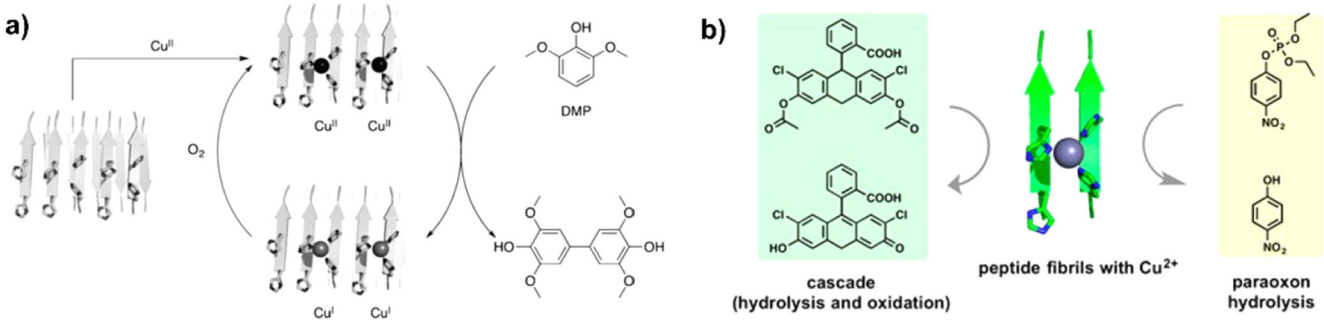

Figure 40.

Schematics of (a) Cu-bound amyloid assembly protein catalyzing the oxidation of DMP and (b) Cu-bound amyloid assembly protein catalyzing the cascade hydrolysis/oxidation of a fluorescence derivative and the hydrolysis of paraoxon. Reprinted with permission from refs 472 and 473. Copyright 2016 and 2018 Wiley-VDH and American Chemical Society.

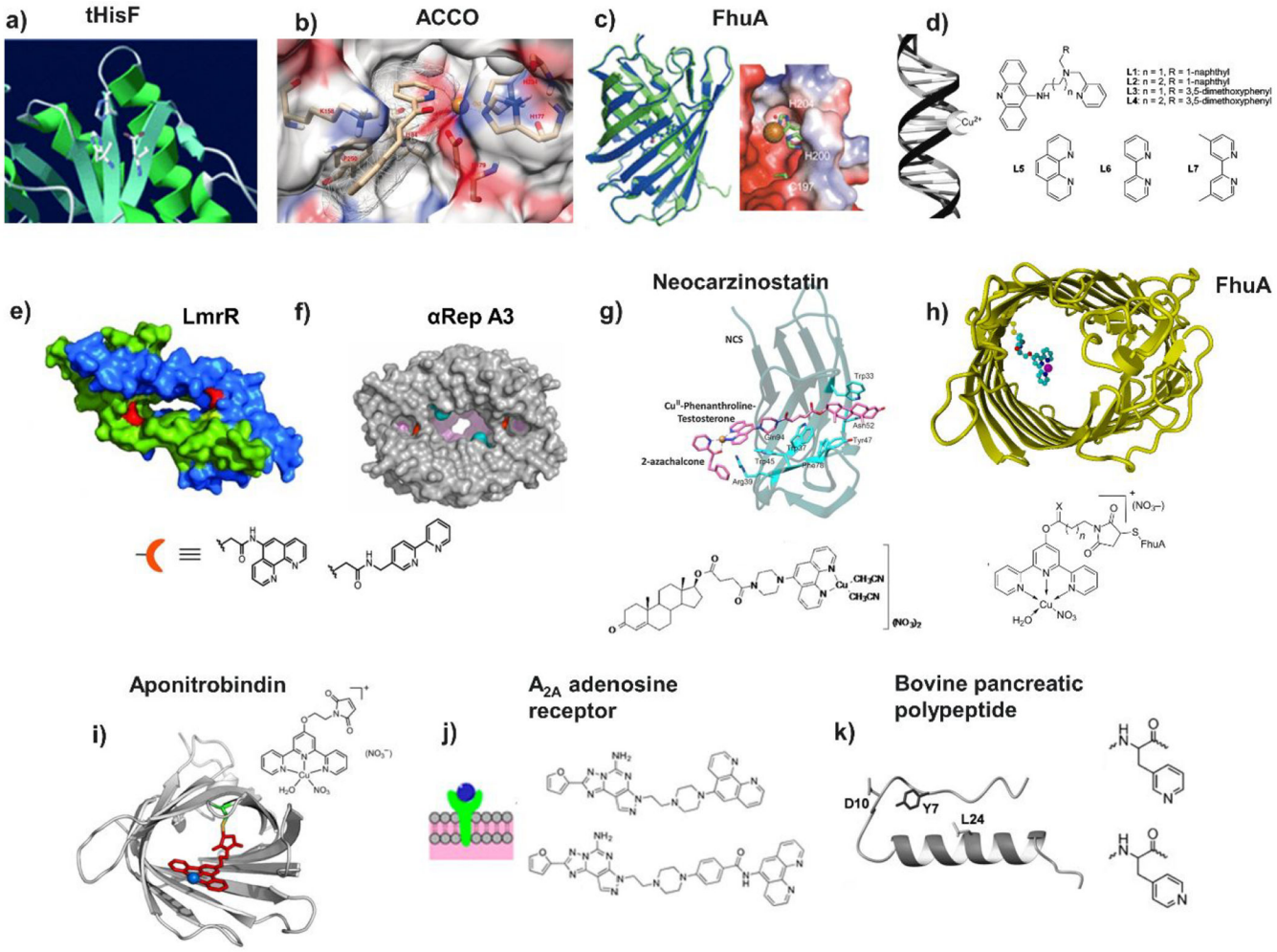

Figure 41.

Examples for artificial Diels—Alderase. (a) tHisF protein with the copper binding site. (b) ACCO protein with the copper-bound cavity and docked substrate. (c) FhuA protein and the copper binding site. (d) Oligonucleotide and the conjugated copper complexes. (e) LmrR protein with the conjugation sites for copper complexes shown in red. (f) αRep A3 protein with the central pocket to conjugate copper complexes. (g) Neocarzinostatin protein with the copper complex noncovalently docked in the pocket via the testosterone tail. (h) FhuA protein with the copper complex conjugated. (i) apo-nitrobindin protein with the covalently conjugated copper complex. (j) Schematic representation that the copper complex with the adenosine tail may bind to the cell-surface receptor and catalyze the D—A reaction. (k) Bovine pancreatic polypeptide and the unnatural amino acid residues introduced to form a copper binding site. Reprinted from references 367, 369, 477-485. Copyright 1021, 2009, 2010, 2019, 2019, 2011, 2017, 2016, 2016, 2016, and 2018 Wiley-VCH and American Chemical Society.

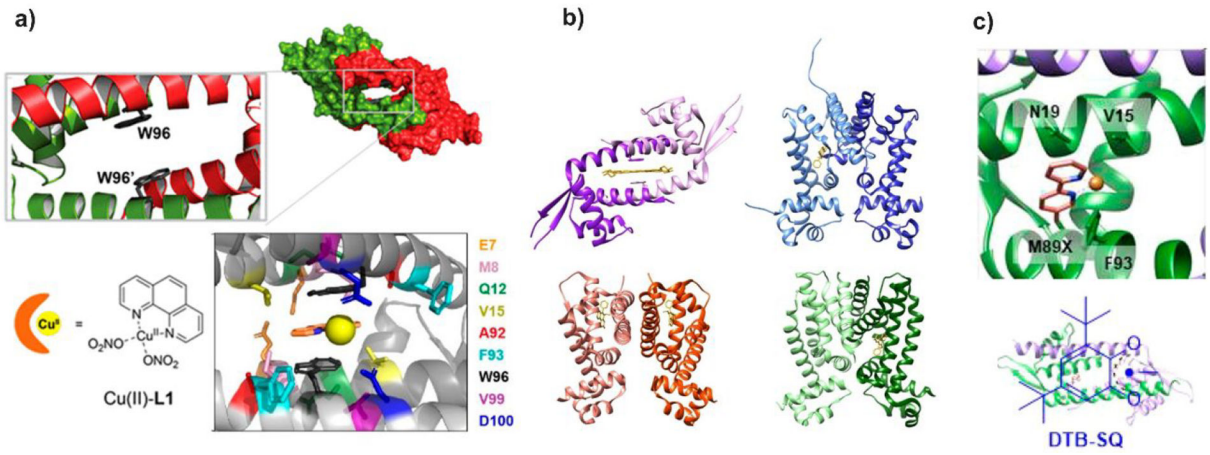

Figure 42.

(a) LmrR protein with two tryptophans that docks the aromatic ligand of the copper complex. The active site structure at the bottom right shows the targets for SCS mutagenesis studies. (b) Different proteins from the TetR family that were engineered for F-C catalysis. The proteins are LmrR (top left), CgmR (top right), RamR (bottom left), and QacR (bottom right). (c) The Ala_{Bpy} LmrR mutant that stabilizes a semiquinone radical. Reprinted with permission from references 286, 368, 492, and 493. Copyright 2017, 2015, and 2020 American Chemical Society and Wiley-VCH.

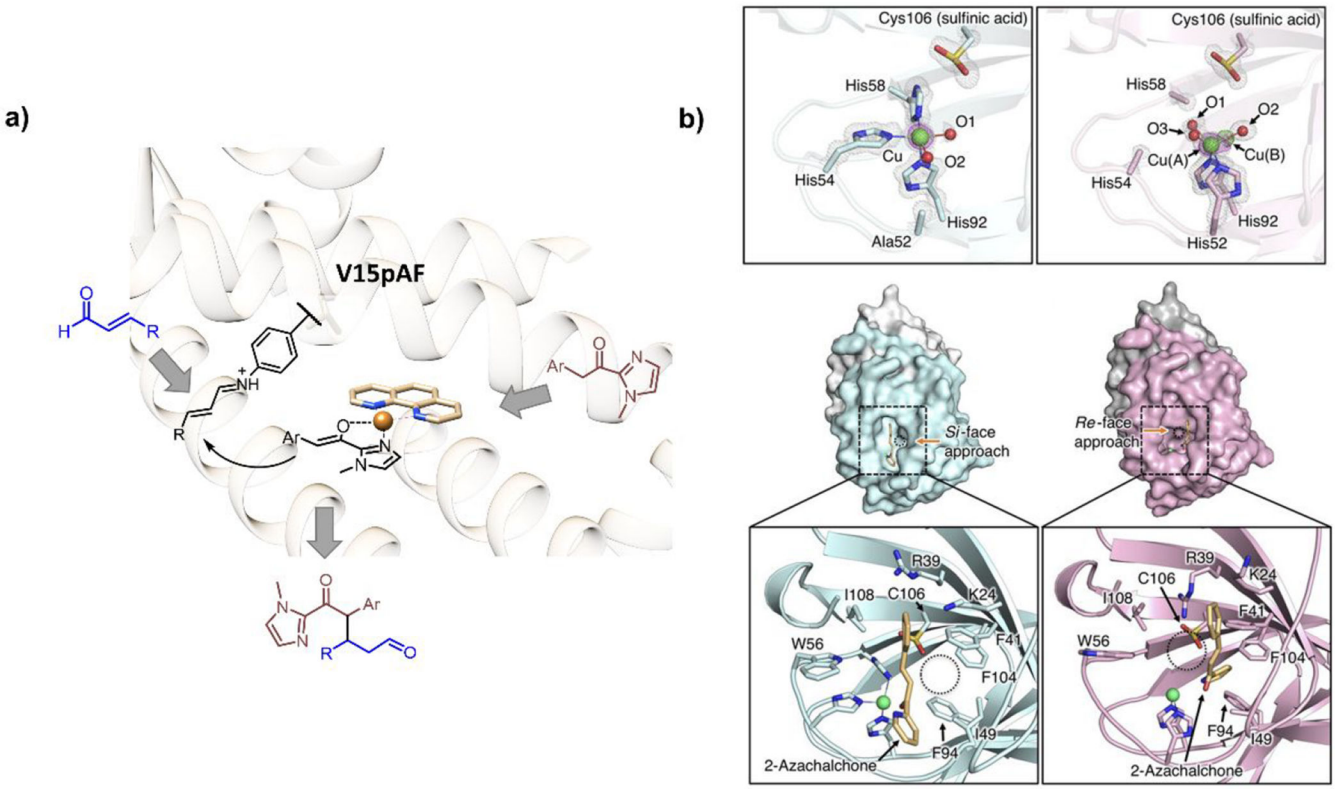

Figure 43.

(a) LmrR variant catalyzing the Michael addition reaction with an aniline moiety on an unnatural amino acid residue to activate the ketone Michael acceptor. The structure was modeled from PDB ID 6R1L,[492] and the scheme was adapted from ref 464. (b) Two cupin variants with different enantioselectivities of the Michael addition reaction. The insets at the bottom demonstrate how the hydrogen bond with Cys106 changes the orientation of the substrate and thereby alters the product enantioselectivity. Reprinted with permission from refs 495 and 496. Copyright 2020 Nature Publishing Group and Wiley-VCH.

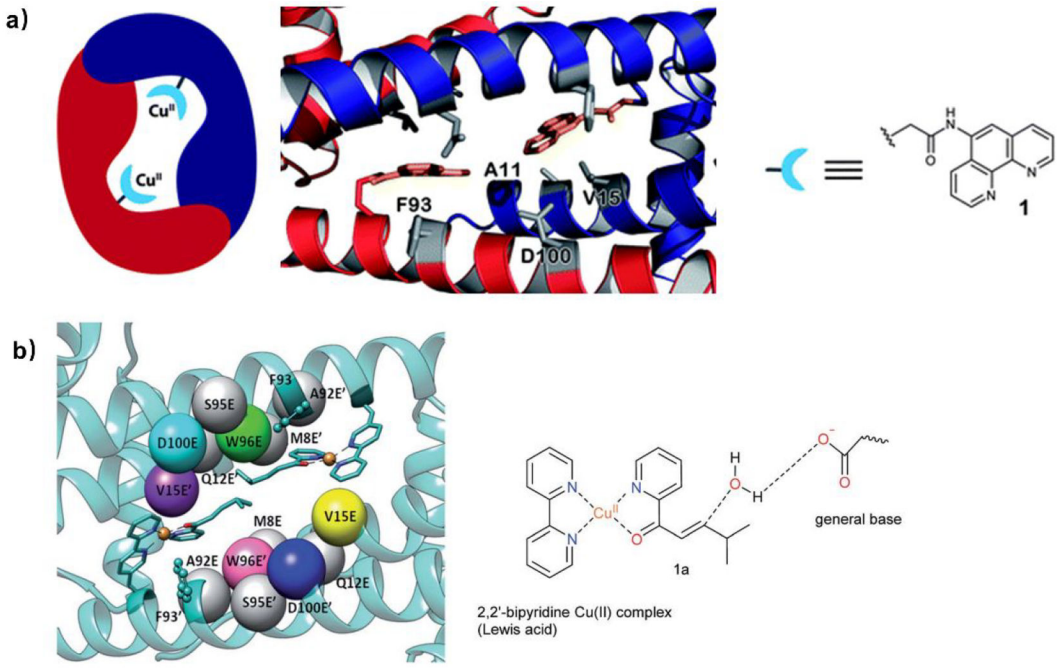

Figure 44.

(a) LmrR variant as a hydratase with important SCS residues shown as sticks. (b) LmrR variant with an Ala_{Bpy} residue to bind copper and carry out hydration of alkene. Reprinted with permission from refs 498 and 499. Copyright 2013 and 2017 Royal Society of Chemistry.

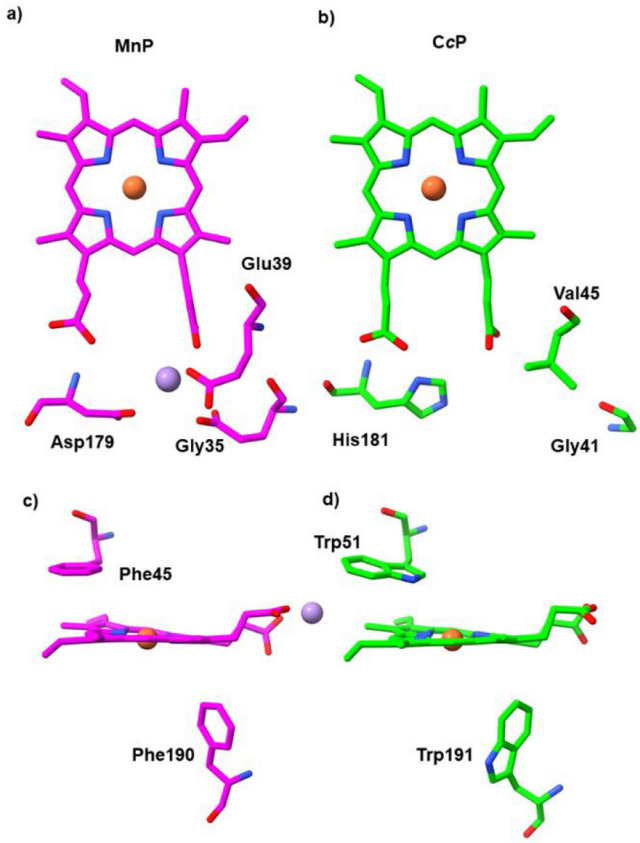

Figure 45.

(a) Mn-binding site in MnP (PDB ID: 1MNP).[513] (b) Putative Mn-binding site in C*c*P, forming MnC*c*P (PDB ID: 2CCP).[139] (c) Position of Phe45 and Phe190 around the active site of MnP. (d) Position of Trp51 and Trp191 around the active site of C*c*P. Atom coloring: N (blue); O (red); C_{MnP} (magenta); C_{CcP} (green); Fe (orange); Mn (lilac).

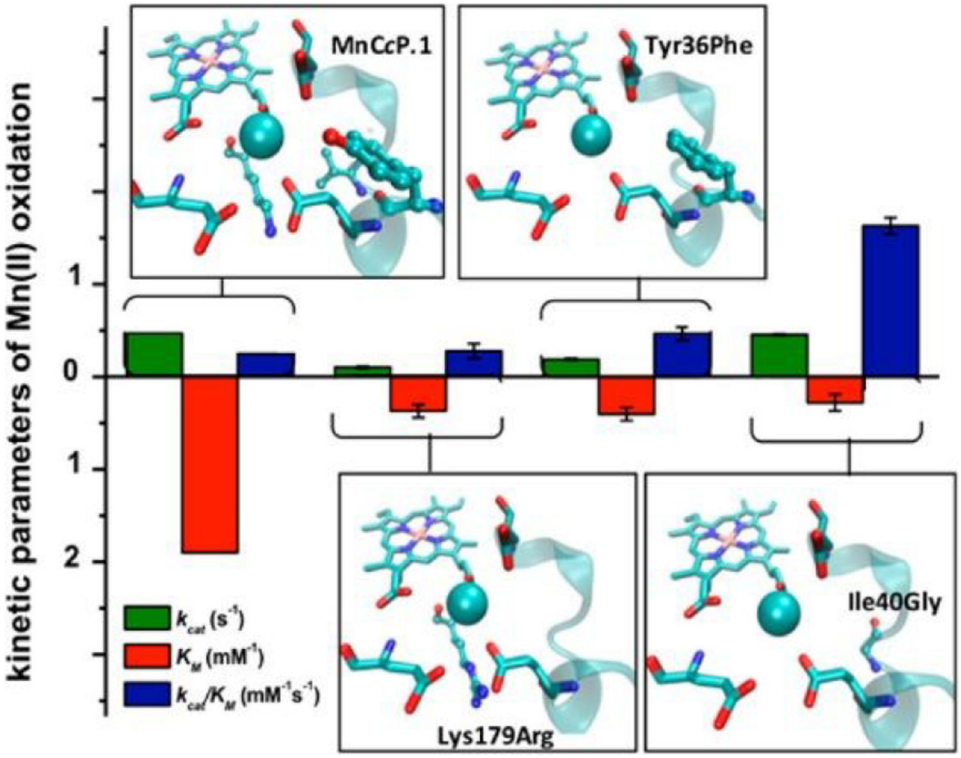

Figure 46.

Different SCS residues included to MnC*c*P.1 and their effects on the catalytic efficiency. Reprinted with permission from ref 515. Copyright 2016 American Chemical Society.

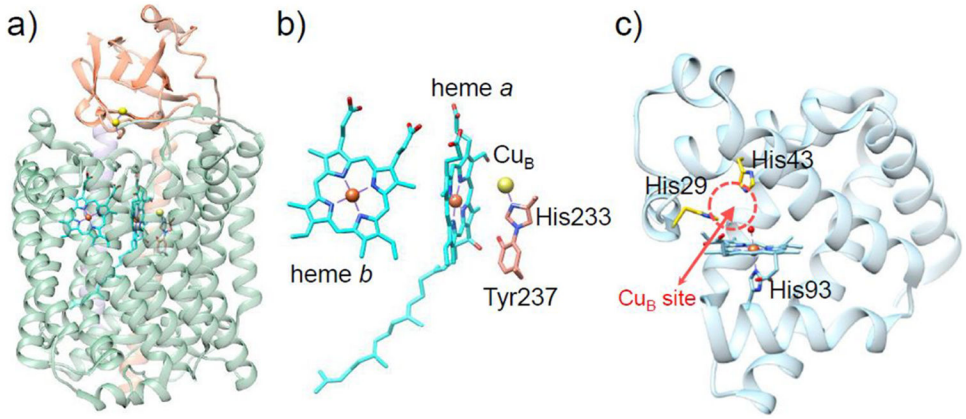

Figure 47.

(a) Crystal structure of ba_3 CcO (PDB ID: 3S8F).[516] (b) Structure of the catalytic site. The low-spin heme *b* and heme a_3 are depicted in cyan; Cu_B is indicated by a yellow sphere. The cross-linked residues His233 and Tyr237, located in proximity of the catalytic site, are shown. (c) Crystal structure of L29H/F43H Mb (PDB ID: 4FWZ).[517]

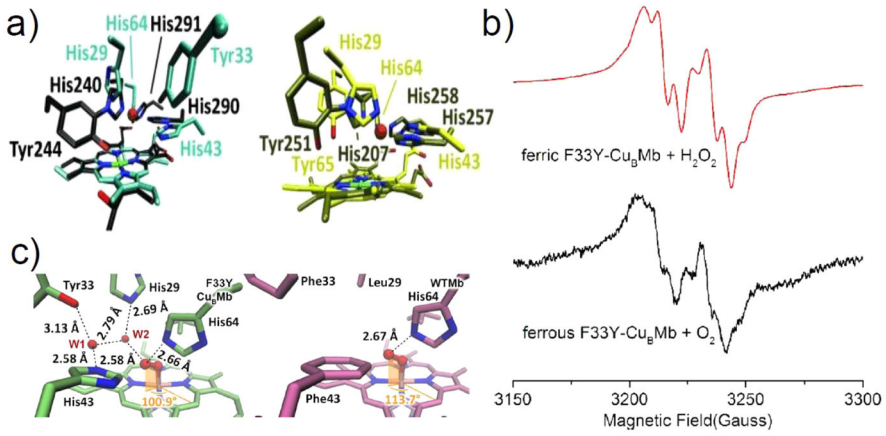

Figure 48.

(a) Structures and computer models of native and designed oxidases. Left panel: overlay of the crystal structures of bovine C*c*O(black) and E-F33Y-Cu_BMb (cyan). Right panel: overlay of the crystal structures of *cbb*$_3$ HCO from *Pseudomonas stutzeri* (tan) and the E-G65Y-Cu_BMb computer model (yellow). The Cu_B copper is represented as an orange sphere. N (blue); O (red); Fe (green). Reproduced with permission from ref 517. Copyright 2012 John Wiley & Sons. (b) EPR spectra of ferric F33Y-Cu_BMb reacted with 1 equiv of H_2O_2 (red) and ferrous F33Y-Cu_BMb with O_2 (black). Reprinted with permission from ref 521. Copyright 2014 American Chemical Society. (c) Crystal structure of oxy-F33Y-Cu_BMb (PDB ID: 5HAV, left panel) compared with that of oxy-WT-Mb (PDB ID: 1A6M).[523] Reprinted with permission from ref 522. Copyright 2016 American Chemical Society.

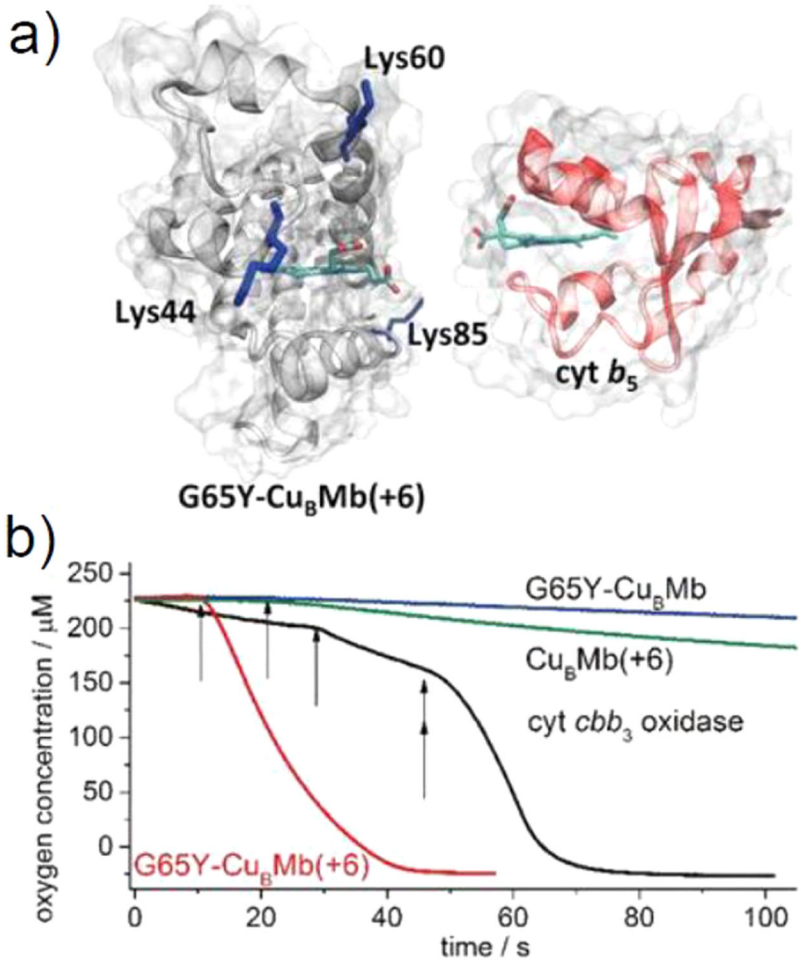

Figure 49.

(a) Structures of G65Y-Cu$_B$Mb(+6), showing the engineered Lys in blue, and cyt b_5 (PDB ID: 1CYO).[526] (b) Oxidase activity of G65Y-Cu$_B$Mb(+6) in comparison with that of native cyt cbb_3 oxidase. The black arrows indicate the addition of reductant, and the double arrow shows the injection of native cyt cbb_3 oxidase. Reprinted with permission from ref 525. Copyright 2015 American Chemical Society.

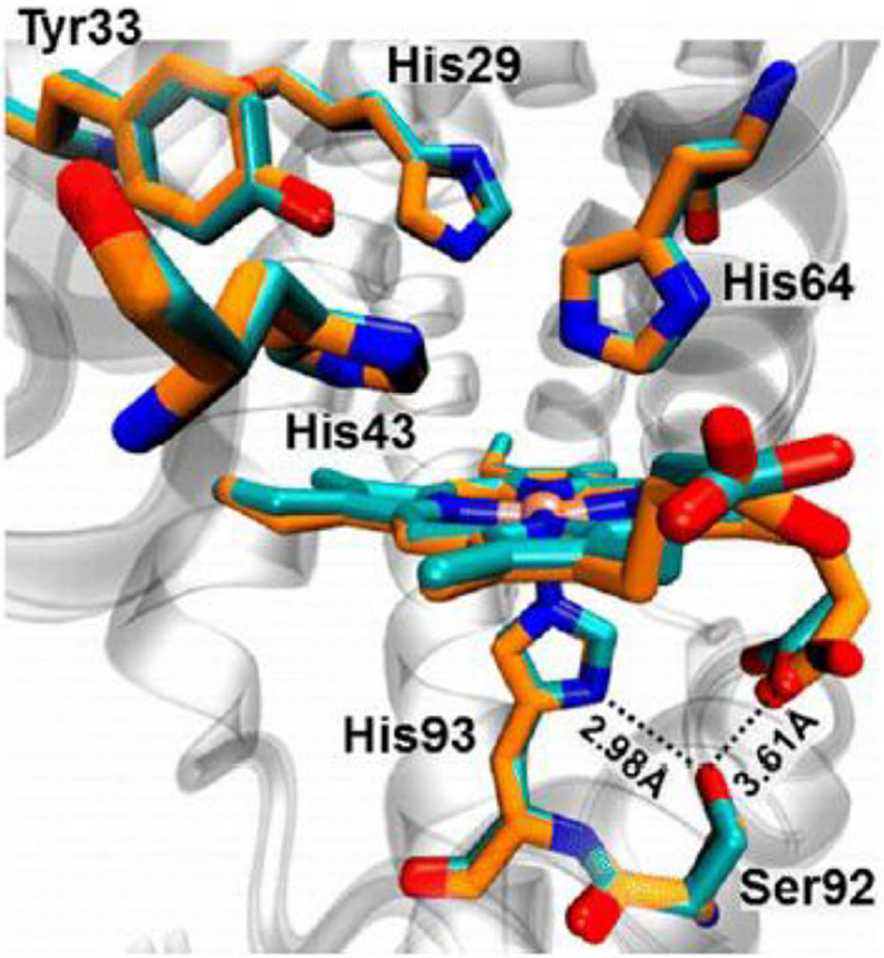

Figure 50.

Overlay of the crystal structures of F33Y-Cu_BMb (PDB ID: 4FWX, cyan)[517] and S92A-F33Y-Cu_BMb (PDB ID: 4TYX, orange).[527] Heme *b* and the side chains of His29, His43, His64, Tyr33, His93, and Ser/Ala92 are shown in licorice. Ser92 forms H-bonds with heme propionate and His93. Reprinted with permission from ref 527. Copyright 2014 American Chemical Society.

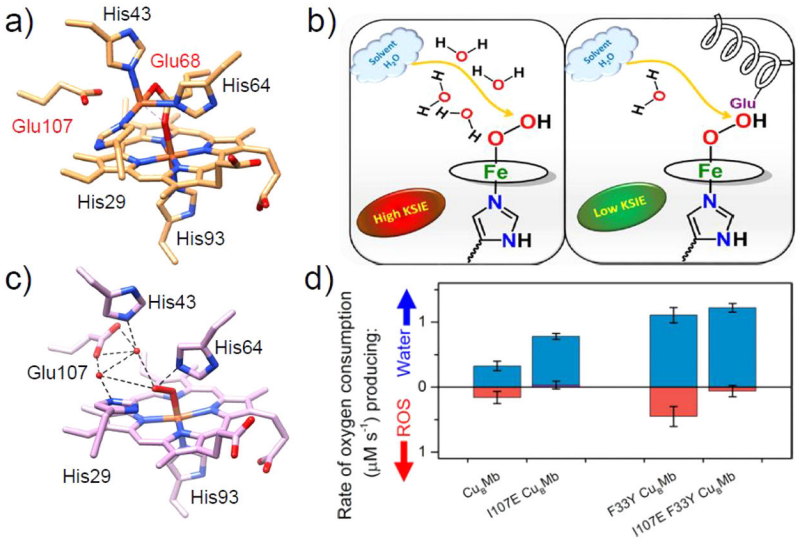

Figure 51.

(a) Crystal structure of Fe_B^{II}-V68E/I107ECu_BMb (PDB ID: 3M39).[529] (b) Cartoon showing that incorporation of the Glu residue near the active site facilitates the proton transfer from the external solvent to the active site, which results in lower KSIE. (c) Structure of the active site of oxy-I107E-Cu_BMb (PDB ID: 7L3Y).[530] (d) Rates of O_2 consumption yielding water (blue) or reactive oxygen species (ROS) (red). Parts c and d are reprinted with permission from ref 530. Copyright 2021 American Chemical Society.

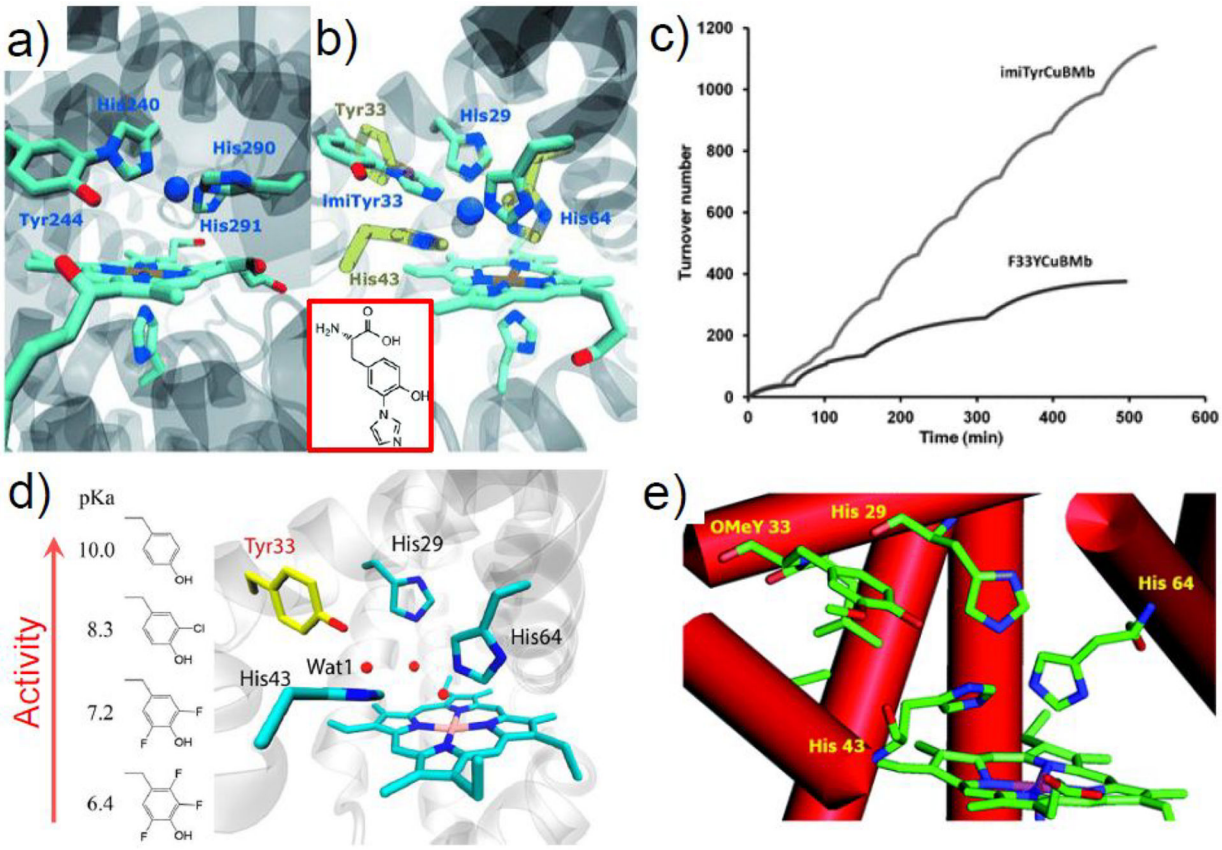

Figure 52.

(a) Cu_B site of C*c*O (bovine numbering). (b) Structural model overlay of imiTyrCu_BMb (cyan) and F33Y Cu_BMb (yellow). (Inset) Chemical structure of imiTyr. (c) O_2 reduction turnover number measured during the stepwise addition of O_2. The reduction was catalyzed by imiTyrCu_BMb or F33Y Cu_BMb. Reprinted with permission from ref 532. Copyright 2012 Wiley-VCH. (d) Crystal structure of F33Y/L29H/F43H swMb (F33Y Cu_BMb, PDB ID: 4FWX)[517] and pK_a values of the Tyr and Tyr analogs. From top to bottom: Tyr, 3-chlorotyrosine (ClTyr), 3,5-difluorotyrosine (F2Tyr), and 2,3,5-trifluorotyrosine (F3Tyr). The red arrow indicates increased activity with the increased pK_a values of Tyr and Tyr analogs. Reprinted with permission from ref 533. Copyright 2015 American Chemical Society. (e) Structural model of the OMeY Mb mutant, constructed based on the crystal structure of F33Y Cu_BMb (PDB ID: 4FWX).[517] Reprinted from ref 534 with permission from The Royal Society of Chemistry.

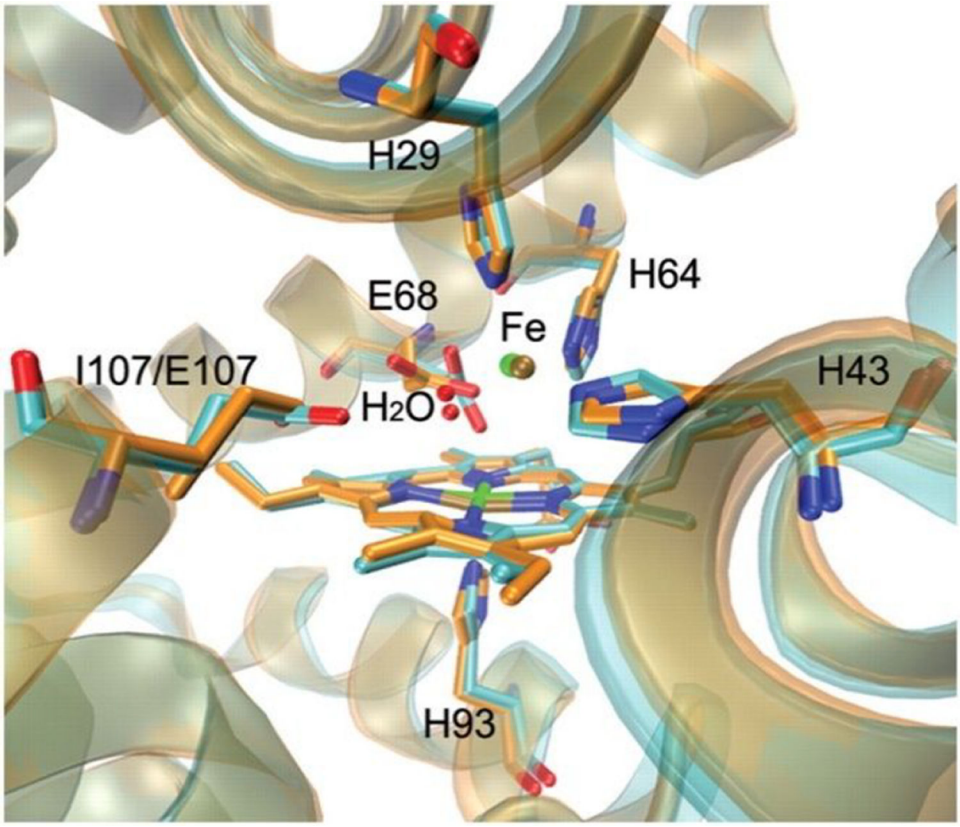

Figure 53.
Overlay of Fe^{II}-Fe_BMb and Fe^{II}-I107E Fe_BMb: Fe^{II}-I107E Fe_BMb, PDB ID: 3M39 (cyan); Fe^{II}-I107E Fe_BMb, PDB ID: 3K9Z (orange).[529] Reprinted with permission from ref 529. Copyright 2010 National Academy of Sciences.

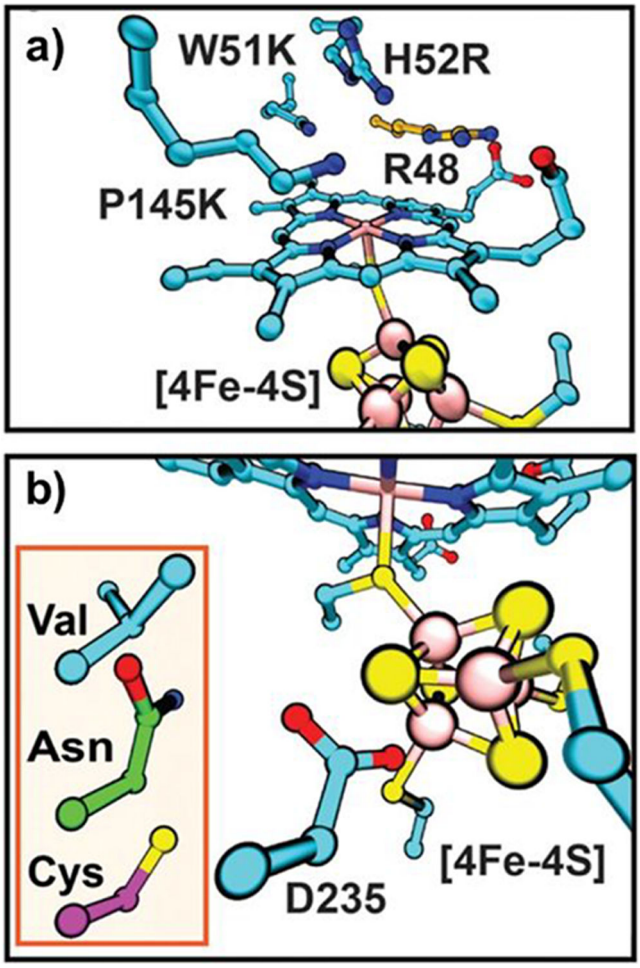

Figure 54.

(a) Computational model of the SiRC*c*P substrate-binding site with mutations W51K, H52R, P145K (cyan), and Arg48 (orange). (b) Computational model of the mutations D235V (SiRC*c*P.1, cyan), D235N (SiRC*c*P.2, green), and D235C (SiRC*c*P.3, magenta) in SiRC*c*P. Reproduced with permission from ref 539. Copyright 2018 American Association for the Advancement of Science.

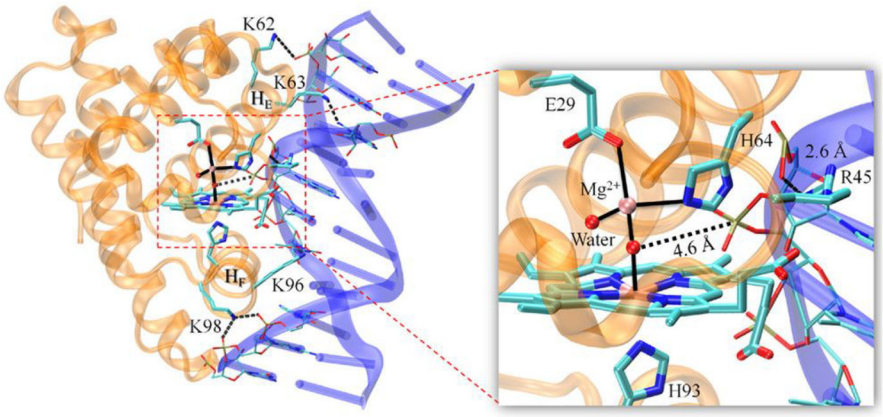

Figure 55.

Docking structure of the Mg^{2+}-L29E Mb-DNA complex (left) and enlarged view of the Mg^{2+}-heme heterodinuclear center (right), highlighting the coordination of the Mg2+ ion and the H-bonding interactions with the sugar phosphate group of DNA. Reprinted with permission from ref 508. Copyright 2020 American Chemical Society.

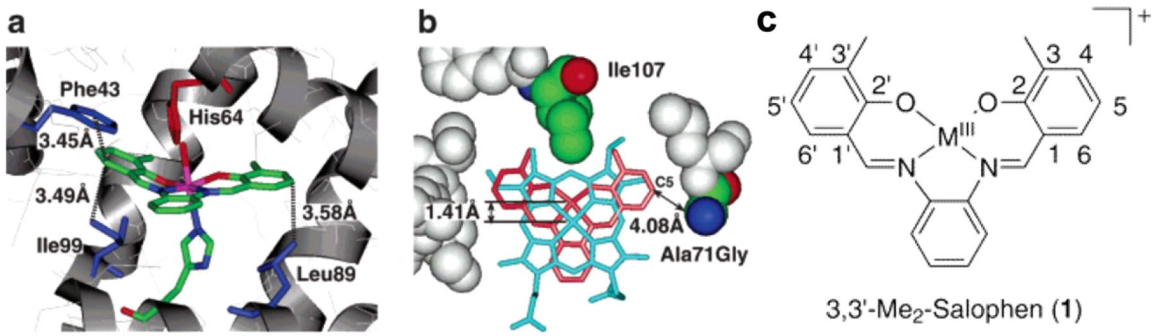

Figure 56.

Active site structure of Mn-1-apo-A71G Mb: (a) side and (b) top views. The heme of met-Mb[128] (blue) is superimposed on Mn-1-apo-A71GMb. (c) Metal-salophen complex (**1**) Reprinted with permission from ref 540. Copyright 2005 American Chemistry Society.

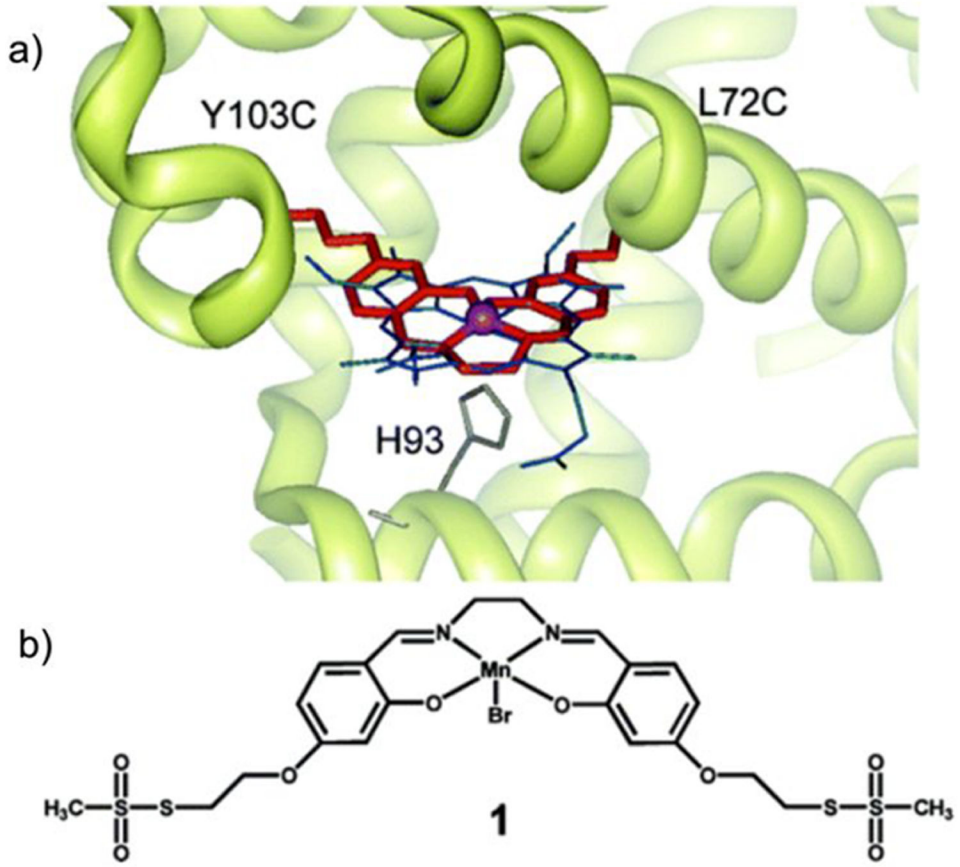

Figure 57.

(a) Computer model of Mb(L72C/Y103C) with **1** covalently attached overlaid with heme. (b) Complex **1**. Reprinted with permission from ref 541. Copyright 2004 American Chemistry Society.

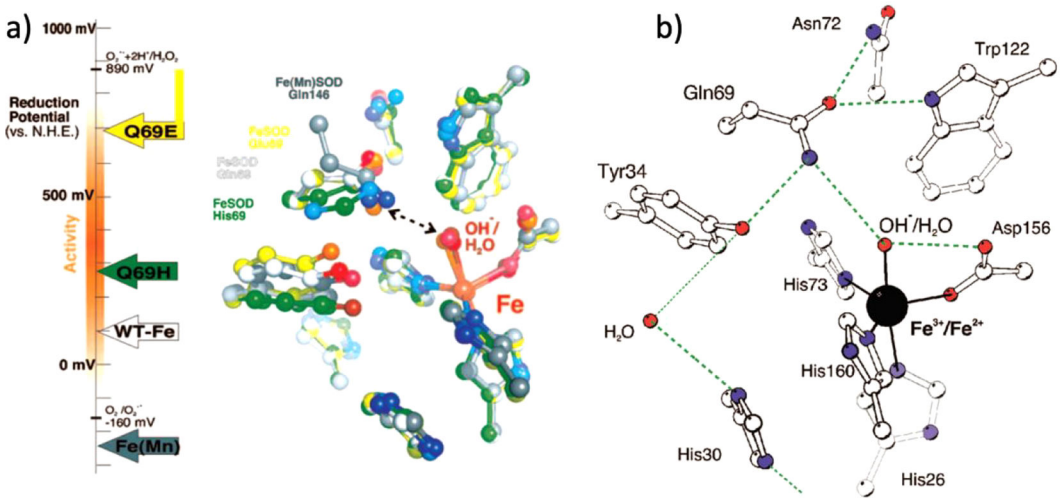

Figure 58.

(a) Redox tuning over almost **1** V of Fe-containing superoxide dismutase. (b) Hydrogen bonds present in the active sites of some FeSOD variants. Reprinted with permission from ref 545. Copyright 2008 American Chemistry Society.

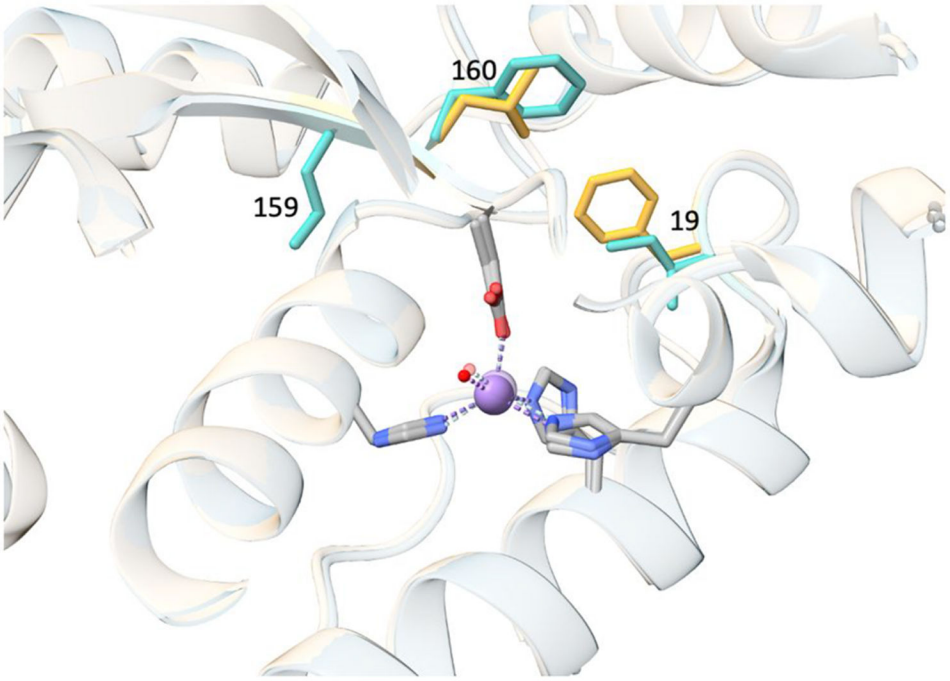

Figure 59.
Structure overlay of MnSOD (PDB ID: 5N56, yellow, F19/G159/L160) and CamSOD (PDB ID: 5N57, blue, I19/L159/F160).[547]

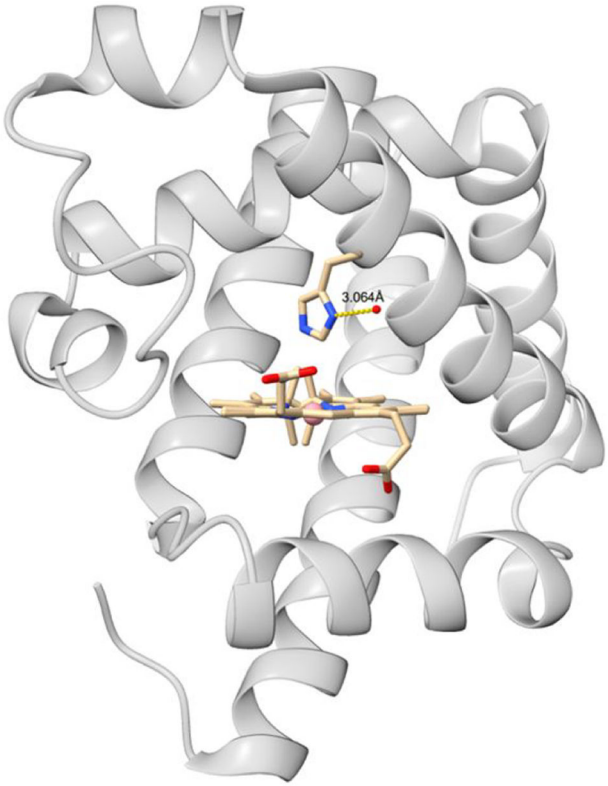

Figure 60.

Crystal structure of horse heart myoglobin reconstituted with Co^{II}-tetradehydrocorrin (PDB ID: 3WFT).[550] The $N_{\delta 1}$ atom of His64 hydrogen bonded to a water molecule is shown.

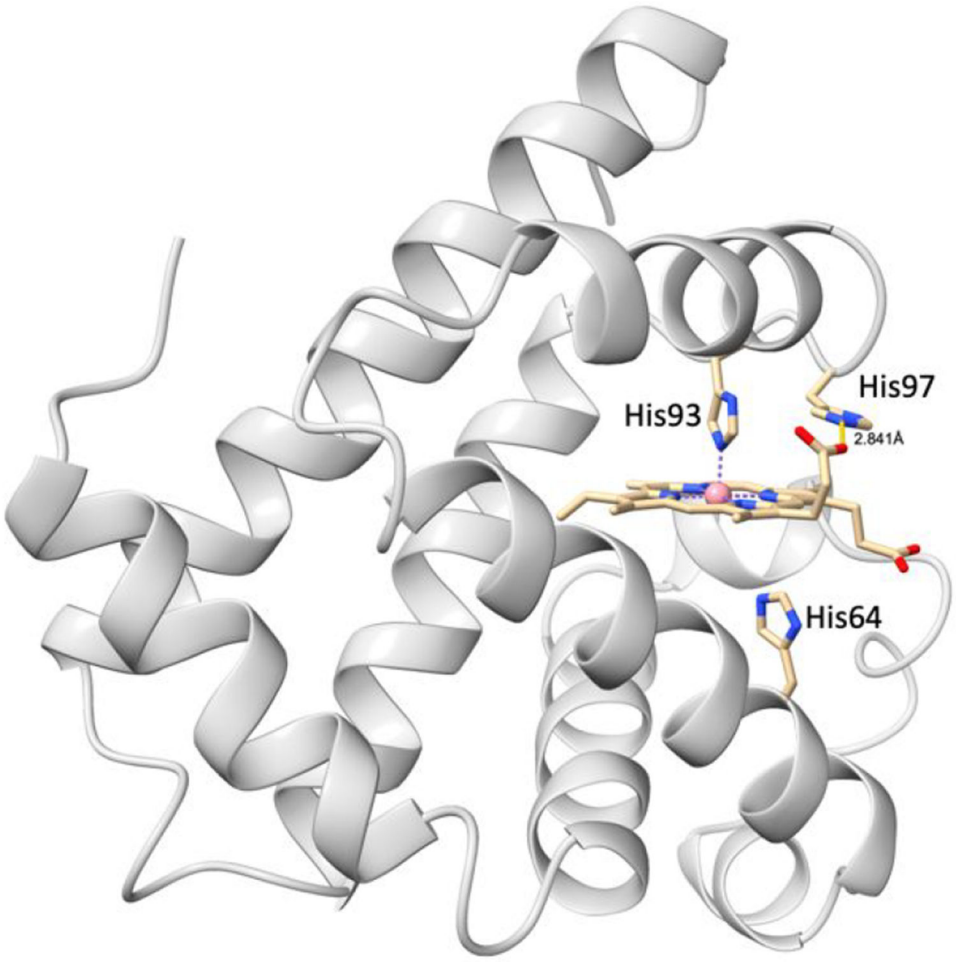

Figure 61.
Crystal structure of Co-Mb highlighting residues His64/93/97 (PDB ID: 1YOI).[552]

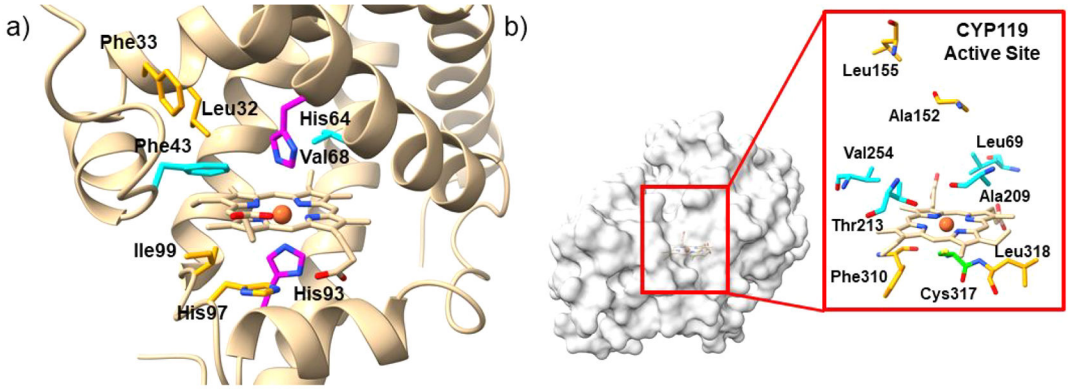

Figure 62.

(a) Inner sphere (red), middle sphere (cyan), and outer sphere (orange) residues of the active site studied in Mb-based ArM for carbene insertion reactions (PDB ID: 1MBN).[558] (b) Residues studied in CYP119-based ArMs: axial ligand for heme (green); residues lining the substrate binding pocket (cyan); residues to the distal sites of the substrate binding pocket (orange) (PDB ID: 1IO7).[559]

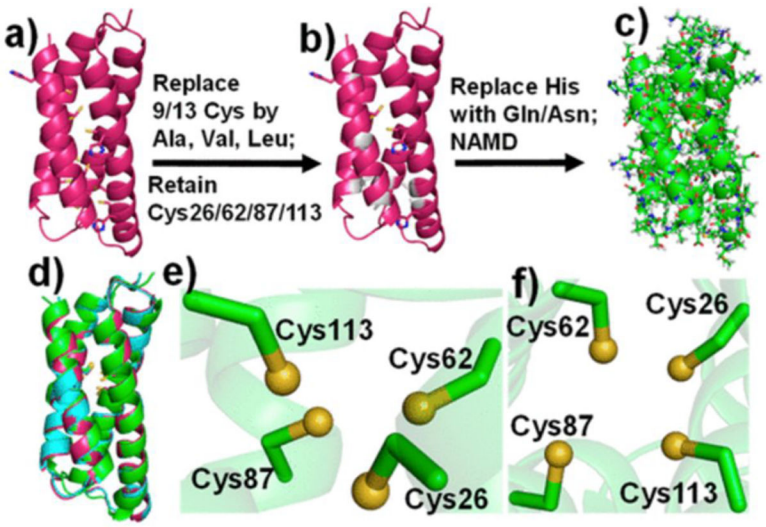

Figure 63.

Redesign approach for the conversion of Csp1 (a and b) to a Ni-binding protein (NBP). Copyright NAMD model of apo NBP. (d) Overlay of the X-ray structures of apo Csp1 (purple, PDB ID: 5FJD) and Cu^{I}-Csp1 (cyan, PDB ID: 5FJE) and the minimized structure of apo NBP (green). Ball and stick model of the tetrathiolate site of minimized NBP viewed perpendicular to the helical axis (e) and from the top of the helical axis (f) with N-terminus at the top. Modeling performed using CHARMM22 force fields. Reprinted with permission from refs 560 and 562. Copyright 2019 and 2015 American Chemistry Society and Nature Publishing Group.

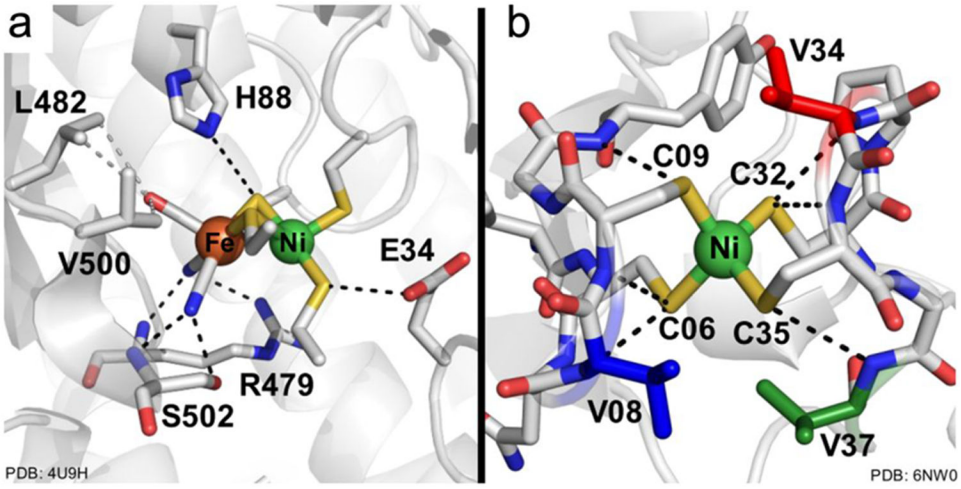

Figure 64.

Structures of the (a) Dv MF NiFe H_2ase and (b) Dd NiRd active sites including key secondary sphere interactions. Reprinted with permission from ref 563. Copyright 2019 American Chemistry Society.

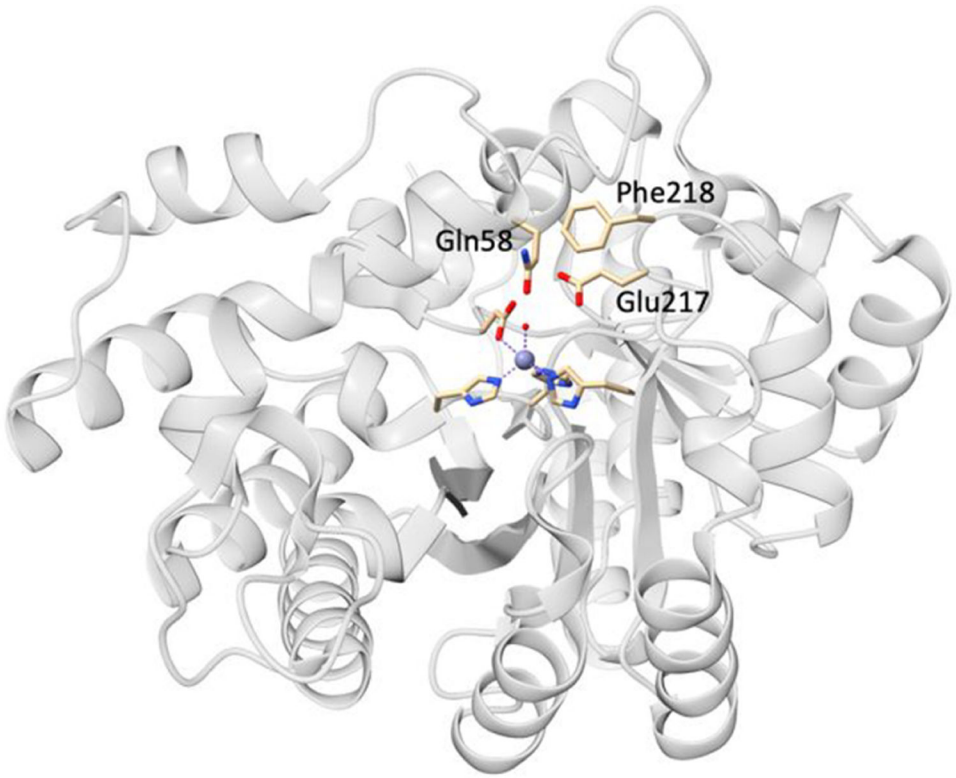

Figure 65.
Structure of engineered organophospate hydrolase PT3.1. Residues 58 and 218 influencing the hydrophobicity of Glu217 are shown in sticks (PDB ID: 3T1G).[565]

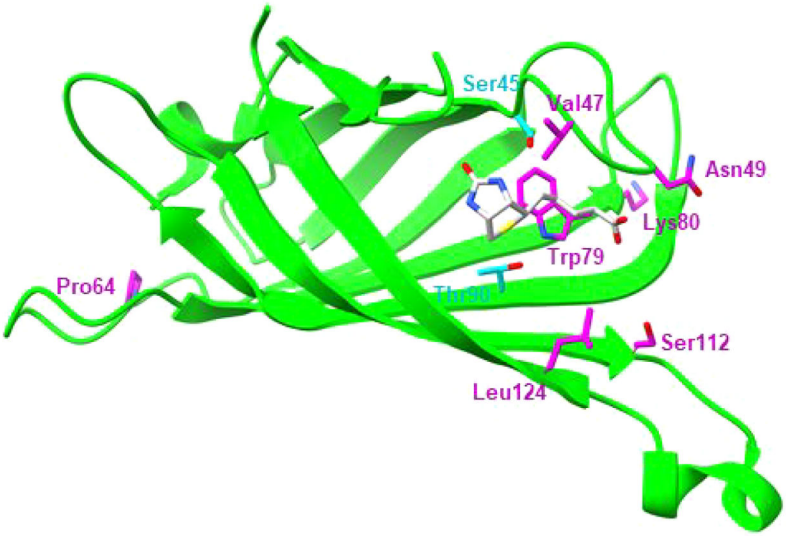

Figure 66.

Crystal structure of a wild-type Sav with bound biotin with the relevant residues show (PDB ID: 1STP).[572] The protein backbone is shown in green, and biotin C atoms are shown in white, relevant residues with direct interaction with biotin in cyan, and relevant residues distal to biotin in magenta.

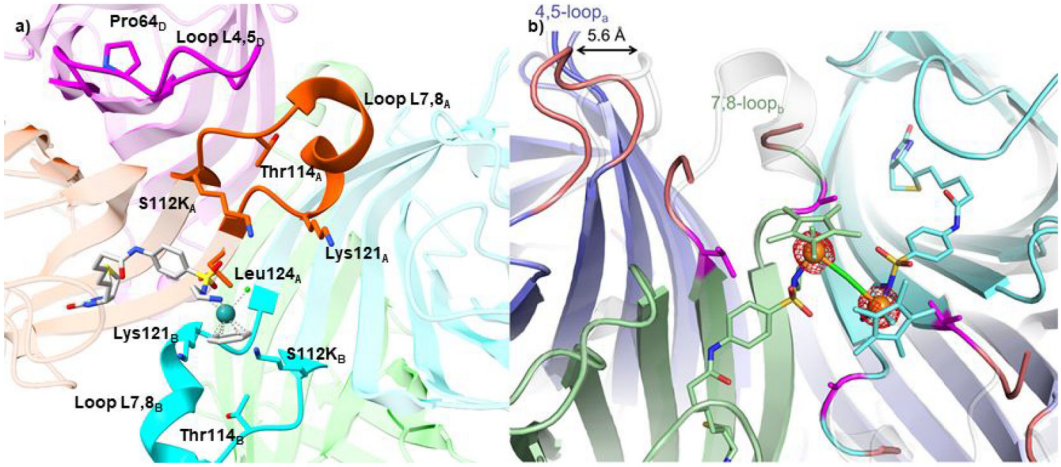

Figure 67.

(a) Crystal structure of a Ru complex-based Sav ArM tetramer showing the positions of relevant protein residues and loops (PDB ID: 2QCB):[576] monomer A (orange); monomer B (cyan); monomer C (green); monomer D (magenta); Ru complex (white). (b) Crystal structure of Ir complex-based Sav-FPD S112V-K121A (PDB ID: 6GMI) overlaid with Ir complex-based Sav S112A (PDB ID: 3PK2): monomer A of Sav-FPD S112V-K121A (blue); monomer B (green); monomer C (lilac); monomer D (cyan); Sav S112A (gray); mutated residues S112V and K121A (magenta). Reprinted with permission from ref 579. Copyright 2018 American Chemical Society.

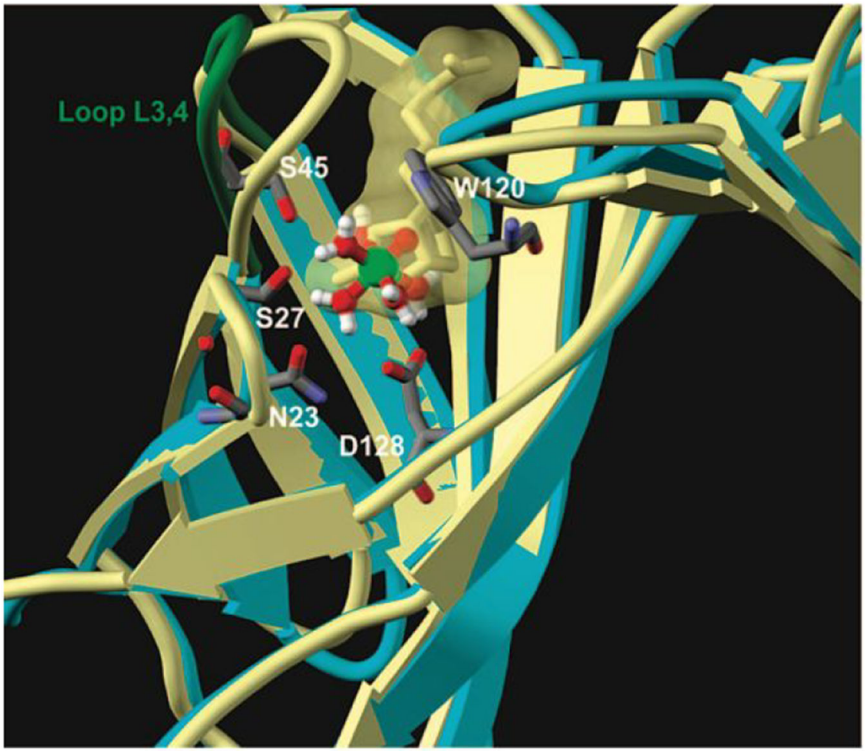

Figure 68.

Superimposition of the docked structure $[VO(H_2O)_5]^{2+}$ (ball-and-stick representation) with WT-Sav (monomers A and D, light blue schematic secondary structure) with the structure of biotin with WT-Sav (PDB ID: 2IZG): biotin (yellow stick and yellow transparent surface); monomers A and D (yellow schematic secondary structure). Reprinted with permission from ref 589. Copyright 2008 American Chemistry Society.

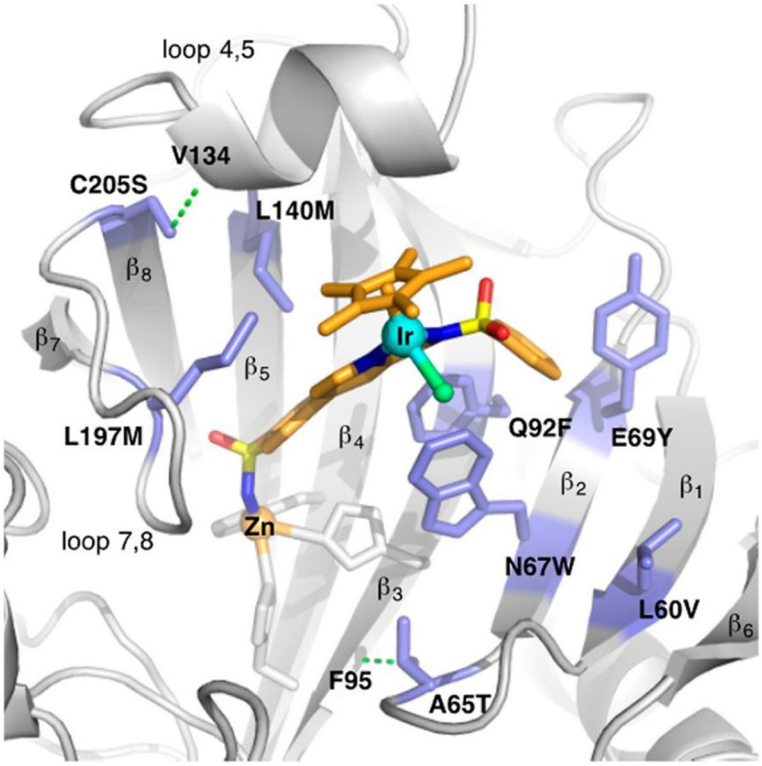

Figure 69.

Model of Rosetta design on the crystal structure of the Ir complex in WT-hCA II (PDB ID: 3ZP9). Designed backbone-stabilizing H-bonds are represented as green dashed lines. Reprinted with permission from ref 597. Copyright 2015 American Chemical Society.

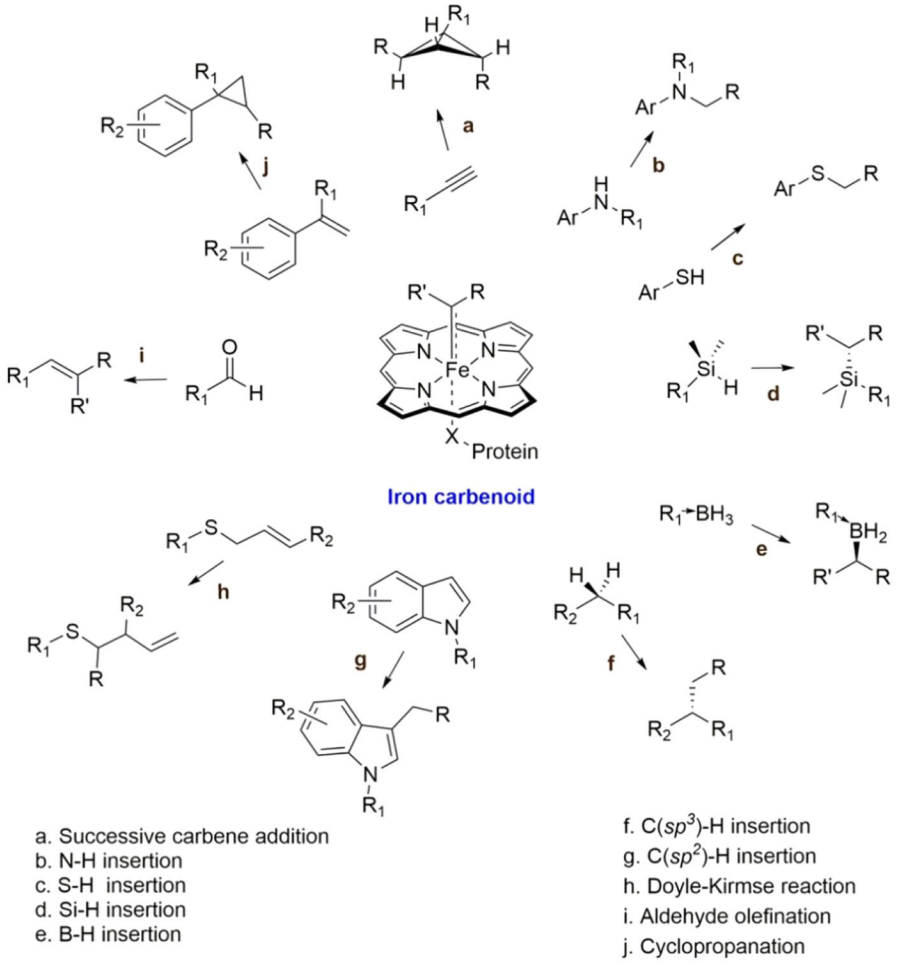

Scheme 1. Carbene Transfer Reactions Catalyzed by Evolved Hemoproteins[a]

[a] Reprinted with permission from ref 130. Copyright 2021 American Chemical Society.

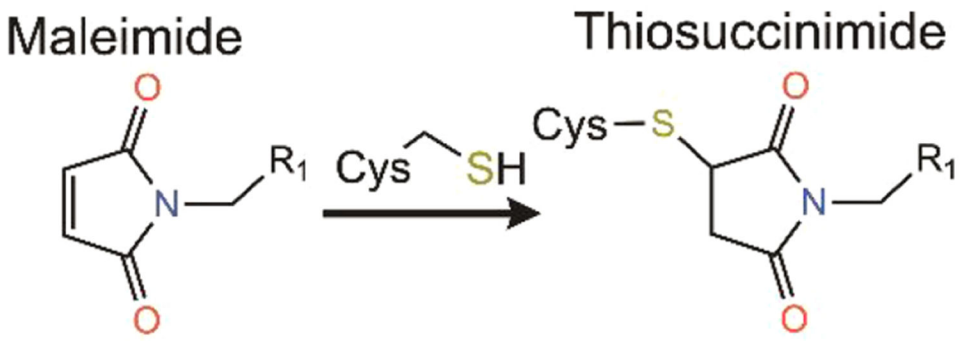

Scheme 2.

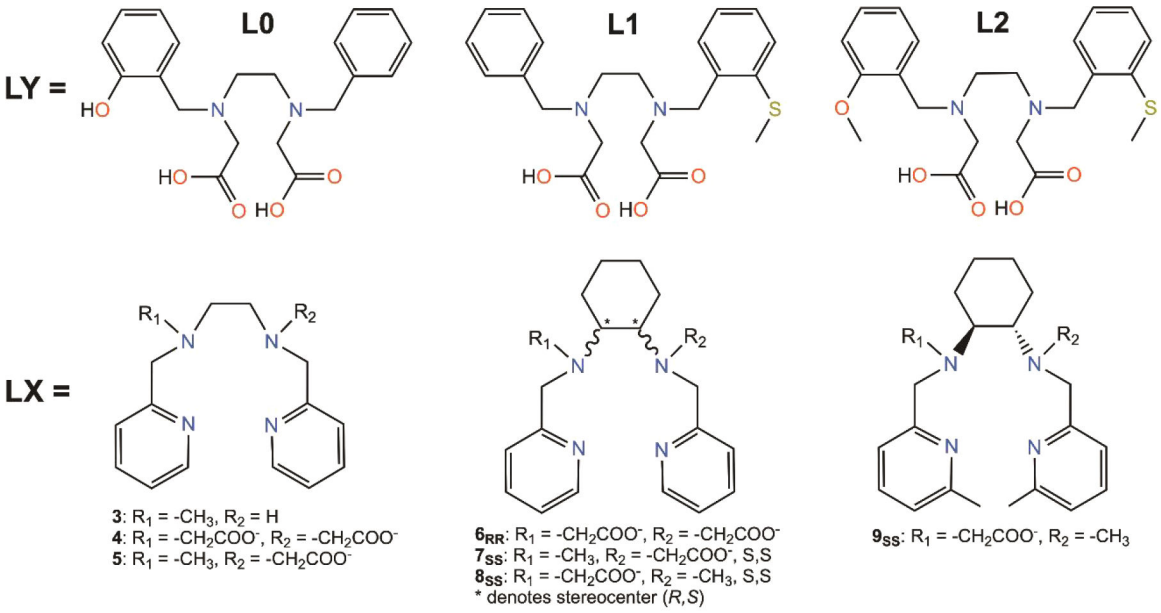

Scheme 3.

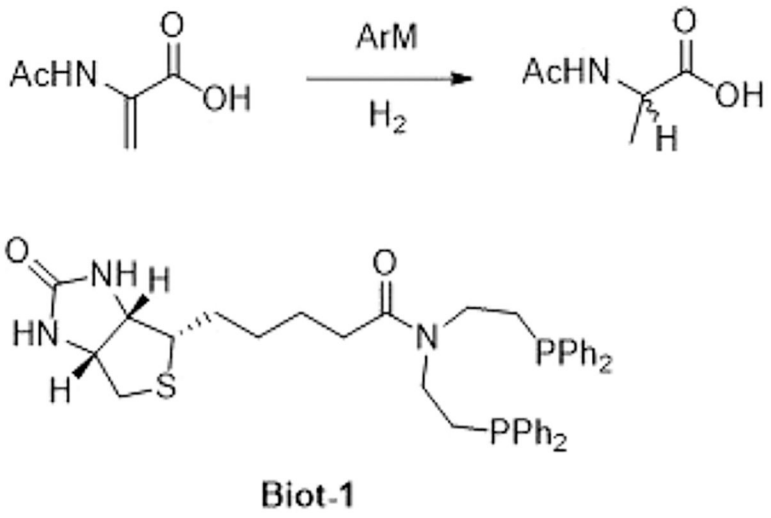

Scheme 4. Enantioselective Hydrogenation of α-Acetamidoacrylic Acid and Structure of Biot-1[568]

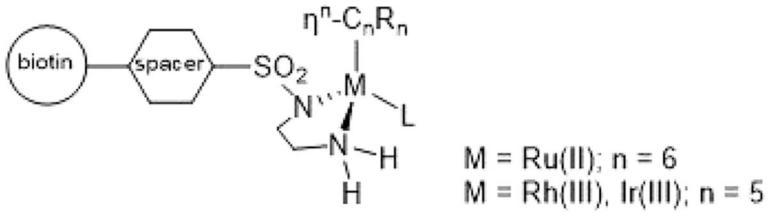

Scheme 5.
Formation of a Series of Artificial Transfer Hydrogenases[574575]

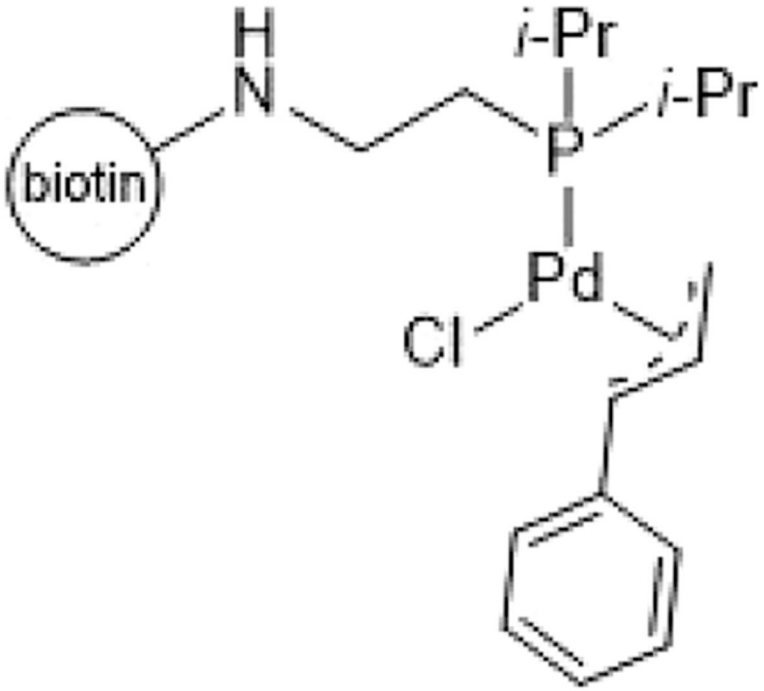

Scheme 6.
Suzuki-ase ArM Generated by Incorporation of a Pd Complex into Sav[586]